Graphene-based superconducting quantum circuits : the Josephson parametric amplifier

Guilliam Butseraen

THÈSE

Pour obtenir le grade de

DOCTEUR DE L'UNIVERSITÉ GRENOBLE ALPES

École doctorale : PHYS - Physique
Spécialité : Physique de la Matière Condensée et du Rayonnement
Unité de recherche : Institut Néel

Circuits quantiques supraconducteurs à base de graphène: l'amplificateur paramétrique Josephson

Graphene-based superconducting quantum circuits: the Josephson parametric amplifier

Présentée par :

Guilliam BUTSERAEN

Direction de thèse :

François LEFLOCH CEA	Directeur de thèse
Julien RENARD Chargé de Recherche, Université Grenoble Alpes	Co-encadrant de thèse

Rapporteurs :

GARY STEELE
Professeur, Delft University of Technology
ZAKI LEGHTAS
Maître de conférences HDR, MINES PARIS TECH

Thèse soutenue publiquement le **8 novembre 2022**, devant le jury composé de :

JULIA MEYER Professeur des Universités, UNIVERSITE GRENOBLE ALPES	Examinatrice
GARY STEELE Professeur, Delft University of Technology	Rapporteur
ZAKI LEGHTAS Maître de conférences HDR, MINES PARIS TECH	Rapporteur
HELENE LE SUEUR Chargé de recherche, CNRS DELEGATION ILE-DE-FRANCE SUD	Examinatrice
JESPER NYGARD Professeur, Københavns Universite	Président

Invités :

JULIEN RENARD
Chargé de Recherche, CNRS DELEGATION ALPES

Abstract

Les circuits quantiques supraconducteurs, comprenant un large éventail d'éléments, ont contribué à des avancées majeures dans le domaine de l'optique quantique micro-onde. Parmi ces éléments, les amplificateurs paramétriques atteignant la limite quantique ont démontré leur importance dans la mesure de systèmes quantiques dont l'énergie est intrinsèquement basse (dizaines d'µeV). Ils peuvent aussi servir à créer des états non-classiques de lumière qui peuvent être utilisés pour créer des détecteurs innovants. Les amplificateurs paramétriques supraconducteurs, tout comme les qubits, utilisent la plupart du temps une jonction Josephson comme source de nonlinéarité non dissipative et contrôlable en champ magnétique. Le contrôle en champ magnétique n'est pas la norme dans l'industrie et commence déjà à être un problème dans les circuits comprenant beaucoup d'éléments. Ces dernières années, un concept alternatif a émergé avec l'utilisation de jonctions Josephson faites à base de semiconducteurs afin d'avoir un contrôle électrique de la nonlinéarité, notamment avec la démonstration de résonateurs micro-ondes et de qubits utilisant des nanofils semiconducteurs, un gaz d'électrons 2D, des nanotubes de carbone ainsi que du graphène. Cependant, les amplificateurs paramétriques n'ont pas encore été réalisés en utilisant une jonction semiconductrice. Le travail présenté dans ce manuscrit de thèse de doctorat montre la conception, la fabrication et les performances d'un amplificateur paramétrique utilisant une jonction Josephson à base de graphène.

Le graphène est encapsulé entre deux couches de h-BN afin d'augmenter sa qualité. En utilisant une telle jonction, nous réalisons une amplification avec un gain de 20 dB qui est un jalon important pour que le bruit ajouté par les amplificateurs classiques du reste de la chaine d'amplification soit négligeable. L'amplificateur paramétrique étant construit à partir d'une structure résonante (autour de 6 GHz), il ne peut qu'amplifier une bande de fréquence réduite de l'ordre de quelques Mégahertz. L'utilisation d'une grille latérale permet de contrôler le graphène électriquement modifiant l'inductance de la jonction Josephson et ainsi la fréquence de résonance de l'amplificateur. Nous démontrons la possibilité d'ajuster la fréquence d'amplification sur un intervalle de l'ordre d'un Gigahertz grâce à cette grille latérale, ce qui est comparable en terme d'ajustabilité à l'utilisation d'un SQUID contrôlé en champ magnétique pour un circuit similaire. Par ailleurs, il a été montré que le graphène possède des pertes nonlinéaires lorsqu'il est exposé à un champ micro-onde important à cause d'excitations / désexcitation d'états d'Andreev. La dissipation est synonyme d'une augmentation du bruit intrinsèque ajouté par les amplificateurs paramétriques et peut donc être un problème pour atteindre la limite quantique. Nous démontrons que malgré la présence de pertes nonlinéaires, l'amplificateur paramétrique à base de graphène se rapproche de la limite quantique. Un modèle de pertes à deux photons est utilisé pour décrire le comportement du

dispositif mais nous démontrons qu'un modèle plus complet est nécessaire afin de prendre en compte la nature complexe de la dissipation ainsi que la relation courant phase non sinusoïdale. Nous avons également étudié la plage dynamique et montrons que l'amplificateur paramétrique à base de graphene peut atteindre un point de compression à 1dB de -123 dBm, ce qui comparable à ce qui peut être obtenu avec une jonction tunnel unique. Nos résultats élargissent l'ensemble des éléments existant pour le contrôle électrique des circuits quantiques supraconducteurs et offrent de nouvelles opportunités pour le développement de technologies quantiques comme l'informatique quantique, la détection quantique ainsi que la science fondamentale.

With a large portfolio of elemental quantum components, superconducting quantum circuits have contributed to dramatic advances in microwave quantum optics. Of these elements, quantum-limited parametric amplifiers have proven to be essential for low noise readout of quantum systems whose energy range is intrinsically low (tens of μeV). They are also used to generate non classical states of light that can be a resource for quantum enhanced detection. Superconducting parametric amplifiers, like quantum bits, typically utilize a Josephson junction as a source of magnetically tunable and dissipation-free nonlinearity. The magnetic control is not an industry standard for devices and starts already to be an issue in large scale circuits. In recent years, efforts have been made to introduce semiconductor weak links as electrically tunable nonlinear elements, with demonstrations of microwave resonators and quantum bits using semiconductor nanowires, a two dimensional electron gas, carbon nanotubes and graphene. However, given the challenge of balancing nonlinearity, dissipation, participation, and energy scale, parametric amplifiers have not yet been implemented with a semiconductor weak link. The work presented in this PhD thesis demonstrates the design, fabrication and performances of a parametric amplifier leveraging a graphene Josephson junction.

The graphene is encapsulated in between h-BN flakes in order to improve its quality. Using such high quality junctions, we demonstrate amplification with 20 dB gain which is the milestone for overcoming noise of the classical amplifiers in the rest of the amplification chain. The Josephson parametric amplifier being based on a resonant structure (around 6 GHz) suffers from the gain bandwidth product limiting the amplification to a few MegaHertz frequency range. The use of a side gate to electrically tune the graphene gives control of the Josephson junction inductance and thus the resonant frequency of the amplifier. We demonstrate a near 1 GHz tunability of the amplification frequency with the use of a side gate which is as good as the tunability offered by using a magnetic flux on a SQUID for similar amplifier designs. Moreover, graphene has shown to exhibit nonlinear loss under a strong microwave irradiation arising because of dynamics in the Andreev states. Dissipation is known to add intrinsic noise on quantum amplifiers and could be a problem for quantum limited parametric amplification. We demonstrate that despite the presence of nonlinear

loss, graphene based Josephson parametric amplifiers can reach near quantum limited amplification. A two photon loss model was used to describe the behaviour of the device but we show that a more complex model is required in order to take into account the nonlinear dissipation and the non-sinusoidal current phase relation. We also studied the dynamic range and showed that the graphene based Josephson parametric amplifier can reach a 1 dB compression point of -123 dBm which is as good as single tunnel junctions based parametric amplifiers. Our results expand the toolset for electrically tunable superconducting quantum circuits and offer new opportunities for the development of quantum technologies such as quantum computing, quantum sensing and fundamental science.

Remerciements

Je ne sais pas à quel point cela est commun, mais ma thèse fut probablement l'une des meilleures expériences de ma vie. Je me rends compte à quel point l'environnement dans lequel elle s'est déroulée, ainsi que l'environnement dans lequel je baigne depuis toujours m'a permis de m'épanouir pendant ces quelques années. Je vais essayer ici de remercier les personnes qui m'ont aidé et accompagné le long de ce chemin. Warning: j'ai parfois une façon de remercier un peu particulière, ne prenez pas tout au premier degré.

Tout d'abord, merci Julien. Je suis si heureux d'avoir croisé ta route par hasard grâce à cette innocente annonce de stage. Tu as tout de suite eu une totale confiance en moi, parfois un peu déconcertante au début, mais tellement agréable au quotidien. Je n'ai jamais eu l'impression d'être sous les ordres de quiconque, mais plutôt d'avancer sous ta bienveillante guidance. Je pense que je ne pouvais pas rêver mieux pour apprendre et aller au bout du projet.

Je remercie également François, qui a accepté d'être mon directeur officiel malgré ses innombrables responsabilités. Au début, je pensais que ton rôle serait purement administratif, mais tu m'as démontré le contraire. J'ai de nombreuses fois pu profiter de ton incroyable expérience et de ta bonne humeur. A chaque fois, tu as réussi à me faire aborder les grands moments de la thèse dans un état d'esprit plus serein si bien que j'ai pu en profiter au lieu d'être stressé.

Un énorme merci à l'équipe HYBRID dans laquelle j'ai eu la chance d'évoluer. Tout d'abord les permanents. Laëtitia, ta joie et ta bonne humeur sont contagieuses, ce fut un plaisir d'interagir avec toi. Nedjma, merci de m'avoir guidé pendant mes années d'enseignement à l'Université, ainsi que d'avoir supporté mes blagues parfois provocatrices (c'était trop tentant avec toi !). Johann, j'ai appris énormément de choses grâce à ta rigueur et tes questions pendant les group meeting. Now a bit of English for the non-permanents, I have so many good memories with all of you, and I would need a full chapter to write my gratitude. Gom, thanks a lot for teaching me all about graphene fab during my internship. Even more importantly, thanks for all the palak paneers, and for our crazy discussions in the city after enjoying Indian food! Kazi, it was so nice to have somebody like you to rely on. I benefited so much sharing the cryostat with you. My only regret is that I never tried your biryani (I was told you make the best) ! Abhishek, thanks a lot for sharing the small cryostat with me when I needed it. I always appreciated your experience in life. Priyank (the famous), thanks a million to have taught me astral projection (Sorry I had to make the joke). More seriously, I feel that if time was going a bit slower we could have had billions of discussions about sports, food, quantum

fluctuations, free will, India, and everything actually. Thanks for all the fun, debates, science, and for opening my mind to become a naga sadhu. I wish we could have had more time to do a bit more crazy hikes. Andrej, your time in the lab was quite short but so many things happened during this period. I think it was the funniest part of my PhD. Thanks for allowing the Hybrid team to win the football competition, for all the jokes, bars and for the strange party near Bastille during a storm. Ana, Roberto and Estelle, when I think about you I cannot do without smiling. You remind me of my very beginning at the lab when I was still young and innocent, before covid and all the other difficulties, a bit like childhood memories. Enzo thanks for being you. You brought a lot of fun, lots of questions and scientific interest. Riadh, I always appreciated our non serious discussions, thanks for all the time we laughed together. Maria-Theresa (I know you love being called by your full name), it was a pleasure to teach you all my knowledge (I hope it was not too limited !). Thanks a lot for helping me with the stacks and with many other things. I miss the gang we used to form with you and Priyank. Nicolas, it is the same for you, I hope you appreciated the time I spent to teach you my knowledge. I always took care of adding a bit of fun in everything, I hope it was not too much. Thanks for helping me with the stacks and the fab, it was so precious at the end of my Phd. You are also so kind with everybody, the team really benefits from your kindness, do not change (and good luck with your PhD !). Aloïs, Suman and Williams, it was a pleasure to share the last moments of my PhD with you. We had a lot of fun, I regret not being more available at this time because I was very busy. I will miss our game on board (the hung guy).

I would also like to thank the Coherence Quantique team for their experience in superconducting circuits, you are all so talented . I learnt so much discussing with you and assisting in your group meetings. I would like to particularly thank Nico, Arpit and Martina for giving me the chance to measure my sample in their amazing setup (and also for helping me to do so). Thanks to you, I think my results reached another level.

Merci également à l'équipe QNES pour avoir partagé tant d'astuces et de savoirs à propos du graphène. En particulier, merci à la petite bande de grincheux (Alexis, Hadrien, Marco, Corentin). J'ai passé des moments exceptionnels à vos côtés autour de bonnes bouteilles de vin.. Corentin, ta rigueur et ta motivation m'ont toujours impressionné. Tes talents dans la dégustation me manquent, maintenant les autres se moquent de moi quand je trouve des goûts de beurre ou de vanille dans le vin. Marco, merci pour ton excentricité, tu es le genre de personne qui brise le quotidien et apporte toujours quelque chose de nouveau. Merci aussi pour tes talents de musicien. Que ce soit avec le saxophone ou le piano, je suis toujours resté sans voix quand j'ai eu la chance de t'écouter. Hadrien, mon petit ducky, mec mec mec mec, mec mec mec mec mec mec, mec mec mec ! Alexis, que dire ? Mage noir, Raptor, Thanos. Ce sont des titres que tu aimerais qu'on utilise pour te décrire, mais c'est dans la noirceur la plus profonde qu'on peut apercevoir la lumière la plus pure. Merci pour toutes les soirées, discussions, bouteilles de vin, sushi, et d'avoir aussi eu le courage de me suivre dans des aventures plus ou moins douteuses (au prix de t'avoir traumatisé parfois comme pour la via ferrata). Thibault, je me rends compte que je ne sais pas trop dans quel paragraphe te remercier. Je te mets donc ici, sois en flatté.

Je veux également remercier les PLUM de la F218. Marco, merci pour tous ces délires, et aussi pour avoir organisé plein de trucs, notamment le tournoi de foot ou on vous a humilié.

Hippolyte, merci pour avoir été mon 'suppléant' en tant que représentant des non permanents au labo. Tu m'as beaucoup 'aidé' (il n'a jamais assisté à une seule réunion et n'a pas pu me remplacer la seule fois ou j'en avais besoin). Julian, merci pour ton accent Allemand et ta voix très grave. Laurie, merci d'être Belge comme moi. Même si tu es Wallonne, la bière coule aussi dans tes veines, et tes os sont aussi fait de frites donc je t'accepte. Blagues à part, merci à tous pour les supers moments passés ensemble.

Je souhaite maintenant remercier un grand nombre de personnes au sein de l'institut Néel, car c'est un lieu que j'ai trouvé formidable. Tout d'abord merci au personnel administratif et en particulier à Florence Pois, Anne-Laure Jaussent, Angélique Simoes, David Magrez et Otmane Benhamed qui m'ont rendu de nombreux services durant ces quelques années. Je remercie également Patrick Belmain et Julien Michel pour leur rapidité à résoudre les problèmes informatiques que j'ai pu rencontrer. Ma gratitude au pôle Ingénierie expérimentale, en particulier à Laurent Del-Rey, Julien Jarreau, Didier Dufeu, Eric Eyraud pour toute l'aide apportée au niveau du cryostat, ainsi que Richard Haettel pour son extrême gentillesse et l'aide apportée à l'utilisation du four de recuit. Un immense merci au pôle nanofabrication pour avoir géré la salle blanche et m'avoir aidé à de nombreuses reprises. En particulier Thierry pour tous mes problèmes de lithographie ou de microbonding. Bruno, Gwenaelle et Jeff pour leur aide au niveau de la RIE ou du dépôt de métal. Latifa pour ces nombreux délires (encore désolé pour le lapin que je t'ai posé pour notre premier rdv litho optique), je ne peux pas trop m'étendre ici, ce serait un peu gênant ! Je remercie également Simon Le-Denmat pour m'avoir enseigné l'art de l'AFM et m'avoir très vite fait confiance. Sébastien Pairis pour avoir géré les plateformes microscopie que j'ai utilisées. Philippe David ainsi que David Barral pour leur aide quant à l'utilisation de la machine de sputtering. Frédéric Gay pour m'avoir aidé malgré un contexte difficile. Je remercie également Valery Reita qui m'a accueilli (et materné) dans son bureau dans mes tous premiers instants au laboratoire. Jérémie Viennot pour son tempérament que j'apprécie beaucoup et qui a toujours été de bon conseil. Olivier Bourgeois pour avoir accepté d'être dans mon CSI. Étienne Bustarret pour sa bienveillance à mon égard pendant les conseils de laboratoire. Now a bit more of English to thank all the non-permanents with whom I interacted, had fun, and learnt a lot. En brisant la causalité, je te remercie également Bekim.

J'ai créé de nombreuses amitiés au laboratoire mais un important soutien vint aussi de mes amis en dehors de celui-ci, notamment tous ceux que j'ai rencontrés pendant mes études à Lyon. Merci à Yannick pour m'avoir introduit à la rando (et avec qui j'ai eu la chance de découvrir le Néron), ça a changé ma vie. Merci à Robin, même si tu me détestais la première fois que tu m'as vu, tout à changé aujourd'hui, tant d'aventures.. Merci à Slava pour ta joie de vivre, c'est très contagieux. Merci à Tudy et Cristina, vous revoir m'a fait un bien fou, j'ai de nombreux souvenirs gravés dans ma mémoire à jamais grâce à vous. Aurélien, pour ton tempérament hors du commun, c'est toujours un plaisir d'être à tes côtés. Merci aussi d'avoir embarrassé Grégoire avec moi en faisant tu sais quoi en CM. Grégoire, pour ta capacité d'analyse sans précédent (il t'arrive aussi d'être drôle). Merci également d'avoir harcelé Aurélien à mes côtés. Léa, pour ton extrême gentillesse et pour avoir carry tant de nouvels ans aux côtés de tous ces 'physiciens' incapables. Grégory, pour tous tes conseils, pour avoir carry la partie musique pendant les nouvels ans avec Guillaume (ainsi que pour tes talents de dessinateur). Merci à Audrey, Cécile et Julie pour avoir rendu mes amis heureux. Charly,

pour être si surprenant et pour être ma référence quand je parle de Caltech ou de la NASA.

Merci à certaines personnes que je connais depuis avant mes études supérieures. Jérémy pour ton extrême sympathie et pour avoir été si patient avec moi. Merci d'avoir pris le temps de venir me voir, j'en garde des souvenirs exceptionnels. Léo, même si on ne s'est pas vu autant de fois que je l'aurais souhaité pendant cette thèse, merci pour tous ces moments passés que je garde dans mon coeur. Marine, pour ton petit caractère, j'ai beaucoup ri à tes côtés. Dommage que tu n'ais pas pu faire un petit morceau de thèse à Grenoble comme prévu. Merci à Marc Champagne pour avoir été un super prof de math et de section euro au Lycée. Grâce à toi je connais Zermelo, et ta vision de la pédagogie m'a toujours guidé. Tu gagnes la palme de mon prof préféré pendant ma longue scolarité.

Merci à Suzanne, rencontrée par hasard au début de la thèse, et qui a tout changé. Grâce à toi la thèse a pris une autre dimension et c'est en partie la raison pour laquelle j'ai été si heureux pendant cette période. Jamais je n'aurais pensé trouver quelqu'un avec qui je peux partager tant de choses, que ce soit au niveau du sport, de la culture, et même de faire des maths pour hobby. Merci d'avoir supporté ma dévotion au travail, ça a rendu les choses tellement belles. Merci à ta famille, Louise, Hector, bébé boule, Isabelle, Nadine et Bruno. Cela fait depuis longtemps que je vis loin de la mienne, et ça fait vraiment plaisir d'en avoir une autre juste à côté.

Pour finir, merci à ma famille qui a toujours eu une confiance absolue en ma personne. Si j'en suis là aujourd'hui, c'est grâce à vous. J'ai tant appris de chacun d'entre vous. Merci infiniment, ma plus grande chance a été d'être né où je l'ai été.

à Ruben

Table of Contents

Appendix

Introduction

The rise of quantum technologies was allowed by the considerable development of nanofrabrication techniques which led to the fabrication of on chip circuits whose quantum degrees of freedom can be controlled individually (i.e. qubits). A leading approach to build such quantum circuits was the use of superconducting materials together with Josephson junctions. By doing so, artificial atoms were created, and like real atoms, they can be controlled by the use of light. The superconducting nature of the circuit imposes the energy scale of photons that can be used to monitor them. Their energy cannot be above twice the superconducting gap which is typically of the order of 1 meV. This is why the operation and control of superconducting quantum circuits rely on the use of microwaves.

Typically, the measurement of qubits rely on measuring a few microwave photons. Their energy being five orders of magnitude smaller than the energy of optical photons makes this task incredibly hard and requires the use of ultra low noise amplification. The best cryogenic 'classical' amplifiers, high electron mobility transistors, add typically 10 to 20 photons of noise because of internal dissipation, which is enough to hide the qubit signal. Therefore, the idea of using a superconducting material presenting no dissipation to build an amplifier emerged, and relied also on the use of Josephson junctions in order to bring the required nonlinearity to perform 'parametric amplification'. Yurke was the first to demonstrate such a Josephson parametric amplifier (JPA) with noise performances close to the minimum allowed by quantum mechanics (also called quantum limited amplifier [1]) in 1989 [2]. JPAs enable also the possibility of squeezing vaccum or thermal noise making one quadrature smaller than the minimum allowed by quantum mechanics [2]. This was 10 years before the first superconducting qubit [3] was even demonstrated which could explain why at this time, his work did not catch a huge interest in the scientific community. In the early 2000', tremendous development was made in superconducting quantum circuits [4, 5, 6, 7] making the need for quantum limited amplifier more important. In this context, Castellanos-Beltran *et al.* [8] developed a Josephson parametric amplifier based on the coupling of a superconducting resonant structure to Josephson junctions. This architecture became the state of the art manner of building such amplifiers for the next decade and allowed numerous advances. One can cite single shot measurement of superconducing qubits as well as the observation of quantum jumps [9], readout of spin qubits [10] but also electron spin resonance detection [11], imporvement in the detection of gravitational waves [12] and in the detection of axionic dark matter [13].

Traditionally, superconducting quantum circuits were built with tunnel Josephson junctions where a thin insulator forms a tunnel barrier between two superconductors. This can be

explained because back at the time of the initial development of superconducting quantum circuits, it was much easier to build tunnel junctions with the required properties than using another material to form the junctions. Nevertheless, the use of an insulator does not allow any intrinsic control of the circuit. Such a control is particularly important when two or more elements are coupled together. For this purpose, single Josephson junctions were replaced by Superconducting quantum interference devices (SQUID) enabling the use of a magnetic flux to control their energy. Nowadays, far from the single qubit demonstration in an academic lab, large companies such as Google and IBM started a race to create a quantum computer and are using circuits containing tens of qubits [14]. However, already in a two-qubit experiment, the use of a magnetic field can create magnetic field cross-talk resulting in unwanted coupling between distant qubits [15]. Moreover, magnetic fields are generated sending current through conductive lines dissipating heat due to Joule effect. One can imagine that this could be a problem in a future device with a large number of qubits because it would make the cooling power required to keep the circuit at cryogenic temperature very important (and even impossible to reach). A possible solution to overcome the two problems cited above and improve the scalability is to change the nature of the Josephson junction and use a gate tunable material instead of the insulating barrier. With such junctions, a gating line creating a very local electric field and no electrical current would directly solve the aforementioned issues while allowing for circuit control. As we will see later in this PhD manuscript, a lot of efforts have been made in this direction since 2015 with the successful achievement of gate tunable qubits and superconducting cavities. However, given the challenge of balancing nonlinearity, dissipation, and energy scale, parametric amplifiers have not yet been implemented with such a gate controllable junction. The work presented here, demonstrates the possibility of using graphene, a gate tunable 2D material, as a Josephson junction in a parametric amplifier using a current pumping scheme.

The manuscript is divided as follows:

Chapter 1 introduces the basic properties of graphene as well as an introduction of proximity effect which is key to understand how graphene can be used as a Josephson junction. Specific results on proximitized graphene will then be given. Eventually, we will present an overview of the use of gate tunable Josephson junctions in superconducting quantum circuits.

Chapter 2 presents the theory behind current pumped parametric amplification. We will see how a Josephson junction coupled to a superconducting resonant structure (lumped or distributed) can give rise to a Kerr type Hamiltonian. Using the input/output formalism we will see how such a system, coupled to external baths, can lead to parametric amplification with the use of a strong microwave tone (called pump tone) giving the required energy for amplification. We will then address the important limits of resonant parametric amplification and present a broad overview of some successful implementations of parametric amplifiers.

Chapter 3 gives the details about the fabrication process of graphene based Josephson parametric amplifiers starting from graphene exfoliation and encapsulation to the superconducting circuit fabrication. In a second part the different measurement setups are presented.

Chapter 4 focuses on the linear characterization of the graphene based Josephson parametric amplifier. First, microwave circuits basics will be presented. Then, explanations about the device geometry as well as electromagnetic simulations will be given and compared to measurements. A characterization of the DC and RF properties of the graphene Josephson junction is also given.

Chapter 5 is the most important chapter of this work because it demonstrates the possibility of using graphene to build a gate tunable Josephson parametric amplifier. All the figures of merit are studied. The first one is the gain provided by the amplifier. This quantity is very important because it should be large enough to overcome the noise added by the other amplifiers in the amplification chain. A 20 dB gain is often taken as a milestone to reach such a purpose. The second figure of merit is the bandwidth of the amplifier i.e. the frequency range that can be amplified. We will show that using a gate voltage one can compensate for a small bandwidth by shifting the amplified frequency. The third figure of merit is the compression point, i.e. how much power can be amplified without losing gain. This quantity is important because the amplifier should be able to amplify at least a few photons for realistic applications. The last figure of merit is the noise added by the amplifier which should be as close as possible to the quantum limit.

Graphene and superconducting weak links

CHAPTER 1

In this chapter we will review some properties of graphene and see how they can be controlled with a gate voltage. We will then introduce the proximity effect and show specific examples on Josephson junctions made of graphene. This will demonstrate the possibility of using SNS junctions as gate tunable element in superconducting quantum circuits and we will show recent examples of such implementations.

Contents

1.1 Introduction to graphene physics

Graphene is a two-dimensional (2D) material made of a monolayer of carbon atoms arranged in a honeycomb lattice as shown in Fig. 1.1a. Its 2D nature and lattice arrangement is responsible for particular electronic properties. It was successfully isolated and measured for the first time in 2004 [16, 17] and was then an active field of research. In this work, graphene was used as a way of controlling a superconducting circuit with an electric field and we will thus only present the properties directly impacting our work. The reader interested in a detailed description of the electronic properties of graphene can refer this review [18] or a very complete PhD thesis [19].

1.1.1 Graphene band structure

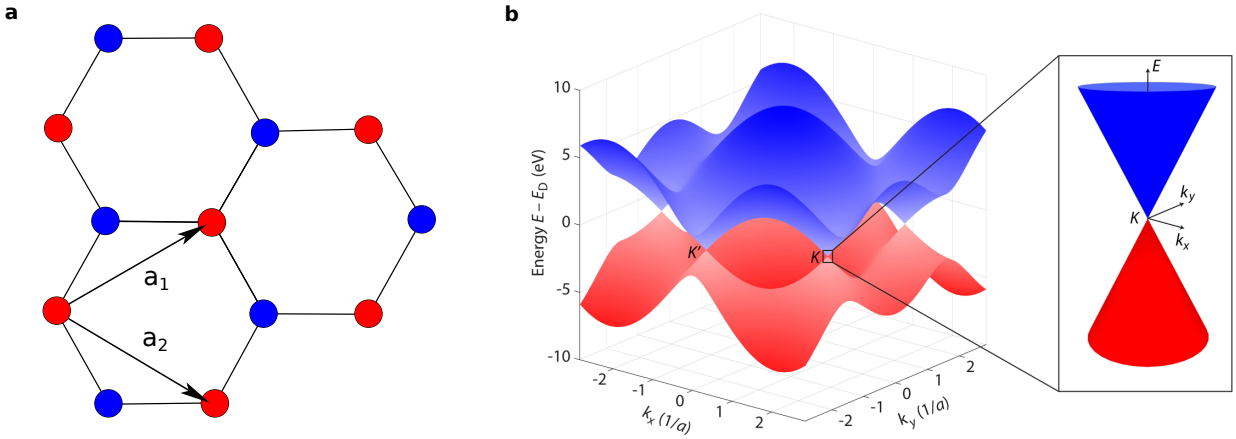

Figure 1.1: (a) Atomic structure of graphene. (b) Graphene band structure. Close to the K and K' points the dispersion relation is linear and charge carriers behave as massless relativistic fermions. Figure (b) adapted from [19].

The graphene atomic structure is shown in Fig. 1.1a. Atoms are arranged in a hexagonal pattern that can be decomposed into two triangular lattices with a basis of two atoms per unit cell and lattice vector a_1 and a_2. The bonds between atoms are made of a sp_2 hybridization between the s, p_x and p_y orbitals of carbon and are responsible of the mechanical and thermal properties of graphene. The p_z orbitals of carbon form π-bonds with neighbor atoms, leading to one free electron per atom determining the electronic properties of the material.

By using a tight-binding model, where we consider that electrons on one site can only hope to the nearest neighbor sites with a characteristic energy $t \approx 2.7$ eV, we can compute the dispersion relation $E(\mathbf{k})$ of electrons in graphene, i.e. its band structure. We obtain this way two solutions:

$$E_{\pm}(\mathbf{k}) = \pm t\sqrt{3 + 2\cos(\sqrt{3}k_y a) + 4\cos\left(\frac{\sqrt{3}}{2}k_y a\right)\cos\left(\frac{3}{2}k_x a\right)} \tag{1.1}$$

with $a \approx 1.42$ Å the inter atomic distance. There are thus two symmetric bands: the valence band (negative energy) and the conduction band (positive energy). Because each site is

occupied by one electron and each level can be occupied by two electrons of opposite spin, all the valance band energy levels are filled for undoped graphene, leaving the conduction band empty. There are particular k points, called Dirac points, for which the valence band and the conductance band are equal and $E_+ = E_- = E_D = 0$:

$$\mathbf{K} = \left(\frac{2\pi}{3a}, \frac{2\pi}{3a\sqrt{3}}\right), \qquad \mathbf{K'} = \left(\frac{2\pi}{3a}, -\frac{2\pi}{3a\sqrt{3}}\right) \tag{1.2}$$

A linearization around the Dirac points gives:

$$E_\pm(\mathbf{q}) = \pm\hbar v_F|\mathbf{q}| + \mathcal{O}\left(\left|\frac{q}{K}\right|^2\right) \tag{1.3}$$

where we introduced $\mathbf{k} = \mathbf{K} + \mathbf{q}$ with $|\mathbf{q}| << \mathbf{K}$, as well as the Fermi velocity:

$$v_F = \frac{1}{\hbar}\frac{\partial E_\pm}{\partial q}\Big|_{\mathbf{k}=\mathbf{K}} \approx \frac{3at}{2\hbar} \tag{1.4}$$

that can be computed from the values we gave previously: $v_F \approx 1 \text{ x } 10^6$ m.s^{-1}. The dispersion relation in the vicinity of the Dirac points is linear in $\mathbf{q}$ and analogous to the dispersion relation of light. Around these points, electrons are thus behaving like massless relativistic fermions. Fig. 1.1b shows the conduction band (blue) and valence band (red) of graphene. We can see that near the Dirac points, the 2D dispersion relation is a cone.

1.1.2 Density of states and gate tunability

1.1.2.a Density of states and carrier density

Using the expression of the dispersion relation close to the Dirac points we can compute the density of state $\rho(E)$:

$$\rho(E) = \frac{2}{\pi(\hbar v_F)^2}|E| \tag{1.5}$$

where we took into account the spin degeneracy as well as the valley degeneracy (K and K' are at the same energy). The density of state is thus symmetric for electrons and holes and vanishes at the Dirac point. We can now compute the charge carrier density n at the temperature $T = 0$:

$$n(T=0) = \int_{-\infty}^{+\infty} \rho(E) f_{FD}(E, T=0) dE = \text{sign}(E_F)\frac{E_F^2}{\pi\hbar^2 v_F^2} \tag{1.6}$$

with f_{FD} the Fermi-Dirac distribution and E_F the Fermi energy. We can thus express the Fermi energy as:

$$E_F = \hbar v_F|\mathbf{k}_F| = \text{sign}(n)\hbar v_F\sqrt{\pi|n|} \tag{1.7}$$

The 2D nature of graphene, as well as its low carrier density close to the Dirac point, makes it an ideal material for field effect because of reduced charge screening. By applying an electric field with a gate voltage V_g, we can thus change the charge carrier density resulting in

a change of the doping (or Fermi energy). The charge carrier density is linked to gate voltage as:

$$n = \frac{C_g |V_g - V_{CNP}|}{e} \tag{1.8}$$

where C_g is the capacitance between the graphene flake and the gate. We also introduced V_{CNP}, because there is always some residual doping coming from the graphene environment or the graphene itself. The residual doping changes the Fermi energy of graphene and pushes the Dirac point away from $V_g = 0$. At $V_g = V_{CNP}$, the charge carrier density is thus zero explaining why this point is also called the charge neutrality point (CNP). At $V_g > V_{CNP}$, electrons are injected in the upper part of the Dirac cone and at $V_g < V_{CNP}$ holes are injected in the lower part of the Dirac cone. Finally we can rewrite the Fermi level dependence on the gate voltage as:

$$E_F = \hbar v_F |\mathbf{k}_F| = \text{sign}(V_g - V_{CNP}) \hbar v_F \sqrt{\frac{\pi C_g}{e} |V_g - V_{CNP}|} \tag{1.9}$$

1.1.2.b Diffusive transport in graphene

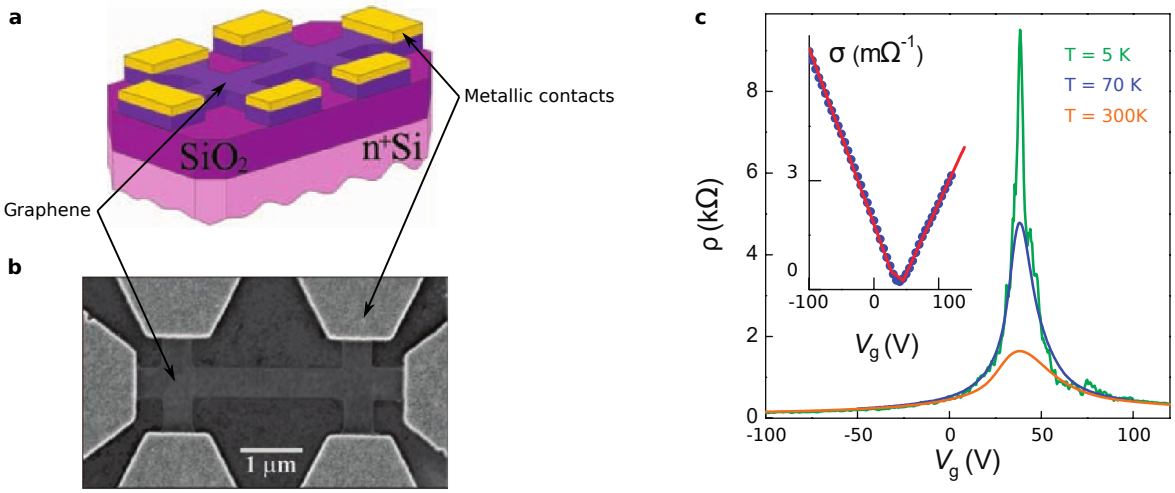

Figure 1.2: (a) Scheme of a graphene Hall bar on a Si/SiO_2 substrate. (b) Scanning electron microscopy of the device presented in (a). (c) Conductivity (at 70 K) and resistivity ρ as a function of the back gate voltage. Figures adapted from [16].

One can also express the conductivity of graphene:

$$\sigma = |e| n \mu \tag{1.10}$$

where μ is the mobility of graphene and can be computed using the Drude model:

$$\mu = \frac{|e| \tau_s}{m^*} \tag{1.11}$$

with τ_s the averaged time between two scattering events and $m^* = \hbar k_F / v_F$ the effective mass of charge carriers. Note that even if the charge carriers are said to behave like massless particles (because of the dispersion relation), they do have an effective mass as accounted for in the Drude model (which vanishes only at the Dirac point) despite the fact that they always travel at the Fermi velocity. The conductivity can thus be expressed as:

$$\sigma = \frac{ne^2\tau_s}{m^*} \tag{1.12}$$

This shows that by controlling n with a gate voltage we can control the conductivity of graphene. It also means that, in this model, the conductivity vanishes at the Dirac point. Fig. 1.2 illustrates the gate dependence of the conductivity. A graphene flake was deposited on a doped Si substrate with a layer of oxide and patterned into a Hall bar as shown in Fig. 1.2a and b. It was possible to apply a back gate to the flake through the insulating oxide part. Fig. 1.2c shows the dependence of the conductivity as well as the resistivity of the graphene with respect to the gate voltage. We can see that the conductivity exhibits a minimum (and the resistivity a maximum) at $V_g \approx 40$ V corresponding to the charge neutrality point where the charge carrier density vanishes. We can see that when the temperature increases, the maximum of resistivity decreases because electrons get thermally excited in the conduction band.

1.1.2.c Ballistic transport in graphene

When the averaged time between two scattering events in the Drude model is bigger than the time the charge carriers need to travel across the full graphene flake, the transport is said to be ballistic (in the former case the transport is diffusive). In this case, they are on average no scattering events and the Drude model does not hold. A more adapted model to describe the transport properties is given by the Landauer formalism where each conducting channel is associated with a transmission coefficient τ and a conductance e^2/h. We can estimate the number of conducting channels by comparing the width W of the graphene to the Fermi wavelength of the charge carriers $\lambda_F = 2\pi/k_F$ which represents the physical size of charge carriers participating to the electrical transport. The number of channels N can be expressed as:

$$N = 4\frac{W}{\lambda_F} = 2\sqrt{\frac{|n|}{\pi}}W \tag{1.13}$$

where we took into account the spin and valley degeneracy. For perfectly transmitting channels ($\tau = 1$) the conductance is thus:

$$G = \frac{2e^2}{h}N = 2\frac{e^2}{h}\sqrt{\frac{|n|}{\pi}}W \tag{1.14}$$

For ballistic transport, the conductance scales as $\sqrt{|n|}$ and not as $|n|$ like in diffusive transport. n being gate voltage dependent, it is still possible to change the conductance of graphene in the ballistic case.

1.2 Superconducting proximity effect

A normal material, coupled to a superconducting material, can acquire superconducting properties. This phenomenon is called the superconducting proximity effect and explains why we can use graphene in a Josephson parametric amplifier. The experimental work presented in this PhD manuscript is mainly focused on the measurement of parametric amplification and not proximity effect signatures. We will thus not develop the full microscopic model of proximity effect and only give important aspects. Details about the microscopic description can be found in PhD manuscripts [20, 21] or review [22] and a very meaningful semi-classical picture is given in [23].

1.2.1 Josephson junctions and different regimes

Josephson junctions (JJ) are an important element in superconducting circuits because they allow to add nonlinearity. We will see in the next chapter that this nonlinearity is a key parameter to perform parametric amplification. A general definition of a JJ would be a weak link separating two superconductors such that supercurrent can flow between each of them. In superconducting quantum circuits, most of the times, JJs are made by creating a thin insulating barrier (typically 1 nm) between two superconductors such that cooper pairs can tunnel through this barrier. This type of junctions are called tunnel or SIS (superconducting-insulating-superconducting) junctions. They obey to the Josephson relation:

$$I(t) = I_c \sin\left(\frac{\phi_J(t)}{\varphi_0}\right) \tag{1.15}$$

where $\phi_J(t)$ is the generalized flux associated to the voltage across the JJ and $\varphi_0 = \hbar/2e$ the superconducting flux quantum. In the following we will change the notation and deal with the phase ϕ across the junction ($\phi = \phi_J(t)/\varphi_0$). Weak links forming the JJ can also be made of normal metals, semiconductors or even semi-metals. These types of junctions are called SNS junctions (superconducting-normal-superconducting) and obey to different physics that we will describe in the next section.

SNS JJs can be in different regimes: long/short, diffusive/ballistic and dirty/clean. The JJ is said to be ballistic when the length L of the JJ is smaller than the mean-free-path l_{mfp} of electrons in the normal material. In this case the coherence length can be expressed as $\xi = \hbar v_F/\Delta$ where Δ is the superconducting gap. If $l_{mfp} < L$, the junction is diffusive and the coherence length is expressed as $\xi = \sqrt{\hbar D/\Delta}$ with D the diffusion coefficient $D = v_F l_{mfp}/2$. The relevant energy scale becomes the Thouless energy $E_t = \hbar D/L^2$ whereas it was the superconducting gap in the ballistic case. Once we know the coherence length of the JJ, we can compare it to its physical length. If $\xi < L$ the JJ is long and if $\xi > L$ the junction is short. We can also compare the coherence length to the mean free path. If $\xi < l_{mfp}$ the JJ is clean and if $\xi > l_{mfp}$ the junction is dirty.

1.2.2 Andreev reflection

Andreev reflection is the key mechanism to understand proximity effect. Let us consider a normal material of Fermi energy E_F in contact with a superconducting material with a

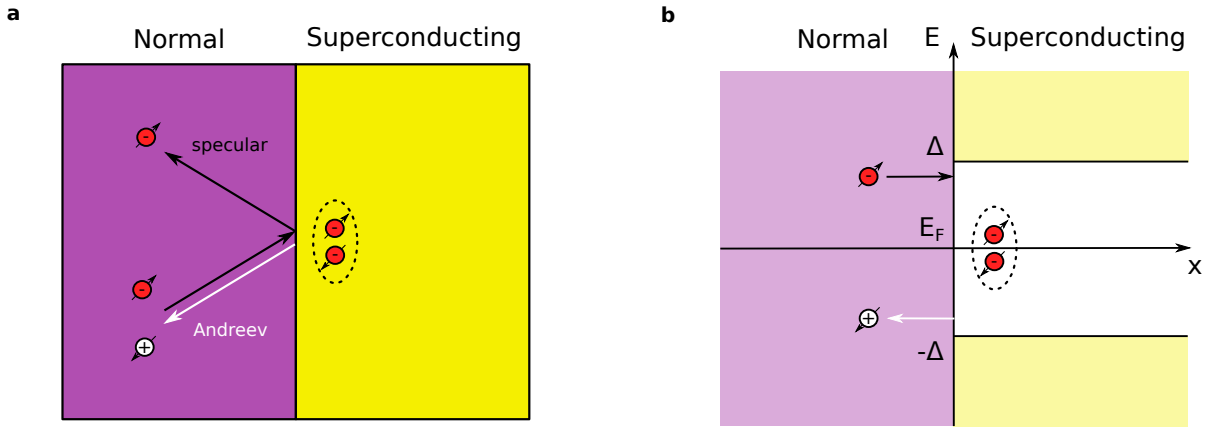

Figure 1.3: (a) Spatial representation of a specular and an Andreev reflection. When the Andreev reflection occurs, a Cooper pair is created into the superconducting material. (b) Energy representation of the Andreev reflection. The electron is reflected as a hole with an opposite energy compared to the Fermi energy and creates a Cooper pair at the Fermi energy in the superconducting material.

superconducting gap Δ as shown in Fig. 1.3. Electrons in the normal material can be described as Bloch waves of wave vector k, energy E_k and spin σ. When an electron of energy $|E_k - E_F| < \Delta$ is incident on the surface, two mechanisms can happen:

- The electron cannot penetrate in the superconducting material because of the superconducting gap forbidding the electron to pass and therefore it undergoes a regular specular reflection.
- The electron undergoes an Andreev reflection.

Andreev reflections [24] is a phase coherent process where an electron can be reflected as a hole of opposite spin and wave vector. This is only possible if a Cooper pair is created in the superconducting material in order to have a conservation of charge, spin and momentum. Fig. 1.3 illustrates the Andreev reflection process.

The microscopic description of this system can be done using the Bogoliubov-de Gennes equation. It allows to compute the wave functions of excitations (electron and hole) in a system with a spatially varying superconducting gap. By doing so we can find that the electrons and holes are linked by a phase coefficient. When Andreev reflection occurs, the reflected hole acquire a phase $\delta\phi_e = \phi_R + \arccos(E_k/\Delta)$ where ϕ_R is the macroscopic phase of the superconductor. The fact that the phase of the incident electron, hole and superconductor are linked makes this mechanism a phase coherent process. Note that the probability of an electron undergoing a regular specular reflection depends on the quality of the electrical contact between the normal and the superconducting material. It is characterized by the transparency $t = 1/(1+Z^2)$ where Z is the barrier strength. In the case of a perfect contact $Z = 0$ and thus $t = 1$, regular specular reflections are forbidden. On the opposite, when $Z = \infty \Rightarrow t = 0$, Andreev reflections are not possible and the system becomes a tunnel barrier.

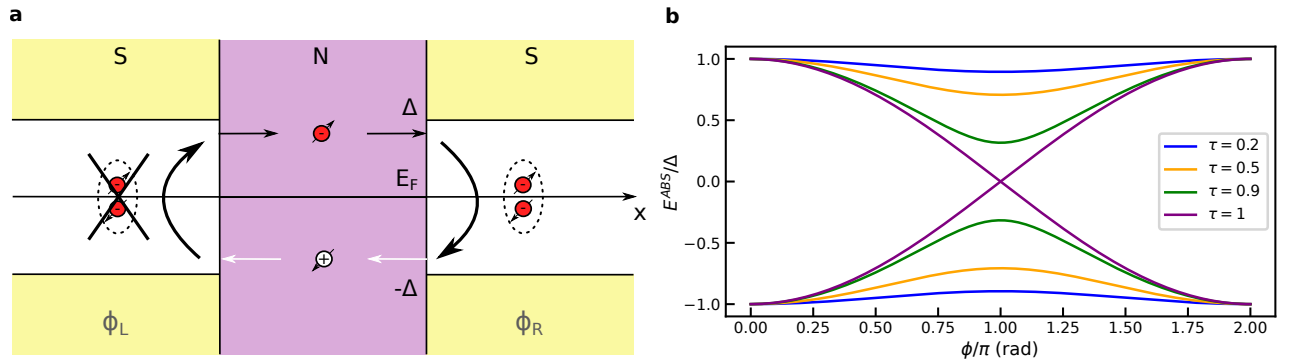

Figure 1.4: (a) Scheme of coherent transfer of Cooper pairs by the Andreev reflection process. (b) Andreev bound states for a short SNS junction with a single conductive channel of transmission τ.

1.2.3 Cooper pair transport in a SNS junction and Andreev bound states

Let us now consider a normal material making a junction between two superconducting materials (SNS junction) as shown in Fig. 1.4a. As we saw earlier, an electron can be Andreev reflected as a hole of opposite spin, energy and wave vector. This hole will travel back the SNS junction, and can be Andreev reflected itself into an electron on the opposite interface. This process requires the destruction of a Cooper pair in the superconducting material in order to have a charge, energy and momentum conservation. This time, the associated phase shift is $\delta\phi_h = -\phi_L + \arccos(E_k/\Delta)$. We can now understand how the phase coherent process of Andreev reflection enables non dissipative Cooper pair transport through a SNS junction. Electrons undergoing an Andreev reflection create Cooper pairs on one side of the junction while holes undergoing Andreev reflection destroy Cooper pairs on the other side of the junction.

The phenomena we just described only dominates the superconducting transport when a resonance condition leading to the formation of energy bound states holds. The resonance condition is that the phase accumulated in the Andreev process should be a multiple of 2π. This ensures constructive interference of the wave functions making the process dominant compared to other transport process that can happen. As we saw earlier, the electron acquires a phase $\delta\phi_e$ when being Andreev reflected, and the conjugated hole a factor $\delta\phi_h$. Moreover they also acquire a dynamic phase when traveling along the normal material:

$$\begin{aligned}\phi_e = k_e L &= \sqrt{\frac{2m}{\hbar^2}(E_F + E)}L \approx \sqrt{\frac{2m}{\hbar^2}E_F}(1 + \frac{E}{2E_F})L \\ \phi_h = k_h L &= \sqrt{\frac{2m}{\hbar^2}(E_F - E)}\Big(-L\Big) \approx \sqrt{\frac{2m}{\hbar^2}E_F}\Big(1 - \frac{E}{2E_F}\Big)\Big(-L\Big)\end{aligned} \tag{1.16}$$

where the approximation holds because in general E_F is of the order of 1 eV and E is smaller than the superconducting gap being of the order of 1 meV. So the resonance condition leads to:

$$\phi_e + \delta\phi_e + \phi_h + \delta\phi_h = 2\arccos(\frac{E}{\Delta}) \pm (\phi_R - \phi_L) + k_F L\frac{E}{E_F} = 2\pi n \tag{1.17}$$

where the $\pm$ sign depends on the direction of the roundtrip made by the Andreev reflected

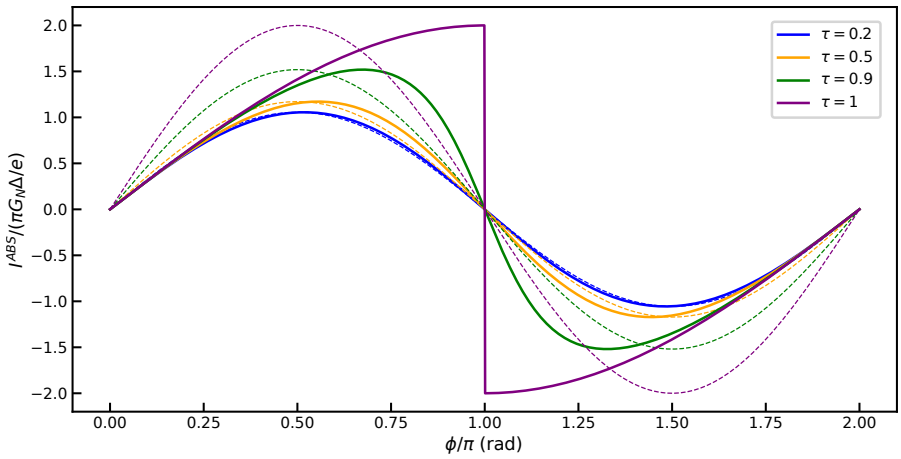

Figure 1.5: Current phase relation for a short SNS junction with a single conductive channel of transmission τ. The dashed curves represent a sine function with the same amplitude as the associated CPR.

hole and electron, and n is an integer. It is possible to show that the resonance condition leads to the presence of bound states called Andreev bound states (ABS). In the one dimensional case and short junction regime, we can neglect the dynamic phase term and each conductive channel i with a transmission probability τ has an ABS energy:

$$E_i^{ABS} = \pm\Delta\sqrt{1 - \tau_i \sin^2(\frac{\phi_R - \phi_L}{2})} \tag{1.18}$$

There are thus two levels of energy for each conductive channel as shown in Fig. 1.4b. We can see that the phase dependence of these levels depends strongly on τ. When τ is close to unity, ABS are very sensitive to the phase difference. We can also see that when the phase difference is zero, all the ABS are pinned to the superconducting gap. When the phase difference is non zero, ABS lay inside the superconducting gap and reach an extremum at $\phi_R - \phi_L = \pi$. When $\tau = 1$, an extremum is reached at $\phi_R - \phi_L = 2\pi$ and there is a crossing of the two ABS at $\phi_R - \phi_L = \pi$. Finally when $\tau = 0$, ABS are not present inside the gap as expected for a tunnel junction. In the case of long junctions, a single conducting channel can create multiple ABS that lay inside the gap (with an energy level spacing of $\pi\hbar v_F/L$) and are less sensitive to phase modulation [25, 26]. Moreover we did not address here the case where the interface between the superconductors and the normal part is not perfect. Such interfaces result in detaching the ABS of the gap at zero phase [26].

1.2.4 Current phase relation

For now we described qualitatively the mechanism of charge transport in a SNS JJ and showed the phase coherent Andreev reflection process leads to the formation of ABS inside the superconducting gap. The current associated with these ABS is the result of a phase difference, and in the short junction regime can be expressed as:

$$I_i^{ABS} = \frac{2e}{\hbar}\frac{dE_i^{ABS}}{d\phi} \tag{1.19}$$

where we adopted the notation $\phi_R - \phi_L = \phi$. Using Eq. 1.18 we find:

$$I_i^{ABS} = \mp \frac{e\Delta}{2\hbar} \frac{\tau_i \sin(\phi)}{\sqrt{1 - \tau_i \sin^2(\phi/2)}} \tag{1.20}$$

We can see that the current of the negative energy ABS flows in opposite direction compared to the positive energy ABS. Eq. 1.20 links the current to the phase and is called the current phase relation (CPR). One can also rewrite Eq. 1.20 using the Landauer formalism where each conductive channel has a conductance $G_N^i = (2e^2/h)\tau_i$ (including the spin degeneracy):

$$I_i^{ABS} = \mp G_N^i \frac{\pi\Delta}{e} \frac{\sin(\phi)}{\sqrt{1 - \tau_i \sin^2(\phi/2)}} \tag{1.21}$$

Fig. 1.5 shows the CPR of a SNS JJ composed of a single conductive channel. We can see that when τ tends to zero, the CPR is sinusoidal as expected for a tunnel junction. When $\tau > 0$, the CPR deviates from the sinusoidal shape and exhibit forward skewness: compared to a sine function of the same amplitude, the CPR is bent forward and reaches a maximum at $\phi > \pi/2$.

For now we considered the temperature being zero ($T = 0$) where only the negative energy states are populated and contribute to the supercurrent. By using the Fermi-Dirac distribution we can compute the total current at a temperature T:

$$I^{ABS} = \sum_i G_N^i \frac{\pi\Delta}{e} \frac{\sin(\phi)}{\sqrt{1 - \tau_i \sin^2(\phi/2)}} \tanh\left(\frac{\Delta}{2k_B T}\sqrt{1 - \tau_i \sin^2(\phi/2)}\right) \tag{1.22}$$

which reduces when $\tau_i << 1 \; \forall i$ to the Ambegaokar-Baratoff formula [27]:

$$I_c R_N = \frac{\pi\Delta}{2e} \tanh\left(\frac{\Delta}{2k_B T}\right) \tag{1.23}$$

which describes well tunnel junctions and where we have defined the normal resistance $R_N = 1/(\sum_i G_N^i)$ and the critical current I_c as the maximum supercurrent that can be carried by the JJ. The demonstration we just provided shows that the supercurrent flowing through the JJ depends on the number of conductive channels. This is a key mechanism to understand how a gate tunable material can be used to tune the properties of the JJ. By applying a gate voltage, it is possible to change the critical current of the JJ which has a direct impact on its nonlinear inductance as we will see in the next chapter.

1.2.5 Multiple Andreev reflections

When a DC voltage V is applied across the JJ, the Fermi level of one of the superconductor will be shifted by eV. It was shown that this could lead to a phenomenon called multiple Andreev reflections (MAR) allowing for dissipative transport [28, 29, 30]. We will present the semi-classical picture of this phenomenon given in [28] and illustrated in Fig. 1.6. An electron of the left superconducting reservoir can enter into the normal region and be Andreev reflected as a hole on the right superconductor because of the presence of the superconducting

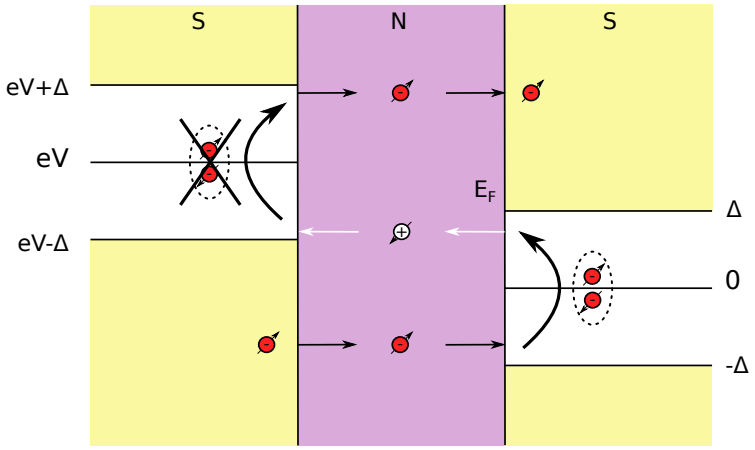

Figure 1.6: Scheme representing the multiple Andreev reflection process.

gap. This hole has an opposite energy compared to the electron with respect to the Fermi energy of the right superconductor. The hole will then be Andreev reflected as an electron on the left superconductor because of the presence of the gap. Again, the electron has an opposite energy compared to the hole with respect to the Fermi energy of the left superconductor. As we can see in Fig. 1.6, the energy acquired during these two Andreev reflections is higher than the superconducting gap and allows thus the electron to be transmitted into the right superconductor. This shows how dissipative current can flow when applying a voltage across a SNS JJ. The example that we described is a third order process implying three trajectories inside the JJ. MARs manifests as peaks in the conductance at voltages $V = 2\Delta/n$ where n is an integer and characterize the number of trajectories leading to the dissipative transport. Note that in the scheme presented in Fig. 1.6, the purple color does not represent the density of states of electrons in the normal material but rather the density of state of the quasiparticles in the BCS theory. Indeed, if it was the opposite, at $T = 0$, in the normal material, the energy levels would have been filled until the Fermi energy, forbidding the electron of the left superconductor to enter in the normal region.

1.3 Proximity effect in graphene

In the previous section we described the ideal case of a SNS junction with transparent contacts and we focused particularly on the short regime. This allowed to understand the mechanism of superconducting proximity effect but it cannot be used directly to model what is happening in graphene. First, the graphene JJs (gJJ) that we are using in this work do not have perfectly transparent contacts. Moreover, the Hamiltonian describing graphene around the Dirac point is not the same as a 2D electron gas which modifies the Bogoliubov-de Gennes equation. This is why we will present here results oriented on proximity effect in graphene. A recent review on the subject can be found here [31].

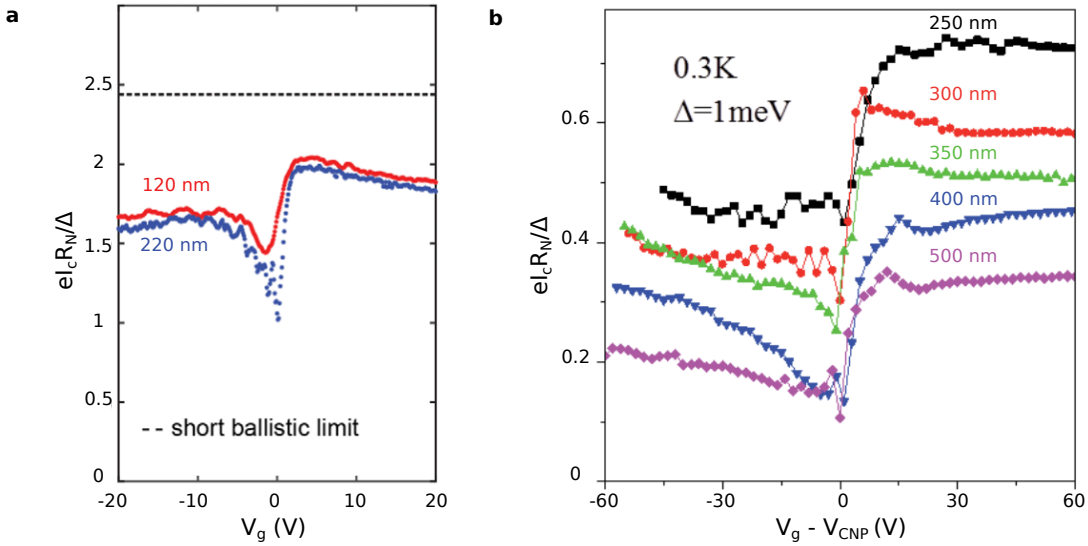

Figure 1.7: (a) and (b) I_cR_N product with respect to the gate voltage for short ballistic gJJs (Ti/Al) and long ballistic gJJs (Nb) respectively. Figure (a) adapted from [32] and Figure (b) adapted from [33].

1.3.1 Short review on superconducting graphene Josephson junctions

The first experiment on proximity effect in graphene was performed by Heersche in 2007 [34]. At this time, most of the work was focused on short diffusive gJJs because the graphene was not isolated from its enviromnent causing important degradation of its electronical properties, and small superconducting gap materials (like Aluminum) where used (giving thus a long coherence length) [34, 35, 36, 37, 38, 39]. The use of higher superconducting gap materials like Niobium or Lead allowed to study the long diffusive regime [40, 41, 42, 43, 44]. The next major improvement was performed by Calado in 2015 [45] where graphene was encapsulated in between hexagonal boron nitride flakes (see Chapter 3) allowing for a drastic improvement of the JJ quality leading to ballistic transport [46, 47, 48, 33, 49, 50, 32]. The coupling of graphene with superconductors offers a unique way of combining relativistic physics to superconductivity and is thus an active subject of research.

Concerning the theoretical part, Titov and Beenakker were the first to solve the Bogoliubov-De Gennes equation with a Dirac Hamiltonian for a short ballistic and large ($W >> L$) gJJ with ideal interfaces [51]. They found that such gJJs should have an I_cR_N product of $\approx 2.5\Delta/e$. Even if this paper refers to an ideal gJJ, this I_cR_N value is often cited as a reference for short ballistic junctions. More complex theories exist but we will not discuss them here and the interested reader can refer to [31]. For long diffusive gJJs, the study of Dubos *et al.* [52] is often used to predict the I_cR_N product and gives $I_cR_N = 10.82E_t/e$. Nevertheless this study was not developed specifically for graphene and does not take into account the relativistic nature of the charge carriers. Here is a complete picture of the I_cR_N product at zero temperature in non-graphene junctions:

- short diffusive $I_cR_N = 2.07\Delta/e$ [53]
- short ballistic $I_cR_N = \pi\Delta/e$ [54]
- long diffusive $I_cR_N = 10.82E_t/e$ [52]

- long ballistic $I_cR_N = E_t/e$ [55]

Fig. 1.7a and b show the measured I_cR_N product for ballistic gJJs made of Ti/Al and Nb respectively. In both cases the transparency of the contact is high, but in (b) the gJJ length are longer than the coherence length meaning that the junctions are in the long ballistic regime. In the case of short junctions, the I_cR_N product is close to what is predicted by Titov and Beenakker (best value reported for planar gJJs to my knowledge). In the case of long gJJs the I_cR_N product decreases as $1/L$. The coherence length is estimated to be around 100 nm and the shorter gJJ (black curve) has a length of 250 nm. Note that to my knowledge, the best I_cR_N product in diffusive gJJs in the literature is $\approx 1\Delta/e$.

The temperature dependence of the critical current of a SNS JJ is often compared to the Kulik-Omel yanchuk (KO) model [54, 53]. Nevertheless this theory is not adapted for graphene because it was designed for point type junctions (with negligible width) [56, 32]. A model developed by Takane and Imura (TI) [57, 58] including both carrier inhomogeneities in graphene and reduced transparency of superconducting contacts, has shown to be effective to predict the temperature dependence of I_c [32].

1.3.2 Current phase relation in graphene

The CPR of graphene has been measured both in diffusive and ballistic regime. Fig. 1.8a shows the measured CPR for a ballistic gJJ in the long regime (but with ξ of the same order of L). We can see that, as for a single channel SNS JJ, the CPR deviates from a sine function that we would expect for a tunnel junction. To characterize this deviation, the skewness of the JJ is defined as $S = 2\phi_{max}/\pi - 1$ such that $S = 1$ when $\phi_{max} = \pi$ (equivalent to a perfectly transparent single channel SNS JJ), and $S = 0$ when $\phi_{max} = \pi/2$ (corresponding to a tunnel JJ). Fig. 1.8b and c show the skewness measured at different gate voltages for diffusive and ballistic gJJs respectively. We can see that both regimes show skewness at any doping and that the ballistic gJJs tend to have larger skewness. This shows that in principle, the models used to describe quantum circuits with gJJs should account for this deviation compared to SIS JJ. Nevertheless, the skewness being rather small (closer to 0 than to 1), a sine approximation of the CPR can be used as a first approximation to understand the general behavior of such system.

1.3.3 Andreev bound states in graphene

ABS can be computed in proximitized graphene using a tight-binding approach. Fig. 1.9a. shows the result of such calculations from diffusive to ballistic in the long regime. We can see that in the diffusive regime, there is a region inside the superconducting gap where no ABS are present. This region is called a minigap and is expected for diffusive SNS junctions [63] and was already measured using tunneling spectroscopy in a SNS junction made of a Ag wire as shown in Fig. 1.9b. When the junction becomes weakly diffusive ($l_{mfp} \approx L$), we can see the appearance of ABS inside the minigap. The extreme case of a purely ballistic junction without doping inhomogeneity shows that ABS can be everywhere inside the superconducting gap. This is due to the fact that the junction is long and wide which can create transverse ABS that are not pinned to the gap. When including doping inhomogeneity in

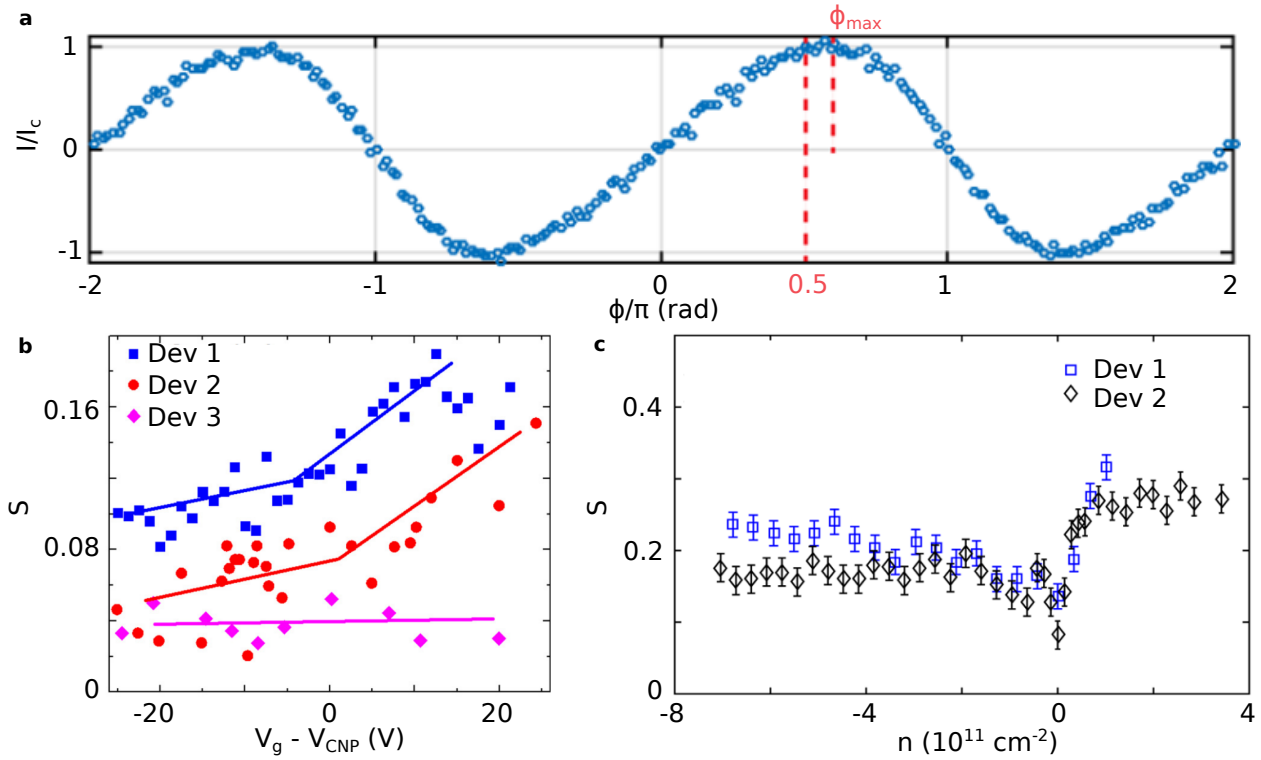

Figure 1.8: (a) Current phase relation of a ballistic gJJ at the limit of the short regime for a fixed gate voltage. (b) Measured skewness for diffusive gJJs and ballistic gJJs (c) with respect to the gate voltage. The skewness is computed by comparing the phase giving a maximum in the CPR to $\pi/2$ (the maximum for a sine CPR). Figure (a) and (c) adapted from [59]. Figure (b) adapted from [60]

.

ballistic graphene, it looks like the number of ABS is reduced inside a region that we can call a soft gap. Interestingly, the mini/soft gap in the ABS reduces when going away from zero phase across the junction and closes at $\phi = \pi$ whatever the regime.

Tunneling spectroscopy has been performed on a ballistic gJJ (Fig. 1.9c) and shows that even at $\phi = 0$ ($B = 258$ μT), there is no minigap but rather a soft gap similar to what is predicted for a long ballistic gJJ with doping inhomogeneity. Going away from $\phi = 0$ reduces the soft gap. Note that in Fig. 1.9c, the gJJ is long but its length is close to the coherence length. For a short ballistic gJJ with doping inhomogeneity, we can expect the number of ABS detached from the gap at $\phi = 0$ to reduce but not vanish because of the finite width allowing transverse ABS to form. A recent study showed evidence of a minigap in a short ballistic gJJ by transport measurement [64]. Such minigap can exist in ballistic SNS JJ and depends on the type of boundary between the normal metal and the superconductor [65]. The fact that in [64] the graphene is only partially proximitized might play a role in the appearance of such a mini gap in a short ballistic device.

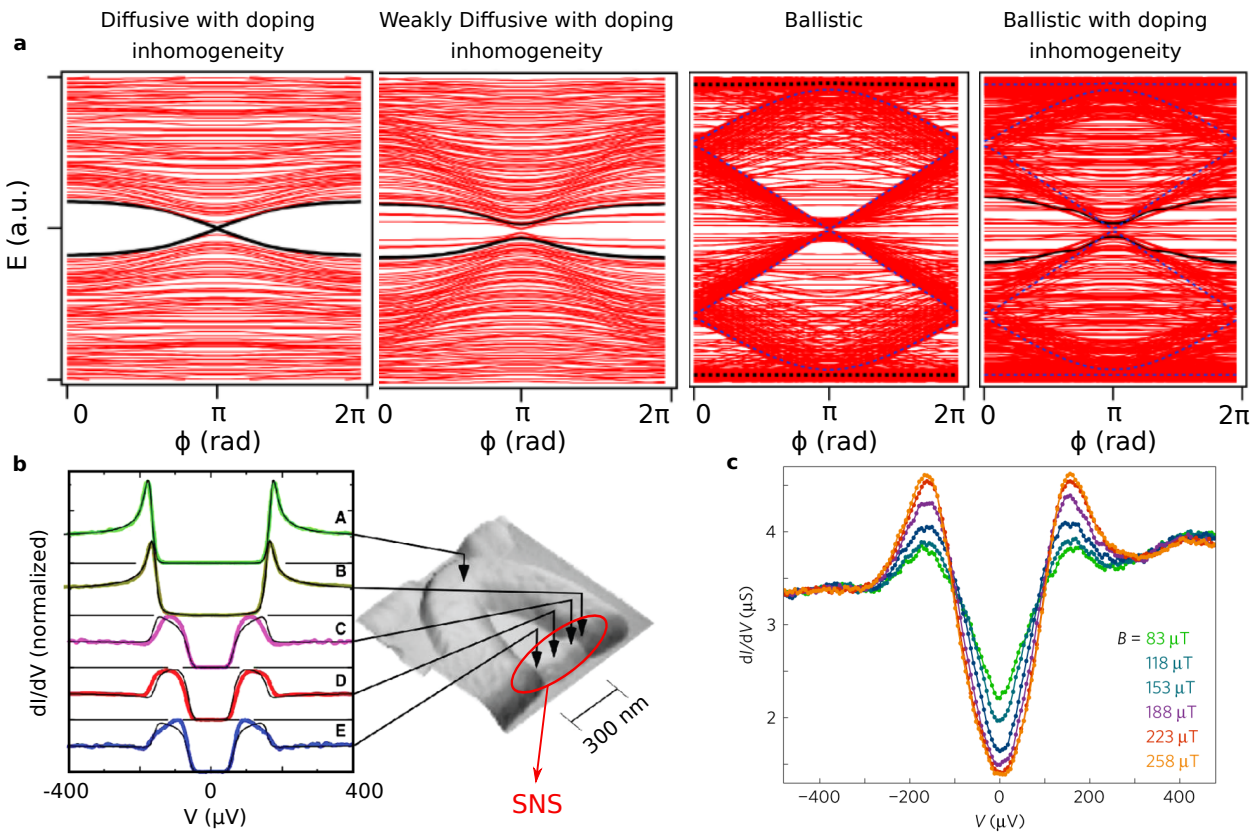

Figure 1.9: (a) Andreev spectrum obtained with tight binding calculations for long gJJs in different regimes. (b) Tunnel spectroscopy on an Ag SNS junction at different locations. The red circle indicates the position of the SNS junction. (c) Tunnel spectroscopy on a long ballistic gJJ placed in a superconducting loop. This geometry allows to tune the phase across the gJJ with the use of a magnetic field B. $B = 258$ μT corresponds to a zero phase. Figure (a) adapted from [61], Figure (b) adapted from [62] and Figure (c) adapted from [26].

1.3.4 Microwave dissipation in graphene

We focused in the last section on the ABS in gJJs because they play an important role in their microwave response or equivalently in their admittance $Y = G_s + iB_j$. Superconducting quantum circuits are working in the microwave regime making the study of this quantity important. While the imaginary part B_j of the admittance is linked to the CPR, the real part G_s is linked to dissipation. A recent study investigated the admittance of a short diffusive gJJ [66] by using a $\lambda/4$ resonator inductively coupled to a gJJ placed in a loop as shown in Fig. 1.10a. By sending a DC magnetic flux they were able to control the phase across the junction and by measuring the reflection response (Γ) of the resonator they were able to extract the inductive part of the admittance (associated to a frequency shift), as well as the dissipative part (associated to a change in the quality factor). Fig. 1.10b shows the measured dissipative part of the admittance with respect to the phase across the gJJ for three different gate voltages. We can see that at $\phi = 0$, $G_s = 0$ for every gate voltages which means that there is no microwave dissipation at 0 phase (in the model G_s is placed in parallel with the inductive part of the JJ meaning that a low G_s is associated to a low dissipation). Nevertheless, when $\phi > \pi/2$ we can see that G_s increases meaning that microwave dissipation is present.

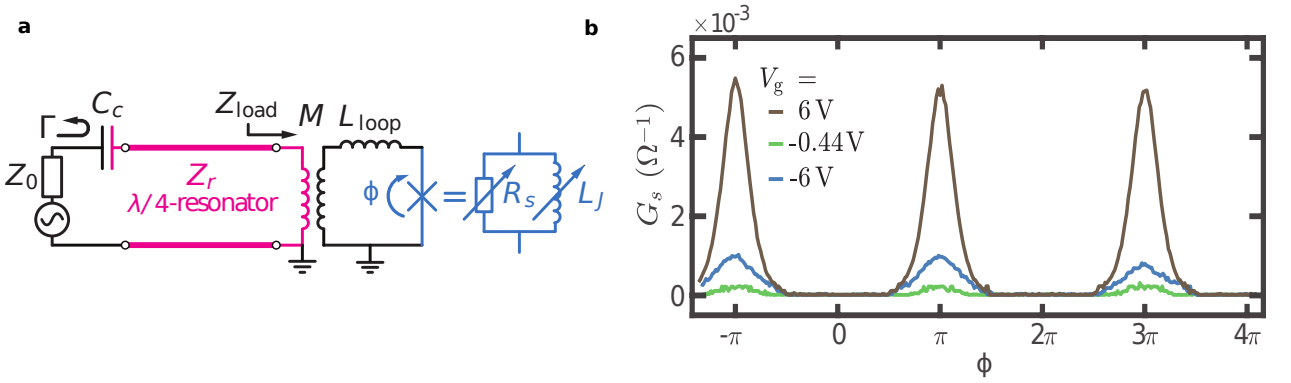

Figure 1.10: (a) Scheme of the circuit to measure the admittance of the gJJ (represented as a cross). The resonator was designed to resonate at 3GHz and was probed such that the mean number of photons inside it is around 100. The gJJ is placed in a loop allowing phase control. (b) Dissipative part of the admittance of the gJJ with respect to the phase for three different gate voltages. The charge neutrality point correspond to V_g = -0.44 V. Figures adapted from [66].

It also seems that dissipation is more important in the n-doped region ($V_{CNP} = -0.44$ V).

As we saw earlier, each ABS participates to the transport of supercurrent. At $T = 0$, only the ABS below the Fermi energy are occupied. Therefore, there is no fluctuation in the critical current meaning that there is no dissipation according to the fluctuation dissipation theorem. Nevertheless, the presence of microwaves changes the distribution function which is no more the Fermi-Dirac distribution. This is why ABS above the Fermi energy can be populated when excited with a sufficiently large energy. This variation of population introduces a variation in the critical current and thus leads to dissipation. We can now understand why the phase across the JJ has an important role on the microwave assisted dissipation. As we saw in the last section, going away from zero phase tends to close the mini/soft gap making the excitation energy smaller between ABS below and above the Fermi level. Therefore, as the phase is increased, the probability of ABS excitation increases as well leading to additional dissipation. Once positive energy ABS are excited, they can also relax creating even more critical current fluctuation. Another study using a similar technique but with a multimode resonator was able to compare the importance of the microwave frequency on a long diffusive gJJ [61]. They compared the dissipation at 2 GHz and 19 GHz and showed that at 19 GHz dissipation could appear even at zero phase. It means that the energy of microwaves photons was large enough to excite ABS above the minigap even at zero phase. One can also mention a study [67] where microwave power dependent dissipation was observed in a gJJ.

Dissipation is not desirable in quantum circuits especially when performing quantum limited amplification because it has the effect of adding noise on the amplified signal (see Chapter 2). One can thus use some strategies to minimize it. We saw that long SNS JJs create more ABS which also detach from the gap at zero phase. Therefore it is critical to be in the short regime. Moreover, the 2D nature of gJJs offers the possibility of transverse ABS to form inside the gap. Therefore there is a compromise between decreasing the width to decrease the number of transverse ABS while keeping enough of critical current (the number of conductive

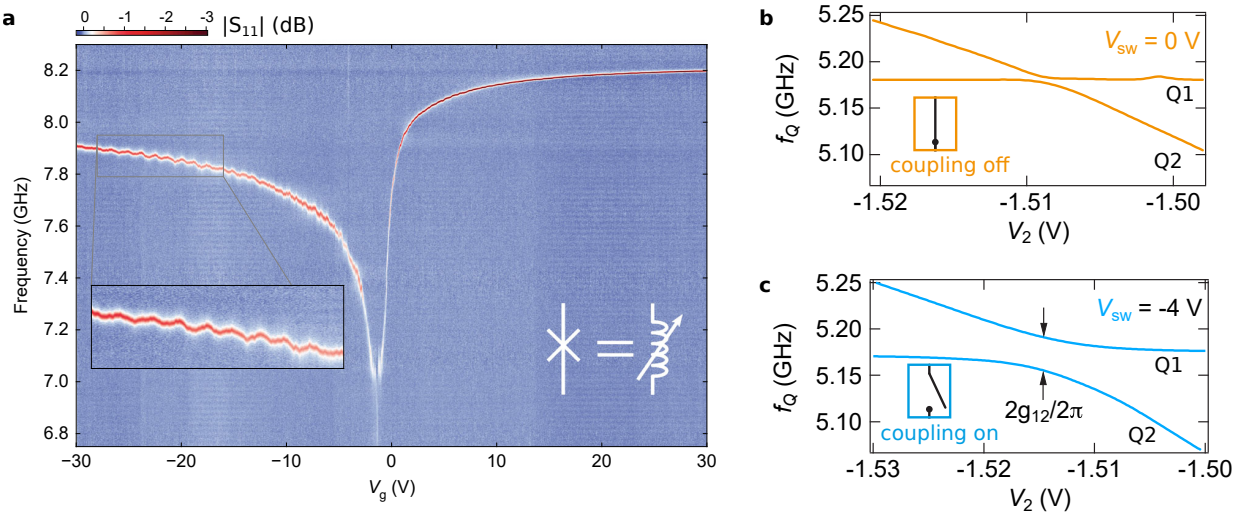

Figure 1.11: (a) Gate voltage tunable superconducting resonator with the use of a gJJ. The reflection coefficient of the resonator is measured with respect to the frequency and gate voltage. The red colored line manifests the presence of a deep in the reflection coefficient which indicates the resonance frequency. By changing the graphene number of conductive channels with the gate, it is possible to change the resonance frequency of the resonator. (b) and (c) Voltage controlled quantum bus. Two gatemons (made with a nanowire) are coupled through a gate tunable resonator (coupled itself to a nanowire serving as a switch). By applying a gate voltage V_{sw} on the switch, it is possible to change the coupling g_{12} between the two qubits. By switching the gate voltage V_2 on the qubit 2, we can change its energy to make it equal to the energy of the qubit 1. The avoided level crossing indicates the strengths of the coupling. We can see that when the switch is on (c) the level avoided crossing is 8 times bigger than when the switch is off (b). Figure (a) adapted from [68], Figure (b) and (c) adapted from [69].

channel scales with the width). Bad contact transparency is not desirable because it detaches the ABS from the gap. Concerning the junction transparency, it could be advantageous to have a low transparency in order to have ABS being less dependent on the phase, but this would also reduce the critical current.

1.4 Conclusion and state of the art on gate tunable quantum circuits

In this chapter we explored the properties of graphene, proximity effect and gJJs. The main goal was to show that by applying a gate voltage on a gJJ, it is possible to change the number of conductive channels and thus the number of ABS carrying supercurrent. By doing so, the gate voltage is a direct way of tuning the JJ properties and offers an alternative to magnetic field control in a SQUID loop geometry. The goal of the project is to use graphene to build a gate tunable Josephson parametric amplifier which was never reported before. Nevertheless, using a SNS JJ to build gate tunable quantum circuits has already been demonstrated and we will briefly present the main achievments here [70].

The first gate tunable qubits were implemented in 2015 [71, 72] in the form of transmons with a SNS junction made of an InAs nanowire. It was possible to tune the qubit frequency from 3 to 6 GHz [71] with a side gate and a coherence time of the order of 1 μs was measured [72]. Such a coherence time is lower than what can be obtained with transmons made with a tunnel junction ($\approx$100 μs) [73] and flux tunable transmons using a SQUID ($\approx$40 μs) [74]. This type of gate tunable transmons are called 'gatemons'. Gatemons also showed a single qubit fidelity above 99% and two-qubit controlled-phase gates with fidelities around 91% [75] which is also much lower to what is obtained with standard flux tunable transmons [76]. Not only nanowires were used to build gatemons but also a 2D electron gas where a coherence time up to 2 μs was measured [77], or even graphene [78] with a coherence time limited to tens of nanoseconds.

The use of gate tunable SNS JJ in a superconducting resonator can also allow for the control of its resonance frequency as it was demonstrated with graphene [68] where a 1 GHz tunability was achieved as shown in Fig. 1.11a. This can be particularly useful to modify the coupling between two qubits. Such a device, called a quantum bus, where two qubits are coupled through a gate tunable superconducting resonator was demonstrated with InAs nanowires [69]. By tuning the resonance frequency of the resonator with a gate voltage, the coupling between the two states could be switched 'on' and 'off' with a ratio of 8 as shown in Fig. 1.11b and c.

Tunnel junctions are most of the time made of Al-Al_2O_3 and cannot resist to magnetic fields above 10 mT. Another advantage of SNS JJ is that they can be made using superconductors with a higher critical field. For example a nanowire was coupled to Pb [79], or graphene was coupled to MoRe [80].

Among all these realizations, gate tunable Josephson parametric amplifiers were still missing. In the following chapters we will present such a realization using a graphene JJ.

Theory of the Josephson parametric amplifier

CHAPTER 2

In this chapter we will review the theory of the Josephson parametric amplifier consisting of a Josephson junction coupled to a resonant structure using the input/output formalism. We will then discuss the limitations of such devices and present a broader view on superconducting parametric amplifiers.

Contents

2.1 Quantum LC oscillator

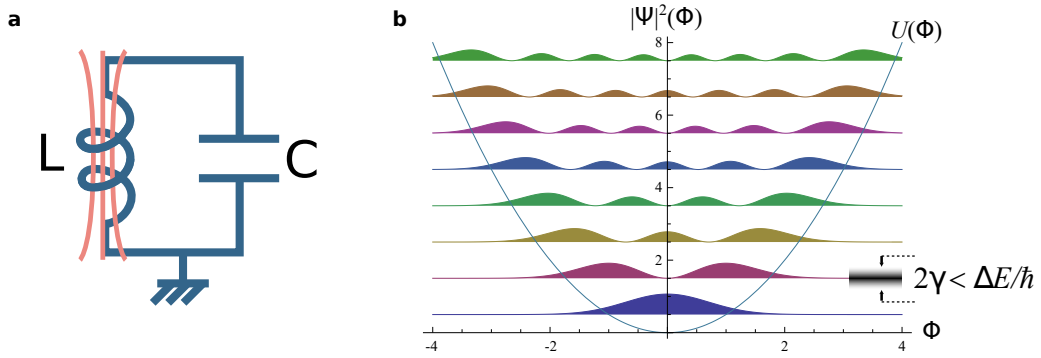

Figure 2.1: (a) LC circuit scheme. (b) Quantum LC circuit energy levels and wavefunctions. The width of the energy levels must be smaller than the energy level spacing. Figure (a) taken from [81] and figure (b) adapteted from [82].

The theory of Josephson parametric amplifiers (JPAs) relies on resonant structures with nonlinearity. It is thus of fundamental importance to study the simplest resonant circuit: the LC oscillator. Quantum circuits are often made of superconducting lines deposited on a low dielectric loss substrate such as sapphire or intrinsic silicon. The superconducting lines have thus an intrinsic inductance and a capacitance with the nearby ground plane, and there is also mutual inductance and mutual capacitance. We can define the total capacitance C and inductance L of the circuit behaving thus as a LC oscillator. Its total energy is the sum of the charging and inductive energy. We can write its Hamiltonian as:

$$H_{LC} = \frac{Q^2}{2C} + \frac{\Phi^2}{2L} \tag{2.1}$$

where $Q(t) = \int_{-\infty}^{t} dt' I(t')$ is the charge on the capacitor and $\Phi = \int_{-\infty}^{t} dt' V(t')$ the magnetic flux threading the inductor created by the circulating current. This circuit is characterized with an angular resonance frequency $\omega_0 = \sqrt{1/LC}$ and a characteristic impedance $Z_0 = \sqrt{L/C}$. It is useful to rewrite Eq. 2.1 in a way we can compare it directly to a mechanical oscillator:

$$H_{LC} = \frac{Q^2}{2C} + \frac{1}{2} C\omega_0^2 \Phi^2 \tag{2.2}$$

This way we see that Φ is equivalent to the position X, Q to the conjugate momentum P and C to the mass m. We can thus follow the standard canonical quantization procedure where Q and Φ become operators satisfying the commutation relation:

$$[\hat{\Phi}, \hat{Q}] = i\hbar \tag{2.3}$$

We define the creation $\hat{A}$ and annihilation $\hat{A}^\dagger$ operators following the same logic as:

$$\hat{\Phi} = \Phi_{zpf}(\hat{A}^\dagger + \hat{A}), \qquad \hat{Q} = iQ_{zpf}(\hat{A}^\dagger - \hat{A}) \tag{2.4}$$

with $\Phi_{zpf} = \sqrt{\hbar Z_0/2}$ and $Q_{zpf} = \sqrt{\hbar/2Z_0}$ being the magnitude of the zero-point fluctuations of the flux and the charge respectively. We can rewrite the Hamiltonian of Eq. 2.1 in terms of the creation and annihilation operators:

$$\hat{H}_{LC} = \hbar\omega_0(\hat{A}^\dagger\hat{A} + \frac{1}{2}) \tag{2.5}$$

resulting in the well known quantum harmonic oscillator Hamiltonian.

We will now briefly explain why a quantum description of the system is needed. First, the superconducting resonators are designed to work at frequencies f above 1 GHz. A quick calculation gives $T = hf/k_B = 50$ mK where h and k_B are the Planck and Boltzmann constant respectively. This proves that in a dilution fridge reaching a temperature of 20 mK, the thermal noise is smaller than the energy level spacing. Moreover, because of the superconducting nature of the circuit, it is possible to reach sufficiently high quality factors such that the energy levels of the LC circuit do not overlap. Thus, the energy damping rate 2γ, corresponding to the frequency width of the energy levels, is such that $2\gamma/\hbar << \Delta E$ where ΔE is the spacing between two consecutive energy levels as shown in Fig. 2.1. Theses two aspects prove that quantum effects are indeed important in superconducting circuits. In the rest of the manuscript we will drop the hat on the operators and precise the nature of variables/operators when confusion can arise. We will also adopt a convention where we drop the zero-point energy corresponding to the factor 1/2 in $\hat{H}_{LC}$.

2.2 Josephson junction

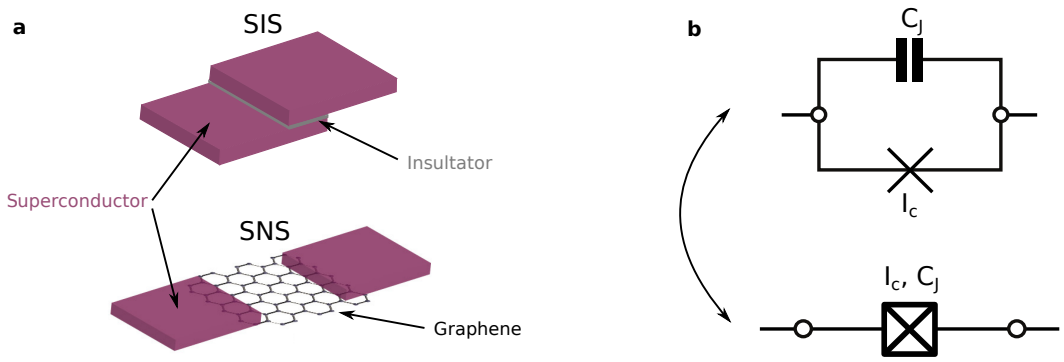

Figure 2.2: (a) Scheme of a SIS JJ and a SNS JJ with graphene as a normal part. (b) Equivalent circuit representation of a JJ. A nonlinear element (cross) of inductance L_J and critical current I_c is shunted by a capacitor C_J. An equivalent representation is a cross in a square.

A simple LC oscillator is not enough to build a JPA. One needs to introduce a source of nonlinearity that can be used to transform a simple oscillator into an amplifier. The key element that is often used for bringing nonlinearity to superconducting circuits is the Josephson junction (JJ). A general definition was given in Chapter 1. We saw that most of the times, JJs are made by creating a thin insulating barrier (typically 1 nm) between two superconductors such that cooper pairs can tunnel through this barrier (superconducting-insulating-superconducting or SIS junctions) as depicted in Fig. 2.2a. While the following

theories we will present are based on SIS junctions, the goal of my work was to use graphene as a JJ to make a JPA (superconducting-normal-superconducting or SNS junctions) as depicted in Fig. 2.2b. For now we come back to SIS JJs, because to my knowledge, no specific theories about SNS JJ based JPAs exist. Such a theory would account for the non-sinusoidal current phase relation (CPR) and would change the form of the Josephson energy that we will introduce in the next paragraphs.

The constitutive equations describing a tunnel junction are:

$$I(t) = I_c \sin(\phi_J(t)/\varphi_0) \tag{2.6}$$

$$\phi_J(t) \equiv \int_{-\infty}^{t} dt' V(t') \tag{2.7}$$

where I is the current, I_c the critical current i.e. the threshold current above which the JJ leaves the superconducting state, V the voltage across the JJ, ϕ_J the generalized flux associated to the voltage across the JJ and $\varphi_0 = \hbar/2e$ the superconducting flux quantum. By differentiating Eq. 2.6 with respect to time and using Eq. 2.7, we find the following equations:

$$\begin{aligned} V &= \frac{L_J}{\cos(\phi_J(t)/\varphi_0)} \frac{\mathrm{d}I}{\mathrm{d}t} \\ &= \frac{L_J}{\sqrt{1-(I/I_c)^2}} \frac{\mathrm{d}I}{\mathrm{d}t} \\ &= L_J' \frac{\mathrm{d}I}{\mathrm{d}t} \end{aligned} \tag{2.8}$$

with $L_J = \varphi_0/I_c$. We can see from these equations that the JJ behaves like a nonlinear inductance L_J'. The nonlinearity comes from the fact that L_J' depends on the current flowing through the JJ. The current (or equivalently power) dependence of the Josephson inductance is a key feature to perform parametric amplification. One can also note that the strength of the nonlinearity is proportional to $1/I_c$. The critical current is thus an important parameter to set the amount of nonlinearity in the system. We saw in Chapter 1 that I_c depends on the charge carrier density that can be controlled with a gate in a gJJ. This proves that gJJs provide a gate tunable Josephson inductance which is a feature that does not exist in SIS junctions. Besides the inductance, the thin insulating barrier between the two superconductors creates an additional capacitance C_J. In a SNS JJ, C_J is often negligible because the distance separating the two superconductors is higher and the total area smaller. The JJ being an inductance as well as a capacitor forms a LC oscillator by itself, and resonates at an angular frequency ω_J called the plasma angular frequency. The plasma frequency is often of the order of tens of Gigahertz, higher than the energy at play in our system such that we can neglect it in our models.

We can also compute the energy of the JJ which will be useful when computing the Hamiltonian of the JPA. By using Eq. 2.6 and the derivative of Eq. 2.7, the energy E can simply be expressed as :

$$\begin{aligned} E &= \int I(t)V(t)dt \\ &= -E_J \cos(\phi_J(t)/\varphi_0) \end{aligned} \tag{2.9}$$

with $E_J = \varphi_0 I_c$. A high Josephson energy corresponds thus to a small Josephson inductance or equivalently a small nonlinearity.

2.3 Josephson junction in a resonant structure

A JJ in a resonant structure can lead to parametric amplification when driven by a strong pump. We will thus derive the Hamiltonian of such a system in this section.

2.3.1 Josephson junction in a lumped LC oscillator

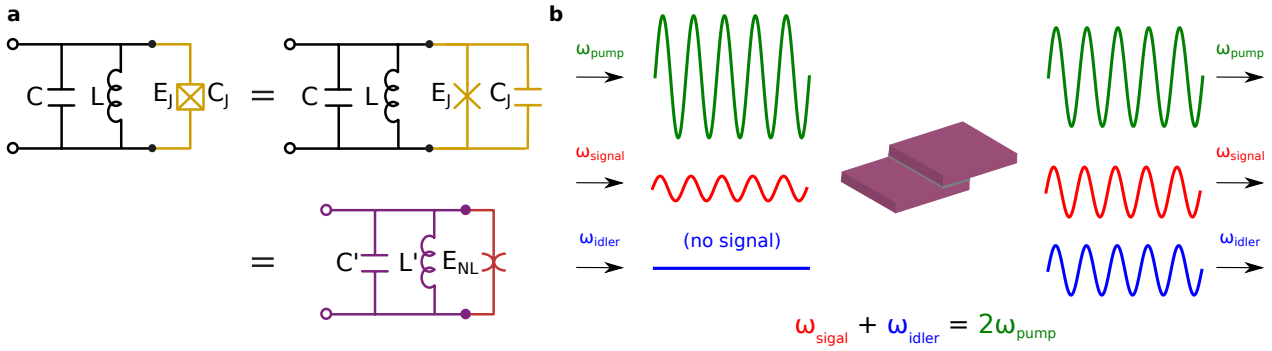

Figure 2.3: (a) Equivalent representation of the JJ integrated in a parallel LC circuit. The spider symbol stems for the nonlinear part of the Josephson potential. (b) Amplification scheme for a Kerr medium. The pump modulates the nonlinear inductance (Eq. 2.8 where L_J' depends on the current going through the JJ) which enables electromagnetic waves conversion from the pump mode to the signal and idler modes. At the input of the JJ the idler mode shows no signal but in practice quantum fluctuations are always present.

We consider a JJ placed in parallel with a lumped LC oscillator as shown in Fig. 2.3a. The total energy of this system is the sum of energy of the LC circuit (Eq. 2.1) and the energy of the JJ (Eq. 2.9):

$$H = \frac{Q^2}{2(C+C_J)} + \frac{\Phi^2}{2L} - E_J \cos\left(\frac{\phi_J}{\varphi_0}\right) \tag{2.10}$$

Because the voltage is the same across each element, the magnetic flux is the same meaning that $\Phi = \phi_J$. For small Φ we can expand the Josephson energy:

$$\begin{aligned} E_J \cos\left(\frac{\Phi}{\varphi_0}\right) &\approx E_J \sum_{n=0} (-1)^n \left(\frac{\Phi}{\varphi_0}\right)^{2n} \frac{1}{2n!} \\ &= E_J - \frac{E_J}{2}\left(\frac{\Phi}{\varphi_0}\right)^2 + \frac{E_J}{24}\left(\frac{\Phi}{\varphi_0}\right)^4 + \mathcal{O}\left(\frac{\Phi}{\varphi_0}\right)^6 \\ &= -\frac{\Phi^2}{2L_J} + E_{NL} \end{aligned} \tag{2.11}$$

where we dropped the constant E_J because it does not impact the dynamics of the system and defined $E_{NL} = \frac{E_J}{24}\left(\frac{\Phi}{\varphi_0}\right)^4 + \mathcal{O}\left(\frac{\Phi}{\varphi_0}\right)^6$. The presence of only even power terms is a direct consequence of the sinusoidal CPR of the SIS JJ. We can thus rewrite the total energy of the system as:

$$H = \frac{Q^2}{2C'} + \frac{\Phi^2}{2L'} + E_{NL}(\Phi) \tag{2.12}$$

This way we isolated the nonlinear part of the Josephson energy (quartic and higher order in Φ). This part is represented as a spider symbol as shown in Fig. 2.3a. We can see that after this transformation the new effective LC oscillator parameters are:

$$L' = \frac{LL_J}{L+L_J} \qquad C' = C + C_J \qquad \omega' = \sqrt{\frac{1}{L'C'}} \qquad Z' = \sqrt{L'/C'} \tag{2.13}$$

In the following calculations we will just keep the quartic term of E_{NL}. By using $\hat{\Phi} = \Phi_{zpf}(\hat{A}^\dagger + \hat{A})$, the commutation relation $[A, A^\dagger] = 1$, and the rotating wave approximation, i.e. neglecting the terms where there is not the same number of A and $A^\dagger$ (because the only way of having energy conservation would be to create photons at different frequencies, but the rotating wave approximation averages out these terms to zero because they oscillate faster than the relevant dynamics of our system) we find:

$$\begin{aligned} E_{NL} &= \frac{1}{24}E_J\left(\frac{\Phi_{zpf}}{\varphi_0}\right)^4 (A + A^\dagger)^4 \\ &= \frac{1}{24}E_J\left(\frac{\Phi_{zpf}}{\varphi_0}\right)^4 (6A^\dagger A^\dagger AA + 12A^\dagger A + 3) \\ &= -\frac{\hbar}{2}K(A^\dagger A^\dagger AA + 2A^\dagger A) \end{aligned} \tag{2.14}$$

where we used the new effective LC oscillator flux zero-point fluctuation $\Phi_{zpf} = \sqrt{\hbar Z'/2}$, dropped the constant term and defined the Kerr coefficient K:

$$K \equiv -\frac{1}{\hbar}\frac{e^2}{2C'}\frac{L'}{L_J} \tag{2.15}$$

We can thus rewrite the total energy of the system as:

$$\begin{aligned} H &= \hbar\omega' A^\dagger A - K\hbar A^\dagger A - \frac{\hbar}{2}KA^\dagger A^\dagger AA \\ &= \hbar\omega_r A^\dagger A - \frac{\hbar}{2}KA^\dagger A^\dagger AA \end{aligned} \tag{2.16}$$

where we defined the angular resonance frequency of the full nonlinear system $\omega_r = \omega' - K$.

The Kerr term is of fundamental importance in the amplification process. It allows the signal we want to amplify to interact with an external source of energy leading to amplification. By using a pump as an external source of photons, it is possible to convert two pump photons ($A(f_p)A(f_p)$) into two entangled signal photons ($A^\dagger(f_s)A^\dagger(f_i)$). This is called a 4-wave mixing process because it implies 4 electromagnetic waves. Conservation of energy imposes that the pump frequency f_p and the entangled photons frequency f_s and f_i, obey to $2f_p = f_s + f_i$. We refer to the photons at frequency f_s as signal photons and the photons at frequency f_i as idler photons. The amplification procedure is shown in Fig. 2.3b.

We will now come back to the Kerr coefficient itself which is the parameter fixing the amount of nonlinearity in the system. First, we can see that K is proportional to the charging

energy $E_C = e^2/(2C')$. Then, while it could have been easy to think that the Josephson inductance was the only parameter determining the amount of nonlinearity, it is actually the ratio of the total inductance L' over the Josephson inductance L_J. The quantity $\eta = L'/L_J$ is called the participation ratio. When $L_J >> L$, $\eta \to 0$ meaning that the Kerr coefficient will be small. This might sound counter intuitive because a strong L_J implies a high nonlinear inductance L'_J with which we would expect a strong Kerr term. But this is the result of considering a parallel resonant circuit. When doing the same calculation but with a series LC circuit, one can find similar results with a participation ratio $\eta = L_J/L'$ where $L' = L + L_J$. This time, a higher Josephson inductance results in a higher Kerr coefficient. We will see later in this chapter conditions on K for operating the JPA in ideal conditions.

2.3.2 Josephson junction in a distributed LC oscillator

The lumped model that we studied in the previous section is important because it allowed to get general results that hold even in more complicated cases. Nevertheless, during this work, the resonant structures I designed could not entirely be considered as lumped because their physical length were of the same order of magnitude than the Gigahertz wavelengths that we used to monitor the device. This means that the electric and magnetic filed, i.e. the current and voltage, cannot be considered as constant on the whole circuit length. I thus used a model closer to the experimental circuit to extract the important parameters. The following demonstration is entirely based on [83] where the Hamiltonian of a JJ embedded in a half wave transmission line resonator is derived.

2.3.2.a Lagrangian of the system

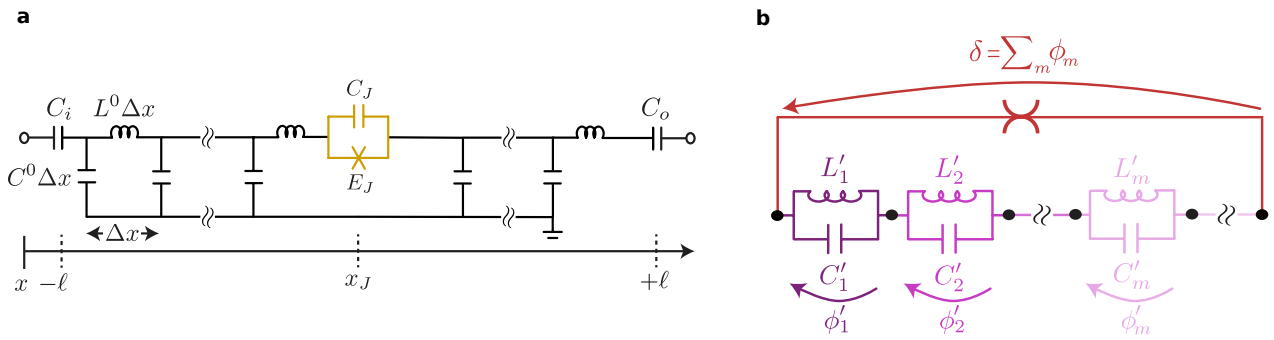

Figure 2.4: (a) Schematic representation of the distributed transmission line with an embedded Josephson junction and input/output capacitance $C_{i,o}$ (b) Lumped representation of the distributed transmission line where the nonlinear part of the Josephson potential is in parallel with the normal modes of the resonator dressed by the Josephson linear inductance and capacitance. (a) and (b) were adapted from [83].

A transmission line (TL) can be decomposed as a succession of infinitesimal lumped LC oscillators as shown in Fig. 2.4a. The total length of the TL is $2l$ and the JJ is placed at position x_J. We will take as a reference the center of the TL for defining the position 0. The TL has a constant inductance and constant capacitance per unit of length of L^0 and C^0 respectively

and is terminated by an input and output capacitance C_i and C_o respectively. One can also define the characteristic impedance $Z = \sqrt{L^0/C^0}$ and the group velocity $v = 1/(\sqrt{L^0 C^0})$. The classical Lagrangian of the bare resonator can be expressed as:

$$\mathcal{L}_r = \int_{-l}^{l} \left[\frac{C^0}{2} \dot{\Phi}^2(x,t) - \frac{[\partial_x \Phi(x,t)]^2}{2L^0} \right] dx \tag{2.17}$$

The Lagrangians associated with the input and output capacitance are:

$$\mathcal{L}_{i,o} = \frac{C_{i,o}}{2} [\dot{\Phi}(\pm l, t) - V_{i,o}(t)]^2 \tag{2.18}$$

where $V_{i,o}$ is the voltage bias at the input and output ports. The contribution of the linear part of the JJ is:

$$\mathcal{L}_J = \frac{C_J}{2} \dot{\delta}^2 - \frac{E_J}{2} \left(\frac{\delta}{\varphi_0} \right)^2 \tag{2.19}$$

where $\delta = \Phi(x_J^+, t) - \Phi(x_J^-, t)$. The contribution of the nonlinear part of the JJ E_{NL} is given in Eq. 2.11 where Φ is replaced by δ. The total Lagrangian is thus :

$$\mathcal{L} = \mathcal{L}_r + \mathcal{L}_J + \mathcal{L}_i + \mathcal{L}_o + E_{NL} \equiv \mathcal{L}_L + E_{NL} \tag{2.20}$$

2.3.2.b Normal modes of the linearized circuit

Solving the Euler-Lagrange equation for the linear Lagrangian:

$$\sum_{\nu=x,t} \partial_\nu \left(\frac{\delta \mathcal{L}_L}{\delta[\partial_\nu \Phi(x,t)]} \right) - \frac{\delta \mathcal{L}_L}{\delta \Phi(x,t)} = 0 \tag{2.21}$$

away from the JJ and the input/output capacitance gives a simple wave equation:

$$\ddot{\Phi}(x,t) = v \partial_{xx} \Phi(x,t) \tag{2.22}$$

The solutions are thus propagating waves with the dispersion relation $\omega_m = k_m v$ with k_m the wave vector of the mode m. We can decompose Φ over all these propagating mode:

$$\Phi(x,t) = \sum_{m \geq 1} \Phi_m(t) u_m(x) \tag{2.23}$$

where $u(x)$ is the envelop of the mode m and Φ_m is oscillating at the frequency ω_m. To find the boundary conditions, it is useful to transform the integral in a discretized form [84]:

$$\mathcal{L}_r = \lim_{n \to \infty} \sum_{j=1}^{n} \Delta x \left(\frac{C^0}{2} \dot{\Phi}_j^2(t) - \frac{[\Phi_j(t) - \Phi_{j-1}(t)]^2}{2L^0 \Delta_x^2} \right) \tag{2.24}$$

where $\Delta_x = 2l/n$. The Euler-Lagrange equations are now $\partial_t(\delta \mathcal{L}/\delta \dot{\Phi}_j) - \delta \mathcal{L}/\delta \Phi_j = 0$. Solving those equations at $x = -l, x_J, l$ gives:

$$\ddot{\Phi}(-l,t) - \frac{1}{C_i L^0} \partial_x \Phi(x = -l, t) = \dot{V}_i \tag{2.25}$$

$$\ddot{\Phi}(l,t) - \frac{1}{C_o L^0}\partial_x \Phi(x=l,t) = \dot{V}_o \tag{2.26}$$

$$\frac{1}{L^0}\partial_x \Phi(x=x_J^-,t) = \frac{1}{L^0}\partial_x \Phi(x=x_J^+,t) = C_J\ddot{\delta} + \frac{\delta}{L_J} \tag{2.27}$$

We note that to obtain these equations, the capacitance $\Delta x C^0$ of the first unit cell, the last unit cell, and the unit cell containing the JJ was neglected compared to the capacitance C_i, C_o and C_J. While this is justified because Δ_x is chosen to be infinitesimal, it should at least be the size of the JJ because we considered the JJ being part of one unit cell. For an SNS JJ C_J can be very small making this approximation wrong. Nevertheless, we will see at the end of the section that it does not change the results of the model. Eq. 2.25 and 2.26 means that the current flowing through the input and output capacitors $I = C_{i,o}\partial_t U = C_{i,o}\partial_t^2 \Phi$ must be equal to the sum of the current flowing through the inductor $I = (1/L^0\Delta x)\int U dt = (1/L^0)\partial_x \Phi$ and the capacitor (but we neglected it). The same principle applies for Eq. 2.27 where the current on the left and on the right of the JJ should be the same as the current flowing through the JJ. At resonance we expect a standing wave forming in the resonator such that at the input and output we expect to have $\dot{V}_{i,o} = 0$. The solutions of the wave equation with these specific constrains are:

$$u_m = a_m \begin{cases} \sin[k_m(x+l) - \varphi_m^i] & -l \leq x \leq x_J^- \\ b_m \sin[k_m(x-l) + \varphi_m^o] & x_J^+ \leq x \leq l \end{cases} \tag{2.28}$$

There are thus 5 parameters to determine: a_m, b_m, k_m, φ_m^i and φ_m^o.

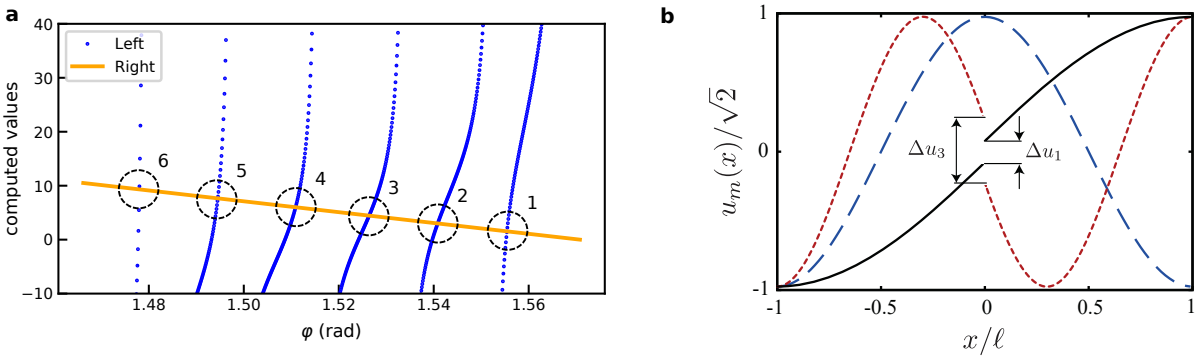

Figure 2.5: (a) Numerical solutions of Eq. 2.31 where we plotted the right and left hand side of the equation. Each solution corresponds to a different mode. (b) Examples of the three first normal modes envelopes with the junction placed in the middle of the resonator. We can see that the junction only affects the odd modes. Figure (b) was taken from [83].

We can now use the previous equations to determine all the parameters. We can solve Eq. 2.25 and 2.26 knowing that $\Phi_m(t)$ is of the form $De^{i\omega t}$ where D is a constant and u_m expressed above, to get an equation on $\varphi_m^{i,o}$ and k_m:

$$\tan(\varphi_m^{i,o}) = \frac{1}{C_{i,o} Z^0 k_m v} \tag{2.29}$$

Using the first equality of Eq. 2.27 we get an equation on b_m, k_m and $\varphi_m^{i,o}$:

$$b_m = \frac{\cos[k_m(x_J + l) - \varphi_m^i]}{\cos[k_m(x_J - l) + \varphi_m^o]} \tag{2.30}$$

By using the expression of u_m in Eq. 2.27 and using Eq. 2.30 we find the following equation:

$$\Big(\tan[k_m(x_J - l) + \varphi_m^o] - \tan[k_m(x_J + l) - \varphi_m^i] \Big) \Big(\frac{L^0 l}{L_J} - (k_m l)^2 \frac{C_J}{C^0 l} \Big) = k_m l \tag{2.31}$$

By using Eq 2.29 we can express k_m as a function of $\varphi_m^{i,o}$ and inject this in Eq. 2.31 to have an equation with a unique unknown parameter $\varphi_m^{i,o}$. This equation has to be solved numerically and one can find several solutions corresponding to the different modes m as shown in Fig. 2.5a. Once we get $\varphi_m^{i,o}$ we can compute k_m with Eq. 2.31 and then b_m with Eq. 2.30. The last parameter to determine is a_m which can be done using the inner product [85]:

$$\langle u_m \cdot u_n \rangle \equiv \int_{-l}^{l} dx C^0 u_m(x) u_n(x) + C_i u_m(-l) u_n(-l) + C_o u_m(l) u_n(l) + C_J \Delta u_m \Delta u_n = C_\Sigma \delta_{mn} \tag{2.32}$$

where we have defined $\Delta u_m = u_m(x_J^+) - u_m(x_J^-)$. One has to mention that Δu_m is the most important parameter of this model because it tells how much the JJ perturbs the mode and plays a role in the participation ratio and the Kerr coefficient as we will see later. Fig. 2.5b shows a typical solution of u_m for the first three modes. We can see that the JJ only affects odds modes by creating a gap Δu_m.

As we will see later, it is also useful to define the inner product of the mode envelopes [85]:

$$\langle \partial_x u_m \cdot \partial_x u_n \rangle = \int_{-l}^{l} \frac{dx}{L^0} \partial_x u_m(x) \partial_x u_n(x) + \frac{1}{L_J} \Delta u_m \Delta u_n = \frac{\delta_{mn}}{L_m} \tag{2.33}$$

where we have defined the mode inductance $L_m^{-1} \equiv C_\Sigma \omega_m^2$ taking into account the linear part of the Josephson inductance. Fig. 2.4b represents thus the lumped representation of the distributed resonator where the nonlinear part of the JJ is biased by a series of LC oscillators corresponding to each resonant mode. Note that when the approximation $C_J >> \Delta x C^0$ leading to Eq. 2.27 is not true, it would transform Eq. 2.31 such that $C_J/(C^0 l) \rightarrow (C_J + \Delta x C^0)/(C^0 l)$. In practice we neglect C_J because we are working far from the plasma frequency, and because $\Delta x << l$ we could also neglect the modification appearing because of the 'wrong' approximation that we did earlier.

2.3.2.c Hamiltonian of the system

The Hamiltonian of the system can be obtained by doing the Legendre transformation of the Lagrangian by using the generalized momenta $Q_m = \partial \mathcal{L} / \partial \dot{\Phi}_m$ corresponding to the charge conjugate of Φ_m. We will directly jump to the final result were we reintroduced the nonlinearity (more details can be found in [83]):

$$H = H_\circ + \sum_{m'} \Big[\frac{Q_{m'}'^2}{2C_{m'}'} + \frac{\Phi_{m'}'^2}{2L_{m'}'} \Big] - E_{NL} \Big(\sum_{m'} \Phi_{m'}' \Big) \tag{2.34}$$

where $H_\circ$ is the Hamiltonian part whose modes are not affected by the junction (even modes), m' the modes affected by the junction (odd modes), $Q'_{m'} = Q_{m'}/\Delta u_{m'}$, $\Phi'_{m'} = \Phi_{m'}\Delta u_{m'}$, $L'_{m'} = L_{m'}\Delta u^2_{m'}$, $C'_{m'} = C_\Sigma/\Delta u^2_{m'}$ and E_{NL} obeying to Eq. 2.11. We can see that the Hamiltonian is similar to the lumped model Hamiltonian given in Eq. 2.12 but with Φ being the sum on all the modes and with parameters renormalized by mode envelope gap $\Delta u_{m'}$ that we can compute thanks to the procedure given in the last section. We can quantize the Hamiltonian by introducing the creation and annihilation operators of excitations in mode m' A_m and $A^\dagger_m$ respectively:

$$\Phi'_{m'} = \sqrt{\frac{\hbar}{2C'_{m'}\omega_{m'}}}(A^\dagger_{m'} + A_{m'}) \tag{2.35}$$

$$Q'_{m'} = \sqrt{\frac{\hbar C_{m'}\omega_{m'}}{2}}(A^\dagger_{m'} - A_{m'}) \tag{2.36}$$

By considering only the modes affected by the junction and expanding E_{NL} only to the quartic term as for the lumped system, we get:

$$H \approx \sum_{m'} \hbar\omega'_{m'} A^\dagger_{m'} A_{m'} - \sum_{m'} \hbar\frac{K_{m'm'}}{2} A^\dagger_{m'} A^\dagger_{m'} A_{m'} A_{m'} \tag{2.37}$$

where we used the rotating wave approximation and neglected terms with interactions between two different modes. In this expression we defined $K_{m'm'}$ as :

$$K_{m'm'} = \frac{1}{\hbar} E'_{C,m'} \eta_{l,m'} = \frac{1}{\hbar}\frac{e^2}{2C_\Sigma}\frac{L_{m'}}{L_J}\Delta u^4_{m'} \tag{2.38}$$

with $E'_{C,m'} = e^2/(2C'_{m'})$ the charging energy associated to the total capacitance $C'_{m'}$ and $\eta_{l,m'} = L'_{m'}/L_J$ the participation ratio of the junction. We also defined:

$$\omega'_{m'} = \omega_{m'} - \sum_{n'} K_{m'n'} \tag{2.39}$$

with $K_{m'n'} = 2\sqrt{K_{m'm'}K_{n'n'}}$ the cross Kerr coefficients. $K_{m'm'}$ has a similar expression as for the lumped resonator but is corrected by a factor $\Delta u^4_{m'}$ because of the renormalization of the total capacitance and inductance caused by the presence of the JJ. In the rest of the manuscript we will only focus on the first mode $m' = 1$. This means that the Hamiltonian of the distributed model is exactly the same as for the lumped model but with a renormalized K and a angular resonance frequency shifted slightly further because of cross Kerr interactions. In practice $\omega_{m'} >> K_{mn}$ meaning that this shift is negligible. We also point out that interactions between different modes that we neglected lead to cross Kerr nonlinear terms and beam-splitter-like terms [83].

2.4 Input/output theory for the JPA

We studied in the previous section the isolated system resonator + JJ and saw that its Hamiltonian presents a four-wave mixing term that could be used for amplification. We will now study this system coupled to external ports and how it should be driven to create

amplification. This is done by using the input/output theory [86] and following carefully the work done by Yurke and Buks [87] where nonlinear loss is included in the model. They created this model to account for the nonlinear loss observed in high kinetic inductance transmission line. In our case we do not have high kinetic inductance, but the SNS nature of the JJ can create nonlinear dissipation as we saw in Chapter 1.

2.4.1 Equations of motion

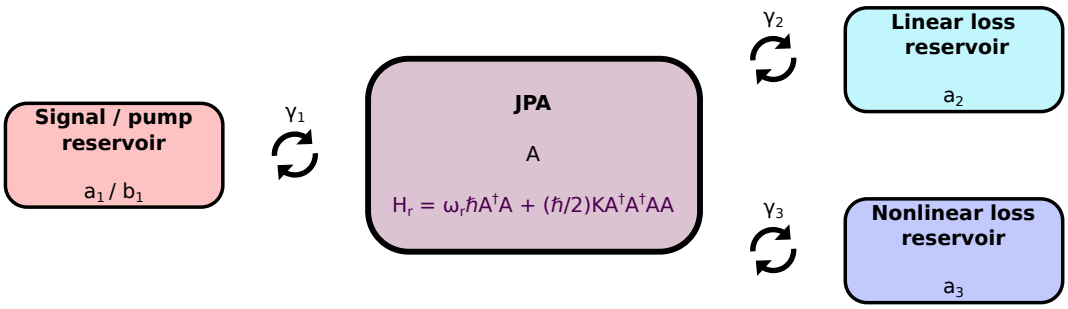

Figure 2.6: Scheme of the model where the JPA is coupled to three ports. The port 1 is the port from where are coming the input tones. The ports 2 and 3 stem for linear and nonlinear loss respectively.

The schematic of the studied system is shown in Fig. 2.6. The JPA is coupled to three thermal baths. The first thermal bath correspond to the port through which are sent input tones and through which we measure what is reflected. The second and the third thermal baths correspond to linear and nonlinear loss (two-photon loss) respectively. In this model, the Hamiltonian of the JJ embedded in a resonator is equivalent to the Hamiltonian that was derived in the last section:

$$H_r = \hbar\omega_r A^\dagger A + \frac{\hbar}{2} K A^\dagger A^\dagger A A \tag{2.40}$$

where A is the intracavity annihilation operator and K and ω_r can be computed from Eq. 2.38 and 2.39 respectively. The Hamiltonians of the thermal bath $i = 1, 2, 3$ are:

$$H_i = \int d\omega \hbar\omega a_i^\dagger(\omega) a_i(\omega) \tag{2.41}$$

with a_i the annihilation operator in the thermal bath i. We define a linear coupling with the bath 1 and 2:

$$H_{c_{1,2}} = \hbar \int d\omega \left[\kappa_{1,2} A^\dagger a_{1,2}(\omega) + \kappa_{1,2}^* a_{1,2}^\dagger(\omega) A\right] \tag{2.42}$$

and the two-photon coupling for the bath corresponding to nonlinear loss:

$$H_{c_3} = \hbar \int d\omega \left[\kappa_3 A^\dagger A^\dagger a_3(\omega) + \kappa_3^* a_3^\dagger(\omega) A A\right] \tag{2.43}$$

The fact that $\kappa_{1,2,3}$ do not depend on ω is part of the Markov approximation [86]. The total Hamiltonian is:

$$H = H_r + H_1 + H_2 + H_3 + H_{c_1} + H_{c_3} + H_{c_3} \tag{2.44}$$

In the Heisenberg picture, we can use the Heisenberg equation to get the equation of motion of A:

$$\begin{aligned}\frac{dA}{dt} &= -\frac{i}{\hbar}[A, H] \\ &= -i\omega_r A - iKA^\dagger AA - i\kappa_1 \int d\omega a_1(\omega) - i\kappa_2 \int d\omega a_2(\omega) - 2i\kappa_3 \int d\omega A^\dagger a_3(\omega)\end{aligned} \tag{2.45}$$

Applying the same procedure for a_i using the commutation relation $\left[a_i(\omega), a_j^\dagger(\omega')\right] = \delta_{i,j}\delta(\omega - \omega')$:

$$\frac{da_{1,2}(\omega)}{dt} = -i\omega a_{1,2}(\omega) - i\kappa_{1,2}^* A \tag{2.46}$$

$$\frac{da_3(\omega)}{dt} = -i\omega a_3(\omega) - i\kappa_3^* AA \tag{2.47}$$

We can integrate Eq. 2.46 to obtain:

$$a_{1,2}(\omega) = a_{1,2}^{t_0}(\omega)e^{-i\omega(t-t_0)} - i\kappa_{1,2}^* \int_{t_0}^{t} A(t')e^{-i\omega(t-t')}dt' \tag{2.48}$$

with $a_{1,2}^{t_0}(\omega)$ the value of $a_{1,2(\omega)}$ at the initial time $t_0 < t$. It is useful to define $a_{1,2}^{in}(t)$ as the inverse Fourier transform of $a_{1,2}^{t_0}(\omega)$ at $t = t_0$. Doing the same procedure but considering a time $t_1 > t$ allows to define $a_{1,2}^{out}(t)$, the inverse Fourier transform of $a_{1,2}^{t_1}(\omega)$ at $t = t_1$. A similar procedure for Eq. 2.47 gives:

$$a_3(\omega) = a_3^{t_0}(\omega)e^{-i\omega(t-t_0)} - i\kappa_3^* \int_{t_0}^{t} A^2(t')e^{-i\omega(t-t')}dt' \tag{2.49}$$

and we can define $a_3^{in/out}$ similarly as for the mode 1 and 2. Inserting the equations on $a_{1,2,3}$ in Eq. 2.45 gives the equation of motion:

$$\frac{dA}{dt} = -i\omega_r A - iKA^\dagger AA - \gamma A - \gamma_3 A^\dagger AA - i\sqrt{2\gamma_1}e^{i\phi_1}a_1^{in} - i\sqrt{2\gamma_2}e^{i\phi_2}a_2^{in} - 2i\sqrt{\gamma_3}e^{i\phi_3}A^\dagger a_3^{in} \tag{2.50}$$

where $\gamma = \gamma_1 + \gamma_2$ and:

$$\kappa_{1,2} = \sqrt{\frac{\gamma_{1,2}}{\pi}}e^{i\phi_{1,2}} \qquad \kappa_3 = \sqrt{\frac{\gamma_3}{2\pi}}e^{i\phi_3} \tag{2.51}$$

We can see in Eq. 2.50 that there are two real terms proportional to A: $-\gamma A - \gamma_3 A^\dagger AA$ meaning that they are dissipation terms. The first one is associated to linear loss in port 1 and 2, the second one is proportional to the number of photons inside the resonator $A^\dagger A$. This means that the nonlinear loss increases linearly with the number of intracavity photons in this model.

One can compute the input-output relations for the ports 1 and 2 by using Eq. 2.48 and the definition of $a_{1,2}^{in}$ and $a_{1,2}^{out}$. A similar procedure can be done for the ports 3. We find:

$$\begin{aligned}a_{1,2}^{out} - a_{1,2}^{in} &= -i\sqrt{2\gamma_{1,2}}e^{-i\phi_{1,2}}A(t) \\ a_3^{out} - a_3^{in} &= -i\sqrt{\gamma_3}e^{-i\phi_3}A(t)A(t)\end{aligned} \tag{2.52}$$

Now that we have expressed all the equation of motions, we will first solve them in the classical limit which is useful to understand the behavior of the JPA biased by a strong pump.

2.4.2 Classical nonlinear response

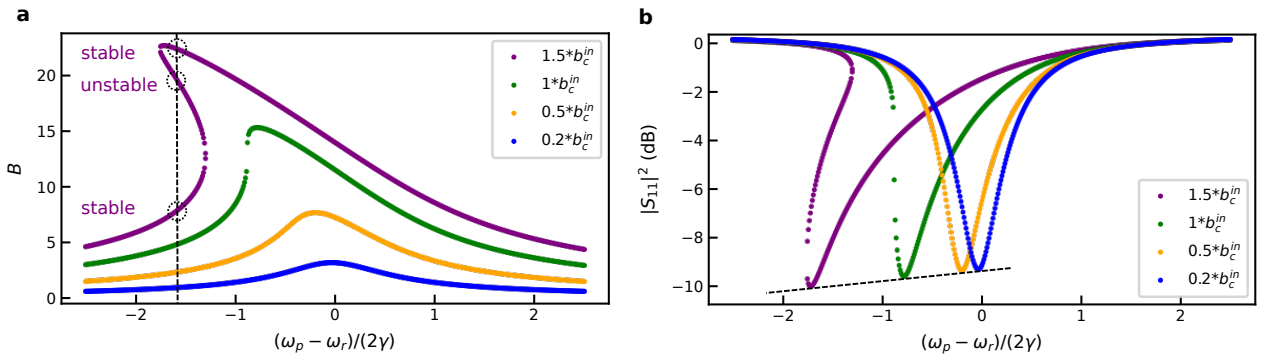

Figure 2.7: (a) Amplitude of the intracavity field with respect to the angular frequency of the pump for different input fields. (b) Magnitude of the S_{11} parameter with respect to pump frequency for different input fields. The dashed line indicates the linear dependence of the minimum of $|S_{11}|$ with respect to the input power. The parameters are: $\gamma_1 = 0.01\omega_r$, $\gamma_2 = 0.5\gamma_1$, $K = -10^{-4}\omega_r$, $\gamma_3 = -0.01K/\sqrt{3}$.

As we saw in Fig. 2.3b, the parametric amplification process needs the presence of a strong pump tone. We will now derive the effects of such a strong incoming and outgoing coherent classical field:

$$a_1^{in,out} = b_1^{in,out} e^{-i(\omega_p t + \Psi_1)} \tag{2.53}$$

where $b_1^{in,out}$, the amplitude of the incoming/outgoing pump field is a real constant number, ω_p the angular frequency of the pump and Ψ_1 its phase. Because of the classical nature of the pump, a_1^{in} is not an operator anymore but a complex number. The incoming fields coming from ports 2 and 3 are noise and quantum fluctuations and can thus be neglected here: $a_{2,3}^{in} = 0$. We can also rewrite the intracavity field:

$$A = Be^{-i(\omega_p t + \phi_B)} \tag{2.54}$$

where B is a real constant number. By using the equation of motion of A we find:

$$[i(\omega_r - \omega_p) + \gamma]B + (iK + \gamma_3)B^3 = -i\sqrt{2\gamma_1} b_1^{in} e^{i(\phi_1 + \phi_B - \Psi_1)} \tag{2.55}$$

and by using the input/output equation on the modes a_1:

$$b_1^{out} = b_1^{in} - i\sqrt{2\gamma_1} B e^{-i(\phi_1 + \phi_B - \Psi_1)} \tag{2.56}$$

By combining these two equations we obtain the reflection coefficient or the S_{11} parameter:

$$\frac{b_1^{out}}{b_1^{in}} = S_{11} = 1 - \frac{2\gamma_1 B}{[i(\omega_r - \omega) + \gamma]B + (iK + \gamma_3)B^3} \tag{2.57}$$

We can see that in the limit where there are no nonlinear effects, i.e. $K = \gamma_3 = 0$, this expression is similar to the S_{11} parameter of a half wave resonator with $\gamma_1 = \omega_r/(2Q_c)$, $\gamma_2 = \omega_r/(2Q_i)$ where Q_c and Q_i are respectively the external and the internal quality factors

(see Chapter 4). By multiplying each side of Eq. 2.55 by its complex conjugate we obtain a cubic equation in B^2 that allows to compute the intracavity field:

$$B^6 + \frac{2[(\omega_r - \omega_p)K + \gamma\gamma_3]}{K^2 + \gamma_3^2} B^4 + \frac{(\omega_r - \omega_p)^2 + \gamma^2}{K^2 + \gamma_3^2} B^2 - \frac{2\gamma_1}{K^2 + \gamma_3^2} (b_1^{in})^2 = 0 \tag{2.58}$$

Fig. 2.7a shows the computed amplitude of the field with respect to the pump angular frequency for different input powers. We can see that at low input power, B is centered around the resonance frequency ω_r. When the input power increases, the maximum of B shifts to lower frequency due to the negative Kerr shift. This can be directly computed, by using $\partial(B^2)/\partial\omega_p = 0$ we find that at resonance:

$$\omega_p = \omega_r + KB^2 \tag{2.59}$$

meaning that the resonance occurs at $\omega_r + KB^2$ instead of ω_r. Once the input field reaches a value above a threshold field called the critical field b_{1c}^{in}, the system goes from having one real solution and two complex solutions (not physical) to three possible real solutions as shown for the purple curve. Two of these solutions are stable and one is unstable. In this case, the device is said to be in a bistable state. While the bistability can be used for amplification (Josephson bifurcation amplifier [88, 89]), the JPA works at power just below the critical power in a region where linear amplification is possible.

The intracavity field at the critical input field leads to a double condition. The first one is that $\partial(B^2)/\partial\omega = \infty$ or equivalently $\partial\omega/\partial(B^2) = 0$. This condition means that the slope is infinite at the critical power. But as we can see in Fig. 2.7a, this condition is also true above the critical power. This leads to the second condition $\partial^2\omega/\partial^2(B^2) = 0$ where the two solutions appearing at the critical power coalesce into a single point. From these two conditions it is possible to derive important equations giving some quantities at the critical point. The first one is on the critical input field b_{1c}^{in}:

$$(b_{1c}^{in})^2 = \frac{4}{3\sqrt{3}} \frac{\gamma^3(K^2 + \gamma_3^2)}{\gamma_1(|K| - \sqrt{3}\gamma_3)^3} \tag{2.60}$$

The intracavity critical field can be expressed as:

$$B_c^2 = \frac{2\gamma}{\sqrt{3}(|K| - \sqrt{3}\gamma_3)} \tag{2.61}$$

and the Kerr frequency shift associated to the critical point:

$$\omega_r - \omega_p = -\gamma \frac{K}{|K|} \left[\frac{4\gamma_3|K| + \sqrt{3}(K^2 + \gamma_3^2)}{K^2 - 3\gamma_3^2} \right] \tag{2.62}$$

These equations show that the linear and nonlinear loss have the effect of pushing the critical point at a higher input power. Because of this, the critical intracavity field is larger as well as the critical Kerr frequency shift. When $\gamma_3 > |K|/\sqrt{3}$, the nonlinear loss is too high and bifurcation is not possible anymore. Eqs. 2.62 and 2.60 are very useful for experimental data fitting because they allow to fix fitting parameters thanks to accessible experimental

parameters like the critical power and the critical frequency shift as long as we are able to find the critical point accurately (see Chapter 5).

It is also instructive to look at the S_{11} power dependency as shown in Fig. 2.7b because it is a quantity that we can directly measure. We can see that at the critical power, the slope of $|S_{11}|$ is also infinite at one point. We can also see that the depth of the resonance dip associated to internal loss is increasing linearly with the input power. This is because of the two-photon loss being proportional to γB^2 according to Eq. 2.50.

2.4.3 Linearized reponse for quantum fields

2.4.3.a Solving the linear equation

In the previous section we studied the effect of a classical field on the system. We will now reintroduce quantum fields on top of the classical field and keep only linear orders in the quantum fields because they are small by nature. This is equivalent of considering both a pump and a small signal at the input of the JPA. We can thus write the input and output fields as:

$$\begin{aligned} A &= Be^{-i(\omega_p t+\phi_B)} + ae^{-i\omega_p t} \\ a_1^{in} &= b_1^{in}e^{-i(\omega_p t+\psi_1)} + c_1^{in}e^{-i\omega_p t} \\ a_{2,3}^{in} &= c_{2,3}^{in}e^{-i\omega_p t} \\ a_1^{out} &= b_1^{out}e^{-i(\omega_p t+\psi_1)} + c_1^{out}e^{-i\omega_p t} \\ a_{2,3}^{out} &= b_{2,3}^{out}e^{-i(\omega_p t)} + c_{2,3}^{out}e^{-i\omega_p t} \end{aligned} \tag{2.63}$$

where a, $c_{1,2,3}^{in}$ and $c_{1,2,3}^{out}$ are quantum fields and B, $b_{1,2,3}^{out}$ classical fields that can be computed from the previous part. Using equation of motion (Eq. 2.50) on A and keeping only linear terms in a, we find:

$$\frac{da}{dt} + Wa + Va^\dagger = F \tag{2.64}$$

with:

$$\begin{aligned} W &= i(\omega_r - \omega_p) + \gamma + 2(iK + \gamma_3)B^2 \\ V &= (iK + \gamma_3)B^2 e^{-2i\phi_B} \\ F &= -i\sqrt{2\gamma_1}e^{i\phi_1}c_1^{in} - i\sqrt{2\gamma_2}e^{i\phi_2}c_2^{in} - 2i\sqrt{\gamma_3}Be^{i(\omega_p t+\phi_B+\phi_3)}c_3^{in} \end{aligned} \tag{2.65}$$

where we also used the equation of motion on the classical intracavity field only (Eq. 2.55) to simplify the terms depending only on B. By doing so, we assumed that the classical field B is not affected by the presence of the quantum field a (which is true as long as a is negligible compared to B). This approximation is called the stiff pump approximation. By isolating $a^\dagger$ in Eq. 2.64 and plugging it into the adjoint of Eq. 2.64 we find (note that according to Eq. 2.58, B does not depend on time):

$$\frac{d^2a}{dt^2} + 2\mathrm{Re}(W)\frac{da}{dt} + (|W^2| - |V|^2)a = \Gamma(t) \tag{2.66}$$

where

$$\Gamma(t) = \frac{dF}{dt} + W^* F - V F^\dagger(t) \tag{2.67}$$

By rewriting the operators using their Fourier decomposition : $O(t) = \frac{1}{2\pi}\int_{-\infty}^{\infty} d\omega O(\omega) e^{-i\omega t}$, we find:

$$a(\omega) = \frac{\Gamma(\omega)}{-\omega^2 - 2i\omega \mathrm{Re}(W) + (|W|^2 - |V|^2)} = \frac{\Gamma(\omega)}{(-i\omega + \lambda_0)(-i\omega + \lambda_1)} \tag{2.68}$$

where we have defined:

$$\begin{aligned} \lambda_0 &= \gamma + 2\gamma_3 B^2 - \sqrt{(K^2 + \gamma_3^2)B^4 - (\omega_r - \omega_p + 2KB^2)^2} \\ \lambda_1 &= \gamma + 2\gamma_3 B^2 + \sqrt{(K^2 + \gamma_3^2)B^4 - (\omega_r - \omega_p + 2KB^2)^2} \end{aligned} \tag{2.69}$$

and where $\Gamma(\omega)$ is expressed as:

$$\begin{aligned} \Gamma(\omega) = &-i\sqrt{2\gamma_1}\Big[(-i\omega + W^*)e^{i\phi_1} c_1^{in}(\omega) - V e^{-i\phi_1} c_1^{in\dagger}(-\omega)\Big] \\ &- i\sqrt{2\gamma_2}\Big[(-i\omega + W^*)e^{i\phi_2} c_2^{in}(\omega) - V e^{-i\phi_2} c_2^{in\dagger}(-\omega)\Big] \\ &- 2i\sqrt{\gamma_3} B\Big[(-i\omega + W^*)e^{i(\phi_3+\phi_B)} c_3^{in}(\omega_p + \omega) - V e^{-i(\phi_3+\phi_B)} c_3^{in\dagger}(\omega_p - \omega)\Big] \end{aligned} \tag{2.70}$$

We want now to express c_1^{out} (i.e. the output quantum field on the measurement port) as a function of all the other input operators in order to compute the gain. For this purpose we use the input/output equation (Eq. 2.52) with the linearized field and find:

$$c_1^{out}(\omega) = c_1^{in}(\omega) - i\sqrt{2\gamma_1} e^{-i\phi_1} a(\omega) \tag{2.71}$$

and insert it in Eq. 2.68 to find:

$$\begin{aligned} c_1^{out}(\omega) = &\Big[(1 - \gamma_1\chi_s)\Big] c_1^{in}(\omega) + \Big[\gamma_1 e^{-2i\phi_1}\chi_i\Big] c_1^{in\dagger}(-\omega) \\ &- \Big[\sqrt{\gamma_1\gamma_2} e^{i(\phi_1-\phi_2)}\chi_s\Big] c_2^{in}(\omega) + \Big[\sqrt{\gamma_1\gamma_2} e^{-i(\phi_1+\phi_2)}\chi_i\Big] c_2^{in\dagger}(-\omega) \\ &- \Big[\sqrt{2\gamma_1\gamma_3} B e^{i(\phi_1-\phi_3-\phi_B)}\chi_s\Big] c_3^{in}(\omega_p + \omega) + \Big[\sqrt{2\gamma_1\gamma_3} B e^{-i(\phi_1+\phi_3+\phi_B)}\chi_i\Big] c_3^{in\dagger}(\omega_p - \omega) \end{aligned} \tag{2.72}$$

Where we defined:

$$\begin{aligned} \chi_s &= \frac{2(-i\omega + W^*)}{(-i\omega + \lambda_0)(-i\omega + \lambda_1)} \\ \chi_i &= \frac{2V}{(-i\omega + \lambda_0)(-i\omega + \lambda_1)} \end{aligned} \tag{2.73}$$

2.4.3.b Kerr medium and frequency mixing

We see here that the output mode $c_1^{out}(\omega)$ is the sum of contributions coming from the input modes 1 and 2 (we ignore the mode 3 for now) at the angular frequency ω with

common factors χ_s, and the sum of contributions of the sames modes but at the angular frequency $-\omega$ and a common factors χ_i. While the terms in χ_s are trivial because one can expect all the incoming field at the a given frequency to impact the outgoing field at the same frequency, the terms in χ_i show that modes at different frequencies contribute also to this outgoing signal. This is a specificity of Kerr mediums which can mix frequencies as shown in Fig. 2.3b. The signal mode has an angular frequency $\omega = \omega_s$ and the idler mode an angular frequency $-\omega = \omega_i$. We point out that we defined the linear fields with a factor $e^{-i\omega_p t}$ on each operator. This means that the angular frequency $\omega = 0$ corresponds to $\omega = \omega_p$. There is thus the relation $\omega_s + \omega_i = 2\omega_p$. One can see that $\chi_i \propto V \propto (iK + \gamma_3)B^2$. This shows that the mixing frequency term would cancel in a system with no Kerr effect and nonlinear loss. An interesting fact is that even without Kerr nonlinearity, the presence of nonlinear loss can create wave mixing. Because of the nonlinear nature of γ_3, the contributions of the mode 3 to the mode 1 corresponds to angular frequencies $2\omega_p$ and 0.

2.4.3.c Discussion on the added noise

Let us consider a system with no intrinsic loss ($\gamma_2 = \gamma_3 = 0$). We can see in Eq. 2.72 that $c_1^{out}(\omega)$ has two contributions, one being $c_1^{in}(\omega)$ the signal we want to amplify, and one being $c_1^{in}(-\omega)$ being the idler mode associated to the signal mode. This means that even if no signal is sent at the idler frequency, there will always be quantum fluctuations on the idler mode that will contribute to the output signal. When the only source of added noise is the quantum fluctuations associated to the idler mode, the amplifier is said to be at the quantum limit. We can see that when there are modes associated to loss ($\gamma_2 \neq 0$, $\gamma_3 \neq 0$), it adds other sources of noise and prevents the JPA to be quantum limited. One can estimate the contribution of the loss modes by putting all the phases to 0, making the approximation $\chi_i \approx \chi_s = \chi >> 1$ which is justified for high amplification gain. In this case Eq. 2.72 can be written as:

$$\begin{aligned} c_1^{out}(\omega) = -\gamma_1\chi c_1^{in}(\omega) + \gamma_1\chi \Bigg[& c_1^{in\dagger}(-\omega) - \sqrt{\frac{\gamma_2}{\gamma_1}} c_2^{in}(\omega) + \sqrt{\frac{\gamma_2}{\gamma_1}} c_2^{in\dagger}(-\omega) \\ & - \sqrt{\frac{\gamma_3}{\gamma_1}} B c_3^{in}(\omega_p + \omega) + \sqrt{\frac{\gamma_3}{\gamma_1}} B c_3^{in\dagger}(\omega_p - \omega) \Bigg] \end{aligned} \tag{2.74}$$

We can see that the linear loss mode will contribute with a factor $\sqrt{\gamma_2/\gamma_1}$ to the added noise and the nonlinear loss mode with a factor $\sqrt{\gamma_3 B^2/\gamma_1}$. For now, we only looked at noise on $c_1^{out}(\omega)$, but we are only able to measure $|c_1^{out}(\omega)|^2$. One can thus expect the loss modes to increase the added noise by a factor $1 + \frac{\gamma_2 + \gamma_3 B^2}{\gamma_1}$.

2.4.4 Gain

2.4.4.a Gain calculation

The previous calculation allowed to explain how the JPA, acting as a Kerr medium, is able to mix frequencies and what is the impact of losses on its noise performances. We will now compute its gain G which is an important figure of merit of the device. We already saw

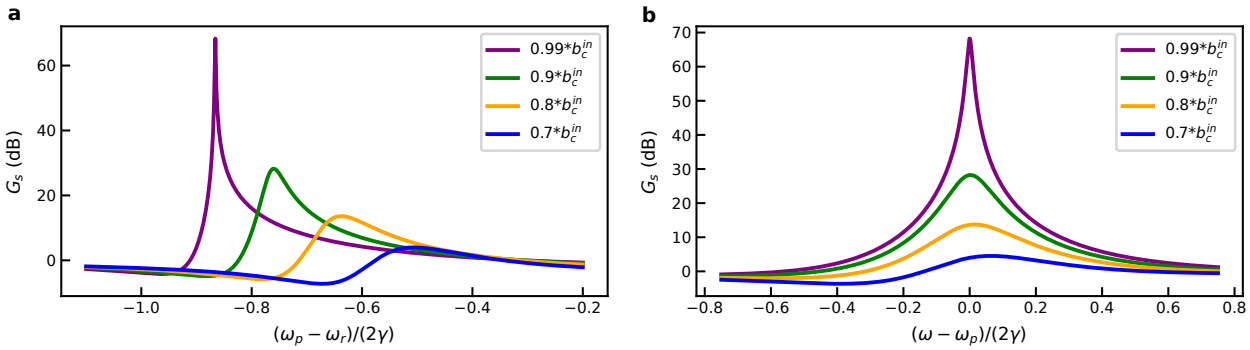

Figure 2.8: (a) Signal gain at $\omega = 0$ with respect to the pump angular frequency for different input powers. (b) Signal gain with respect to the signal frequency. The pump frequency was chosen to maximize the gain and was extracted from (a). The parameters are: $\gamma_1 = 0.01\omega_r$, $\gamma_2 = 0.5\gamma_1$, $K = -10^{-4}\omega_r$, $\gamma_3 = -0.01K/\sqrt{3}$.

that the output mode is a combination of many different inputs such that it is not possible to define a unique gain because we cannot write $|c_1^{out}|^2 = G|c_1^{in}|^2$. We thus define the classical parametric gain or signal gain G_s as the gain where $c_1^{in}(\omega)$ represents a classical signal at frequency ω and all the other modes are set to zero:

$$G_s \equiv \frac{|c_1^{out}(\omega)|^2}{|c_1^{in}(\omega)|^2} = |1 - \gamma_1\chi_s|^2 = \frac{|(-i\omega + \lambda_0)(-i\omega + \lambda_1) - 2\gamma_1(-i\omega + W^*)|^2}{(\omega^2 + \lambda_0^2)(\omega^2 + \lambda_1^2)} \tag{2.75}$$

where the last expression shows the explicit signal angular frequency dependence of G_s. One can also define the intermodulation gain G_i as the gain where $c_1^{in}(-\omega)$ represents a classical signal and all the other modes are put to zero:

$$G_i \equiv \frac{|c_1^{out}(\omega)|^2}{|c_1^{in}(-\omega)|^2} = |\gamma_1\chi_i|^2 = \frac{4\gamma_1^2|V|^2}{(\omega^2 + \lambda_0^2)(\omega^2 + \lambda_1^2)} \tag{2.76}$$

We can see that G_i and G_s are maximal at $\omega = 0$, i.e. when the signal frequency is at the pump frequency. It is possible to show that the bifurcation conditions $\partial\omega_p/\partial(B^2) = 0$ and $\partial^2\omega_p/\partial(B^2)^2 = 0$ implies $\lambda_0 = 0$. It means that getting close to the bifurcation point makes the maximum gain higher and even infinite when the JPA is exactly at the bifurcation point. This is of course not physical because the gain takes its energy from the pump which has not an infinite energy. This arises because we considered the pump as stiff in the calculations. Fig. 2.8a shows the signal gain as a function of the pump angular frequency for $\omega = 0$ in order to have the maximum of gain. We can see that the higher is the input power, the higher is the gain and the higher is the Kerr shift. It also shows that for a given pump power, one has first to find the optimal pump frequency to get the maximum of gain. Once the optimal pump frequency is found, one can plot the gain with respect to the signal frequency as shown in Fig. 2.8b. We can also see parameters for which the gain is negative (i.e. smaller than 1 in linear unit). This happens because we did put loss in the model through γ_2 and γ_3 (see parameters in the caption of Fig. 2.8).

2.4.4.b Gain approximation

We will now make approximations on the gain equations in order to derive useful results. We will work in the vicinity of the pump frequency such that $\omega << \gamma$. Moreover we will only consider the high gain regime i.e. close to the bifurcation point where $\lambda_0 << \gamma$ and thus $\lambda_1 \approx 2(\gamma + \gamma_3 B^2)$. Close to the critical point, we can rewrite W taking into account Eq. 2.62 and taking $K >> \gamma_3$:

$$W = \gamma + \gamma_3 B^2 + i(2KB^2 + \omega_r - \omega_p) \approx \gamma + \gamma_3 B^2 + i\frac{K}{|K|}\frac{\sqrt{3}}{3}\gamma \tag{2.77}$$

The numerator of Eq. 2.75 has only one dominant term: $-2\gamma_1 W^*$ and we neglect the term in ω^4 in the denominator. The parametric gain can thus be written as:

$$G_s \approx \frac{(4\gamma_1^2|W|^2)/(\lambda_0\lambda_1)}{1 + \omega^2/\lambda_0^2} \tag{2.78}$$

Which is a lorentzian of maximal gain $G = (4\gamma_1^2|W|^2)/(\lambda_0\lambda_1)$ and width Δ_{bw}:

$$\Delta_{bw} = 2\lambda_0 \approx \frac{2\gamma_1|W|}{\sqrt{G}(\gamma + \gamma_3 B^2)} \approx \frac{2\gamma_1\sqrt{(\gamma + \gamma_3 B^2)^2 + \gamma^2/3}}{\sqrt{G}(\gamma + \gamma_3 B^2)} \approx \frac{2\gamma_1}{\sqrt{G}} \tag{2.79}$$

Thus, the JPA follows a gain bandwidth product of the form $\Delta_{bw}\sqrt{G} = 2\gamma_1$ meaning that the bandwidth of the gain will reduce with increasing gain and be larger with a better coupling to the input signal port.

One can also compare the signal gain to the idler gain. By keeping the same approximation as before, the gains just differ by one term, $|W|^2$ for G_s and $|V|^2$ for G_i. We have :

$$|W|^2 = (\gamma + \gamma_3 B^2)^2 + \frac{\gamma^2}{3} \qquad |V|^2 = \frac{4}{3}\gamma^2 + (\gamma_3)B^2 \tag{2.80}$$

Because in practice $\gamma >> \gamma_3 B^2$, the idler and signal gains are very close to each other in the high gain limit. Precise calculations, in the limit where $\gamma_2 = \gamma_3 = 0$ shows that $G_i = G_s - 1$ even away of the high amplification limit [90].

2.5 Gain limitation

We saw in the last section that an infinite gain could occur when the JPA is driven exactly at the bifurcation point. This is obviously not possible because an infinite gain implies an infinite energy. It is strongly related to the linearization procedure we did to solve the equation of motion of $A = Be^{-i(\omega_p t + \phi_B)} + ae^{-i\omega_p t}$. We first solved Eq. 2.58 which is the equation of motion of the classical intracavity field B when the pump is sent to the JPA. We then used B computed this way to solve Eq. 2.66 which is the linearized equation of motion on the quantum field a. By doing so, we considered that the pump field (B) is not affected by the quantum field (stiff pump approximation), and we dropped nonlinear terms in a. These dropped nonlinear terms are $(-iK - \gamma_3)(B^* e^{i\phi_B} a^2 + 2Be^{-i\phi_B} a^\dagger a + a^\dagger a^2)$. We can decompose

them in second order terms that are names c_2 terms (terms in a^2 and $a^\dagger a$), and third order terms that are names c_3 terms (terms in $a^\dagger a^2$). These two approximations fail when the JPA is in the high gain regime, i.e. when the quantum field is not negligible compared to the classical field. Moreover, to obtain the Kerr type Hamiltonian, we only developed the Josephson energy to the quartic order. This is also an approximation that can probably change the computed gain. We will study the impacts on the gain of all these approximations in the rest of the section.

2.5.1 Pump back-action

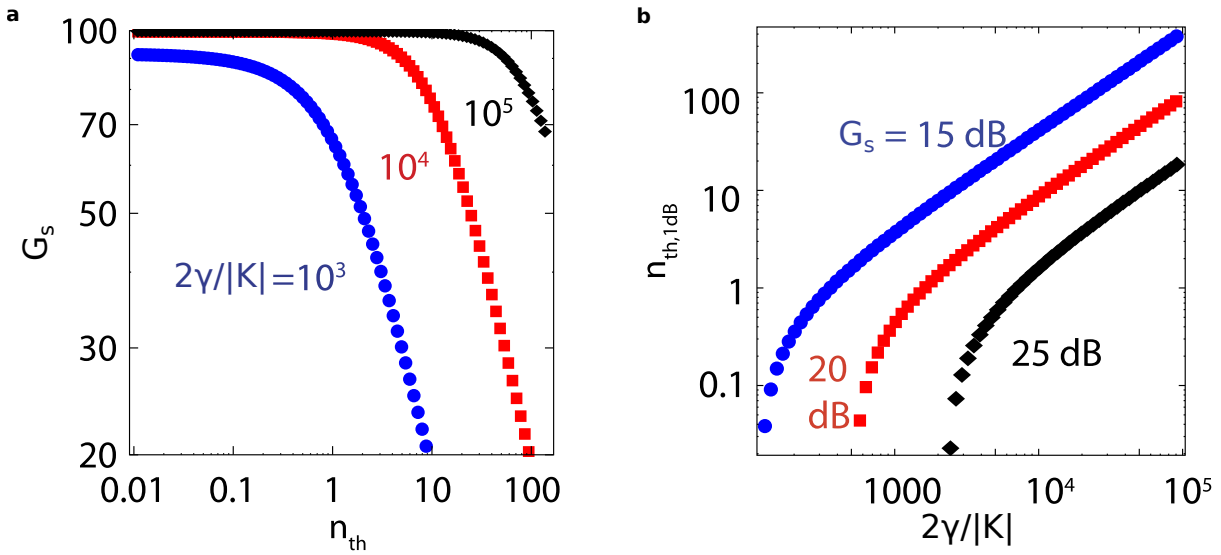

Figure 2.9: (a) Gain as a function of the input number of photon per unit of bandwidth for different ratio $2\gamma/K$. (b) 1-dB compression point as a function of the ratios $2\gamma/K$ for different gains. Figure (a) and (b) adapted from [90].

A way to include back-action on the pump is developed in [91, 90]. It is a mean field approach that takes into account the c_2 terms that we neglected in the linearized equation of motion (Eq. 2.64) : $2iK\langle a^\dagger a\rangle B$ and $iK\langle a^2\rangle B$. These terms are not incorporated in the linearized equation of motion (Eq. 2.64) but in the equation of motion (Eq. 2.58) for the classical field $A = Be^{-i(\omega_p t+\psi_1)}$. So, the classical equation of motion has terms depending on the quantum operator a. This is why we refer to this mechanism as pump back-action. By solving the modified Eq. 2.50 and Eq. 2.64 self-consistently, we can obtain the gain dependence with respect to the input quantum signal power.

In [90], they considered the incoming signal field as white noise with an average photon number n_{th} per unit of time and bandwidth, and no internal loss. They show the maximum gain as a function of n_{th} (Fig. 2.9a). We can see that the gain is constant at low input number of photons and then starts to decrease above a certain value. This value scales with the ratio $2\gamma/K$. The blue curve shows that for a ratio $2\gamma/K = 10^3$, even at $n_{th} = 0$ the gain is limited. When this ratio is small, the quantum fluctuations in the JPA are enough to affect the gain. We can define $n_{th,1dB}$, the input number of photons at which the gain is decreased by 1 dB.

Fig. 2.9b shows the dependence of $n_{th,1dB}$ with the ratio $2\gamma/K$ for different maximal gains. One can see that the ratio $2\gamma/K$ should be above 1000 to be able to amplify at least one photon with a 20 dB gain without being in the pump back-action regime.

We can also understand the pump back-action mechanism by thinking about the Kerr effect itself. The amplified quantum operator a (that is taken into account in the classical field equation of motion with the mean field approach) is making the total field inside the JPA more intense. Because of this, the Kerr frequency shift is more pronounced making the pump power and frequency not optimal anymore to reach the maximum of amplification. It can be shown that by shifting the pump at slightly lower frequency, one can push the compression point at higher input powers [92] because the Kerr 'extra' shift is compensated. Note that the mechanism we named 'pump back-action' is sometimes named pump depletion [90]. Nevertheless I find this name misleading. Indeed, pump depletion seems to indicate that the gain decreases because the pump lost too much of energy. However, it looks like gain decreases because of an extra Kerr shift appearing because the field is too intense in the cavity.

We can also guess the importance of γ and K without introducing a more complex theory. Let us assume that the output signal has a form $|c_1^{out}|^2 = G|c_1^{in}|^2$ and that back-action of this amplified field affects the pump when the ratio of the pump amplitude over the amplified amplitude $|b_1^{in}|^2/|c_1^{out}|^2$ reaches a threshold value r_T (typically 20 to 15 dB). The JPA works close to the bifurcation point and this fixes the pump power to a value dependent on the JPA parameters according to Eq. 2.60. It shows that we cannot put an arbitrarily large pump power to compensate for a large gain because in this case, the JPA would be out of the good operation point. We can compute the threshold input field amplitude $|c_{1,T}^{in}|^2$ above which pump back-action starts to occur (using Eq. 2.60 in the limit where $\gamma_2 = \gamma_3 = 0$):

$$\begin{aligned} \frac{|b_{1c}^{in}|^2}{|c_{1,T}^{out}|^2} &\propto \frac{\gamma^2}{K}\frac{1}{G|c_{1,T}^{in}|^2} = r_T \\ \iff |c_{1,T}^{in}|^2 &\propto \frac{\gamma^2}{K}\frac{1}{Gr_T} \end{aligned} \tag{2.81}$$

We can thus see that the maximum input field amplitude before the saturation occurs increases with higher γ and decreases with higher K.

2.5.2 Neglected nonlinear terms during the linearization procedure

Kochetov *et al.* studied the compression mechanism in a different way. Instead of considering the back-action of the amplified signal on the pump, they went beyond the linearization procedure leading to Eq. 2.64 where only linear terms in a and $a^\dagger$ were kept. In their model, they modified the equation of motion on the quantum field (Eq. 2.64) by keeping the c_2 terms as well as the c_3 terms. The classical field equation being not modified, this procedure cannot be considered as back-action on the pump. Moreover, it goes beyond the pump back-action model because it also incorporates terms arising only from the nonlinearity itself, i.e. terms depending on powers of a without a prefactor depending on the classical field B (c_3 terms that where not accounted for in the pump back-action model). They were also able to separate the saturation effect contribution of the specific contribution of the c_3 terms as shown in Fig. 2.10.

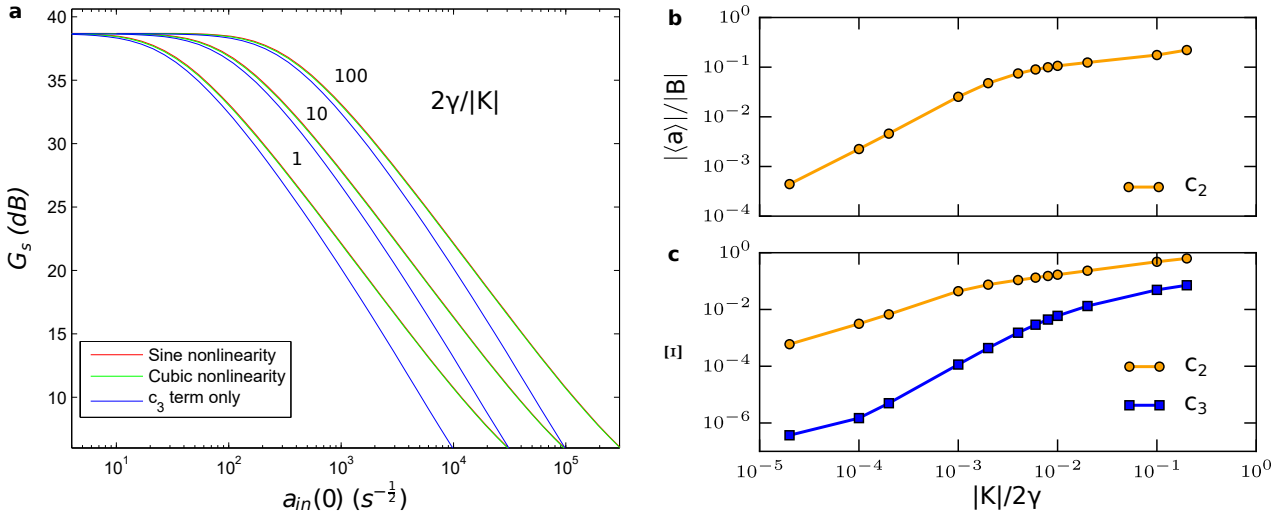

Figure 2.10: (a) Maximum gain as a function of the input field operator for different ratios $2\gamma/|K|$. The computation was done for the full sine nonlinearity (red), the cubic nonlinearity (green), and only with c_3 terms correction (blue). (b) $|\langle a\rangle|/|B|$ ratio as a function of $|K|/2\gamma$ computed with a mean field approach where only c_2 terms contribute (for a fixed input power). Ξ as a function of $|K|/2\gamma$ for c_2 and c_3 contributions. Figure (a) adapted from [93]. Figures (b) and (c) adapted from [94].

It shows that the main contribution to saturation are the c_3 cubic terms that were not taken into account in the back-action model. We can also see that the saturation scales with the ratio $2\gamma/K$ as for the pump back-action.

Another approach was developed by Boutin *et al.* [94] by solving the steady state of the master equation with a Hamiltonian taking into account c_2 and c_3 terms. As for the Kochetov *et al.* study, the equation of the classical field is not modified (no back-action on the pump field). In this mean field approach, c_3 terms do not participate to the equation of motion because $[a, \langle a^\dagger a^\dagger\rangle\langle aa\rangle] = 0$, but c_2 terms do because $[a, a^\dagger\langle aa\rangle] \neq 0$. Fig. 2.10b shows the evolution of a/B (the ratio of the quantum filed and the pump field) with respect to the ratio $|K|/2\gamma$ coming from the c_2 terms. We can see that they are responsible for an increase of $\langle a\rangle/B$ for increasing $|K|/2\gamma$. This means that saturation will occur faster at higher ratio $|K|/2\gamma$. One can also compute a quantity Ξ translating how the moments $\langle a^2\rangle - \langle a\rangle^2$ and $\langle a^\dagger a\rangle - \langle a\rangle^2$ deviates from the ideal JPA ($\Xi \to 0$ for an ideal JPA and $\Xi \to 1$ when the corrections are important). Fig. 2.10c shows Ξ as a function of the ratio $|K|/2\gamma$. We can again see that higher $|K|/2\gamma$ makes the JPA deviate from the ideal JPA, but it looks like c_2 corrections have a greater impact than c_3 terms which is opposite to what was found in [93].

2.5.3 Neglected nonlinear terms in the Josephson potential

During the calculation of the Hamiltonian, we only developed the Josephson energy up to the quartic term (or equivalently the CPR up to the cubic term). Considering higher nonlinear terms would modify the behavior of the JPA with respect to the input power. The full development of the CPR in the Hamiltonian was also taken into account by Kochetov

et al. [93] where the full Taylor expansion of the sinus term can be expressed with respect to Bessel functions. Such an analysis shows that the gain decreases when keeping the same driving parameters as for the simple quartic Hamiltonian. Nevertheless, by adjusting the pump power and frequency it is always possible to get back the same gain as for a quartic Hamiltonian. The only measurable difference is an increase of the Kerr shift for reaching the same gain. We note that this model did not take any source of loss into account. Concerning the saturation behavior, they were able to compare the saturation power of the quartic Hamiltonian (cubic nonlinearity in the CPR) to the full cosine development (sine nonlinearity in the CPR). Fig. 2.10a shows that considering the full cosine development in the Josephson energy barely changes the saturation power (green curves overlapping the red curves).

To conclude, while the full development of the Josephson energy does not have a great impact on the saturation point, it is not fully clear whether c_2 or c_3 terms are dominant in the saturation mechanism. The fact that the approach of Boutin shows that c_2 terms are dominating while the study of Kochetov shows it is c_3 terms might come the mean field approach where c_3 terms do not impact $\langle a \rangle$ in Boutin's approach. Moreover, Boutin does not study the input power dependence meaning that c_2 terms might dominate at low input powers while c_3 terms have a larger impact at higher input powers. Nevertheless, it has been shown that for JPA working in a three wave mixing scheme, the main source of gain saturation is the c_3 terms [94, 95, 96].

2.6 Stability conditions and parameters optimization

While the previous section showed that the exact mechanism causing limitation of the gain and the dynamic range is unclear, it showed that all the detrimental effects scale as $|K|/(2\gamma)$. One could think that we just need to make K arbitrarily small and γ arbitrary large to improve infinitely the JPA performances. Nevertheless, it is not as simple as that because there are other conditions that the JPA needs to fulfill in order to operate correctly.

2.6.1 Classical description of the JPA

For now we used quantum mechanics to describe the JPA and were able to understand the amplification mechanism as a four wave mixing process arising because of the nonlinear inductance of the JJ creating a Kerr type Hamiltonian. It is also useful to describe the system classically because we can gain some insight on the type of physics we can expect. For this purpose let us consider a JJ biased by an arbitrary linear network as shown in Fig. 2.11a. It is always possible to consider the Norton equivalent circuit where the arbitrary linear network is replaced by a current source shunted with an admittance $Y(\omega)$ as shown in Fig. 2.11b. If $Y(\omega)$ has a resonance, it is always possible to model it as a parallel or series RLC resonator [97]. We will here briefly study the case where $Y(\omega)$ can be approximated by a parallel resonator as shown in Fig. 2.11c in which we decomposed the nonlinear part of the inductance of the JJ as in Fig. 2.3a. Here, the inductance $L' = LL_J/(L + L_J)$ is the total inductance with the parallel contribution of the linear part of the Josephson inductance L_J and the inductance of the resonator L. As we saw in Sec. 2.2, the current phase relation of the

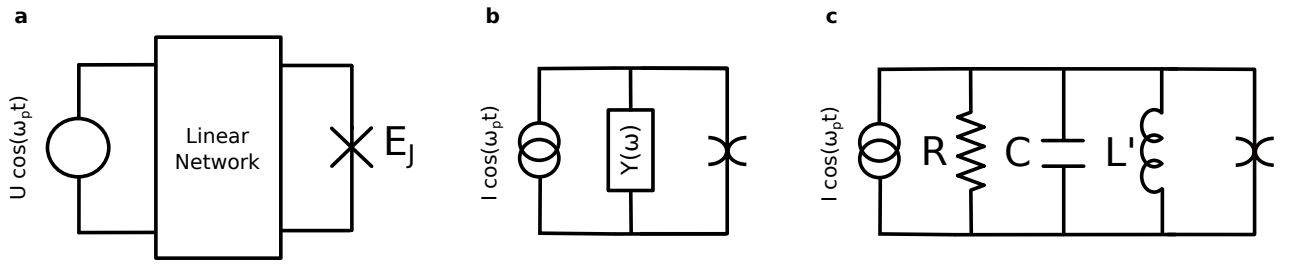

Figure 2.11: (a) Josephson junction biased through a linear network. The Josephson capacitance was neglected. (b) Norton representation of the circuit where the voltage source and linear network have been replaced by a equivalent current source and shunted admittance. The shunted admittance takes into account the linear inductance part of the Josephson junction. The spider-like symbol represent the nonlinear contribution of the Josephson inductance. (c) The admittance of (b) has been replaced by an RLC circuit.

JJ is:

$$I = I_c \sin(\phi_J/\varphi_0) \approx \frac{1}{L_J}\phi_J(t) - \frac{1}{6L_J\varphi_0^2}\phi_J^3(t) + O[\phi_J^5(t)] \tag{2.82}$$

Where the last approximation is true for small ϕ_J/φ_0. By applying the Kirchoff law we find that the circuit obeys the following relation:

$$C\frac{\ddot{\phi_J}}{\varphi_0} + \frac{1}{R}\frac{\dot{\phi_J}}{\varphi_0} + \frac{1}{L'}\frac{\phi_J}{\varphi_0}\left(1 - \frac{L'}{6L_J}\left(\frac{\phi_J}{\varphi_0}\right)^2\right) = I_p\cos(\omega t) \tag{2.83}$$

This system is thus equivalent to a driven oscillator with a mass $1/C$, a friction coefficient $1/R$, quality factor $Q = R\sqrt{C/L'}$ a spring constant $1/L'$ containing a quadratic nonlinear part proportional to $L'/6(L_J) = \eta/6$ where we defined the parallel participation ratio $\eta = L'/L_J$. This type of driven oscillator is called a Duffing oscillator.

Duffing oscillators are known to show the same kind of bifurcation physics that we found with the semi-classical approach when solving the equation of motion for the classical field B [98]. They are also known to show chaotic behavior when the small oscillation approximation ($\phi_J/\varphi_0 << 1$) is not true anymore. By increasing ϕ_J/φ_0, the solution of the equation of motion can exhibit a period doubling, transitioning in between regular and chaotic dynamics (pitchfork bifurcations) and eventually reach a full chaotic behavior [93]. The important ratio to look at is I^{bif}/I_c where I^{bif} is the current in the system at the critical point when bifurcation is reached, and I_c is the critical current above which the JJ exhibits a resistive behavior. The higher is this ratio, the higher will be ϕ_J/φ_0. It was shown that I^{bif}/I_c scales as $\sqrt{1/(Q\eta)}$, and thus ensuring the condition:

$$\eta Q >> 1 \tag{2.84}$$

is necessary to avoid chaotic behavior [98].

We focused here on a parallel RLC resonator but similar results can be found for a series RCL resonator (using the Thevenin theorem). In this case the equations of motion are not of Duffing type, because the nonlinearity is on the effective mass of the oscillator and not the

spring constant. Nevertheless, at low drives and large Q one can show that we can recover Duffing type dynamics. In this case, the participation ratio is defined as L_J/L' and the same stability condition can be derived [98].

2.6.2 Stability conditions for a distributed system

We can try to derive the condition of the bifurcation current being smaller than the critical current, for a distributed system, in order to operate the JPA in a non chaotic behavior. This approach is similar to what was develop in [90]. Let us consider again the same system as in Sec. 2.3.2 where a distributed resonator is coupled to an input port with a capacitance C_i and an output port with a capacitance C_o. Now we will consider that C_i and C_o are very small such that $\varphi_m^i = \varphi_m^o = \pi/2$ and we will consider the JJ in the middle of the resonator ($x_J = 0$). In this case we find $b_m = 1$ and $\Delta u_m = 2a_m \cos(k_m l)$. We will also consider that $C_J \approx 0$ (which is valid because we are interested in frequencies well below the plasma frequency of the JJ) such that Eq. 2.31 becomes:

$$2lk_m \tan k_m l = \frac{L^0 l}{L_J} \tag{2.85}$$

We will study what is happening at the position of the JJ ($x = 0^-$ but we could do the same for $x = 0^+$) because it is precisely at this position that the current ratio has to be respected. At the JJ's position ($x = 0^-$) we can express: $u_m = a_m \cos(k_m l)$. So, the total flux is :

$$\Phi_m(t, x = 0^-) = \Phi_m(t) u_m(x = 0^-) = \Phi_{zpf,m}(A_m + A_m^\dagger) a_m \cos(k_m l) \approx \Phi_{zpf,m} \alpha a_m \cos(k_m l) \tag{2.86}$$

Where the last approximation consists of considering a classical coherent field.

One can now define the maximum classical field inside the junction as the coherent field $\alpha_{max,m}$ making $\Phi_m(t, x = 0^-) = \varphi_0$, or equivalently, the coherent field at which the current flowing into the JJ reaches the critical current I_c. We have thus the relation:

$$\alpha_{max,m} = \frac{\varphi_0}{\Phi_{zpf}} \frac{1}{a_m \cos(k_m l)} = \frac{\varphi_0}{\Phi_{zpf}} \frac{L^0 l}{2 a_m L_J k_m l \sin(k_m l)} \tag{2.87}$$

where the last equation was obtained using Eq. 2.85.

From the input/output model, we know the number of photons inside the JPA at the bifurcation point (Eq. 2.61) $B_c^2 = 2\gamma/(\sqrt{3}|K|)$ (we neglected γ_3) with K obtained from the distributed model:

$$K = K_{mm} = E_c \eta (\Delta u_m)^4 = \frac{1}{\hbar} \frac{e^2}{2C_\Sigma} \frac{L_m}{L_J} (2\cos(k_m l))^4 = \left(\frac{\Phi_{zpf}}{\varphi_0}\right)^2 \omega_m 4 \cos^4(k_m l) \frac{L_m}{L_J} \tag{2.88}$$

We can now express the ratio of the number of photons at the bifurcation power and the number of photons such that the current reaches the critical current:

$$\frac{N_{bif}}{N_{max}} = \frac{B_c^2}{|\alpha_{max,m}|^2} = \frac{2\gamma}{\sqrt{3}} \frac{|a_m|^2}{\omega_m 4 \cos^2(k_m l)} \frac{L_J}{L_m} \tag{2.89}$$

We will now focus on the limit $L_J << lL^0$ (i.e. the Josephson inductance being small compared to the geometric inductance). In this case the solution of Eq. 2.85 is of the form $k_m l \approx \pi/2 + \epsilon$ where epsilon is a small quantity. By doing so we find:

$$k_m l \approx \frac{\pi}{2}\frac{1}{1+2L_J/(L^0 l)} \approx \frac{\pi}{2}(1-\frac{2L_J}{L^0 l}) \tag{2.90}$$

Using this result we have $\cos(k_m l) \approx (\pi L_J/L^0 l)$, $a_m \approx 1$ (obtained with Eq. 2.32) and $L_m \approx L^0 l$ (obtained with Eq. 2.33). By noting that the quality factor is expressed as $2\gamma/\omega_m$ and using the approximation $L_J << L^0 l$ we obtain finally:

$$\frac{N_{bif}}{N_{max}} \propto \frac{1}{Q}\frac{L^0 l}{L_J} \tag{2.91}$$

In the limit $L_J >> lL_0$, solution of Eq. 2.85 gives $k_m l \approx 0$, $\cos(k_m l) \approx 1$, $a_m \approx 1$ and $L_m \approx L_J$ such that we get:

$$\frac{N_{bif}}{N_{max}} \propto \frac{1}{Q} \tag{2.92}$$

We obtain a similar result as in the previous section but for a distributed system. It is not surprising because any distributed resonant structure can be modeled as a lumped circuit close to its resonance.

To conclude on the ideal JPA parameters, we saw that the dynamic range scales as $2\gamma/|K|$ and it is thus desirable to have a low Kerr coefficient (absolute value) and a low quality factor. Nevertheless we just saw that we cannot decrease arbitrarily the quality factor because then, the ratio between the current at the bifurcation point and the critical current increases and can lead to chaotic behavior. The other possibility is to reduce the Kerr coefficient and this can be done by integrating the JJ inside a distributed resonator such that the nonlinearity of the JJ gets diluted by the geometric inductance of the transmission line resonator. Nevertheless there is also a limit to this strategy because when $L_J << L^0 l$, the ratio of the current at the bifurcation point over the critical current increases as $L^0 l/L_J$ such that it is not possible to dilute infinitely the Josephson inductance.

2.7 Broader view on superconducting parametric amplifiers

For now we only analyzed the resonant JPA in a four wave mixing (4WM) scheme because the graphene JPAs that are studied in this work are of this type. We will now have a broader look on the vast topic of superconducting parametric amplifiers.

2.7.1 Definitions

2.7.1.a Degenerate and non-degenerate parametric amplifier

The degenerate parametric amplifier (DPA) is an amplifier with only one physical cavity mode $\hat{A}$. For example, the resonant 4WM JPA that we studied is a degenerate JPA because

there is only one cavity (with many modes but they are all located in a single cavity). We can define the ideal DPA Hamiltonian as:

$$\frac{\hat{H}_{DPA}}{\hbar} = \omega_A \hat{A}^\dagger \hat{A} + i g_{AA}\left(\hat{A}^2 e^{i(\Omega_{AA}t+\theta)} - \hat{A}^{\dagger 2} e^{-i(\Omega_{AA}t+\theta)}\right) \tag{2.93}$$

It is easy to show that in the case of the resonant 4WM JPA, when we decomposed the fields in a classical part and a quantum part (Eq. 2.63), keeping only the linear terms in $\hat{a}$ in the equation of motion and neglecting the loss terms is equivalent to have this ideal DPA Hamiltonian. Therefore, an ideal DPA gives an output field:

$$\hat{c}_1^{out}(\omega) = \sqrt{G}\hat{c}_1^{in}(\omega) + \sqrt{G-1}e^{i(\theta)}\hat{c}_1^{\dagger in}(-\omega) \tag{2.94}$$

On the other hand, the non-degenerate parametric amplifier (NDPA) have several physical cavity modes ($\hat{A}$ and $\hat{B}$ for example, note that $\hat{B}$ is an operator and is not related to the semiclassical field B introduced earlier). Its Hamiltonian can be written (in the case of two physical cavity modes):

$$\frac{\hat{H}_{NDPA}}{\hbar} = \omega_A \hat{A}^\dagger \hat{A} + \omega_B \hat{B}^\dagger \hat{B} + i g_{AB}\left(\hat{A}\hat{B} e^{i(\Omega_{AB}t+\theta)} - \hat{B}^\dagger \hat{A}^\dagger e^{-i(\Omega_{AB}t+\theta)}\right) \tag{2.95}$$

In this case the ideal NDPA gives an output field:

$$\hat{c}_1^{out}(\omega_s) = \sqrt{G}\hat{c}_1^{in}(\omega_s) + \sqrt{G-1}e^{i(\theta)}\hat{d}_1^{\dagger in}(-\omega_i) \tag{2.96}$$

where $\hat{d}_1^{in}$ is the input mode on the physical cavity associated with the mode $\hat{B}$. Note that in this case, the signal frequency lays in mode $\hat{A}$ while the idler frequency lays in the mode $\hat{B}$. This can be useful to have a large separation between the idler and the signal modes.

2.7.1.b Phase preserving and phase sensitive

The creation and annihilation operators can be decomposed in the phase plane as in-plane and out-of-plane quadratures. They can be defined as:

$$\hat{X} = \hat{A}(\omega) + e^{-i\theta}\hat{A}^\dagger(-\omega) \qquad \hat{P} = \hat{A}(\omega) - e^{i\theta}\hat{A}^\dagger(-\omega) \tag{2.97}$$

with θ the phase difference between the signal and the pump. An amplifier is said to be phase preserving if both the quadratures are amplified the same way, which is equivalent to conserve their phase in the phase space. On the other hand, a phase sensitive amplifier amplifies one quadrature by $\sqrt{G}$ and the other one by $1/\sqrt{G}$ such that amplification depends on the phase (in the $(\hat{X}, \hat{P})$ plane) of the incoming signal compared to the pump.
It is easy to check that in the case of a DPA, because the output field mode depends on the same input field at signal and idler frequency, one has $X^{out} = \sqrt{G}X^{in}$ and $P^{out} = (1/\sqrt{G})P^{in}$. Therefore we can conclude that resonant 4WM JPAs that are studied in this work are phase sensitive amplifier. The fact that a phase sensitive amplifier amplifies a quadrature while reducing the other, means that it is possible to squeeze quantum noise where the uncertainty on one quadradure becomes lower than the quantum limit (associated to a standard deviation corresponding to the square root of a quarter of a photon) [99]. We note that there is another definition of phase sensitive amplifiers. In our definition, when measuring the gain at an

angular frequency $\omega_s \neq \omega_p \implies \omega_s \neq \omega_i$, we will not measure any phase dependence because the operators $c_1(\omega)$ and $c_1^\dagger(-\omega)$ are not correlated. Phase dependence only arises when $\omega_s \approx \omega_i$. This is why another definition commonly found for a phase sensitive amplifier is a degenerate amplifier working at $\omega_s = \omega_i$ [100, 92]. We emphasize here that in this PhD we did not perform measurements precisely at $\omega_s = \omega_i$ and therefore no phase dependence is expected. In addition, it means that the minimal amount of noise added by the amplifier is half a photon coming from the quantum fluctuations at the idler frequency being added to the amplified signal frequency.

2.7.2 Other works on parametric amplification in superconducting circuits

2.7.2.a Josephson bifurcation amplifier

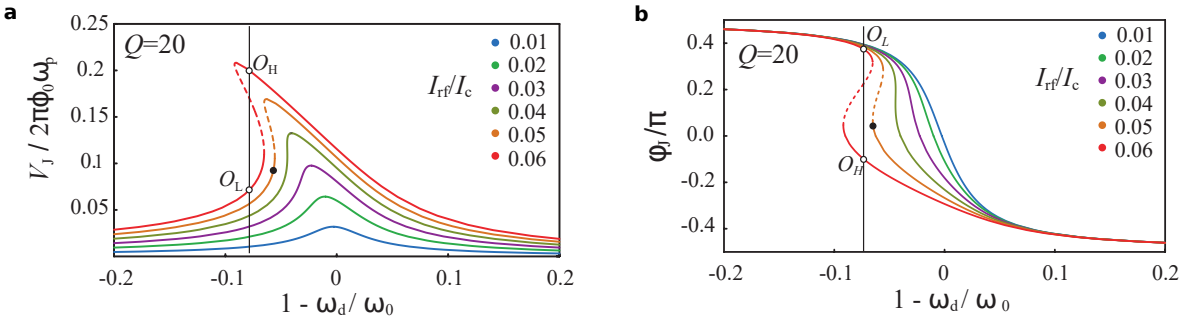

Figure 2.12: (a) Voltage as a function of the drive frequency for different drive current. At a given drive frequency and current, the system can be either in the state O_L or O_H. (b) Associated phase response. Figures adapted from [89].

Josephson bifurcation amplifiers (JBA) are very close to the JPA we studied throughout this chapter in the sense that it is the same system but operated in another regime. While for parametric amplification we have to drive the JPA with a pump just below the critical power (just before bifurcation), the bifurcation amplifier works with a drive above the critical power where the system shows a bistability. In this regime, the JBA can be either in a low amplitude state O_L or a high amplitude state O_H as shown in Fig. 2.12. A small signal coupled to this system can change the critical current I_c and make the system switch from O_L to O_H. This results in an important phase shift as shown in Fig. 2.12b making the JBA a sensitive detector to variation in I_c. Successful qubit readout measurements were done using this system [88, 89].

2.7.2.b RF flux driven Josephson parametric amplifier

The use of a SQUID instead of a single JJ offers a new way of modulating the Josephson inductance (and thus energy) by the use of a RF magnetic flux Φ_{ext}. The Josephson energy of a SQUID composed of identical JJs can be written as:

$$E_J^{SQUID} = E_J \cos(|\frac{\Phi_{ext}}{2\varphi_0}|) \tag{2.98}$$

By using an external flux of the form:

$$\Phi_{ext} = \frac{\pi}{2}\varphi_0(1 + \epsilon\cos(\Omega t)) \tag{2.99}$$

with $\epsilon << 1$, and $\Omega = 2\omega_A$ (ω_A being the angular resonant frequency of the mode of the resonator coupled to the SQUID), we can expand the term $E_J^{SQUID}\cos(\Phi)$ in Φ and in $\epsilon\cos(\Omega t)$ to obtain the DPA hamiltonian [99, 96]. Note that the terms in $\hat{A}^2$ and $\hat{A}^{\dagger 2}$ do not vanish because they are multiplied by the flux pump at a frequency $2\omega_A$ such that the total energy is conserved. This amplification scheme is thus a three wave mixing (3WM) scheme because one photon of the pump is converted into one idler and one signal photon. This has the advantage of having the pump at a different frequency than the signal. Indeed when $\omega_s = \omega_i$, the pump is at twice the frequency of the signal which makes the pump tone elimination obsolete [8]. Note that it is also possible to use a double pump tone avoiding the pump frequency issue in the case of current pumped JPA [91, 95]. But having a double pump makes the scheme more complicated and increases the number of parameters to adapt in order to get amplification.

The first implementation of the RF flux driven JPA was made using a $\lambda/4$ resonator with a SQUID terminating the line [101] and repeated for squeezing experiments [102, 100]. Typical gains of 20 dB were reached together with a 1 dB compression point around -130 dBm (equivalent to a single JJ current pumped JPA) and added noise close to the quantum limit. Another study [103] used a lumped model version of the flux driven JPA and also used the possibility of tuning the resonance frequency by applying a DC magnetic flux through the SQUID (changing the total inductance of the resonator). They managed to obtain gains above 20 dB with a frequency tunability between 5 and 7 GHz. They also measured saturation power above -120 dBm and added noise corresponding to the quantum limit.

2.7.2.c Josephson ring modulator

For now we have only discussed about DPA which are intrinsically phase sensitive. As we saw earlier, DPAs will always amplify one quadrature while reducing the other one. But if the information on both the quadrature are important one might need a NDPA. Moreover, the fact that the idler mode of the NDPA is located at a frequency nearby a second physical mode ($\hat{B}$) means that the difference in frequency of the signal and idler is not limited to the bandwidth of the amplifier and can be arbitrarily large. Therefore, such a system is also useful as a photon converter (Josephson parametric converter). The Josephson ring modulator was implemented by several groups [105, 106, 104, 107, 108] and consists of four identical JJs forming a loop as shown in Fig. 2.13a. To this ring are coupled three electrical modes $\hat{A}$, $\hat{B}$, $\hat{C}$ such that the Hamiltonian can be written as:

$$\frac{\hat{H}}{\hbar} = \omega_A\hat{A}^\dagger\hat{A} + \omega_B\hat{B}^\dagger\hat{B} + \omega_C\hat{C}^\dagger\hat{C} + g_{ABC}(\hat{A} + \hat{A}^\dagger)(\hat{B} + \hat{B}^\dagger)(\hat{C} + \hat{C}^\dagger) \tag{2.100}$$

One can show that for the specific conditions:

$$\omega_c > \omega_b > \omega_a > \gamma_{1,C} >> \gamma_{1,A} \approx \gamma_{1,B} >> g_{ABC} \tag{2.101}$$

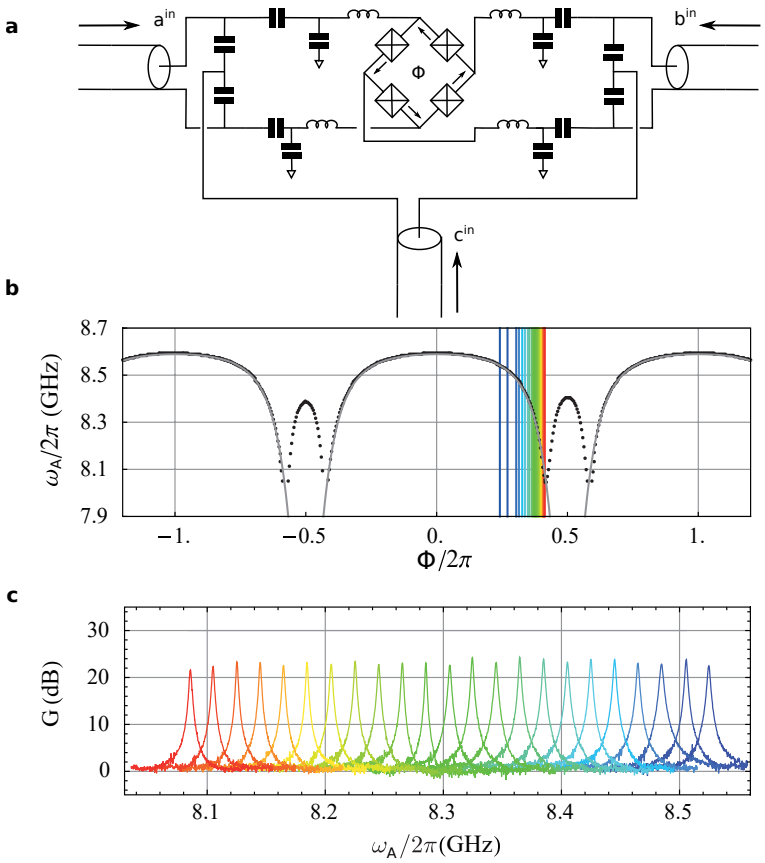

Figure 2.13: (a) Electrical scheme of the Josephson ring modulator coupled to three modes. It is possible to tune the resonance frequency of the modes by applying a magnetic flux through the loop. (b) Angular resonant frequency of the mode A with respect to the external magnetic flux applied to the loop without the pump. (c) Gain profiles with respect to the angular resonance frequency ω_A. Figure (a) adapted from [99] and figures (b) and (c) adapted from [104].

and when the C mode is driven by a strong coherent field at an angular frequency $\omega_c = \omega_a + \omega_b$, the Hamiltonian can be approximated by :

$$\frac{\hat{H}}{\hbar} = \omega_A \hat{A}^\dagger \hat{A} + \omega_B \hat{B}^\dagger \hat{B} + i g_{AB} \left(\hat{A}\hat{B} e^{i(\Omega_{AB} t + \theta)} - \hat{B}^\dagger \hat{A}^\dagger e^{-i(\Omega_{AB} t + \theta)} \right) \tag{2.102}$$

which is the NDPA Hamiltonian in a 3WM scheme. With such a device, amplification over 20 dB was performed with 1 dB compression points reaching -118 dBm together with quantum limited noise performances. Thanks to the JJ loop it was also possible to tune the amplification frequency on a 500 MHz frequency range by applying a magnetic flux as shown in Fig. 2.13b and c [104].

2.7.2.d Josephson junction chain

We saw that the limiting factor for JPAs comes from the ratio $K/(2\gamma)$ (both for 3WM and 4WM because even in the 3WM there are parasitic Kerr terms). The goal is to reduce this factor either by reducing K or increasing γ. The stability conditions make that it is not

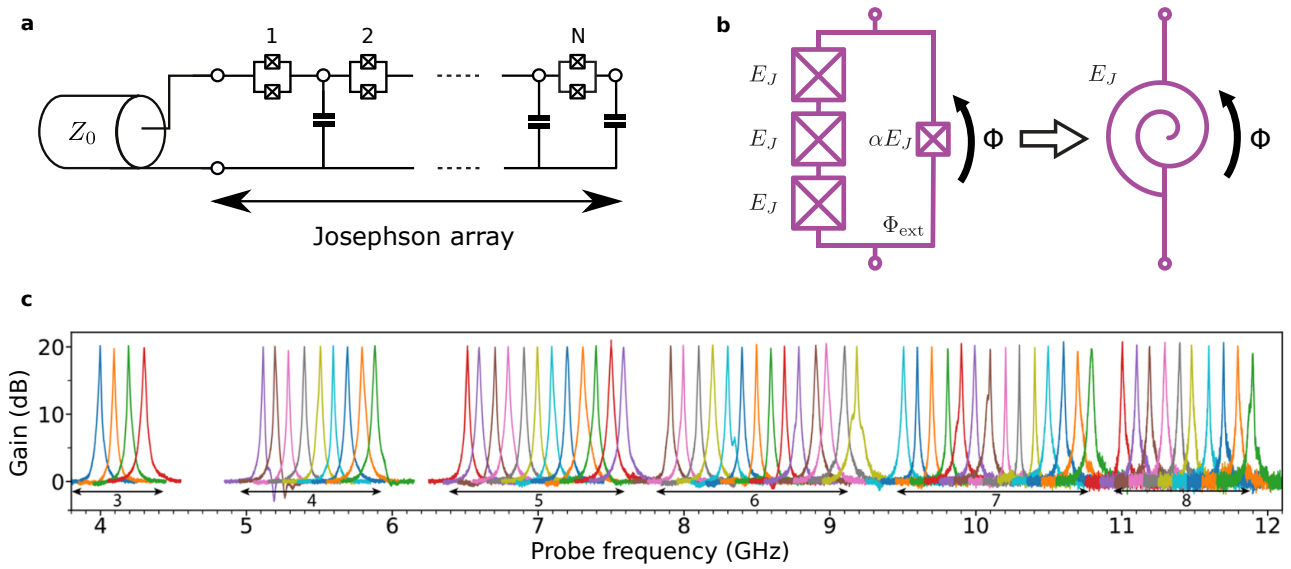

Figure 2.14: (a) Scheme of a SQUID chain coupled to a transmission line of impedance Z_0. (b) Asymmetric SQUID scheme. This building block is also called a SNAIL (Superconducting Nonlinear Asymmetric Inductive eLement). (c) Gain profiles of a SNAIL chain with a large number of unit cells such that many modes are present in between 4 and 12 GHz. The numbers below the double arrows indicate the mode number. The different colors correspond to different magnetic flux tuning the frequency of the mode. Figure (b) adapted from [109] and (c) adapted from [110].

possible to have an arbitrarily large γ, and that adding geometrical inductance to dilute the Josephson inductance and thus decrease K creates instability as well. Another way of decreasing K is by using a chain of JJs. It might sound counter-intuitive because one could think JJs as nonlinear elements, and thus adding JJs would increase the nonlinearity and thus K. But by doing so, the total flux Φ is divided into N equal parts across the N JJs forming the chain (if the chain is sufficiently small to be considered as lumped). Therefore, the quadratic term in the development of the Josephson energy (Eq. 2.11) becomes:

$$\frac{E_J}{2}\left(\frac{\Phi}{\varphi_0}\right)^2 \rightarrow \sum_{i=1}^{N} \frac{E_J}{2}\left(\frac{\Phi}{N\varphi_0}\right)^2 = \frac{E_J}{2N}\left(\frac{\Phi}{\varphi_0}\right)^2 \tag{2.103}$$

and the quartic term becomes:

$$\frac{E_J}{24}\left(\frac{\Phi}{\varphi_0}\right)^4 \rightarrow \sum_{i=1}^{N} \frac{NE_J}{24}\left(\frac{\Phi}{N\varphi_0}\right)^4 = \frac{1}{N^3}\frac{E_J}{24}\left(\frac{\Phi}{\varphi_0}\right)^4 \tag{2.104}$$

We see that the quadratic term scales as $1/N$ meaning that additional capacitance is needed to compensate for change in the linear part of the Josephson inductance. Compensating the factor N with an increase of capacitance makes the impedance grow as $1/N$ (because the inductance scales as N and the capacitor as $1/N$) and thus Φ_{zpf} scales as $\sqrt{N}$. Because the quartic term scales as $\Phi_{zpf}^4/N^3 \propto 1/N$, the Kerr coefficient does too. In an inductor the relation $\Phi = LI$ means that if the flux Φ is divided equally across all the JJs, the current seen by each junction is Φ/N which is equivalent of having a critical current increased by a

factor N. The quantity N_{bif} and N_{max} scale thus both as N making the ratio N_{bif}/N_{max} unchanged together with a smaller Kerr coefficient [90]. Note that considering the flux equally distributed along all the JJs is an approximation and that a precise study of the nonlinearity is needed and can be found in [111].

In practice SQUID chain (Fig. 2.14a) are used rather than JJ chain because they allow for the control of the resonant mode frequency and thus the gain frequency. The first successful use of a SQUID chain for a resonant current pumped JPA was done by Castellanos-Beltran *et al.* where they obtained frequency controllable gains above 20 dB, close to the quantum limit [8] and they also performed squeezing experiments [112]. Moreover, multiple SQUIDs can also be used in a 3WM process (with RF flux pump) [113] where the compression point was 18 dB above what it would have been with a single SQUID thanks to the reduced nonlinearity. Coupling of two SQUID arrays allowed also to obtain a resonant 4WM JPA that can be operated either in a degenerate or non-degenerate mode [114]. One can also cite the use of asymmetric SQUIDs (Fig. 2.14b) to reduce the parasitic Kerr terms (c_3 terms) in a 3WM process and push further the dynamic range (a compression point of -110 dBm was reached this way) [109, 115, 116]. Last but not least, the SQUID chain has many resonant modes with frequency spacing depending on the number SQUIDs inside the chain. By using chains containing more than 1000 SQUIDs it was possible to have several frequency tunable modes between 4-12 GHz which is the typical frequency range used for microwave experiments [117, 110]. By using the tunability of each mode it was possible to perform quantum limited amplification of 20 dB on almost the full 4-12 GHz frequency range as shown in Fig. 2.14c, with an averaged 1 dB compression point of -108 dBm (using asymmetric SQUIDs) [110].

2.7.2.e Kinetic inductance as a source of nonlinearity

For now we only focused on JJs as a source of nonlinearity for parametric amplification in superconducting circuits. It is also possible to use the kinetic inductance of superconducting materials. Kinetic inductance (L_k) arises when the carrier density of the superconducting material is low in the normal state. Its current dependence can be written as:

$$L_k(I) = L_0\left[1 + \left(\frac{I}{I_*}\right)^2\right] \tag{2.105}$$

where L_0 is the per-unit-length kinetic inductance of the material without a current I, and I_* determines the strength of the current dependence and scales as I_c, the critical current of the material. This relation is equivalent to the Josephson inductance meaning that kinetic inductance can be used in JPA and is equivalent to a Kerr process [87]. Tholén *et al.* used a Niobium resonator to perform kinetic inductance based parametric amplification [118]. Because the kinetic inductance is linked to the carrier density they used in another study some local superconducting constrictions (width < 50 nm) to increase the nonlinear effect [119]. A recent study [120] used NbTiN which has a high kinetic inductance and used an additional DC current in addition to the microwave pump making the kinetic inductance take the form:

$$L_k(I) = L_0\left[1 + \left(\frac{I_{DC}}{I_*}\right)^2 + 2\frac{I_{DC}I_{mw}}{I_*^2} + \left(\frac{I_{mw}}{I_*}\right)^2\right] \tag{2.106}$$

The term proportional to I_{mw}^2 is a standard Kerr term but the term proportional to I_{mw} makes 3WM process possible. By measuring I_* they found that the Kerr terms leading to parasitic c_3

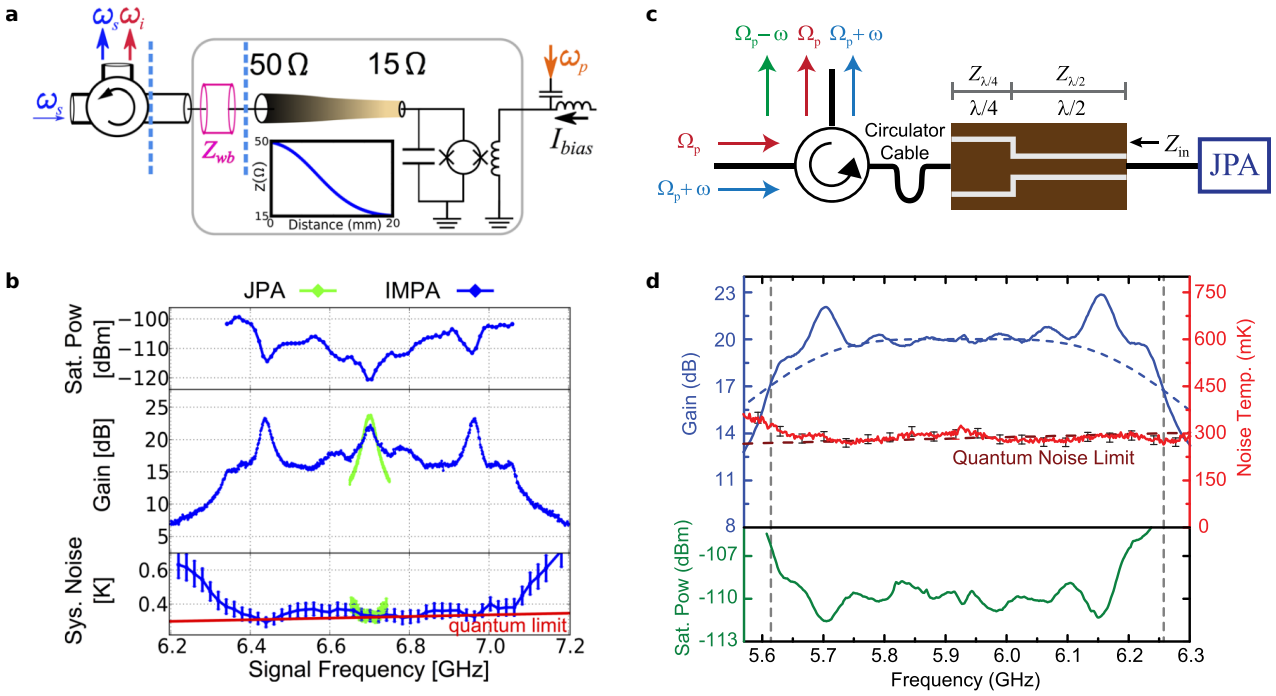

Figure 2.15: (a) Klopfenstein impedance taper of a RF flux pumped JPA. Z_{wb} is the wirebonds impedance. The inset shows the spatial dependence of the impedance in the impedance taper. (b) Gain profile, saturation and noise of the impedance matched JPA (IMPA, blue) with the impedance matching element shown in (a), and JPA without impedance matching (green). (c) JPA matched with a combination of a $\lambda/4$ and $\lambda/2$ transformer. (d) Gain profile, saturation and noise of the impedance matched JPA with the impedance matching element shown in (c). Figures (a) and (b) taken from [121]. Figures (c) and (d) taken from [122].

terms (see Sec. 2.5) were negligible (effective Kerr coefficient $K/2\pi \approx 0.13$ Hz) making the ratio $2\gamma/K > 10^8$. With this, they were able to measure quantum limited gains above 40 dB and 1 dB compression points of -70 dBm at a 20 dB gain which is far above all the studies we presented earlier.

2.7.2.f Impedance engineered JPA

For now, all the JPAs presented were based on a the presence of a nonlinear element coupled to resonator modes. This makes the gain profile lorentzian with the gain bandwidth relation $\Delta_{BW}\sqrt{G} \propto 2\gamma$ (Sec. 2.4.4.b) with γ limited because of JPA stability reasons (Sec. 2.6). Therefore, for a 8 GHz amplifier with a quality factor $Q = 10$ (which is on the lower limit of what can be used), a gain of 20 dB makes the bandwidth of the amplifier being 80 MHz which is small compared to the frequency ranged used in superconducting circuits (typically 1-12 GHz). As we saw, the tunability of the resonance frequency can make the full frequency accessible, but at the cost of parameters tuning. This is why broader band parametric amplifiers are needed to be able to amplify signals at multiple frequencies without adapting any parameters. A way of doing that it to use impedance engineering on the resonant structure. In standard resonant JPA there is an abrupt change in impedance between the 50 Ω transmission line through which the signal is sent and the resonant structure of the JPA. By

using an impedance matching element it is possible to make a smooth change of impedance between the 50 Ω transmission line and the resonant structure as shown in Fig. 2.15a. Doing that is equivalent to changing the coupling Hamiltonian in Eq. 2.42 with κ being frequency dependent. The pumpistor model [123, 124] allows to describe JPAs as a negative resistance elements and implies that the gain-bandwidth product is only limited by the Bode-Fano theorem [125, 126].

Mutus *et al.* were the first to use an impedance matching technique on a JPA and did it on a RF flux pump device with a Klopfenstein taper in order to minimize the wiggles in the gain profile (Fig. 2.15a). They managed to get a quantum limited gain of 15 to 20 dB with a compression point between -120 and -110 dBm and a gain-bandwidth product of 700 MHz as shown in Fig. 2.15b. A similar device was used later for qubit measurement [127]. Roy *et al.* used an easier-to-build impedance matching element consisting of a combination of a $\lambda/4$ and $\lambda/2$ transmission line resonator transformer to match a current pumped JPA as shown in Fig 2.15c. They managed to obtain quantum limited gains above 20 dB with a 640 MHz bandwidth and a compression point of -110 dBm as shown in Fig. 2.15d. Similar results were performed later with a RF flux pumped JPA [128]. We can see that the impedance engineering allows to increase the saturation point and the bandwidth by one order of magnitude compared to similar single JJ resonant JPA. Another study used a SQUID chain together with an impedance matching element consisting of a three-pole coupled-resonator bandpass network [125]. Combining these two techniques allowed to get gains above 20 dB with a 1.6 GHz bandwidth and a saturation point of -90 dB which is two orders of magnitude above single JJ impedance matched JPA. Nevertheless, no information was given about the added noise.

2.7.2.g Traveling wave parametric amplifier

We saw that resonant JPA could be impedance matched in order to increase their gain-bandwidth product. Another approach consists of not using any resonant structure but a transmission element with the same impedance as the 50 Ω line through which is arriving the input signal. This type of amplifier is called traveling wave parametric amplifier (TWPA). While resonant JPAs allow strong interaction between the nonlinear cavity and the signal by increasing their interaction time, TWPAs amplify the signal during its traveling time and require thus a long nonlinear element. As for the JPAs, the nonlinearity can come either from a long JJ chain [129] or from kinetic inductance [130]. The first near quantum limited TWPA was demonstrated in 2015 [131].

TWPAs are more difficult to build than JPAs because of the necessity of creating a long nonlinear element, matched to the 50 Ω impedance of the external environment, and it requires phase matching condition for the pump, the signal and the idler fields [132]. This is why TWPAs are a full topic of research and we will not go in a detailed description of their behavior. We just point that one of the main challenge is to avoid the phase mismatch caused by the nonlinear interaction of the pump with the medium making the pump traveling faster than the idler and signal fields, as well as linear phase mismatch caused by the dispersion relation of the medium itself. Several approaches were proposed to correct the phase mismatch [92]:

- Opening a stop band in the dispersion relation of a Josephson array [129, 131, 133] or a

photonic gap in the dispersion of a high kinetic inductance transmission line [130, 134, 135, 136]

- Changing the sign of the Kerr nonlinearity [137, 138, 139]
- Switching from 4WM to 3WM and neutralizing the Kerr terms [116, 140].

TWPAs performances show that it is possible to have gains over 20 dB with a bandwidth of a few GHz and compression points over -100 dBm. Nevertheless the added noise by TWPAs is at best twice the standard quantum limit and it is still an active subject of research to improve this value [132].

2.8 Conclusion

We demonstrated that JPAs work as a nonlinear medium where pump photons can be converted into signal and idler photons. The JPAs studied in this work are pumped with a microwave current which corresponds to a four wave mixing process where two pump photons are converted into one idler and one signal photon. We studied this mechanism theoretically using the input/output formalism and demonstrated the possibility of having large gains when tuning the pump with optimal power and frequency, and that the JPA follows a gain bandwidth relation $\Delta_{BW}\sqrt{G} \approx 2\gamma$. We also showed that the ratio $|K|/(2\gamma)$ was limiting the dynamic range of the JPA. Because of stability conditions it is not possible to have an arbitrarily large γ ($Q \geqslant 10$) and it is not possible to dilute infinitely the Josephson nonlinearity with geometric inductance. A study of the literature about JPAs showed that other schemes of amplification exist, that nonlinearity can also be provided by kinetic inductance and that the gain-bandwidth product can be developed by using impedance engineering techniques or TWPAs. Other ways of performing quantum limited amplification were not detailed like dissipation engineering allowing to escape the gain-bandwidth product [141, 142, 143] or the DC SQUID amplifier [144, 145, 146, 147, 143].

Device fabrication and experimental techniques

CHAPTER 3

A important part of the work was dedicated to the fabrication of samples. This chapter aims to describe how we created graphene Josephson parametric amplifiers, from empty substrates and macroscopic van der Waals crystals, to sub-micron structures and manipulation of atomic monolayers. In a second part, we describe the experimental needs to measure such devices and our experimental setups.

Contents

3.1 Device fabrication

All the parameters involved in the fabrication process are detailed in Sec. 3.1.5.

3.1.1 Substrates preparation

3.1.1.a RF substrates

The first step is to prepare the substrates that will host the circuits. We use *Sil'tronix* 2 inches intrinsic Si wafers with a 275±25 μm thickness and a room temperature resistivity >8000 Ω.cm. The circuits being in a microstrip geometry, we first back-coat the wafer with 200 nm of gold in order to have a well defined ground plane when the substrate is in a copper sample holder (rather than relying only on the copper sample holder whose distance to the microstrip might slightly vary from sample to sample). We create alignment markers by electron-beam (ebeam) lithography (Nanobeam NB5 system, 80 kV). The ebeam is only able to shift the electron beam in a limited squared area called main field ($\approx$ 500 μm^2) when writing a pattern. Every pattern is divided in numerous main fields such that when one main field is written, the ebeam precisely shifts the chuck holding the sample to give access to the next main field. We make sure that all the markers are in the center of a main field because it is the position where the ebeam writing is the most accurate. This is important because all the further lithography steps will use these markers and we want an alignment precision better than 100 nm between two successive writings. After the marker deposition (Ti/Au), we dice the wafer into 7.5x7.5 cm^2 substrates. We cannot prepare the samples on a wafer scale because of the uniqueness of h-BN/graphene/h-BN stacks that are manually deposited on the top of each of them.

Before depositing any stack, we perform an additional lithography step in order to protect the substrate from parasitic flakes. During the stacking process, a lot of flakes are picked-up next to the stack and deposited on the final substrate. These parasitic flakes can have a thickness larger than the circuit metallic lines and can thus break them. It is possible to modify the geometry of the device to avoid these parasitic flakes, but the geometry being complex, and for the sake of reproducibility, we found a way of getting rid of them. We cover the substrate with a 70 nm thick Polymethyl methacrylate (PMMA) layer and write a $\approx$ 100x100 μm^2 square. After development, the whole substrate is protected except the square where we deposit the stack. Removing the PMMA removes all the parasitic flakes that were deposited on the top of it. An illustration will be shown in Sec. 3.1.2.d.

3.1.1.b Exfoliation substrates

In addition to the substrates hosting the RF circuits, we also prepare substrates just for exfoliation and flakes selection. We use 4 inches *Sil'tronix* Si wafers with a 285 nm layer of SiO_2. This thickness of oxide gives the best optical contrast on graphene allowing to see graphene flakes under an optical microscope. We do not use this type of substrate to design the circuit because the oxide layer is known to induce RF losses. Nevertheless, we are aware of recent works where decent internal quality factors are reached using this type of substrate [148, 66]. The cleanliness of these substrates is of great importance. Any contamination on a 2D material can affect its properties. Therefore we do not put any resist on the wafer before

manually dicing it in 1 cm^2 substrates. We thus have silicon particles on the surface that we partially wash with a 5 to 10 mins ultrasonic acetone bath. We then rinse out acetone with isopropyl alcohol (IPA) and dry the substrates with a nitrogen gun. At this point, it is possible to functionalize the SiO_2 surface by doing an oxygen plasma in order to have a better adhesion. This makes the flakes bigger during the exfoliation step. We do not perform this step because the final Josephson junction is very small ≈0.3x1.5 μm making big flakes not necessary, and greater adhesion can make the stacking process more complicated because the flakes stick more to the substrate making them more difficult to extract.

3.1.2 Stack fabrication

3.1.2.a The need of high quality devices

Unlike qubits, JPAs are designed to work in a weak nonlinear regime in order to have a decent dynamic range. In the previous chapter we saw that the nonlinearity depends on the inductance of the Josephson junction (JJ) which is inversely proportional to its critical current I_c. Therefore, a high critical current is needed and we aimed to have a value around 1 μA. As we saw in the Chapter 1, the critical current scales as $1/R_N$ where R_N is the normal resistance of the graphene JJ (gJJ) [51]. It is thus of crucial importance to have a low normal resistance. The natural answer to do this would be to make the junction large enough in order to increase the number of conductive channels and thus lower R_N. But we wanted to limit the width, because as we saw in Chapter 1, a large width increases as well the number of Andreev bound states and especially the number of transverse Andreev bound states. Transverse Andreev bound states are known to lay in the gap region [26], which is increasing microwave induced nonlinear dissipation in the system [66, 67]. A high dissipation can lead to an increase of the added noise by the JPA and is thus not desirable. We can conclude that a prerequisite for reducing R_N without relying on a very wide junction is to make a high quality device with low normal resistance.

3.1.2.b h-BN as an ideal substrate

Graphene is extremely sensitive to its direct environment because of its two-dimensional nature. SiO_2 substrates have shown to create charge puddles, strain and local doping on graphene devices reducing their electronic performances from what is theoreticaly predicted [149, 150, 151]. Indeed, all these effects can create charge scattering because of local electrostatic potentials. Electrons scattering has the same effect of adding disorder in graphene resulting in lower conductivity. Therefore SiO_2 substrates are not well suited for making gJPAs because we want to minimize the resistivity in order to get high critical currents. This discussion also applies to Si substrates because there is always a thin layer of natural oxide on the surface. Therefore, we use another Van der Waals material, hexagonal boron nitrite (h-BN), to isolate graphene from its environment. h-BN is an insulator with a dielectric bandgap of 5.9 eV, has a honeycomb lattice structure with a 1.7% mismatch compared to graphene and is atomically flat [152, 153]. Strong in-plane ionic bonding makes the probability of dangling bonds and charge trapping relatively low. This makes h-BN ideal to reduce all the disorder effects mentioned previously. By making h-BN/graphene/h-BN stacks, we drastically increase the quality of the device by isolating the graphene flake both from the substrate and from contamination with the resists used during the further fabrication

steps [154]. Moreover, this allows to make one-dimensional metallic contacts on graphene improving the contact transparency. This is also good to limit the number of Andreev bound states in the superconducting gap of the JJ [26] as mentioned in the chapter 1.

3.1.2.c Exfoliation method

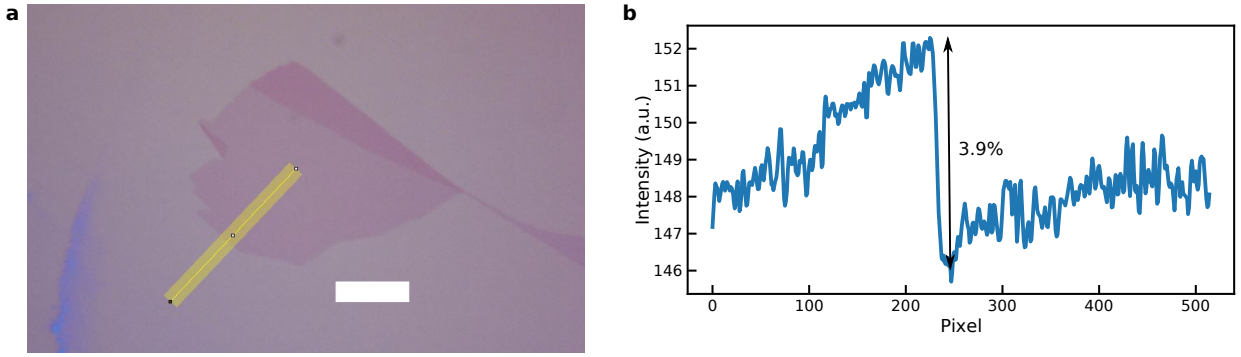

Figure 3.1: (a) Picture of an exfoliated graphene flake on an Si/SiO_2 substrate with a 285 nm SiO_2 layer taken with an optical microscope. The white length scale is 10 μm. The yellow bar represents the linecut taken to plot the intensity profile presented in (b) with the software *ImageJ*.

Thanks to the configuration of Van der Waals materials, i.e successive layers of atomic planes bonded to each other with a weak Van der Waals force, it is possible to extract single or few layers of these materials with an exfoliation technique. The exfoliation is carried out by putting a thin piece of graphite or h-BN crystal (≈ 1 mm^2) on a scotch tape (3M *Magic Scotch* tape). We then repeatedly fold, press and unfold the tape without overlaps such that the initial crystal is now separated in thinner crystals overall the tape. We then put the tape on a Si/SiO_2 substrate and wait a few minutes. Only for graphene exfoliation, we heat the substrate to 60-90 °C for a few minutes. We finally peel off the tape from the substrate making a final exfoliation step. It is worth mentioning that when peeling off the tape from the substrate, because some of the crystals are once more divided, the final remaining thin layers on the substrate were thus never in contact with the scotch tape glue, ensuring a minimal contamination. We then find graphene and h-BN flakes by checking the substrates under an optical microscope. We are aiming at graphene monolayers and can distinguish them from multilayers thanks to color and contrast analysis. The microscope parameters are kept constant between each exfoliation and we use the software *ImageJ* to plot the intensity profile of a line cut on the flake. We used Raman spectroscopy to match the contrast obtained by optical pictures to the number of layers. We found that the optical contrast of monolayers is 3-4% and 5-6% for bilayers. Fig. 3.1a shows an optical picture of a graphene monolayer. We analyzed the contrast in Fig. 3.1b and obtained 3.9%. This indicates that it is indeed a monolayer. For h-BN flakes, we are able to distinguish the thickness with a ± 5 nm precision by looking at the color of the flakes.

We did not perform AFM on each exfoliated flakes before making a h-BN/graphene/h-BN stack for a few reasons. First, by playing with the optical contrast on h-BN pictures, we were able to see thickness inhomogeneities and glue contamination. Of course, this is limited

to the resolution of the optical microscope but it is giving a good hint of the cleanliness of the flake. Then, the final JJ being small compared to the size of the encapsulated graphene (0.3x1.5 μm^2), we can always choose a clean spot to make the JJ (we perform AFM on the finished stack). We found that for our purpose it was then enough to perform AFM only on the final stack.

3.1.2.d Encapsulation process

The encapsulation process that I will describe here was first developed by a former PhD student, Goutham Nayak who shared his process with me when I started my PhD. Modifications have been made since, but more in depth view of the process can be found in his thesis [155].

Pick-up stamp

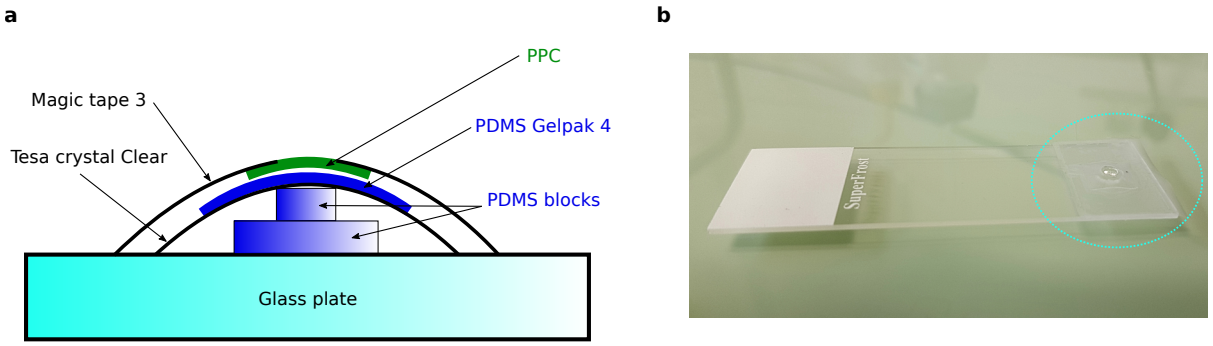

Figure 3.2: Scheme (a) and picture (b) of the stamp used to make h-BN/graphene/h-BN heterostructure. The dotted circle indicates the position of the assembly shown in (a).

The encapsulation process is made possible thanks to polymers that have two crucial properties. They need to have a greater adhesion with h-BN flakes than the adhesion between h-BN and SiO_2. This allows to pick up h-BN flakes from the substrate. h-BN is also ideal because its adhesion to graphene is greater than the adhesion between graphene and SiO_2. This allows to pick up graphene flakes from the substrate. Moreover, they need to have an appropriate response with temperature. We want the polymer to be solid at room temperature, and liquid at a temperature easily accessible in a lab in order to release the picked-up flakes. We used polypropylene carbonate (PPC) for this purpose which has a melting temperature near 120 °C. The PPC layer is prepared by dissolving 3 g of PPC crystals in 20 mL of anisole. The solution is kept at 50 °C and agitated with a magnetic stirrer for one day minimum. We then filter the solution with a 1-2 μm particles filter and spincoat it on clean substrates.

The PPC layer needs to be integrated to a stamp in order to be manipulated and make the stack. Fig. 3.2a and b show respectively a scheme and a picture of the stamp. The first element is a glass plate that we can easily manipulate with hands, on top of which we place the other small elements. We then add two blocks of polydimethylsiloxane (PDMS *Gelpak* 4) that are maintained on the glass plate with *Tesa* crystal clear tape. This creates a dome shape which is very important to pick-up the flakes slowly and smoothly. The PDMS blocks

have the advantage of being soft which helps to reduce the mechanical stress on the flakes during the pick-up. The tape is chosen transparent because we need to see through the whole stamp with an optical microscope when making the stack. Because the tape is not perfectly flat, harder than PDMS and might presents some dirt, we add a layer of PDMS Gelpak 4 on top of it. This is important because the PPC layer lays on the top of this part and is very thin (<= 1 μm) making it very sensitive to its support layer. To extract the PPC layer from the substrate on which it is spincoated, we take a piece of Magic tape 3 through which we dig a hole. We then put the tape on the substrate hosting the PPC layer and peel it off from the substrate. We then put this tape with the PPC stuck on it onto the dome. Because peeling off the PPC from the substrate induces stress making ripples in the PPC, we heat the stamp at 90 °C close to the melting temperature during 2-5 min in order to relax it.

Transfer setup

The transfer setup is shown in Fig. 3.3. Its purpose is to enable a fine control of the stamp and a precise alignment of the successive picked up flakes. Therefore, an optical microscope is needed to see the flakes and optically align them. A camera is added to the microscope in order to numerically zoom, increase contrast and use other numerical tools that can be very useful when manipulating very low contrast and very small objects like graphene flakes. In order to control the stamp, we use a 3-axis micro-manipulator allowing to move the stamp with a precision close to one micron. The substrate hosting the flakes is placed on a sample stage maintaining it via pumping through a hole. The sample stage also integrates a heater enabling the control of the temperature with a 0.1 °C precision. A piezoelectric platform allows to control the position of the sample stage in the three dimensions of space helping the alignment between the stamp and the substrate.

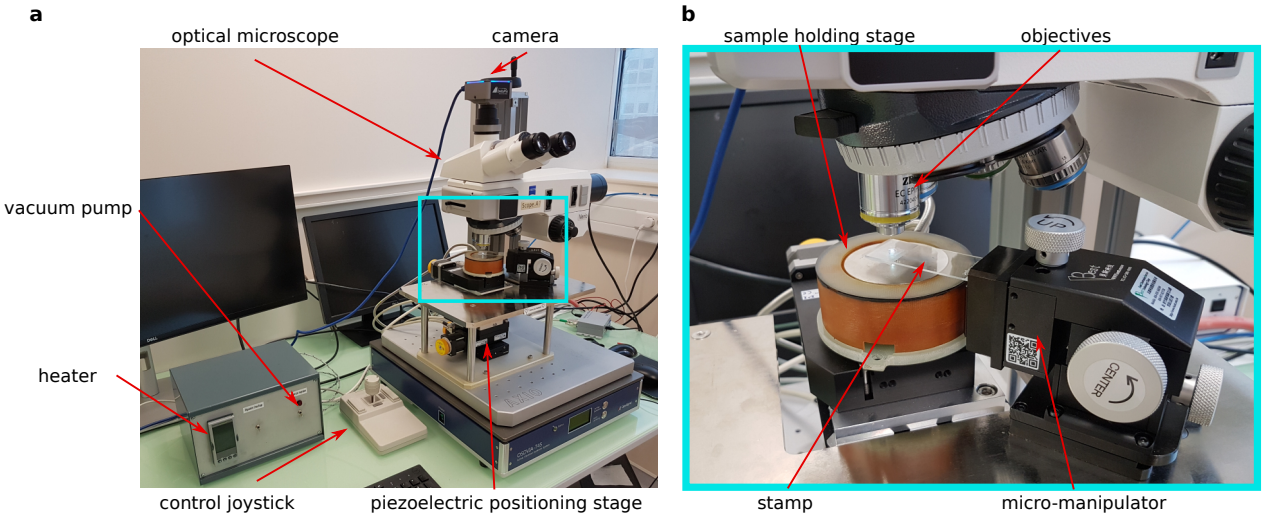

Figure 3.3: (a) and (b): pictures of the transfer setup. (b) corresponds to a zoom of the region inside the blue rectangle in (a).

Stacking process

Fig. 3.4 shows a scheme of the successive steps required to make a h-BN/graphene/h-BN heterostructure. We first place the stamp in the micro-manipulator and put a substrate with h-BN flakes on the substrate stage heated at 38 °C. We then move the stage such that the flake of interest is seen under the microscope. We align the stamp above the flake thanks to the microscope. We can now slowly move down the stamp until a single point of contact appears. If the contact point is too far from the flake we lift up the stamp and move it thanks to the micro-manipulator. The idea is to move the position of the stamp in order to have a contact point a few hundreds of micrometers away from the flake. Once the contact point is in a good spot, we can slowly move down the stamp. This will expand the contact zone and we stop when the contact zone it at the limit of the flake. Even if the micro-manipulator allows to move in the vertical direction slowly, it is still too fast to slowly cover the flake. We thus increases the temperature of the substrate holder with 0.5 °C steps. This creates a thermal expansion of the PPC allowing to cover the flake with PPC very slowly. We want to go as slow as possible in this step to limit the stress on the h-BN flake. Once the flake is fully covered (usually around 43 °C), we perform what we call a "hard pick-up". h-BN adhesion with SiO_2 can prevent the flake from being picked-up when lifting the stamp. We figured out that lifting the stamp very fast increases drastically the probability of picking up the flake, this is the hard pick-up technique. Once the h-BN flake is picked up, we put the glass plate on a hot plate at 90 °C in order to relax the stress on the PPC.

We can now perform the same process but with the graphene flake. This requires to align the picked-up h-BN with the graphene with a precision of a few microns and we use the same temperature steps to put the flakes into contact. This time, it is not the PPC that will stick to the graphene, but the picked-up h-BN flake itself. Because the adhesion between graphene and h-BN is way stronger than the adhesion between graphene and SiO_2, there is no need to do a hard pick-up. We thus pick up the flake very slowly by controlling the vertical position with the micro-manipulator. Once the graphene is picked up, we again put the glass plate on the heater at 90 °C.

We pick up the last h-BN flake with the same technique as for the first h-BN flake. Efforts are made to go as slowly as possible to limit air trapped between the flakes.

The last step consists of dropping the stack on the intrinsic Si substrate that will host the final device. As mentioned in Sec. 3.1.1.a, there is PMMA on the final substrate, preventing the deposition of parasitic picked up flakes, except on the spot where we drop the stack. We first put the stack in contact with the substrate with the help of the micro-manipulator and a slow increase of temperature. Once the stack is in contact with the substrate, we increase the temperature up to 140 °C with 20 °C steps. The PPC being in a liquid state at this temperature, we can slowly lift up the stamp without picking up the stack. At the end, the stack lays on the substrate with melted PPC residues on the top.

An additional cleaning step is then performed. We put the substrate in acetone for 12 hours minimum and use a pipette to gently blow acetone all over the substrate, rinsing with IPA and drying it with nitrogen. This removes the PPC residues and the PMMA enabling to lift all the parasitic flakes. During the stacking process, bubbles of hydrocarbon and water can form in between the different flakes. They might appear because the flakes were put in contact

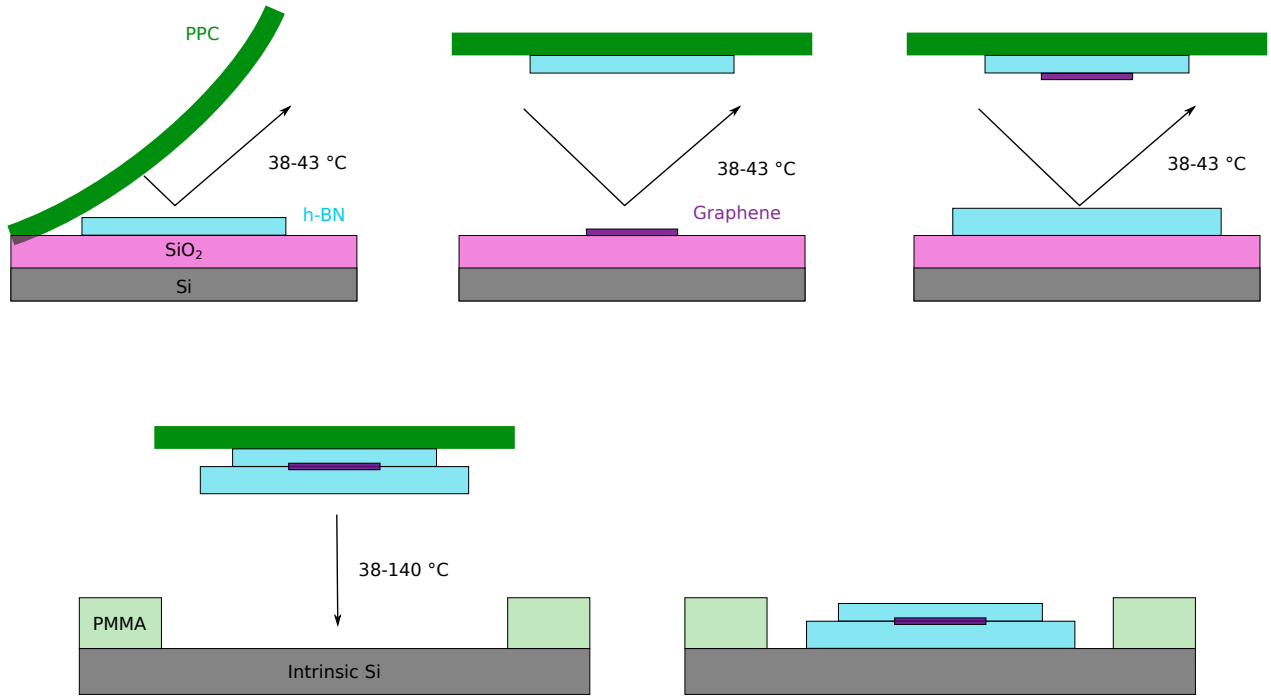

Figure 3.4: Scheme of the stacking process. The flakes are succesively picked up from the Si/SiO_2 substrates with the PPC stamp. During each step, the PCC stamp is put in contact with flakes very slowly by gradually increasing the temperature in order to limit stress and the apparition of gas trapped bubbles. When the stack is finished, we slowly put it in contact with the intrinsic Si substrate and increase the temperature up to 140 °C to release it from the PPC.

too fast, or just because the surface of h-BN and graphene is covered by these substances in ambient conditions [156]. The presence of bubbles induces local strain and possible charge effects limiting the benefits of using h-BN to isolate graphene from its environment. Therefore, it is crucial not making a JJ in a area where bubbles are present. By annealing the sample at 350 °C in high vacuum ($\approx 10^{-7}$ mbar) during two hours, we manage to make the bubbles move and merge either on the edges of the graphene flake, or on places were a defect is present. Therefore, we go from a large number of bubbles uniformly spread on the flakes to few large bubbles at precise location. It then possible to chose a clean spot to make the gJJ. Fig. 3.5 shows a picture taken with an optical microscope of the stack before and after the annealing step. We can see that bubbles (dark dots) tend to migrate further on the edges of the flake or can even totally disappear.

3.1.3 One dimensional contacts

The one dimensional contact process is inspired by the pioneering work of Wang *et al.* who developed an etch-fill technique [154].

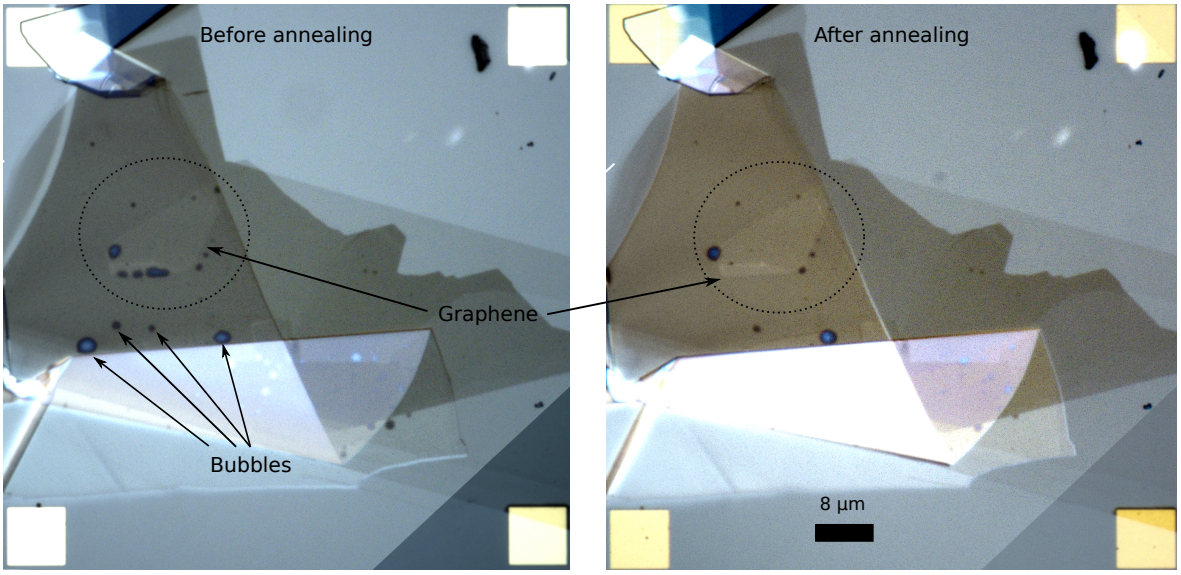

Figure 3.5: Pictures of the stack with an optical microscope before and after annealing. The graphene flake being invisible when the stack is finished and deposited on the intrinsic Si substrate, we superimposed the picture of the stack with a picture taken during the encapsulation process when the stack consisted only of one flake of h-BN and one flake of graphene. At this step, the graphene flake being visible, we superimpose this picture with the final stack picture to locate graphene. We circled the graphene part which appears as a lighter color compare to its surrounding. The bubbles appear as dark blue dots. We indicated a few of them with arrows.

3.1.3.a AFM and alignment

Once the stack is annealed we perform atomic force microscopy (AFM) in order to localize precisely the trapped bubbles. Fig. 3.6a shows the thickness of a stack with respect to position taken with AFM. We added a dotted line around the graphene flakes edges in order to make it easier to see. One can note that there are still bubbles inside the stack despite the annealing step, appearing on the AFM data as dots with a greater thickness. We can align the AFM picture with optical pictures taken with an optical microscope containing alignment markers. This allows to chose the JJ spot with a 100-200 nm precision. Fig. 3.6b shows an optical picture of the stack, right after the development of the contact lithography step, superimposed with the AFM picture shown in Fig. 3.6a. There are two lines coming from right and left separated with a small gap. This gap is not exposed and is the future gJJ. Thanks to the AFM picture it was possible to chose a spot without bubbles which is crucial to have a high quality device. The line coming from the bottom part of the picture is the side gate that will tune graphene doping (see Chapter 4).

3.1.3.b One dimensional contacts fabrication

All the metallic lines (transmission line, resonator, gate and DC lines) and the one dimensional contacts on graphene are made in one electronic lithography step. Fig. 3.7 shows the different fabrication steps. We first spincoat PMMA on the substrate. In order to keep a good

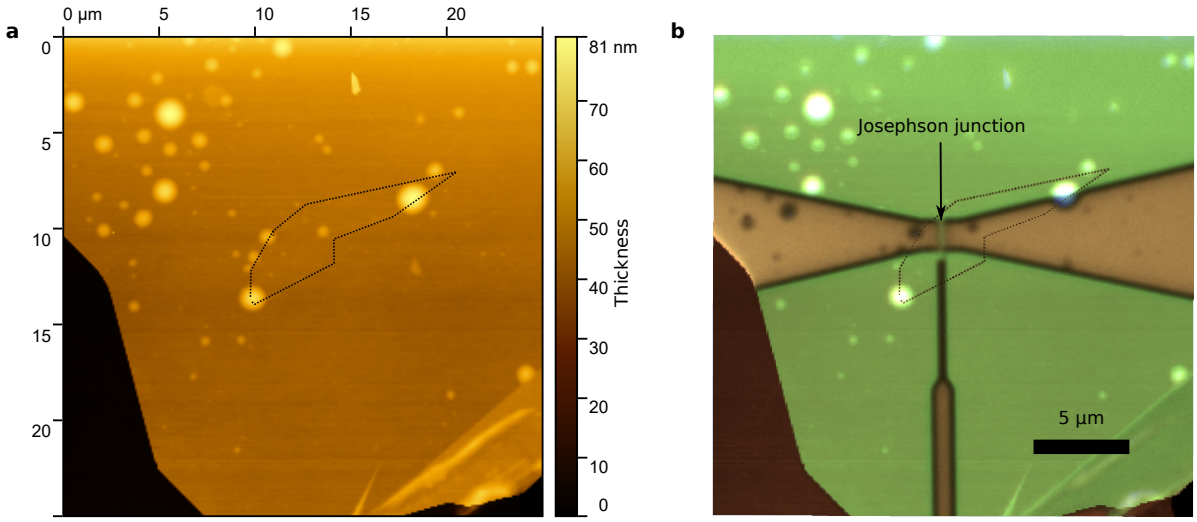

Figure 3.6: (a) AFM picture showing the thickness of the stack. The graphene has been surrounded by a dotted line to improve its visibility. (b) Optical picture taken right after the development of the contact lithography step superimposed with the AFM picture. An arrow indicates the location of the future JJ.

focus everywhere on the substrate, four global markers close to each corner of the substrate are used to detect and correct a tilt in the substrate plane. The JJ is placed in the center of a square delimited by four markers placed at 500 μm of each other allowing to correct the focus specifically around the JJ and to perform alignment. Once the development is done, resist remains on the graphene part that we want to keep in order to make a JJ. We perform a 10s O_2 reactive ion etching (RIE) in order to remove potential resist residues that would still be there after the development. We then perform a CHF_3 and O_2 RIE in order to etch the top h-BN flake and give access to the graphene flake edges. We calibrated the etching rate to be 17 ± 2 nm/s. To be safe, we always etch 10 nm more than the top h-BN thickness in order to be sure that the graphene edges are accessible. The stack is not etched exactly vertically because the PMMA is also etched from the sides during the process making a slope in the etched stack sides. This makes the graphene edges more exposed to the metal deposition. We like not to etch fully the bottom h-BN flake because keeping h-BN helps to reduce the gate voltage at which we start to see current leakage between the gate and the device. After the etching, we can see that the graphene edges are exposed to the environment. We therefore quickly transfer the device from the RIE machine to the electron beam metal deposition machine. We then deposit 5 nm of Ti with a speed of 0.5 nm/s and 60 nm of Al with a speed of 0.1nm/s, both with a angle of 4°. We use a thin layer of Ti because its work function is close to the work function of graphene enabling a good contact transparency [157]. The 4° angle deposition makes sure that metal is well deposited on graphene edges. We then perform a lift-off by putting the sample in acetone over the night and with the help of a pipette we blow acetone and remove the unwanted metallic parts.

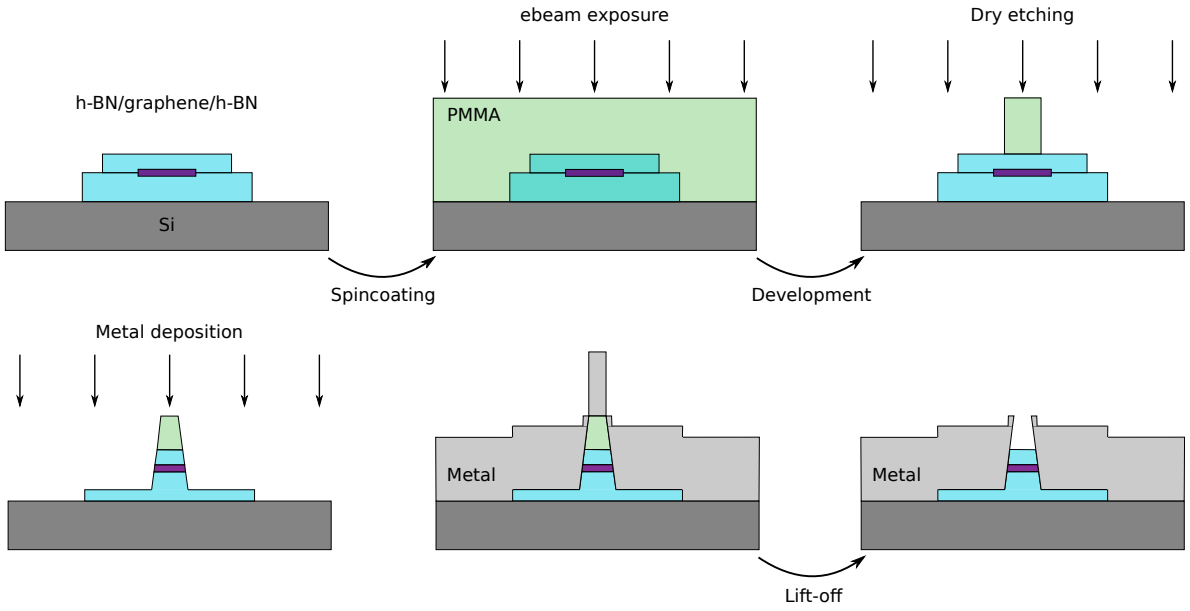

Figure 3.7: Schematics of the etch-fill technique steps in order to make one dimensional contacts on graphene. All the schemes show a side view of the substrate.

3.1.3.c Discussion about the resist layer

The thickness of PMMA is of great importance because it sets limits on the length of the gJJ. Ideally, one wants to have the minimum resist thickness such that the lift-off is still possible. Thicker resist induces a loss of precision of the ebeam pattern because of forward scattering of the ebeam electrons (electrons scattered by the resist molecules) and secondary generated electrons (electrons created by the ionization of the resist molecules) that will expose unwanted areas. The rule of thumb is to have a 1:3 ratio between the thickness of metal and resist in order to have a reproducible lift-off. The ebeam exposition is done with a 80 kV gun helping to reduce the forward scattering in the resist. As we saw in the previous section, etching is done in order to access the graphene edges. This results in a thinner resist layer and compromises the 1:3 ratio. Using a thicker resist lowers the precision of the writing but also increases the "dog ears" on the edges of the JJ. Fig. 3.7 shows what dog ears are: when the metal is deposited, it will also be deposited on the edges of the resist placed above the junction. Because they have a strong adhesion with the bottom layer of metal, these parts are not always removed during the lift off. When the resist thickness increases, the height of the dog ears increases. If they are high enough and bend above the JJ, they can create a short circuit bypassing the JJ.

To remove the dog ears we tried to use a PMMA double layer. If the molecular weight of the first PMMA layer is lower than the molecular weight of the second one, the first PMMA layer will have more exposed areas than the second one. This creates resist undercuts helping the removal of dog ears. Nevertheless, we also found that superposing two different resist layers was increasing the global strain caused by the presence of the stack. Because of this strain, we observed cracks in the resist after development, located between sharp angles of the written pattern (from either side of the JJ or between the side gate and bottom corners of

the JJ) as shown in Fig. 3.8a and b. Making round angles helps a lot to reduce the probability of cracks but is sometimes not enough when the h-BN flakes are small. Small h-BN flakes means that the JJ might be located closer to edges of the stack where the strain in the resist is maximal. So, getting rid of the dog ears with a PMMA double layer is at the cost of possible shorts, and getting rid of them by decreasing the resist thickness is at the cost of lift-off difficulties.

In addition, we noticed that when the device contains a lot of exposed areas (broad lines and big bonding pads), there is a thin line of resist above the center of the JJ that will be exposed despite not being on the writing layout. When metal is deposited, the JJ is thus shorted as shown in Fig. 3.8c. Because this is never happening when there is no stack, and because it does not look like a crack appearing at sharp corners, we suspect that the h-BN acts as an insulating substrate perturbing the lithography. Because electrons do not find an easy path to the ground beneath the substrate, they can travel back to the resist exposing unwanted areas. To cancel this effect we spincoat an additional conductive resist (Electra 92) on the top of the PMMA. After the writing, we simply remove this resist with deionized water (DI) before developing the PMMA.

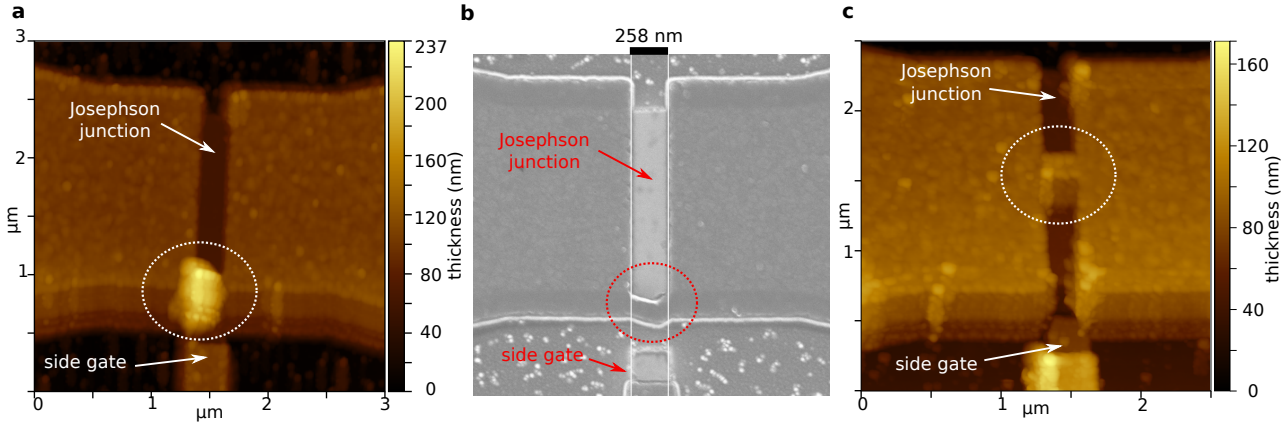

Figure 3.8: (a) Topography of a device around the JJ taken with AFM and (b) scanning electronic microscopy (SEM) of the same device. We can see a bridge of metal linking the bottom corners of the JJ. The AFM image shows that the metal has not the same thickness than the other metallic lines of the circuit. This indicates that is was probably a thin crack in the resist that we often observed between sharp angles of the circuit around the stack. (c) Topography of another device around the JJ taken with AFM. We can see a metallic line in the middle part of the JJ (dotted circle) despite it was not in the writing layout. This line is straight and has the same thickness as the other metallic lines of the circuit. It indicates that it is not a crack in the resist (which usually happen in the sharp corners of the pattern) but an unwanted exposed area which might occur because of proximity effect and the insulating nature of h-BN (this pattern does not appear without a stack). Using a conductive resist solves the problem.

3.1.4 Delimiting the Josephson junction

While the first lithography step allows to create the whole circuit and the contacts on graphene, the JJ geometry is still not well defined. Fig. 3.9 shows the steps to finalize the device. The first scheme is a top view of the device corresponding to the last step of Fig. 3.7. We can see that the graphene is shorting the circuit (two horizontal lines) and the side gate (bottom line). Moreover, we want the JJ to be located in the gap between the two horizontal metallic lines which is not the case here. Therefore, we do an additional ebeam lithography step and expose the parts of the stack that we want to remove. We take advantage of the graphene being contacted with the side gate in order to extend the side gate closer to the JJ. By doing so we bring the side gate at a distance of 200 nm from the JJ. We use the same alignment markers and focus mapping technique as in the previous lithography step in order to have good alignment between the two writings. We perform RIE with 10s of O_2 plasma followed by the same recipe as in the previous lithography step and etch 10 nm more than the top h-BN flake thickness. After etching, graphene is only located at the end of the side gate line and in-between the two superconducting lines. After this nanofabrication process, we perform AFM on the JJ and side gate area in order to check if there is no shorts connecting both sides of the JJ or connecting the JJ to the side gate. The device is then ready to be measured.

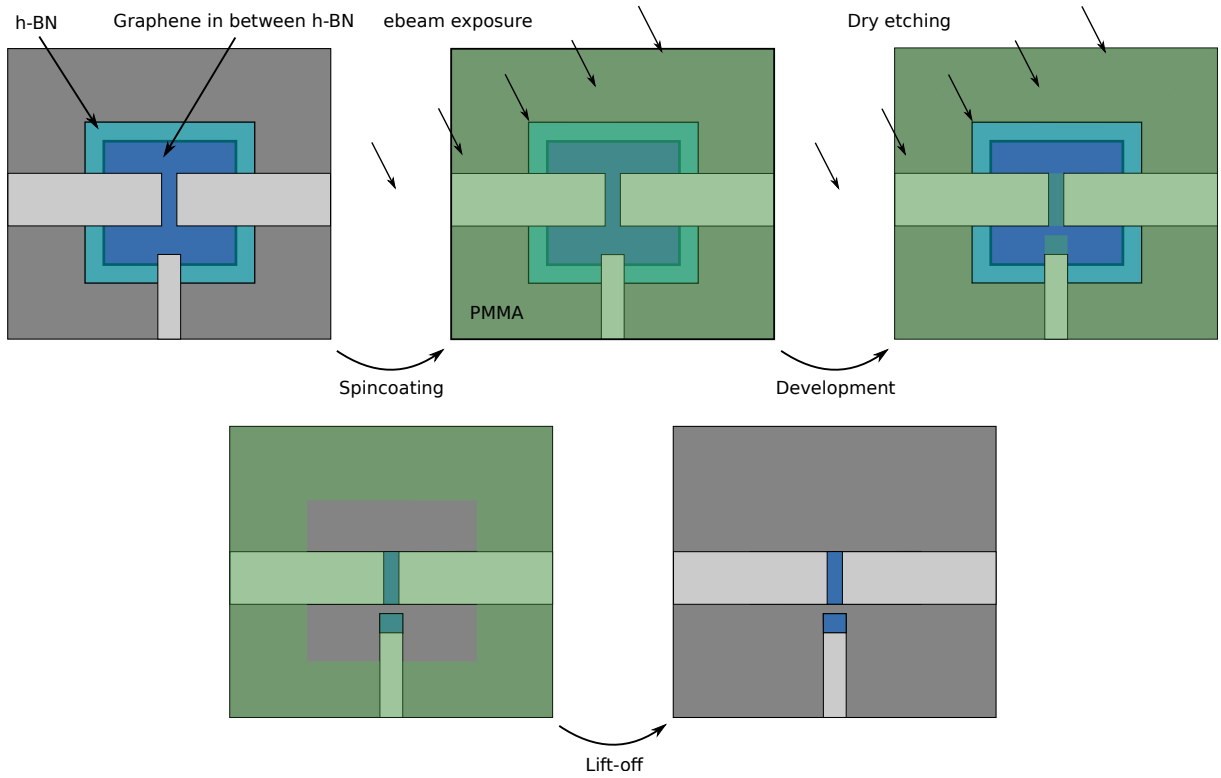

Figure 3.9: Schematics of the last lithography delimiting the JJ and extending the side gate. All the schemes show a top view of the substrate.

3.1.5 Nanofabrication parameters

We present here all the parameters used during the fabrication of the device.

steps	parameters
preparation	3 g of PPC crystal in 20 mL of anisole
resting	minimum 1 day at 50 °C + stirring
filtering	1-2 μm particle filter
spincoating	3750 rpm, 2000 rpm/s, bake 90 °C for 5 min

Table 3.1: PPC preparation

steps	parameters
Undercut resist (optional)	prebake 180 °C 2 min, PMMA 4% 50K, 4000 rpm, 4000 rpm/s, 30 s, bake 180 °C 5 min
ebeam resist	PMMA 4% 950K, 4000 rpm, 4000 rpm/s, 30 s, bake 180 °C 5 min
Conductive resist	electra 92, 3500 rpm, 3500 rpm/s, 60s, bake 90 °C 2 min
ebeam writing	70 to 100 $\mu C/cm^{-2}$
Development	1 min DI, 1 min MIBK:IPA (1:3), 30 s IPA
RIE chamber cleaning	O_2, 45 sccm, 0.07 mbar, 20 W, 10 min
On sample	O_2, 45 sccm, 0.07 mbar, 10 W, 10 s
RIE chamber preparation	CHF_3 20 sccm + O_2 2 sccm , 0.02 mbar, 15 W, 5 min
On sample	CHF_3 20 sccm + O_2 2 sccm , 0.02 mbar, 15 W, 17 nm/min
Ti deposition	5 nm, 0.5 nm/s, 4°
Al deposition	60 nm, 0.1 nm/s, 4°
Lift-off	acetone over night, IPA 30 s

Table 3.2: Etch-fill techinique

steps	parameters
ebeam resist	prebake 180 °C 2 min, PMMA 4% 950K, 4000 rpm, 4000 rpm/s, 30 s, bake 180 °C 5 min
ebeam writing	100 $\mu C/cm^{-2}$
Development	1 min MIBK:IPA (1:3), 30 s IPA
RIE chamber cleaning	O_2, 45 sccm, 0.07 mbar, 20 W, 10 min
On sample	O_2, 45 sccm, 0.07 mbar, 10 W, 10 s
RIE chamber preparation	CHF_3 20 sccm + O_2 2 sccm , 0.02 mbar, 15 W, 5 min
On sample	CHF_3 20 sccm + O_2 2 sccm , 0.02 mbar, 15 W, 17 nm/min
Lift-off	acetone over night, IPA 30 s

Table 3.3: Junction patterning

3.2 Measurement setup

We will now discuss the measurement requirements and how we can reach them experimentally. Our way of interacting with the system is through electromagnetic radiations. The superconducting nature of the device imposes conditions on the energy scales involved in the measurement. The superconducting gap of bulk aluminum is around 200 μeV corresponding to a frequency $2\Delta \approx 100$ GHz. This sets the maximum frequency we can use to irradiate the device because exciting with a higher frequency would destroy Cooper pairs and thus the superconductivity. The temperature is also very important because we want it to be below the critical temperature of aluminum (1.2 K), but also low enough to have almost no thermal photons compared to the number of photons involved in our experiment. Because our experiment deals with vacuum noise, we want the number of thermal photons way below one in average. This sets a lower limit on the frequency we can use. We thus use a dilution fridge that can reach a base temperature of 25 mK corresponding to $k_B T/h \approx$500 MHz. Therefore, the frequency range should be such that 500 MHz$<< f <$100 GHz. Having this frequency range as a physical limit, the setup was designed to work from 4 to 12 GHz.

3.2.1 Dilution fridge

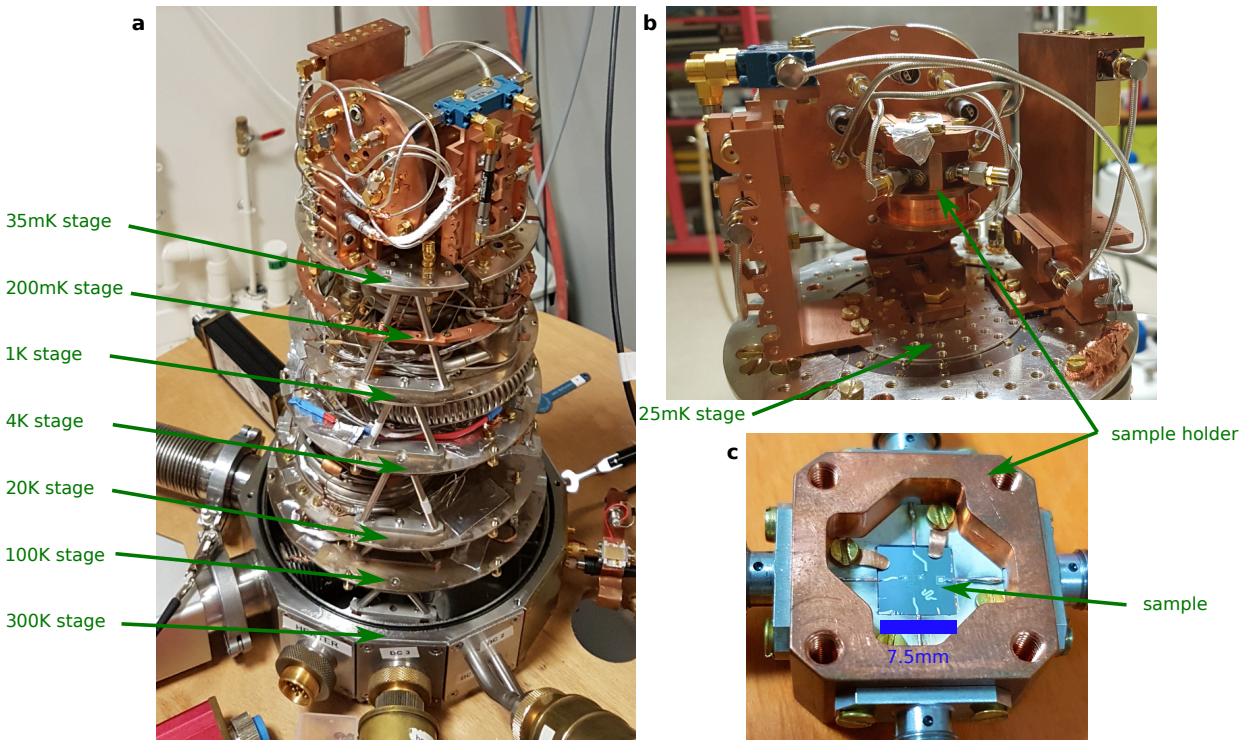

Figure 3.10: (a) Picture of the sionludi L showing all the different temperature stages. On this picture only the 25 mK shields are mounted. (b) Zoom on the 25 mK stage without the shield. The sample holder is closed. (c) Picture of the sample holder with a sample microbonded to the PCB.

During the PhD, three different fridges were used. A small inverted wet dilution fridge (sionludi L) in which most of the microwaves measurement were performed, a large inverted

wet dilution fridge (sionludi XL in the team of Nicolas Roch) on which noise measurements were performed, and a small wet fridge (Diluette) to perform DC measurements with the possibility of an additional large magnetic field. Pictures of the sionludi L are shown in Fig. 3.10a and b. It was designed and fabricated in the lab thanks to Eric Eyraud and Wolfgang Wernsdorfer. Its small size makes the cool-down duration very short such that it is possible to reach 25 mK in 8 hours, with a fully equipped fridge, making it a precious tool for device testing. It is composed of successive stages at different temperatures, some of them being shielded with a cooper shield (100K, 20K, 4K, 25mK) to block black body radiation coming from hotter stages. The 25 mK stage also includes a magnetic shield made for magnetic field screening because even small magnetic fields can perturb and decrease the critical current of the gJJ. The fridge has two input microwave lines (only one was used during the experiment) and was improved by adding 12 DC lines thanks to Kazi Rafsanjani Amin, a post-doc with whom I was sharing the setup, and who made most of the fridge improvements.

The sample is put in a copper sample holder as shown in Fig. 3.10c. A printed circuit board (PCB) allows to connect the sample microstrip lines to the fridge semirigid coaxial cables. The connection between the sample and the PCB is made by microbonds which can induce parasitic resonances due to their inductance. The PCB is thus designed such that the sample fits perfectly the center hole and such that the 50 Ω copper lines are aligned with the lines of the circuit. This allows to reduce the length or the wirebonds and thus their inductance. Moreover, each connection is made with a minimum of three wirebonds in order to also reduce the total inductance. When installing the sample in the dilution fridge, we close the sample holder with an additional copper part as show in Fig. 3.10b to provide further shielding of the sample.

3.2.2 Microwave setup

Fig. 3.11a and b show the measurement setup of the sionludi L and the sionludi XL respectively. Both the setups allow standard microwave measurements. A vector network analyzer (VNA) it used to send microwaves and to measure the scattering parameters of the device. An additional microwave source is used as a pump tone to reach parametric amplification, and is coupled to the VNA tone with a power splitter. The lines are then heavily attenuated in order to reduce the 300 K noise coming from the instruments at room temperature. Because we measure the reflection of the JPA, we add a directional coupler in Fig. 3.11a and a circulator in Fig. 3.11b to separate the reflected signal from the input signal. Isolators are then used to attenuate the output lines from the noise that could be sent by the high electron mobility transistor (HEMT) amplifier at 4K. We also used low pass filters (*K&L* 6L250-00089) at the input and output of the sample to cut the high frequency noise coming from inner part of the cables. We amplify the output signal with a HEMT having an added noise of ≈4-6 K and a gain of 41-42 dB. We then use room temperature amplifiers to amplify even more the signal.

It is of crucial importance that the first amplifier of the chain adds the minimum amount of noise because in a chain of amplifiers with gain G_i and added noise N_i, the total added noise is: $N_{tot} = N_1 + N_2/G_1 + N_3/(G_1G_2) + ...$ Therefore, having a high G_1 makes the total noise being $N_{tot} = N_1$. It is thus the noise of the first amplifier who determines the noise of

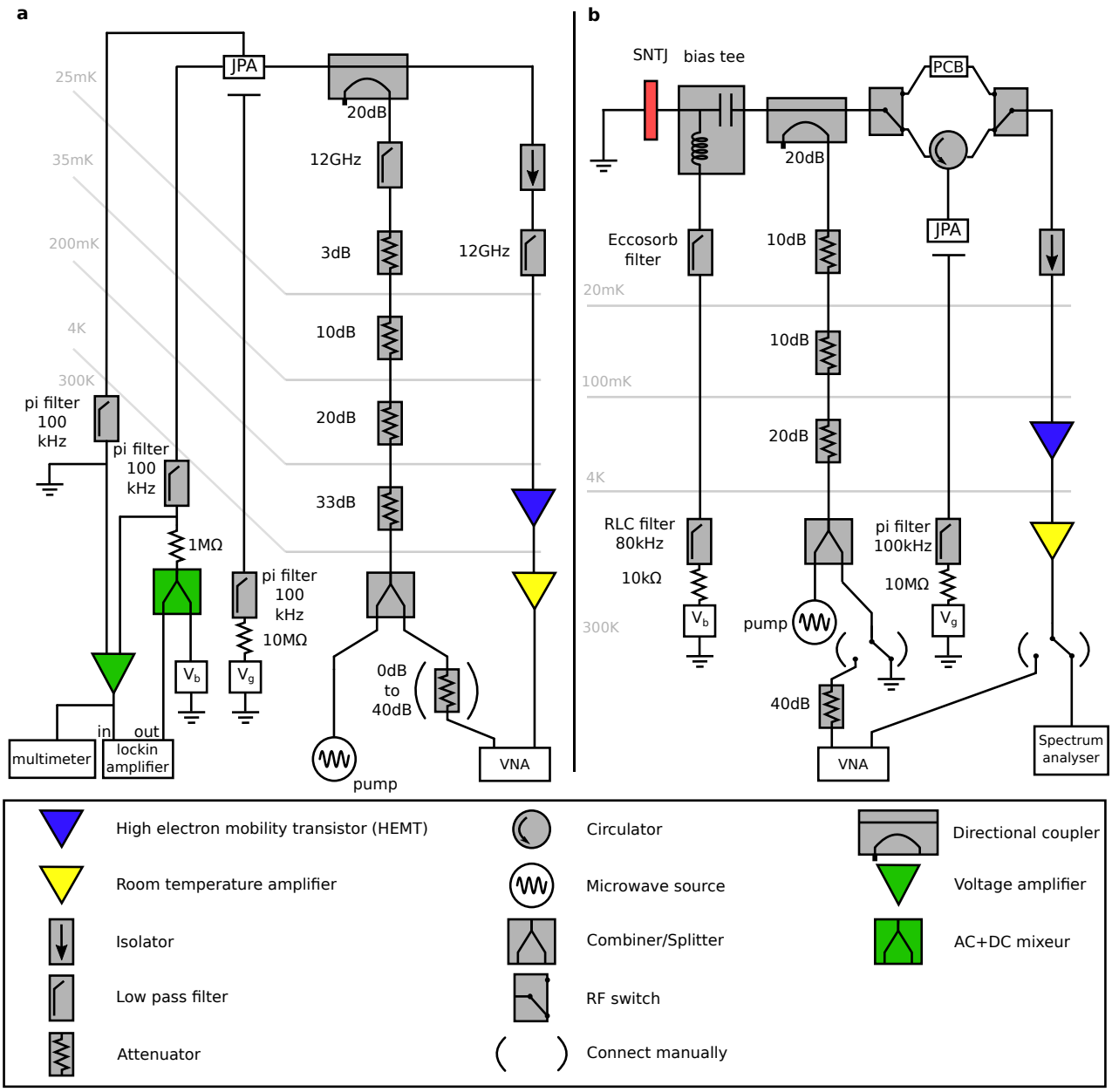

Figure 3.11: Measurement setup of the sionludi L (a) and sionludi XL (b).

the chain of amplifiers (if G_1 is sufficiently high). This is why HEMT are used because they are the best high gain and low noise amplifier on the market.

Both the setups have a filtered DC line used to gate the gJJ with a DC generator delivering a voltage V_g. The sionludi setup integrates other filtered DC lines: a lockin is used to measure the differential resistance of the gJJ and another DC source allows to DC bias the system (V_b). We also added a multimeter in order to measure the integrated resistance of the device. The sionludi XL setup integrates a shot noise tunnel junction (SNTJ) provided by the NIST (José Aumentado and Florent Lecocq) biased through a filtered DC line. The SNTJ acts as a self calibrated noise source allowing noise measurement of the JPA. To do so, we use the SNTJ as a source instead of the VNA, and measure the power spectral density with a spectrum analyzer. References of the instruments can be found in here.

3.2.3 Importance of microwave lines attenuation and filtering

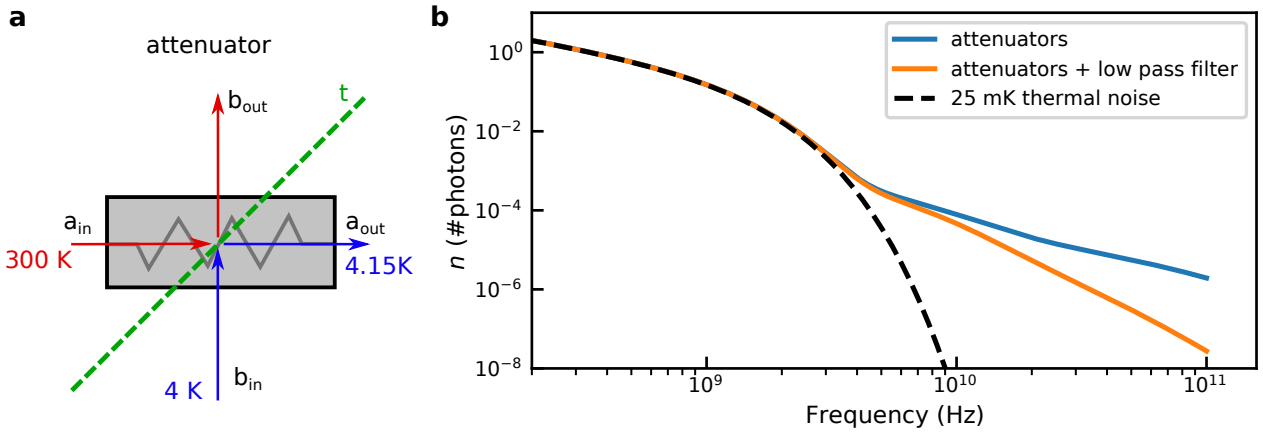

Figure 3.12: (a) Beam splitter model of an attenuator. We show here the dissipation happening at the 4 K stage with an attenuation of 33 dB equivalent to t=0.0005 (b) Thermal noise coming from the inner part of the cables on the sample with respect to the frequency. The blue curve shows the mean number of noise photons at the output of the last attenuator before the sample. The orange curve shows the noise when a 12 GHz low pass filter is added after the last attenuator. The dotted line indicates the thermal noise of a 25mK black body.

As we saw in the introduction, the sample needs to be at a temperature of 25 mK to limit the population of thermal photons that can either perturb the noise measurement of the JPA or destroy cooper pairs if the noise frequency is above twice the superconducting gap. In the setup, the sample is thermalized at 25 mK, but what about the cables linking the instruments at room temperature to the sample ? In order to limit the thermal conductivity, we use stainless steel instead of copper for the microwave cables outer conductor and we thermalize them to each stage of the fridge. By doing so we thermilize the outer part of the cables but not the inner part. The only way of thermalizing the inner part is to use a dissipative element like an attenuator. Attenuators have a double advantage: they allow the thermalization of the inner part of the cable, and they attenuate the high temperature noise coming through them. This is why attenuators are anchored at the different stages in order to be well thermalized because heat will be dissipated through them.

We can make a model to compute the power spectral density coming from the thermal noise following [158]. The attenuator can be modeled as a beam splitter (Fig. 3.12a) with two incoming amplitudes a_{in} and b_{in} being respectively the hot noise that we want to thermalize and the stage noise coming from the stage on which the attenuator is anchored. The outgoing amplitudes are a_{out} and b_{out} being respectively the noise signal going at lower temperature and the noise signal dissipated by the attenuator. If the noise amplitudes are not correlated, i.e. $\langle a_{in} b_{in} \rangle = 0$ and if $\langle a_{in} \rangle = \langle b_{in} \rangle = 0$, we have the relations:

$$\langle |a_{out}|^2 \rangle = t \langle |a_{in}|^2 \rangle + (1-t) \langle |b_{in}|^2 \rangle \tag{3.1}$$

$$\langle |b_{out}|^2 \rangle = t \langle |b_{in}|^2 \rangle + (1-t) \langle |a_{in}|^2 \rangle \tag{3.2}$$

where t is the transparency of the attenuator (t=1/attenuation). The goal is to have on the sample an averaged input noise photon number n equivalent to the black body radiation of a 25 mK source that we can compute with the Bose-Einstein distribution:

$$n = \frac{1}{\exp(\frac{\hbar\omega}{k_B T}) - 1} \tag{3.3}$$

For $\omega/2\pi$=6 GHz we find $n \approx 5.10^{-6}$. We can compute the PSD associated to the noise amplitude:

$$PSD(\omega) = \frac{\langle |a_{out}|^2 \rangle}{4 Z_0} = \frac{\hbar\omega}{\exp(\frac{\hbar\omega}{k_B T}) - 1} \tag{3.4}$$

where Z_0 is the 50 Ω impedance of the cable. Here we do not use the Johnson-Nyquist relation because it does not hold for the temperature and frequencies at play. Indeed, the Johnson-Nyquist relation is valid only when the frequencies of interest are smaller than $f = k_B T/h \approx 500$ MHz $<<$ 6 GHz for T =25 mK. In the sionludi L there is 33 dB of attenuation at the 4K stage. We can compute the number of noise photons after the attenuators $n_{out}(\omega) = PSD(\omega)/(\hbar\omega)$ using Eq. 3.4 and 3.1. We find n_{out}=13 photons at 6 GHz which is equivalent to a 4.15 K noise emitted by the 50 Ω line at the output of the attenuator (dominated by the 4K stage thermal noise).

By using this method on the successive attenuators, we can compute the input thermal noise coming from room temperature through the cables to the sample. We plotted in Fig. 3.12b the number of incoming noise photons due to the thermal noise propagating in the inner part of the cable through all the attenuators with respect to the frequency. We can see that until 2 GHz, the incoming noise is well thermalized to 25 mK. But at larger frequencies, the incoming noise starts to be hotter than a 25 mK black body (due to the strong 4K noise coming from the 4K stage). Near 6 GHz where most of the experiments are carried out, the incoming noise is $n \approx 10^{-4}$ photons which is one order of magnitude higher than a 25 mK black body but still very low compared to the vacuum fluctuations. In order to improve the thermal noise at higher frequencies we added 12 GHz low pass filters at the input and output of the device. By considering the low pass filter as a perfect first order low pass filter acting like an attenuator (following the beam splitter model), we computed the incoming noise using Eq. 3.4 and 3.1. We can see in Fig. 3.12b that it lowers the thermal noise by one order of magnitude at 26 GHz. Above this frequency, the microwave cables start to add a lot of attenuation giving even more filtering (not computed in Fig. 3.12b).

3.3 Conclusion

We showed that to minimize the nonlinearity of the graphene Josephson junction while avoiding losses due to the dynamics in the population of the Andreev bound states, the junction should be as narrow as possible with a sufficiently high critical current. To reach this purpose, a high quality graphene junction is required. We described the encapsulation procedure of graphene in between h-BN flakes allowing to reach such high quality devices. A first lithographic step allows to create all the superconducting lines of the circuit while connecting the graphene stack with one dimensional contacts. A second lithographic step allows to etch the graphene stack in order to define its shape and disconnect it from the side gate. Finally we gave a description of the different cryogenic setups used in this work. While we focused on the device fabrication in this chapter, the next chapter will describe the device geometry and characterization.

Device linear characterization and modeling

CHAPTER 4

In this chapter we will provide the linear characterization of graphene based Josephson parametric amplifiers (gJPA). We will briefly introduce the basic notions of microwave engineering allowing to create and understand resonant structures. We will then present the geometry of the device and the modeling of its microwave response. DC measurements and linear characterization are then detailed in order to extract the key physical parameters of the gJPA that will help to understand its behavior when operated in the nonlinear regime.

Contents

4.1 Microwave circuits basics

In low frequency circuits, the wavelength are often much larger than the physical size of the circuit. For example, a $f = 50$ Hz electromagnetic wave propagating in vacuum has a wavelength $\lambda = c/f = 6000$ km where c is the speed of light. Therefore, we can consider elements of the circuit as lumped because the electromagnetic wave is spatially constant over the size of these elements. This is what we are used to do when we describe circuits with simple resistors, capacitors, inductors... In the case of microwaves, at $f = 6$ GHz, we have $\lambda = 5$ cm in vacuum which is smaller than some part of the experimental setup (cables for instance). We saw in the previous chapter that the silicon chip on which the JPA lays has a length of 7.5 mm which is smaller than 5 cm. But the wavelength of the wave propagating through silicon with a relative dielectric constant $\epsilon_r = 11.4$ can be approximated by $\lambda = c/(f\sqrt{\epsilon_r}) = 1.4$ cm which is very close to the size of the chip. Thus it is impossible to consider the wave constant over the size of the circuit. We will now recapitulate the basics of microwave physics needed to understand the geometry of the device. More details can be found in [97].

4.1.1 Modeling a transmission line

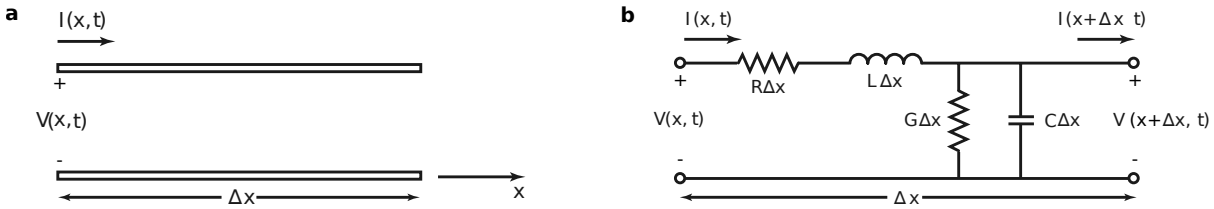

Figure 4.1: (a) Schematic of a section of transmission line of length Δz. (b) Lumped element modeling of a section of transmission line. Figure adaptated from [97]

Cables or conductive lines on a chip making a circuit can be described as transmission lines (TL). Fig. 4.1a shows a schematic of a TL. Microwaves are sent in the top part representing the conducting wire. This creates a current I and a voltage V between the wire and the ground. It is possible to use lumped element theory by dividing the TL into infinitesimal sections of size Δx such that $\lambda >> \Delta x$. This way, the electrical quantities (I, V) can be considered as constant over each section. Fig. 4.1b shows the lumped element representation of such a small section of TL where R is the series resistance per unit of length, L the series inductance per unit of length, G the shunt conductance per unit of length and C the capacitance per unit of length. We can use Kirchhoff's laws on a section and derive what are called the telegrapher equations:

$$\begin{aligned} \frac{\partial V(x,t)}{\partial x} &= -RI(x,t) - L\frac{\partial I(x,t)}{\partial t} \\ \frac{\partial I(x,t)}{\partial x} &= -GV(x,t) - C\frac{\partial V(x,t)}{\partial t} \end{aligned} \tag{4.1}$$

If the input wave has a cosine form with angular frequency ω, we can combine these equations

with steady state condition and find:

$$\begin{aligned} \frac{d^2V(x)}{dx^2} - \gamma^2 V(x) = 0 \\ \frac{d^2I(x)}{dx^2} - \gamma^2 I(x) = 0 \end{aligned} \tag{4.2}$$

where:

$$\gamma = \alpha + i\beta = \sqrt{(R + i\omega L)(G + i\omega C)} \tag{4.3}$$

These are propagation equations with solutions:

$$\begin{aligned} V(x) = V_0^+ e^{-\gamma x} + V_0^- e^{\gamma x} \\ I(x) = I_0^+ e^{-\gamma x} + I_0^- e^{\gamma x} \end{aligned} \tag{4.4}$$

where V_0^+, V_0^-, I_0^+ and I_0^- are determined with boundaries conditions. We define the characteristic impedance Z_0 such that:

$$\frac{V_0^+}{I_0^+} = Z_0 = \frac{-V_0^-}{I_0^-} \tag{4.5}$$

Giving:

$$Z_0 = \sqrt{\frac{R + i\omega L}{G + i\omega C}} \tag{4.6}$$

4.1.2 Terminated transmission line

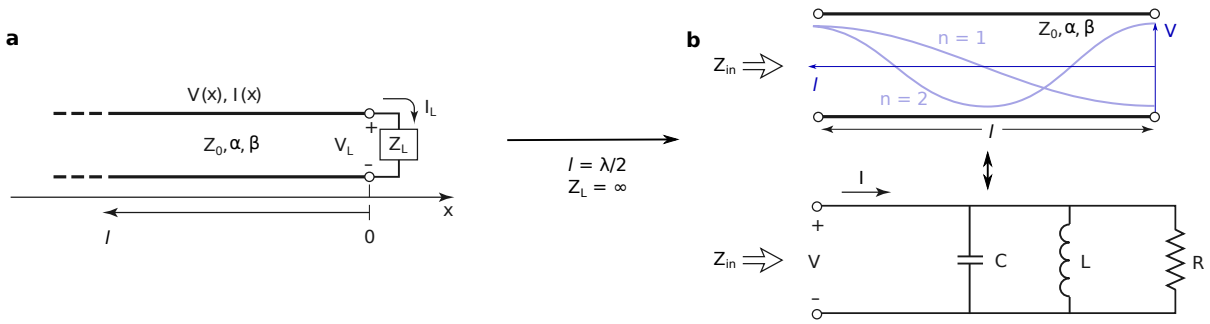

Figure 4.2: (a) Transmission line terminated by a loaded impedance Z_L. (b) Transmission line of length $l = \lambda/2$ terminated by an open circuit. In blue are shown the first two modes of the renonance. Figure adaptated from [97]

The previous formalism allows to describe how microwaves or equivalently current and voltage propagate in a TL of characteristic impedance Z_0 with a complex propagation constant $\gamma = \alpha + i\beta$. We will now show that terminating a TL with a loaded impedance Z_L necessarily creates a reflected wave and that it can be used to create resonant structures. Fig. 4.2a shows such a terminated TL. This imposes the impedance of the transmission line at the position $x = 0$: $V(0)/I(0) = Z_L$ leading to:

$$V_0^- = V_0^+ \frac{Z_L - Z_0}{Z_L + Z_0} = \Gamma V_0^+ \tag{4.7}$$

This means that the presence of the load impedance will create a reflected wave if Z_L is not perfectly matched with Z_0, i.e $Z_L \neq Z_0$. The reflection coefficient is $\Gamma = \frac{Z_L - Z_0}{Z_L + Z_0}$. We can compute the impedance at an arbitrary position x using Eq. 4.4 with the boundary condition at $x = 0$ and find:

$$Z(x) = \frac{V(x)}{I(x)} = Z_0 \frac{e^{i\gamma x} + \Gamma e^{-i\gamma x}}{e^{i\gamma x} - \Gamma e^{-i\gamma x}} \tag{4.8}$$

If the TL is terminated with an open-circuit, then $Z_L = \infty$ meaning that the wave is fully reflected ($\Gamma = 1$). At this position there is no current and a maximum voltage. In addition, if the length l of the TL is such that $l = \lambda/2$, it can behave as a resonant structure as shown in Fig. 4.2b where we plotted the two first modes of the resonator. In the mode $n = 1$, only half a wavelength is resonant inside the TL, this is why we call it a $\lambda/2$ resonator. Using Eq. 4.8 with $\Gamma = 1$ and $x = l$ we find impedance at the input of the transmission line:

$$Z_{in} = \frac{Z_0}{\tan(\gamma l)} = Z_0 \frac{1 + i\tan(\beta l)\tanh(\alpha l)}{\tanh(\alpha l) + i\tan(\beta l)} \tag{4.9}$$

Taking $l = \lambda/2$ and working around the resonance frequency $\omega = \omega_0 + \Delta\omega$ such that $\Delta\omega << \omega_0$, it is possible to approximate Z_{in} in the following form:

$$Z_{in} \approx \frac{Z_0}{\alpha l + i(\Delta\omega\pi/\omega_0)} \tag{4.10}$$

which has the same form as the impedance of a lumped parallel RLC circuit resonator:

$$Z_{||} \approx \frac{R}{1 + 2i\Delta\omega RC} \tag{4.11}$$

This shows that a $l = \lambda/2$ transmission line terminated by an open-circuit behaves like a resonator and that it can be modeled by an effective lumped element circuit.

4.1.3 Capacitively coupled $\lambda/2$ resonator

In this work, the JPA is made of a $\lambda/2$ resonator that is capacitively coupled to a 50 Ω transmission line (see Sec. 4.2). We will derive useful equations about this system in this section.

4.1.3.a Impedance computation

Let us consider a resonator with an impedance Z_0 coupled to a TL by a capacitance C_i. This is equivalent to having the $\lambda/2$ resonator in series with a capacitance. We can thus write the normalized input impedance of this circuit using Eq. 4.9 as:

$$z = \frac{Z_{in}}{Z_0} = -i\left(\frac{1}{\omega C_i Z_0} + \cot(\beta l)\right) = -i\left(\frac{\tan(\beta l) + b_c}{b_c \tan(\beta l)}\right) \tag{4.12}$$

with $b_c = Z_0\omega C_i$. We have for now put $\alpha = 0$ meaning that we compute z in the dissipationless limit. When the system is at resonance, the magnetic and electric energy stored by the circuit are equal, which imposes the impedance to be real, i.e. $\mathrm{Im}(z) = 0$ [97], thus:

$$\tan(\beta l) + b_c = 0 \tag{4.13}$$

We can now make a Taylor expansion around resonant angular frequency ω_0:

$$z \approx z(\omega_0) + (\omega - \omega_0)\frac{dz}{d\omega}(\omega_0) + \dots \tag{4.14}$$

Because z is purely imaginary, at resonance $z(\omega_0) = 0$. Thus:

$$z \approx (\omega - \omega_0)\frac{dz}{d(\beta l)}\frac{d(\beta l)}{d\omega}(\omega_0) \tag{4.15}$$

We can compute $\frac{dz}{d(\beta l)}$:

$$\frac{dz}{d(\beta l)} = i\frac{1}{\sin^2(\beta l)} = i\frac{1+\tan^2(\beta l)}{\tan^2(\beta l)} = i\frac{1+b_c^2}{b_c^2} \tag{4.16}$$

where we used Eq. 4.13 to obtain the right part of the equation. We will see later from the extracted Z_0, ω_0 and C_i of our circuit that in practice $b_c << 1$. Thus:

$$\frac{dz}{d(\beta l)} \approx i\frac{1}{b_c^2} \tag{4.17}$$

Knowing that $\beta = \frac{\omega}{v_p}$ where v_p is the phase velocity and injecting Eq. 4.17 in Eq. 4.15 we get:

$$z \approx i(\omega - \omega_0)\frac{1}{b_c^2}\frac{l}{v_p} \approx i(\omega - \omega_0)\frac{1}{b_c^2}\frac{\pi}{\omega_0} \tag{4.18}$$

Where we used $f_0 = \frac{v_p}{2l}$ with $l = \lambda/2$.

We can now reintroduce small losses for a high internal quality factor (Q_i) resonator by taking a complex resonance angular frequency: $\omega_0 \to \omega_0(1 + \frac{i}{2Q_i})$. So:

$$z = \frac{\omega - \omega_0}{\omega_0}\frac{\pi}{b_c^2}\frac{1}{2Q_i} + \frac{\pi}{b_c^2}\frac{1}{2Q_i} + i\left[\frac{\omega - \omega_0}{\omega_0} - \frac{1}{(2Q_i)^2}\right]\frac{\pi}{b_c^2} \tag{4.19}$$

We can simplify the real part by dropping the first term because: $\frac{\omega-\omega_0}{\omega_0} << 1$. We can also simplify the imaginary part by dropping the second term, because by assumption the quality factor is high, thus: $\frac{1}{(2Q_i)^2} << \frac{(\omega-\omega_0)}{\omega_0}$. We can write the final expression for z:

$$z = \frac{\pi}{b_c^2}\frac{1}{2Q_i} + i\left((\omega - \omega_0)\frac{\pi}{\omega_0 b_c^2}\right) \tag{4.20}$$

The system is working like a series RLC resonator because its impedance has the form $Z = R + i\omega L - i\frac{1}{\omega C}$. We can thus derive the equivalent resistance:

$$R = \frac{Z_0\pi}{2b_c^2 Q_i} \tag{4.21}$$

The coupling coefficient is defined as $g = Z_0/R = Q_i/Q_c$, where Q_c is the coupling quality factor, thus:

$$Q_c = \frac{\pi}{2b_c^2} \tag{4.22}$$

We can rewrite z as:

$$z = \frac{Q_c}{Q_i} + 2iQ_c\frac{\omega - \omega_0}{\omega_0} \tag{4.23}$$

4.1.3.b Computation of S_{11}

In practice, during the microwave measurement, we will measure the S_{11} parameter which is the reflection coefficient of the microwave on the resonator. We saw in Sec: 4.1.2 that the reflection coefficient Γ can be written as $\Gamma = \frac{Z_{in}-Z_0}{Z_{in}+Z_0} = 1 - \frac{2}{1+z} = S_{11}$. By introducing the loaded quality factor: $Q_l^{-1} = Q_c^{-1} + Q_i^{-1}$, we get the important equation:

$$S_{11} = 1 - \frac{2Q_l/Q_c}{1 + 2iQ_l\frac{\omega-\omega_0}{\omega_0}} \tag{4.24}$$

It is worth noting that this result is similar to what is obtained in a quantum model using input/output formalism where a resonator is coupled to both a transmission line and a linear loss channel as shown in Chapter 2. We only note an exactly opposite phase sign on the imaginary part of S_{11} obtained this way which manifests as a positive phase shift at resonance. We chose the sign of the imaginary term such that it corresponds to the measured phase shift (i.e. negative phase shift at resonance). We believe this difference arises because of some conventions made in the equations describing the quantum system.

4.1.4 Microstrip geometry

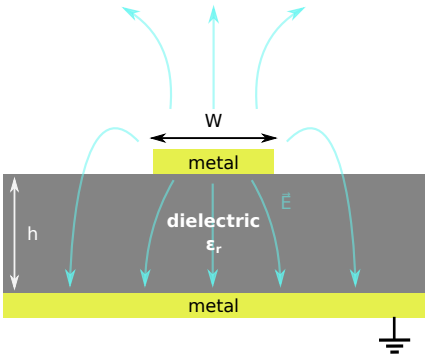

Figure 4.3: Schematic of a microstrip line with a cross section view.

So far we have been quite general on what is a transmission line and how it can be used to create resonant circuits. We will now focus on how we make them on chip. As we saw earlier, one needs to have a minimum of two conductors in order to create a TL. There are many possibilities with respect to geometry having each advantages and drawbacks. In this work we made all the circuits with a microstrip geometry. Fig. 4.3 shows a schematic of what is a microstrip circuit. It consists of a metallic line deposited on a dielectric substrate with a relative electric permittivity ϵ_r with a ground plane on the bottom surface. The microstrip geometry has the advantage of being easy to fabricate with lithographic methods because one needs to draw only one line. Because the dielectric medium is not the same above (vacuum) and beneath (dielectric) the metallic line, there is an effective dielectric constant ϵ_e such that $1 < \epsilon_e < \epsilon_r$. We can approximate ϵ_e:

$$\epsilon_e = \frac{\epsilon_r + 1}{2} + \frac{\epsilon_r - 1}{2}\frac{1}{\sqrt{1 + 12h/W}} \tag{4.25}$$

It is also possible to approximate the characteristic impedance of the microstrip line:

$$Z_0 = \frac{60}{\sqrt{\epsilon_e}} \ln\left(\frac{8h}{W} + \frac{W}{4h}\right) \tag{4.26}$$

valid in the case $W/h \leq 1$.

4.2 Device modeling

In this part we will focus on how we were able to simulate the device and what we can extract from the simulations.

4.2.1 Geometry of the device

An on-scale scheme of the top view of the graphene Josephson parametric amplifiers (gJPA) we built is shown in Fig. 4.4. The colored parts represent areas where metal is deposited and different colors are used for different elements of the circuit. White parts represent the bare substrate. The red part is a 50 Ω TL making the link between the PCB and the device. All the incoming microwaves are sent through this line. A $\lambda/2$ resonator (purple) is capacitively coupled to this TL thanks to a gap of 5 μm between the two interconnected structures (inset 1). We showed previously that a capacitively coupled $\lambda/2$ resonator does not behave like a parallel RLC resonator anymore but like a series RLC resonator. The resonator has a length $l = 8.950$ mm, a width of 10 μm and locally narrows down in the center where the graphene Josephson junction (gJJ) is located (inset 2). It allows to incorporate DC lines (blue) from each side of the gJJ with a minimal effect on the resonator. In fact, to DC probe the gJJ, there must be at least one probe line from each side of the gJJ. The center of the resonator being at a voltage node, resonant microwaves are not leaking too much in these added lines (simulations will be shown later). The DC lines are terminated with a pad and a loop inductor for filtering purpose. The pads are then wirebonded to 50 Ω transmission lines wirebonded themselves to the PCB. A side gate (green) allows to tune the doping of the gJJ (also visible in the inset 2). The width variation of the gating line and the loop inductor are also made for filtering purposes.

We made the choice of using a side gate because it has the advantage of being easy to do with respect to the lithographic process. Indeed we saw in the previous chapter that all the circuit can be written in only one lithographic step. Moreover, the main reason pushing us using a side gate was the fear of additional loss processes coming from another way of gating. Top gates or bottom gates are very 'intrusive' in the sense that they are very close to the device. This is why we did not wanted to introduce additional dielectric materials for a topgate nor a graphite backgate. These losses can limit the properties of a Josephson parametric amplifier and we wanted thus to minimize other potential sources because gJPA were not yet demonstrated. For example, a graphite bottom gate or a HSQ top gate could induce additional losses. Nevertheless a recent work showed that gJPA can work with a graphite bottom gate [148].

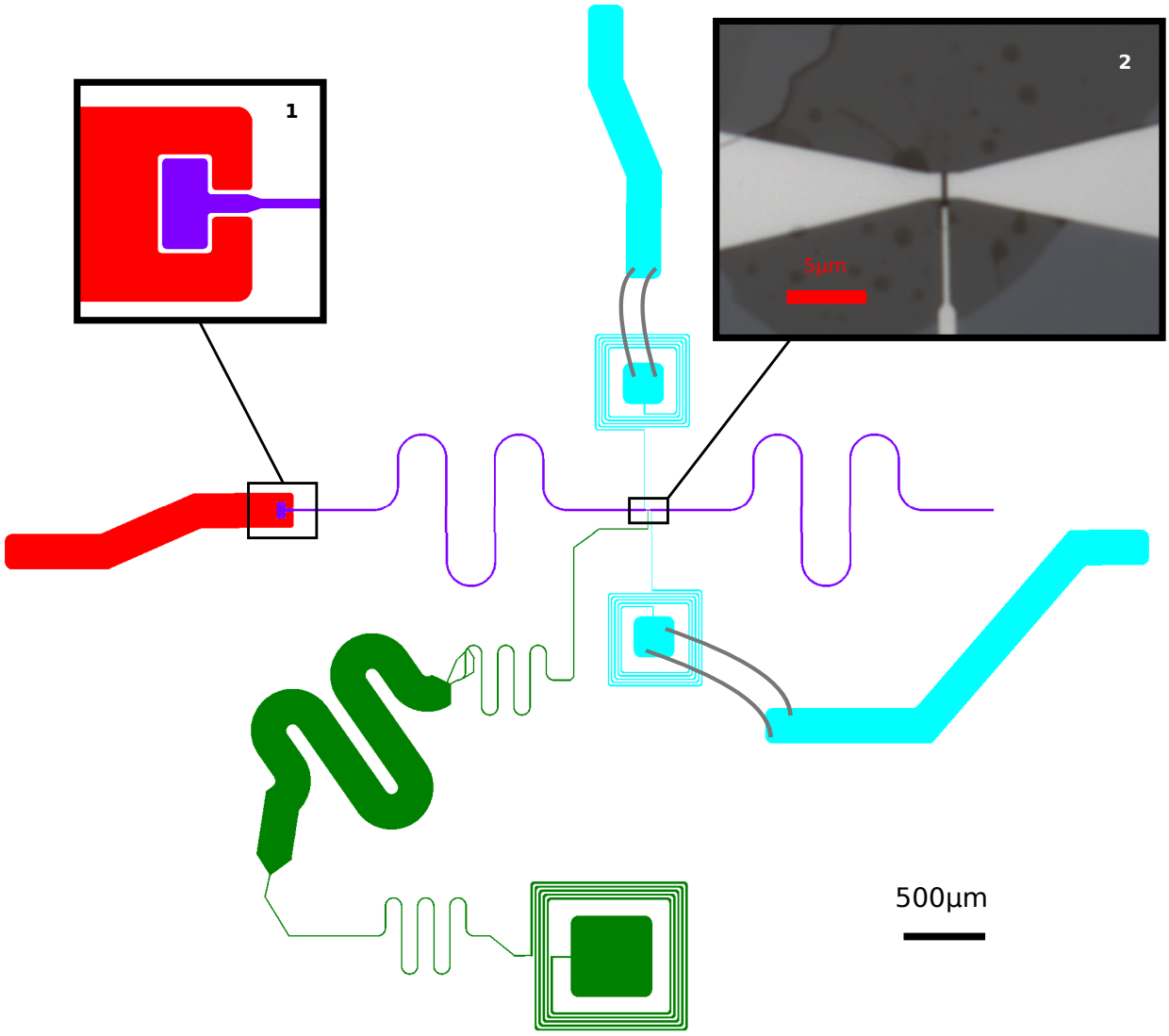

Figure 4.4: On scale scheme of the top view of the microstrip graphene Josephson parametric amplifier. Inset 1 shows a zoom on the interconnected transmission line and resonator. Inset 2 is an optical picture of the gJJ on which we can also see the side gate (vertical line). The gJJ length is $\approx$ 300 nm and the width is 1.5 or 2.0 μm depending on the device.

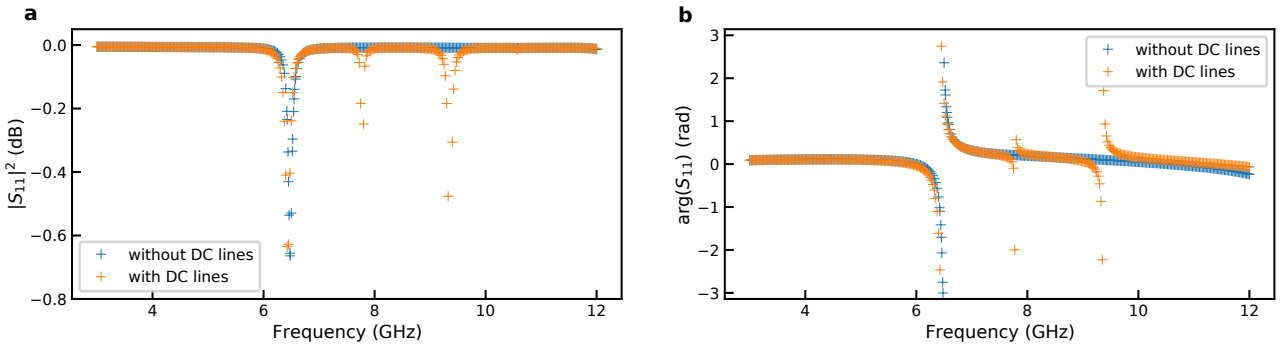

Figure 4.5: Simulated microwave response (amplitude (a) and phase (b) of the S_{11} parameter) with *Sonnet* with and without the DC lines.

4.2.2 DC probe lines

We modeled the microwave response of the device using the software *Sonnet* v16.54. The gJJ is simulated by a lumped inductor whose inductance is put to 0 to simulate the bare device (device where the gJJ is replaced by a superconducting continuum). This allows to model the device at low input power where the non linear Josephson inductance can be approximated by a linear inductance. Simulations were important because of the numerous circuit free parameters: coupling between the resonator and the 50 Ω transmission line, length and width of the resonator, length of the DC lines, position of the DC lines. Making and measuring a device for each set of parameters would have taken a lot of time and resources. The most challenging part was to incorporate the DC probe lines without affecting the resonator first mode, and without creating resonance features below the resonator first mode. Indeed, the Josephson inductance L_J being tunable with a gate voltage, it is possible to lower the resonance frequency of the resonator. This makes the presence of parasitic resonance features due to DC probe lines not desirable below the resonance frequency of the bare resonator.

Fig. 4.5a and b show the simulated magnitude and the phase of the reflection coefficient (S_{11}) respectively with respect to the incoming wave frequency, for the device with and without DC probe lines. The dips in the magnitude are caused by resonant effects where the incoming wave can enter into the resonator and exhibit dissipation due to internal losses. The resonances also create a shift in the phase of S_{11}. We can see that without the DC lines there is only one peak in the amplitude associated with a 2π phase shift corresponding to the first mode of the resonator. The 2π phase shift indicates that the resonator is overcoupled, meaning that the coupling quality factor is smaller than the internal quality factor. Because of the capacitance between the transmission line and the resonator, the rate at which photons are dissipated inside the resonator (internal loss) is low compared to the rate at which photons can escape from the resonator through this capacitance. When comparing the response with and without the DC probe lines, we can see that adding these lines creates resonant features above the first mode frequency. As we explained before, this is not a problem for our experiment because the tunable gJPA will work below the bare resonance frequency. We need also to compare the effect of DC lines on the first resonant mode. With the presence of DC lines, the resonance frequency slightly shifts downwards (50 MHz) maybe due to an increased capacitance caused by the additional lines. We also see that the width of the first

mode is similar, indicating that the quality factor does not change. The width is ≈ 90 MHz with and without the DC lines giving a quality factor $Q = 72$. This shows that the additional DC lines are not degrading the performance of the resonator because microwave leakage through theses lines would have lowered the quality factor.

4.2.3 Gating line

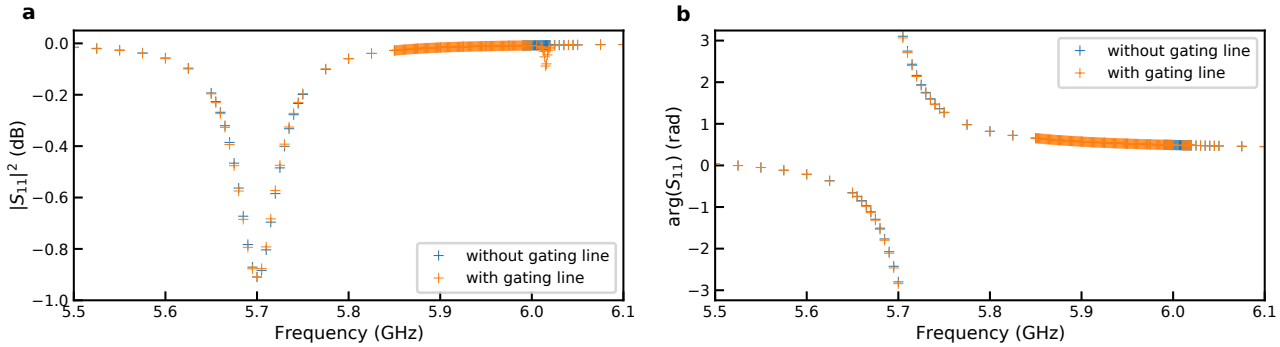

Figure 4.6: Simulated microwave response (amplitude (a) and phase (b) of the S_{11} parameter) with *Sonnet* with and without the gating line.

We performed additional simplified simulation to study the effect of the gating line. The simplified device resonator consists of a straight line of the same length than the real resonator, with a constant width of 10 μm, without DC probe lines, and with a different coupling gap with the transmission line. We wanted the total capacitance of the gating line to be high in order to lower the cutoff frequency of the RC filter formed by the DC wires in the fridge up to the end of the gating line. This is why we put a 500 μm^2 pad as well as a long gating line. The problem of a long gating line is that it can be a resonant structure at frequencies similar or lower than the resonance frequency of the resonator. Because there is a coupling between the two structures, it means that microwaves can leak from the resonator to the gating line, or that noise coming from the gating line can enter into the resonator. To limit this effect, we adopted a Bragg geometry for the gating line: we alternated elements of length $\lambda/4$ with a different intrinsic impedance Z_0 by varying the width of the line. It is similar to what we can find in optics where refractive index of a medium is alternated to create destructive interference at a given frequency. Fig. 4.6 shows the S_{11} parameter of the simplified resonator without a gating line, and with a gating line length of $3\lambda/4$ with alternating width (10 μm/ 220 μm/ 10 μm). We see in Fig. 4.6a that the presence of the gating line induces a small narrow peak in the magnitude of S_{11} at $f \approx 6$ Ghz . The peak having an intensity smaller than 0.1 dB, it is actually very hard to see it on experimental data. We can see in Fig. 4.6b that the phase shift associated with this resonance feature is also very small ($\approx 10^{-2}$ rad) which is also too small to be measured. We can conclude that the presence of the gating line does not affect the circuit.

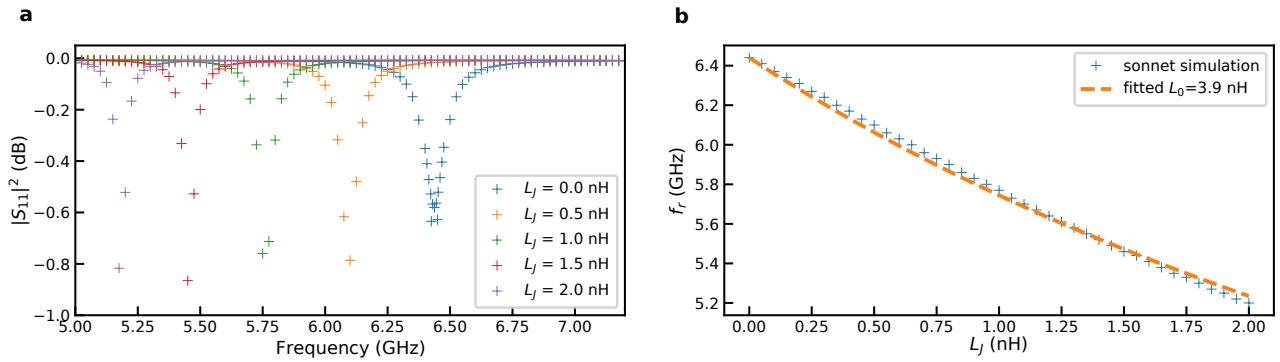

Figure 4.7: (a) Simulated magnitude of the reflection coefficient of the device for different values of L_J. (b) Extracted resonance frequency as a function of L_J from the *Sonnet* simulation. The fit correspond to a lumped element model where we used Eq. 4.29.

4.2.4 Josephson inductance

The presence of the gJJ can also be simulated by *Sonnet* when the input power is low enough such that we can neglect the nonlinearity of the junction. The gJJ is thus modeled as a discrete inductor L_J. Close to the resonance frequency, we saw that the resonator can be modeled by a lumped element RLC resonator. Therefore its resonance frequency can be written as:

$$2\pi f_0 = \frac{1}{\sqrt{L_0 C}} \tag{4.27}$$

where L_0 and C are the equivalent inductance and capacitance of the resonator. When there is no gJJ, L_0 and C are purely geometry dependent (L_0 having however a small kinetic part). But when the gJJ is added in the middle of the resonator we can consider that it adds a series inductance such that $L = L_0 + L_J$ (L_0 being the geometric inductance). We can then rewrite the resonance frequency of the resonator with a gJJ:

$$2\pi f_r = \frac{1}{\sqrt{(L_0 + L_J)C}} \tag{4.28}$$

Where we neglected the change in capacitance due to the junction because of its small size. Fig. 4.7a shows the magnitude of the S_{11} parameter simulated for different values of L_J. As predicted by Eq. 4.28, the additional inductance caused by the presence of the gJJ lowers the resonant frequency of the resonator. By combining Eq. 4.27 and Eq. 4.28 we get:

$$f_r = \sqrt{\frac{L_0}{L_0 + L_J}} f_0 \tag{4.29}$$

L_J being fixed to a known value and f_r and f_0 being obtained by the simulation, it is possible to extract the geometric inductance L_0. Fig. 4.7b shows the simulated f_r with respect L_J and the fit we did with Eq. 4.29. We can see that the lumped element model is very close to the simulated distributed resonator with an average error on f_r of 4 MHz. The fit allowed to extract L_0 = 3.9±0.1 nH. Having L_0 and f_0 we can compute the total capacitance of the device and find C = 0.157 pF.

4.3 Bare device and DC characterization

After the simulations, we will now focus on measurements prior to gJPA measurements. The first step is to characterize the bare device, i.e. the device where the gJJ is replaced by a superconducting continuum such that $L_J = 0$ nH, in order to compare it to the simulations. Then, we also created purely DC devices to characterize the gJJs themselves.

4.3.1 Bare device characterization

4.3.1.a Normalization

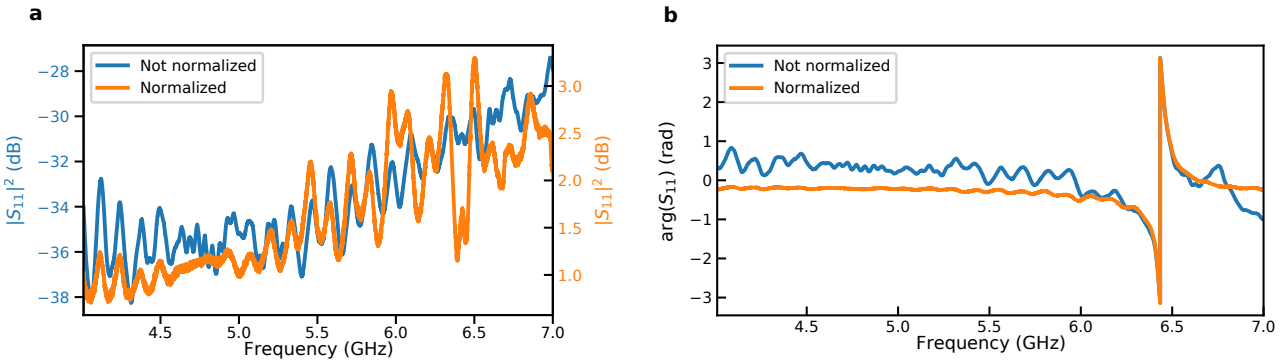

Figure 4.8: Magnitude (a) and phase (b) of the S_{11} parameter with and without a normalization with the S_{11} parameter measured at 1.1 K.

We measured the bare resonator in the sionludi L fridge at a base temperature of 25 mK. Fig. 4.8a and b show the measured S_{11} parameter (blue). We can see oscillations in the amplitude of a few dB such that it is not possible to see the resonance peak. There is also a positive linear slope after 5 GHz. The phase also exhibits oscillations, but because the resonance creates a 2π phase shift (overcoupled resonator), it is easy to see where it is located. We call this non-flat background the microwave background. Ideally it should be flat if all the impedances of the elements in the measurement setup would be exactly 50 Ω at each frequency (by assuming a flat gain of the amplifiers present in the measurement setup). But it is of course not the case for various reasons: it is very hard to have a constant impedance over a wide frequency range, each connection made by hand can slightly change the impedance depending on the tightening strength, there is a temperature dependence which differs depending on the element, the amplifiers are frequency dependent... Therefore, we use trace taken right before the Ti/Al resonator transits to a superconducting state to normalize the trace at 25 mK. In practice, when the metal is not in a superconducting state, the resonator is way too lossy to show any resonance feature in S_{11}. So, in theory we only measure the microwave background. We see in Fig. 4.8 that normalizing with such a trace allows to reduce the magnitude and phase wiggles such that it is possible to guess a resonance peak in the magnitude around 6.4 GHz. Nevertheless, we see that the microwave background is not perfectly suppressed. This might come from the aluminum microbonds transiting as well to a superconducting state between the two measurements. This induces an impedance modification that is not corrected by the trace at 1.1 K. The change in temperature might

also slightly change the impedance of the other elements on the 35 and 25 mK stages of the dilution fridge.

4.3.1.b Circle fit method

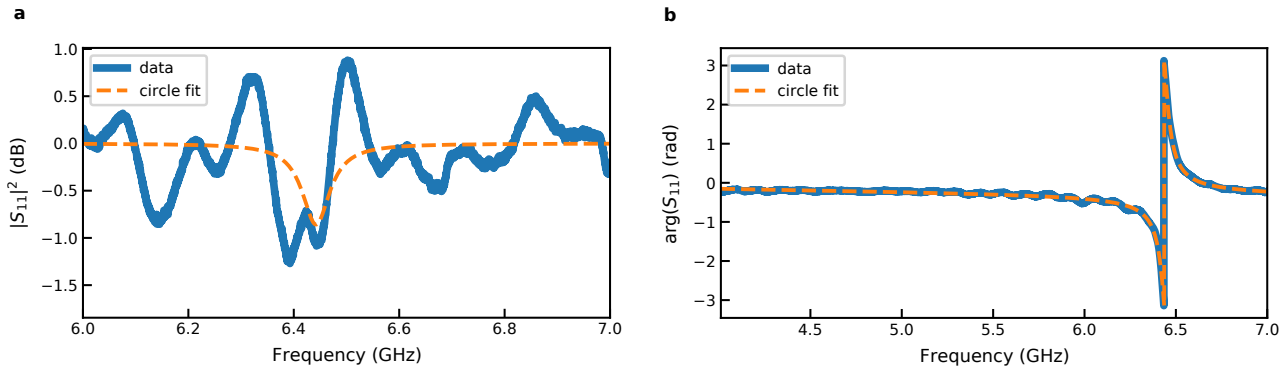

Figure 4.9: Magnitude (a) and phase (b) of the normalized S_{11} parameter and corresponding fit obtained by the circle fit method. The environment amplitude term a has been removed from the amplitude in order to have $|S_{11}| = 0$ dB when the wave is fully reflected.

After the normalization method, we used a fitting method to extract the interesting parameters of the device. We showed in Sec. 4.1.3.b that the S_{11} parameter of a capacitively coupled $\lambda/2$ resonator can be written as:

$$S_{11}^{\lambda/2}(\omega) = 1 - \frac{2Q_l/Q_c}{1 + 2iQ_l\frac{\omega-\omega_0}{\omega_0}} \tag{4.30}$$

where ω_0 is the resonant angular frequency, Q_c the coupling quality factor, Q_l the loaded quality factor such that $Q_l^{-1} = Q_i^{-1} + Q_c^{-1}$, where Q_i is the internal quality factor. In practice, we have to take into account the environment effect by multiplying the ideal $S_{11}^{\lambda/2}$ by a complex term and by taking a complex coupling quality factor $|Q_c|e^{-i\phi}$ [159]:

$$S_{11}(\omega) = ae^{i\alpha}e^{-i\omega\tau}\left[1 - \frac{2(Q_l/|Q_c|)e^{-i\phi}}{1 + 2iQ_l\frac{\omega-\omega_0}{\omega_0}}\right] \tag{4.31}$$

where a takes into account a modification of the amplitude, α quantifies a phase offset and τ an electronic delay happening because the microwaves do not propagate at infinite speed in the cables. We point out that this expression is derived for a notch type resonator (a capacitively coupled resonator to a two ports transmission line) which is not the case here. Especially the complex quality factor with a phase ϕ accounts for a asymmetric coupling at the port 1 and 2 of the transmission line. Here we have a one port circuit so we should have $\phi = 0$.

To fit the data with Eq. 4.31 we used the circle fit method [160]. This method has been shown to be robust to fit noisy S_{11}. It is based on the fact that S_{11} form a circle in the complex plane whose diameter and position are linked to the fitting parameters. We used the code

circle_fit2019 released be the authors of [160] to perform the fit. Fig. 4.9a and b show the amplitude and the phase of the S_{11} parameter and the corresponding fit. We can see that the phase is very well fitted allowing to extract Q_c precisely: $Q_c = 101 \pm 1$. Because the microwave background oscillations have a weight comparable to the resonance peak, the magnitude fit is less accurate making the estimation of Q_i less accurate too: $Q_i = 2.1 \text{ x } 10^3 \pm 2 \text{ x } 10^2$. The difficulty of extracting Q_i comes from the fact that the loaded quality factor is dominated by Q_c which is way smaller than Q_i. In order to get a more accurate estimation of Q_i we performed additional measurements on notch type resonators where $Q_c > Q_i$. Depending on the device we got internal quality factors ranging between 2000 and 10000 which is coherent with what we got from the bare device circle fit. Finally we extracted a bare resonance frequency $f_0 = 6.44$ GHz. The measurement of the bare device allowed thus to extract important parameters for the gJPA. We can see that the simulations predicted accurately the bare resonance frequency and the absence of the resonant features below the first mode of the resonator which will be essential when the g-JPA will be tuned at lower frequency. We note that the predicted quality factor is higher in the real device than in the simulation. In fact, from the width at half maximum, we extracted a quality factor of 70 in the case of the simulation. As we will see later in this chapter, it might come from an unexpected oscillation behavior of the coupling quality factor with respect to the resonance frequency of the circuit.

4.3.2 DC devices for critical current and gate tunability characterization

4.3.2.a Room temperature DC measurement

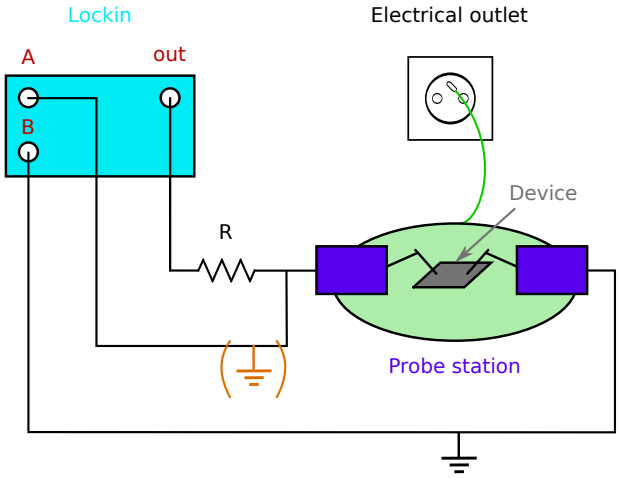

Figure 4.10: Measurement setup to test the device integrity at room temperature before cooling down. The metallic plate holding the device substrate is grounded by connecting it to the grounding pin of an electrical outlet. The orange ground in bracket is removed once the left probe is in contact with the device.

Before cooling down any device with a gJJ, we performed basic room temperature DC measurements to verify the device integrity. This step is important because in case there is a problem with the device, we can know it before cooling down the fridge allowing to save time and resources. Particular caution must be taken during this step because gJJs are extremely

sensitive to electrostatic discharge such that it is very easy to destroy them if grounding is not made carefully. Fig 4.10 shows the experimental setup used to perform room temperature DC measurement. It is a 2 probes current bias experiment made with a lockin and a probe station under a binocular microscope. The user must always be grounded when touching the setup. The plate carrying the probes and on which the sample is deposited is grounded by connecting it to the grounding pin of an electrical outlet. An additional ground is connected after the resistor (orange) when we put the probes in contact with the sample. This ground is then removed to allow the current to flow in the device. By doing that, both the probes are grounded when put in contact with the sample. We use a 1 or 10 MΩ resistor and bias with 10-100 mV such that the bias current is 10-100 nA. The differential resistance of a working device ranges between a few hundred Ohms to two thousand Ohms. We also measure the differential resistance between the side gate and each side of the gJJ in order to check if the gate is not shorted. Typical values range between 20 and 30 kΩ because the intrinsic silicon is not insulating at room temperature.

4.3.2.b Critical current and tunability

The critical current is a crucial parameter because it fixes the Josephson inductance and thus the nonlinearity of the device as shown in Chapter 2. Before making gJPAs, we had to make sure that the critical current for a given junction width was high enough to have a sufficiently low nonlinearity. Moreover, we had to make sure that a side gate was able to control the carrier density well enough in order to have a good critical current control. In this prospect we fabricated pure DC devices, i.e. devices without a resonator and only gJJs connected to DC pads with a side gate. We tested two different metals for the superconducting contacts: Ti/Al with a low superconducting gap ($\approx 200\ \mu$eV) implying a large coherence length, and sputtered MoGe, a disordered superconductor with a large superconducting gap (> 1 meV) implying a smaller coherence length. Fig. 4.11a and b show DC devices with Ti/Al and MoGe superconducting contacts respectively. When the encaspuslated graphene was big enough, is was possible to create several gJJs from the same stack.

The measurement of the DC devices was done in the small Diluette fridge at a base temperature of ≈ 100 mK. The measurement setup is the same as the DC measurement setup in the sionludi L but with additional low pass filters at low temperature. It consists of a two probes current bias experiment where a small AC probe current (17 Hz) is sent together with a DC bias current I_b. Fig. 4.11c and d show the differential resistance $\mathrm{d}V/\mathrm{d}I$ measured by the output of the lockin amplifier with respect to the DC current bias and gate voltage V_g for a Ti/Al device and a MoGe device respectively. We can see dark areas where the differential resistance vanishes meaning that the device is in the superconducting state. When the bias current goes above a threshold value, the device starts to be resistive, meaning that it is no longer in the superconducting state. This value of current is called the switching current: the current at which the device switches from a superconducting to a normal state. We can see that the switching current is not the same at negative bias and at positive bias especially for the MoGe device. We will discuss the possible reasons later in this section.

In this work, we define the critical current I_c of the gJJ being the maximal switching current for a given gate voltage, i.e. the value of the switching current measured when the device switches from the superconducting to the normal state. We can see in Fig. 4.11c and d

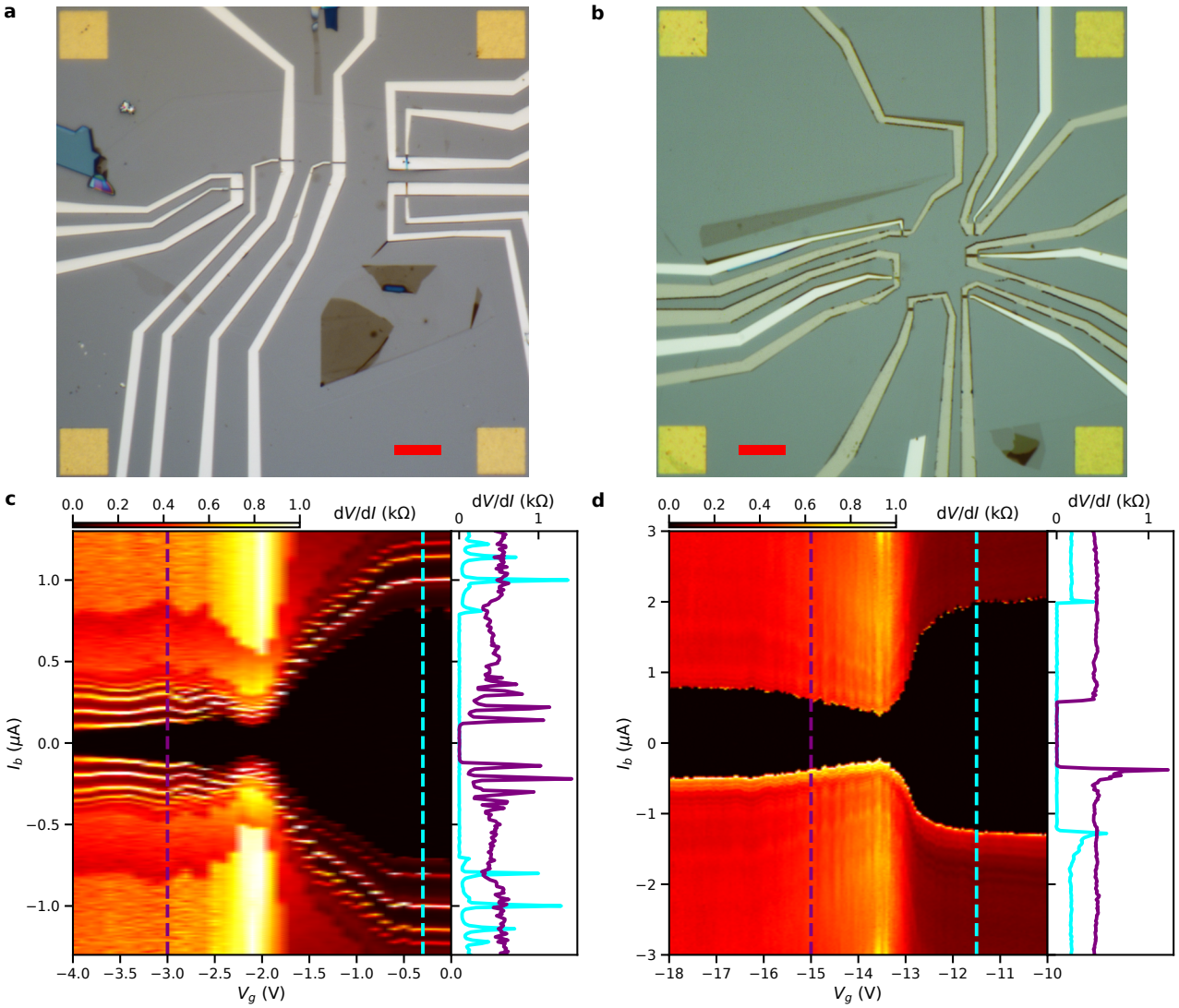

Figure 4.11: (a) and (b) optical microscope picture of DC devices with superconducting contacts made of Ti/Al and MoGe respectively. Each DC device consists of a gJJ with a side gate (5 devices in (a) and 6 devices in (b)). The red bar indicates 8 μm. (c) and (d) differential resistance of a Ti/Al and a MoGe device respectively. The wire resistance has been subtracted such that the differential resistance is zero when the device is in the superconducting state. The bias current is swept from negative to positive for each gate voltage. Cyan and purple linecuts are plotted on the right of the 2D graphs.

that the critical current reaches 0.8 μA for the Ti/Al device and 2 μA for the MoGe device. By considering the device quality and contact transparency as equal between the two devices, and by neglecting the SNS junction specificity, it is possible to understand why the MoGe device has a bigger critical current. According to the Ambegaokar-Baratoff formula [27], at $T = 0$:

$$I_c R_N = \frac{2\Delta}{e} \tag{4.32}$$

where R_N is the normal resistance. This means that for the same normal resistance, $\Delta_{MoGe} \approx 1$ meV $> \Delta_{Ti/Al} \approx 0.2$ meV implies a bigger critical current for MoGe devices. Note that the Ambegaokar-Baratoff formula is working only for tunnel junctions, but we saw in the Chapter 1 that similar expressions exist depending on the regime of the SNS junction. We can conclude from the DC devices that both MoGe and Ti/Al give critical current of the order of 1 μA which is typically used for parametric amplification [88].

Fig. 4.11c and d also show that a side gate allows to tune the critical current on almost one order of magnitude. As we saw in Chapter 1, increasing the doping in the graphene, i.e. reducing its normal resistance, will increase its critical current. The electric field created by the side gate only penetrates the graphene flake locally such that the carrier density is modified only in a portion of less than 500 nm on the edge of the junction [161]. We can thus consider the junction as two parallel sections, one being doped by the side gate with a 500 nm width, and one being at the native doping with a width equals to W minus 500 nm where W is the total width of the gJJ. Therefore, the section with the smaller resistance dominates the behavior of the gJJ. For example, it is always possible to increase the critical current with the side gate because the associated section resistance is made low and thus dominates the behavior. But it is harder to reduce the critical current, because when increasing the resistance of the gate controlled section, it no longer dominates the total resistance because the other section will have a lower resistance. It shows that it is important to have low native doping in order to have more control over the critical current.

The asymmetry of the critical current between negative and positive gate doping is always seen in gJJs. The Fermi level mismatch between the electrodes and graphene induces local electron doping close to the contacts. Thus, when the gate induces a positive doping in graphene, it forms a *n-p-n* junction [32]. As a result, the resistance of the gJJ is higher for positive doping than for negative doping. And as we saw previously, the critical current is scaling as $1/R_N$ explaining the asymmetry. We can also note in Fig. 4.11c that the differential resistance shows intense peak features with respect to the bias current at fixed gate voltage. Theses peaks are attributed to multiple Andreev reflections (MAR) that were presented in Chapter 1 [28, 162]. The fact that the intensity of these peaks is way stronger in the Ti/Al device might come from the fact that the coherence length in Ti/Al device is higher than in MoGe device because of the superconducting gap difference. This means that electrons and holes will lose coherence faster in MoGe devices leading to a less pronounced effect.

We now come back to the asymmetry in the switching current. It can have two possible origins: an increase in the electronic temperature or a junction in the underdamped regime. During the experiment, the bias current is swept from negative to positive values. By doing so, when the measurement starts, the device is in a normal state because $I_b > I_c$, meaning

that heat is dissipated due to Joule effect. This is locally heating the device, increasing the temperature of the electrons inside the gJJ, and in turn reducing the switching current [163]. This could be the reason why at negative bias current, the switching current is lower than at positive bias current, where the device switches from a superconducting state to normal state, meaning that no heating was done before the switch. Another reason would be that the junction is in the underdamped regime. A Josephson junction can be described by the resistively and capacitively shunted junction (RCSJ) model. In this model, the junction is shunted by a resistor R and capacitance C. When computing the voltage current relation there are two possible regimes depending on the Stewart-McCumber parameter $\beta_c = \frac{2\pi R^2 C I_c}{\Phi_0}$ where Φ_0 is the flux quantum. If $\beta_c << 1$, the junction is in the underdamped regime which shows hysteresis behavior in the switching current. For a typical resistance of 200 Ω and a critical current of 1 μA one find that $\beta_c = 1$ will be obtained for $C \approx 10^{-14}$ F. The difficulty is to know what are the contributions to the capacitance. In practice, the small size of the junction makes its capacitance to be way lower than femto Farads. But the capacitance of the leads might also have an effect on the capacitance that we have to consider in the model [68]. We can estimate the capacitance of the DC device by approximating it as a l = 5 mm long microstrip line with a width of w = 75 μm (approximation close to the geometry and dimensions of the device) such that [164]:

$$C = \frac{\epsilon_r l}{60c \ln(\frac{8h}{w} + \frac{w}{4h})} \tag{4.33}$$

where h = 275 μm is the thickness of the substrate, c the speed of light in vacuum and ϵ_r = 11.9 the relative permittivity of intrinsic silicon. We find $C \approx 10^{-14}$ F which corresponds to $\beta_c \approx 1$. So, if we consider that the whole capacitance of the device must contribute, the junction might be indeed in or close to the underdamped regime. The fact that the effect is stronger in MoGe devices where the critical current is higher than for Ti/Al devices let us think that the hysteresis is more a temperature effect because higher power is dissipated. But the fact that the critical current is higher means that β_c is higher too, making the junction more likely to be in the underdamped regime.

The DC devices allowed to see that the critical current measured on both Ti/Al and MoGe devices is suitable for parametric amplification purposes and that the side gate allows a good control of its value. Because of a lack of time we could not test the two materials for the fabrication of gJPA and we finally chose to use Ti/Al. The fabrication of the devices is indeed easier with metal evaporation of Ti/Al than with MoGe sputtering (especially during the lift off). Moreover, the smaller superconducting gap of Ti/Al ensure the junction to be in the short regime. As shown in Chapter 1, this helps to reduce the number of Andreev bound states inside the junction which are held responsible for microwave dissipation in gJJs.

4.4 Characterization of the parametric amplifier in the linear regime

We will now focus on the characterization of the gJPA itself in the linear regime, i.e when the incoming power is low enough to neglect the non linear effects coming from the junction.

The device presented here corresponds to a gJJ width of 1.5 μm and was measured in the Sionludi L dilution fridge.

4.4.1 Gate tunability

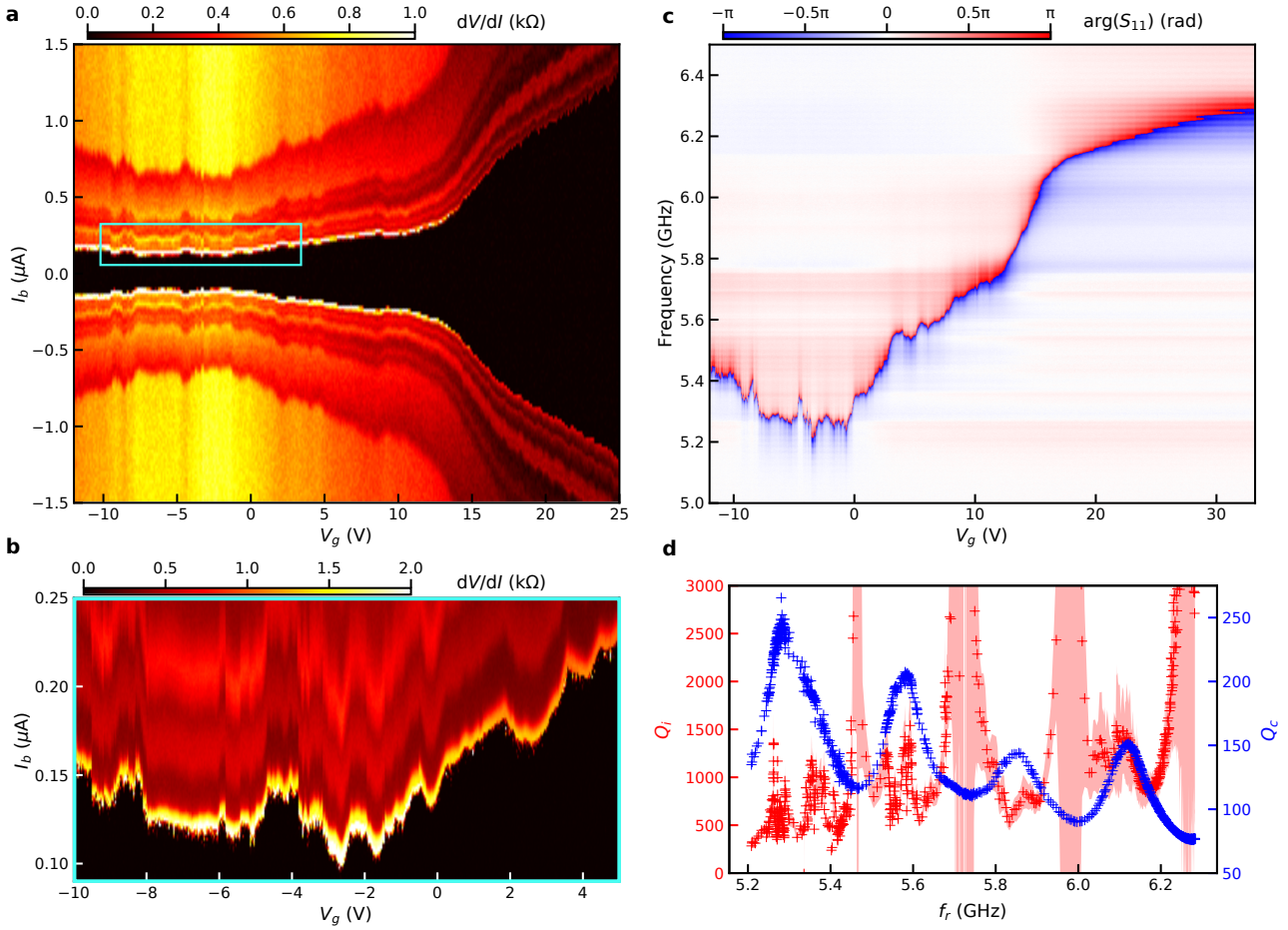

Figure 4.12: (a) Measurement of the differential resistance with respect to the bias current and gate voltage. For each gate voltage the bias current was swept from negative value to positive value. The resistance of the wires was subtracted such that the resistance of the device vanishes in the superconducting state. The blue rectangle shows the area where we did a more precise measurement shown in (b). (c) Phase of the S_{11} parameter with respect to the gate voltage and input microwave frequency. The input microwave power was $\approx$ -140 dBm such that non linear effects can be neglected. (d) Fitted coupling (blue) and internal (red) quality factors with respect to the fitted resonance frequency. The red shaded area corresponds to the standard deviation error on the internal quality factor given by the fit.

Fig. 4.12a and b shows the differential resistance of the device with respect to the gate voltage and bias current. We can see that the critical current is tunable from 100 nA up to more than 1.3 μA. The critical current is minimum near V_g = -3 V corresponding to the Dirac point of graphene where the normal resistance is maximum. We could not go at lower gate voltages because below V_g = -12 V, a gate leakage current was observed. As we saw earlier,

the critical current of the device is compatible with parametric amplification purposes.

Fig. 4.12c shows the phase of the S_{11} parameter with respect to the input microwave frequency and gate voltage. For each gate voltage, we swept the microwave frequency and measured the S_{11} parameter. As for the bare device, the resonance corresponds to a 2π phase shift because the resonator is overcoupled. The limit between the red and blue part of the 2D map corresponds thus to the resonance frequency of the device. As we saw earlier, changing the critical current allows to change the Josephson inductance L_J such that the resonance frequency of the resonator changes. We can indeed see that when the critical current is large (corresponding to a small L_J) on Fig. 4.12a, the resonance frequency $f_r \approx 6.2$ GHz is close to the bare resonance frequency $f_0 = 6.44$ GHz of the device without a gJJ. And when the critical current reaches its minimal value at the Dirac point (maximum of L_J), the resonance frequency is minimal: $f_r \approx 5.2$ GHz. Thanks to the control of the critical current with a gate voltage, we have a 1 GHz tunability of the resonance frequency.

Fig. 4.12c allows to create a normalization procedure to remove the microwave background. In the case of the bare resonator we used a trace at 1.1 K before the device transited to a superconducting state. Here, in order to avoid the impedance mismatch created by the aluminum microbonds becoming superconducting, we averaged the S_{11} parameter measured between -4.5 V and 18 V, corresponding to the gate voltages at which $\partial f_r / \partial V_g$ is the highest. By doing so, we averaged out the resonance features and obtained a microwave background cleaner than the one obtained by using at trace at 1.1 K. Fig. 4.12c was itself normalized with this method.

We performed the circle fit method on the S_{11} trace measured at each gate voltage. This allowed to extract the resonance frequency and the coupling quality factor for each gate voltage. Fig. 4.12d shows the fitted coupling (blue) and internal (red) quality factors with respect to the fitted resonance frequency. We can see that the coupling quality factor oscillates between 75 and 250. We did not simulate the effect of the Josephson inductance on the coupling quality factor and it is not clear why an oscillation behavior appears. It might come from the impedance of the environment changing with respect to the frequency. We see that the coupling quality factor decreases with the resonance frequency which is expected because Q_c scales as $1/f_r^2$. As for the bare resonator, it is difficult to extract the internal quality factor because $Q_i > Q_c$. The error is computed only by comparing the fit to the data altered by the microwave background. We can imagine a situation where a decent fit is obtained, but where the resonance dip amplitude is mostly due to the microwave background. This would create a small error but the extracted Q_i would be far from the real value. Therefore, the computed error is shown as an indication but is not trustful. We can see a correlation between the coupling quality factor and the error on the internal quality factor. When the coupling quality factor decreases, the error on Q_i increases because the ratio Q_i/Q_c gets higher making the fit more difficult. It is hard to rely on the extracted values of Q_i but it looks like the sample exhibit more loss when the resonance frequency is close to its lowest value, corresponding to graphene being close to the Dirac point. It is not clear why the dissipation increases close to the charge neutrality point. A recent study did not find an increased dissipation at this point [66] but it is hard to extrapolate because the physics depends a lot on the device itself, i.e the size and width, corresponding to different regimes. They used a diffusive Ti/Al device with

a 1 μm width and a width over length ratio of ≈ 2 giving a maximum critical current of $\approx$ 200 nA. In our case the width is 1.5 μm for a width over length ratio > 5 and a maximum critical current of 1.3 μA. The big difference in the critical current for a similar width shows that our junction might be in a different regime (ballistic).

4.4.2 Josephson inductance and current phase relation

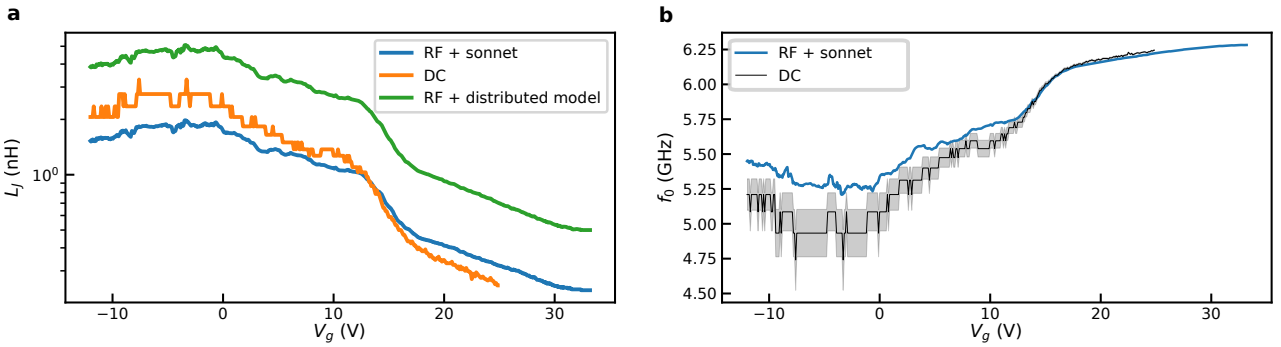

Figure 4.13: (a) Josephson inductance extracted by the critical current measurement (DC) and by the microwave measurement (RF). (b) Resonance frequency extracted by the critical current measurement (DC), and by the fit of the measured S_{11} parameter (RF). The shaded area represents the error on the resonance frequency extracted by DC method.

All the models used to understand the behavior of JPAs developed in Chapter 2 are based on sinusoidal current phase relation (CPR). Nevertheless, we saw in Chapter 1 that gJJs do not to follow an exact sinusoidal CPR and it is thus important to see how it deviates from it. The Josephson inductance L_J of the gJJ is directly linked to the CPR and influences the Kerr coefficient which is a key parameter for parametric amplification. It can be defined as :

$$L_J = \frac{\Phi_0}{2\pi}\left(\frac{\partial I}{\partial \phi}\right)^{-1} \tag{4.34}$$

where ϕ is the phase across the gJJ. In practice, ϕ is small for a weakly driven junction such that

$$L_J = \frac{\Phi_0}{2\pi I_c} \tag{4.35}$$

for a sinusoidal CPR. With the measured critical current we can thus compute L_J and see what would be L_J with a sinusoidal CPR. On the other hand, we measured $f_r(V_g)$, and from the sonnet simulation with a discrete inductance L_J, it is possible to map the measured f_r to the simulated f_r and thus to L_J such that we get the gate dependence of L_J. By comparing L_J obtained from the critical current measurement and from the RF measurement, it is possible to see how the CPR deviates from a sinusoidal form.

We also used another method to extract L_J from the measured $f_r(V_g)$ which is useful to compute the Kerr coefficient. Unlike the lumped element model, this method consists of finding the normal modes of a distributed transmission line resonator with an embedded JJ [83]. We developed this model in details in Chapter 2. The input parameters of this model are the inductance and capacitance per unit of length l_0 and c_0, the coupling capacitance with the

50 Ω transmission line C_i and the bare angular resonance frequency ω_0. C_i can be computed from Eq. 4.22 and the measured coupling quality factor that we approximated to a constant value of Q_c = 150:

$$C_i \approx \sqrt{\frac{\pi}{2Z_0^2\omega_0^2 Q_c}} \tag{4.36}$$

$Z_0 = \sqrt{l_0/c_0}$ being the characteristic impedance of the resonator. Because $Z_0 = \sqrt{l_0/c_0}$ depends on the unknown c_0, we used the total capacitance (C = 0.157 pF) obtained from the lumped model to have an additional equation:

$$C = \frac{x}{2}c_0 + C_i \tag{4.37}$$

where x is the total length of the resonator. By doing so we get an equation on Z_0 with only known parameters:

$$Z_0^2 C - Z_0\sqrt{\frac{\pi}{2\omega_0^2 Q_c}} = l_0\frac{x}{2} \tag{4.38}$$

with l_0 obtained from the total inductance extracted from the lumped element model (L_0 = 3.9 nH):

$$L_0 = \frac{2x}{\pi^2}l_0 \tag{4.39}$$

By solving Eq. 4.38 we find $C_i \approx 10$ fF and $Z_0 \approx 256$ Ω. By using standard calculation for microstrip lines (Eq. 4.25 and 4.26) we find Z_0 = 125 Ω. One reason of such a discrepancy could come from the fact that Eq. 4.25 and 4.26 are valid when the width w of the microstrip line is of the same order of magnitude than the substrate thickness h. Here w = 10 μm and h = 275 μm which is far from the approximation $w \approx h$.

Using the model with the previously obtained parameters allows to compute f_r with respect to L_J. By mapping the measured $f_r(V_g)$ to the model, we can extract $L_J(V_g)$. Fig. 4.13a shows the computed L_J from the DC critical current measurement assuming a sinusoidal CPR (orange), L_J extracted from the microwave measurement and the sonnet simulation (blue), and L_J extracted from the microwave measurement and the distributed model (green). We can see that at high electron doping, L_J extracted by the RF measurement and sonnet is higher than L_J extracted by DC measurement. This is compatible with a forward skewness of the CPR, because a forward skewness for an equivalent critical current means that the term $\frac{\partial I}{\partial \phi}$ is smaller and thus makes L_J higher. This result is compatible with the previous studies about gJJ CPR [59, 61, 66]. On the other hand, below V_g = 12 V it looks like the opposite way. This was also seen in [67] and was attributed to the definition of the critical current that we use. Indeed, we define the critical current as the switching current when the device switches from the superconducting state to the normal state. It means that we give a lower bound on the critical current because the switching current is always impacted by thermal effects for example. When looking at Fig. 4.12c, we can see that the time spent in the normal state is way higher when the critical current is low. This might cause an increase in the electronic temperature which is not decreasing fast enough to be neglected (because the time spent in the superconducting state is low at low critical current). Therefore it could explain why the switching current is smaller than the critical current. Moreover, the DC lines of the sionludi

dilution fridge L used to perform the measurement of the critical current was not equipped with low pass filters thermalized on a cold stage. This results in a the presence of a thermal noise that can also decrease the switching current.

On the other hand, the Josephson inductance obtained by mapping the measured f_r to the distributed model is always higher than the one obtained by the critical current, which is compatible with a forward skewness of the CPR whatever the gate voltage. Nevertheless, it is not clear why L_J is higher than what is obtained with the sonnet simulation. In a 1D SNS point contact JJ, for a fixed critical current, the maximum skewness is achieved for a perfect contact transparency in the zero temperature limit, and leads to a Josephson inductance twice higher than what would give a sinusoidal CPR. We thus doubt of the extracted L_J by this method which is higher by a factor ranging between 2 and 2.6 with respect to L_J extracted by sonnet simulations. A possibility would be that the computed L_0 and C from the lumped element model cannot be used for determining l_0 and c_0. The fact that the predicted resonance frequency with the distributed model at very low L_J matches the measured bare resonance frequency indicates that the product of these parameters must be correct, but that they might differ individually. In the distributed model, the DC lines are not taken into account, but we performed similar sonnet simulation without the DC lines and it is not enough to explain the difference (at best there is a 0.5 nH increase). We also used the distributed model with different coupling capacitance C_i because we assumed above that the quality factor was constant which is not the case. This was also not able to make the extracted L_J smaller. The computed C_i is such that it is negligible compared to the total capacitance C. Decreasing C_i does not change the extracted L_J but increasing C_i increases the extracted L_J. So, the high value of L_J are not caused by a problem on the estimated coupling capacitance.

Fig. 4.13b shows the predicted resonance frequency from the DC measurement (by injecting the computed L_J from the critical current measurement in Eq. 4.28) and the fitted resonance frequency from the RF measurement with respect to the gate voltage. We can clearly see that there is a correlation between the DC and RF measurements proving that the resonance frequency variation is caused by a variation in the critical current and thus in L_J. At high electron doping the difference in inductance between DC and RF does not affect a lot the resonance frequency because L_J is negligible compared to L_0 = 3.9 nH. On the other hand, the difference has a stronger effect when L_J gets closer to L_0.

The Josephson inductance and resonance frequency extracted by the DC method shows some abrupt variation close to the charge neutrality point where the critical current is low. This comes from the fact that the critical current measurement used to compute these values was done by sweeping the bias current with steps of 20 nA, meaning that the extracted critical current is a multiple of this value. This step size is not negligible compared to 100 nA, the minimum critical current, and explains the discrete jumps in L_J and f_r. We used Eq. 4.29 and 4.35 to compute the error Δf_r on the resonance frequency considering only the error on the critical current ΔI_c being 20 nA (the bias current step):

$$\Delta f_r = \frac{f_0 \phi_0}{4\pi L_0 I_c^2} \left(1 + \frac{\phi_0}{2\pi L_0 I_c}\right)^{-\frac{3}{2}} \Delta I_c \tag{4.40}$$

4.4.3 Estimation of the Kerr coefficient

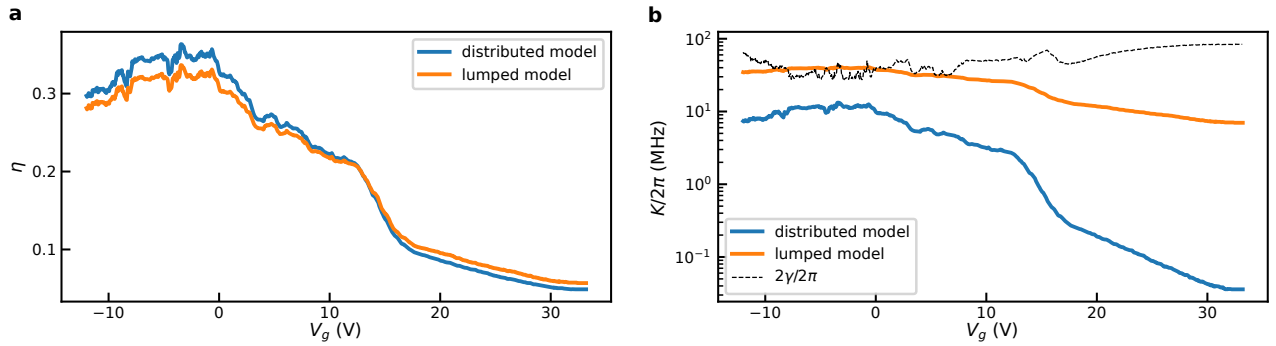

Figure 4.14: (a) Computed participation ratio with respect to the gate voltage. The orange curve is obtained by using L_J extracted from the RF measurement associated with sonnet simulations and using the lumped equation of η. The blue curve is obtained with the distributed model. (b) Kerr coefficient computed from η obtained in (a). The distributed model accounts for a correction on the total capacitance making K smaller. The energy damping rate 2γ is computed from the fitted Q_l.

With the determination of L_J it is possible to estimate the Kerr coefficient:

$$K = E_C \eta / \hbar \tag{4.41}$$

where $E_C = e^2/(2C)$ is the charging energy and η is the participation ratio of the gJJ. By taking the lumped element model we built for the device, we can express η as:

$$\eta_{lumped} = \frac{L_J}{L_J + L_0} \tag{4.42}$$

In the distributed model discussed in the previous section, η can also be computed and is corrected by a factor $(\Delta u)^2$ where Δu is the flux mode amplitude envelop difference across the JJ (see Chapter 2). Fig 4.14a shows the computed η from the distributed model and from L_J and L_0 obtained from a lumped model by associating sonnet simulations and measurements. We can see that the participation ratio is very similar between the two models despite the distributed model giving higher L_J. This comes from the fact that η is corrected by $(\Delta u)^2$:

$$\eta_{distributed} = \frac{L_J L_0}{L_J + L_0} \frac{1}{L_J} (\Delta u)^2 \tag{4.43}$$

Note that in the distributed model, the junction is in parallel with the rest of the circuit justifying the difference between the definition of $\eta_{distributed}$ and η_{lumped}.

We can now compute K thanks to Eq. 4.41. In the distributed model, the total capacitance is corrected by a factor $1/(\Delta u)^2$ as shown in Chapter 2. The total expression of K in this model is thus:

$$K = E_C \frac{L_0}{L_J + L_0} (\Delta u)^4 \tag{4.44}$$

Fig 4.14b shows the computed K from the distributed model and from L_J and L_0 obtained from a lumped model by associating sonnet simulations and measurements. We can see that K estimated with the distributed model is always smaller than the one estimated with the lumped model especially at higher gate voltages. Indeed, at higher gate voltages, the inductance of the JJ is smaller making the jump in the flux mode amplitude envelop across the JJ (Δu) smaller resulting in an important decrease of K. It is hard to trust fully the distributed model because we saw that the Josephson inductance estimated this way is probably too high. Nevertheless, we saw that the correction factor $(\Delta u)^2$ specific to the distributed model on η allowed to obtain similar participation ratio than the lumped model associated with sonnet simulation. This let us think that the distributed model can be trusted here. Knowing that $\Delta u < 1$, the values obtained by the lumped model are an upper limit of the real K.

The values of K have to be compared to the total energy damping rate 2γ in order to predict the behavior of the JPA. Indeed, we saw in Chapter 2 that the dynamic was dependent on the ratio K/γ meaning that when this ratio is high, the compression point is low, which is a problem in the limit where less than one photon can be amplified without reducing the gain. From the fitted Q_i and Q_c we can compute the loaded quality factor $Q_l^{-1} = Q_i^{-1} + Q_c^{-1}$ for each gate voltage and thus compute γ:

$$\gamma = \frac{\omega_r}{2Q_l} \tag{4.45}$$

We can see in Fig 4.14b that close to the charge neutrality point, both models predict a value of K close to 2γ meaning that the compression point of the JPA will be low. On the other hand, the lumped model predicts a ratio K/γ close to one on the whole gate voltage range whereas this ratio decreases drastically in the distributed model. The fact that the nonlinearity is diluted with the geometric inductance can also be a problem for the stability of the JPA as shown in Chapter 2.

4.4.4 I_cR_N Product

The I_cR_N product is often used as an indicator of the quality of a Josephson junction. It has been predicted for a short ballistic gJJ without defects that $eR_NI_c/\Delta \approx 2.5$ where Δ is the induced superconducting gap [51]. In order to extract Δ, we analyzed the differential conductance with respect to the voltage across the gJJ (V_b). Experimentally we performed a current bias experiment, we did thus not have a direct access to V_b. We extracted V_b using the total voltage measured with a multimeter and subtracting the bias current times the resistance of the wires. We show in Fig. 4.15a the differential resistance with respect to the bias current and the associated bias voltage. When the device is in the superconducting state ($dV/dI = 0$), we see that the voltage vanishes as expected for a JJ. By combining these two sets of data we plotted the differential conductance dI/dV with respect to the bias voltage in Fig. 4.15b. In a SNS Josephson junction, multiple Andreev reflections (MAR) manifest themselves as peaks in the differential conductance at voltage values equal to $2\Delta/n$ where Δ is the induced superconducting gap and n integer values [28]. From the n=1 peak we can extract an induced gap Δ=147.5 μeV. Fig. 4.15c shows the normal resistance of the gJJ at 25 mK with respect to the gate voltage measured with a bias current I_b=7 μA such that $I_b >> I_c$. As expected for graphene, the resistance profile shows a maximum at the charge neutrality point

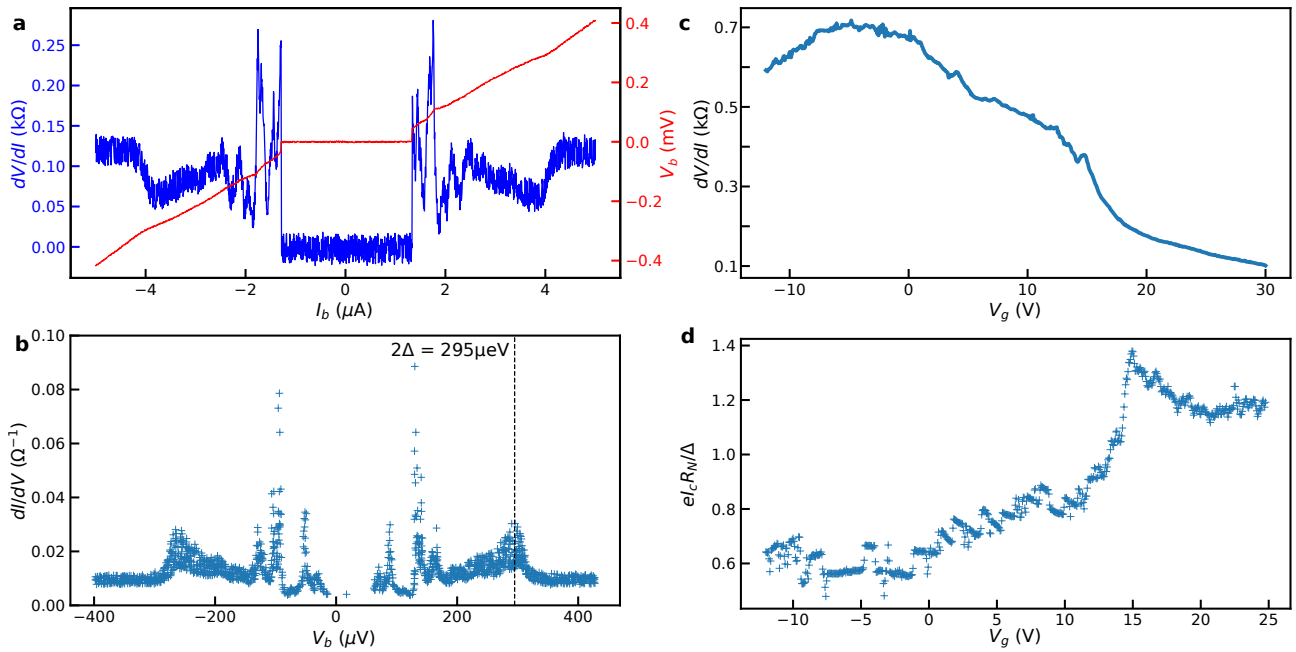

Figure 4.15: (a) Two-probes measurement of the differential resistance (blue) and voltage (red) across the gJJ with respect to the bias current at V_g = 25 V. We subtracted the resistance of the wires. (b) Differential conductance with respect to the voltage across the gJJ. The dotted line indicates the position of the first conductance peak at a voltage $2\Delta/e$. (c) Normal resistance of the gJJ with respect to the gate voltage at 25 mK measured at $I_b = 7\ \mu A$. We subtracted the resistance of the wires. (d) I_cR_N product in induced superconducting gap unit with respect to the gate voltage. The induced superconducting gap is extracted from (c) and is approximated as independent of the gate voltage.

at $V_g \approx$ -3 V which is consistent with the value extracted by the critical current measurement. The important broadness of the peak is explained by the low efficiency of the side gate. The measured dV/dI (=R_N) and critical current enables to plot the eR_NI_c/Δ product with respect to the gate voltage in Fig. 4.15d. We see that the product reaches 1.4 and decreases close to the Dirac point which is generally observed in gJJ [32]. The high eR_NI_c/Δ product indicates the high quality of the device. To my knowledge, the best eR_NI_c/Δ product in a diffusive gJJ that we can find in the literature is of the order of unity. This means that our gJJ is probably ballistic with a coherence length $\xi = \hbar v_F/\Delta \approx 4.5\ \mu$m making the junction in the short regime. The fact that a side gate is used to change the doping might limit the maximum value of the eR_NI_c/Δ product because the charge carrier concentration is not homogeneous in the junction. Moreover, we supposed the superconducting induced gap as constant with respect to V_g which is probably not accurate. Another analysis suggesting the high transparency of the gJJ in presented in Appendix A.

4.4.5 Gate instability

By using the gate on the device, we noticed some effects that we attribute to charge fluctuations and trapping, and also to the use of a side gate. The first noticeable effect is a different behavior when sweeping the gate voltage from positive to negative voltages and the opposite

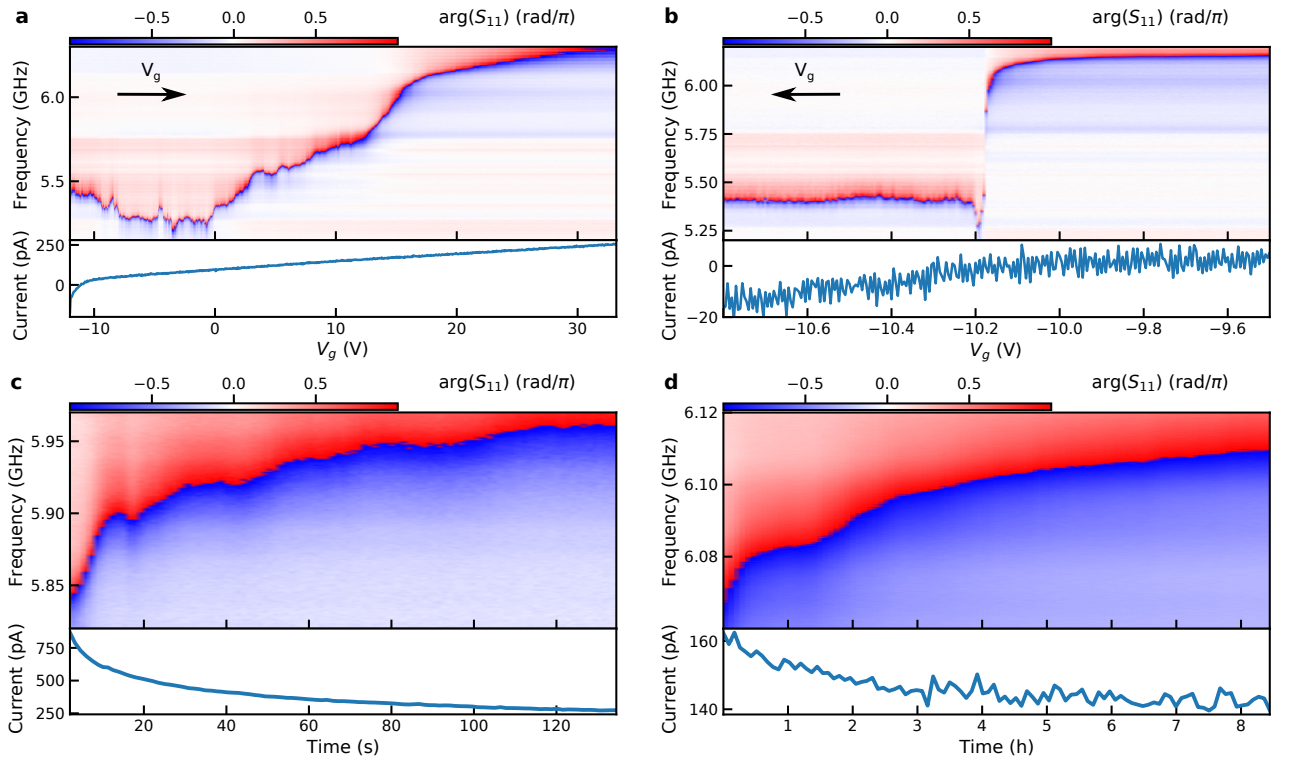

Figure 4.16: Phase of S_{11} with respect to the gate voltage when sweeping the gate from negative to positive voltages (a) and positive to negative voltages (b). Phase of S_{11} with respect to time on a short (c) and a long (d) timescale. (c) is taken right after a voltage sweep from -12 V to 17.5 V with a speed of 0.17 V.s^{-1}, (d) is taken a few minutes after (c). The gate leakage current is plotted beneath each graph.

way. In Fig. 4.16a and b, we plot the phase of S_{11} when sweeping the gate voltage from negative to positive values (a) and positive to negative values (b). We see in Fig. 4.16a that gating in this direction allows a precise control of the resonance frequency (corresponding to a 2π phase shift). On the other hand, gating in the other direction (Fig. 4.16b) shows little effect until an abrupt change around V_g = -10.2 V. All the measurements relying on a gate presented in this work were taken in the configuration of Fig. 4.16a, i.e. sweeping from negative to positive gate voltages.

We also plotted the current leaking from the gate in the bottom panel of Fig. 4.16a and b. We can see that in Fig. 4.16a a small leakage current of 250 pA at $V_g > 30$ V with a linear slope corresponding to a resistance of 20 GΩ. It is also possible to see that the leakage current increases exponentially close to V_g = -12 V forbidding lower gating. It was shown that gating current leakage can be responsible for reduction of the critical current in narrow superconductor constrictions. High energy electrons can tunnel from the gate contact to the constriction, resulting in quasiparticle generation that can reduce the critical current [165, 166]. We argue that this mechanism is negligible hear because we are able to increase the critical current (associated to an increase of f_r) even if the gate current leakage increases. Moreover Fig. 4.16b shows that there is no correlation between the gate current leakage and the abrupt change in the resonance frequency. The gate leakage is probably due to

standard gate leakage mechanisms as Frenkel-Poole transport through the Si substrate or Fowler-Nordheim tunneling [167].

The second effect is an evolution of the resonance frequency as a function of time after a gate voltage sweep. In Fig. 4.16c and d, we plotted the phase of S_{11} with respect to time for a fixed gate voltage. Fig. 4.16c was taken right after a large gate sweep (parameters in the description of the figure) and Fig. 4.16d a few minutes after the gate sweep. We see in Fig. 4.16c a resonance frequency shift of more than 100 MHz in 2 minutes. The shift is faster during the first seconds and is associated with a high leakage current (up to 750 pA). In Fig. 4.16d we see that the drift continues even over hours but on a slower pace. We noticed that the speed of the drift depends on the speed of the gate sweep leading to the gate voltage of interest. By looking at the gate leakage current, we see a correlation between the speed of the frequency shift and the intensity of the current. We argue that the gate leakage current is created by some charge reorganization in the gJJ (leading to the associated change in resonance frequency or equivalently critical current) and not the opposite. In the previous paragraph describing the 'adiabatic' case where the gate is swept very slowly, the charges had enough of time to reorganize while the measurement of a single gate was performed. This explains why in this case, a change in the resonance frequency is not correlated with a gate leakage current.

We also noticed that the time frequency shift was more intense for gate voltages at which f_r is more sensitive to V_g. For example, it is more important between V_g = 10 V and V_g = 18 V making the JPA less stable in the associated frequency range. In order to limit the drift and to obtain reproducible datasets, we swept the gate voltage very slowly and waited after each gate change. For instance in Fig. 4.16a, we used the following parameters: a gate voltage step of 0.05 V and a S_{11} trace time of 75 s for each gate voltage.

In the future, we believe that the use of a top (or bottom) gate should allow to suppress those effects. It will indeed be much more efficient than the side gate presented here, allowing the use of smaller voltages, and also screening charges in an efficient manner. Interestingly, recent experiments of Nicolas Aparicio, a PhD student in our research team, showed that the hysteresis on the critical current is reduced for narrow gJJs (width < 500 nm). Narrower gJJ are fully penetrated by the gating electric field, indicating that the hysteresis behavior might come from the charging of areas not directly affected by the gate voltage.

4.4.6 Summary of the parameters of the gJPA

We showed that the device resonance frequency can be tuned in a frequency range going from 5.2 to 6.3 GHz and that the presence of DC lines does not affect the resonance. The comparison of L_J extracted from DC measurement and RF measurement showed evidence of a forward skewness of the CPR which indicates that JPA models based on a sinusoidal CPR might lose accuracy. Calculations in Appendix A show that the skewness can be estimated to 0.2. Moreover, the quality factor of the device depends on the gate voltage such that the loaded quality factor ranges between 75 and 200. From the estimation of the Josephson inductance, we could deduce the participation ratio η of the gJJ. The estimations given by the lumped model and the distributed model are very close and give a participation ratio

ranging between 0.05 and 0.35. This satisfies the condition $\eta Q >> 1$ needed to keep the microwave current small enough compared to the critical current which avoids chaotic behavior [98, 93, 90] as we saw in Chapter 2. We note that at high electron doping, the product ηQ reaches a minimal value of 4 which does not exactly satisfies the condition. We also computed the values of K and compared them to the total energy damping rate 2γ. This allowed to see that the compression point of the gJPA should be low close to the charge neutrality point but should increase at higher electron doping.

Graphene based Josephson parametric amplifier

CHAPTER 5

In this chapter we present the main results about the graphene based Josephson parametric amplifier (gJPA). We first show the nonlinear behavior of the device and the limits of the theoretical model. We then address the amplifier key characteristics: the gain, the added noise and the compression point.

Contents

5.1 Nonlinear resonator

5.1.1 Model to describe the gJPA

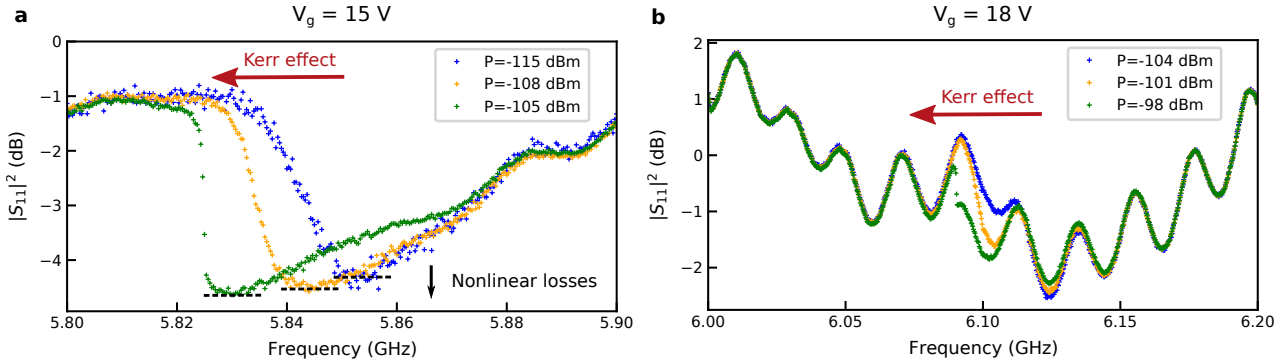

Figure 5.1: (a) and (b) Magnitude of the S_{11} parameter with respect to the input frequency at different input powers for a gate voltage of 15 V and 18 V respectively. The measurement were taken with a VNA by making a frequency sweep and then changing the power. In both (a) and (b) the blue curve corresponds to $P << P_c$ and the green curve to $P = P_c$. Both (a) and (b) were normalized with an average of the gate dependence of S_{11} at low power. The red arrows shows the negative frequency shift due to Kerr effect. The black arrow and dotted lines show an increase in the resonance dip amplitude corresponding to nonlinear losses.

The presence of the graphene Josephson junction (gJJ) inside the resonator provides nonlinearity. Fig. 5.1 shows the magnitude of the reflection coefficient $|S_{11}|^2$ with respect to the incoming microwave frequency at different incoming microwave powers P. In Fig. 5.1a, the lowest input power (P = -115 dBm) corresponds to the limit where nonlinear effects are negligible. The resonance manifests as a dip in the magnitude around the resonance frequency. We can see that when the input power increases, the resonance frequency shifts toward lower frequencies. This is the Kerr effect happening because of the presence of the gJJ. When the input power reaches the critical power P_c, the derivative of the S_{11} with respect to the frequency diverges in one point such that there is a infinite slope at this point. The green curve (P = -105 dBm) corresponds to the measured magnitude at the critical power. We will call the frequency shift between the low power resonance frequency and the critical power resonance frequency $\Delta\omega_c$. Besides the Kerr effect, we can see that the amplitude of the resonance dip increases with the input power. We saw in the previous chapter that the internal quality factor Q_i is higher than the coupling quality factor Q_c. This means that either the internal losses are increasing or that the coupling is decreasing with increased power. We saw that Q_c depends on the resonance frequency but the shift in Q_c associated to the frequency shift at the critical power is negligible and do not explain the increased resonance dip. Therefore, the only possibility is that the internal loss is power dependent which is also confirmed by the literature in gJJs [67] and is attributed to dynamics in the Andreev bound state as we showed in Chapter 1.

Because of the nonlinear loss, we chose to use the two-photon loss model of Yurke [87] which is the only model of JPAs taking it into account to our knowledge. This model is studied in details in Chapter 2. In this model, the nonlinear loss is proportional to the number

of photons inside the resonator. We will briefly recapitulate the important results that we used to fit our data. The S_{11} parameter can be expressed as:

$$S_{11} = 1 - \frac{2\gamma_1 A}{\left[i(\omega_r - \omega) + \gamma\right] A + (iK + \gamma_3) A^3} \tag{5.1}$$

where A is the intracavity field, ω_r the resonant angular frequency, $2\gamma_1 = \omega_r/(Q_c)$ the coupling energy damping rate, $2\gamma = 2\gamma_1 + 2\gamma_2 = \omega_r/(Q_l)$ the total energy damping rate, $2\gamma_2 = \omega_r/(Q_i)$ the internal energy damping rate, $2\gamma_3$ the two-photon loss energy damping rate and K the Kerr coefficient. In the limit $K = \gamma_3 = 0$, S_{11} does not depend on the intracavity field intensity anymore and is equivalent to S_{11} found with basic circuit theory (Eq. 4.24). The intracavity field A can be found by solving a cubic equation in A^2:

$$A^6 + \frac{2\left[(\omega_r - \omega)K + \gamma\gamma_3\right]}{K^2 + \gamma_3^2} A^4 + \frac{(\omega_r - \omega)^2 + \gamma^2}{K^2 + \gamma_3^2} A^2 - \frac{2\gamma_1}{K^2 + \gamma_3^2} \left(b^{in}\right)^2 = 0 \tag{5.2}$$

where b^{in} is the classical incoming field that we can relate to the incoming microwave power by $b^{in} = \sqrt{P/(\hbar\omega)}$. It is also possible to compute the critical incoming field b_c^{in} at which the device bifurcates:

$$(b_c^{in})^2 = \frac{4}{3\sqrt{3}} \frac{\gamma^3 (K^2 + \gamma_3^2)}{\gamma_1 (|K| - \sqrt{3}\gamma_3)^3} \tag{5.3}$$

and the resonance frequency shift due to Kerr effect at the critical power:

$$\Delta\omega_c = -\gamma \frac{K}{|K|} \left[\frac{4\gamma_3 |K| + \sqrt{3}(K^2 + \gamma_3^2)}{K^2 - 3\gamma_3^2} \right] \approx -\sqrt{3}\gamma \frac{K}{|K|} \tag{5.4}$$

where the last approximation can be done when $\gamma_3 << K$.

The model depends thus on six parameters: ω_r, γ_1, γ_2, γ_3, K and b^{in} making the fit difficult because of the large parameter space. Moreover, as we saw in the previous chapter, microwave background can be non negligible compared to the magnitude of S_{11}. This is particularly a problem for extracting the internal loss because $\gamma_1 >> \gamma_2$. Fig. 5.1a and b have been normalized with an averaged gate dependence of S_{11} as in the previous chapter. Nevertheless, the gate dependence was taken with an additional room temperature 20 dB attenuator such that impedance mismatch is not exactly the same between the power dependence and the gate dependence. We can see in Fig. 5.1b that the amplitude of the resonance dip is small compared to wiggles of the microwave background despite the normalization. In this condition, we barely see the resonance and it is thus very complicated to deduce the internal loss and the two-photon loss. This is why we had to develop a special fitting method in order to get rid of the microwave background.

5.1.2 Fitting methods

Because it was not possible to fit directly the data with all the free parameters for reasons we explained in the previous section, we developed two fitting methods. The first method is the simplest one but is strongly affected by the microwave background. The second one allows to get rid of the microwave background at the cost of making the fitting procedure easily trapped in local minimums, and more sensitive to discrepancies in the model.

5.1.2.a Fitting method 1

This first fitting method does not allow to remove perfectly the microwave background and is thus not ideal to extract γ_2 and γ_3. The first step consists of fitting S_{11} at low power with the circle fit method [160] which allows to remove some environmental contributions and get ω_r, γ_1 and γ_2 with an important error on γ_2 when the internal losses are low. It means that only three parameters have to be found: K, b^{in} and γ_3. b^{in} is not a free parameter as such because it is linked to the input power that we control. We thus compute b^{in} with the experimental input power. Even with only two parameters we had issues for fitting the data and we will show the reasons later. We thus adopted another procedure.

First, we noticed that at the critical power, K can be computed from Eq. 5.3 if γ_1, γ_2, γ_3 and b_c^{in} are known. Therefore we manually picked the critical power from the power dependence on S_{11} by looking at which input power an infinite slope appeared in phase and amplitude. Then, because the change in the magnitude dip with power is only caused by nonlinear loss, we fitted the minimal value of $|S_{11}|$ with γ_3 as only free parameter. During the fitting procedure, K is computed from Eq. 5.3 at each iteration because all the parameters are known. This way of fitting allows to obtain all the parameters but suffer from the fact that it relies on the minimum of $|S_{11}|$ which can be strongly perturbed by the microwave background. For example, in Fig. 5.1b, the minimum does not correspond to the resonance dip amplitude meaning that we would find $\gamma_3 = 0$ Hz.

Fig. 5.2a and b show the measured phase of the S_{11} parameter with respect to the frequency at the critical input power P_c and at low power $P_0 << P_c$ for two different operating frequencies. We can see that for both operating frequencies, the fitted shift in the angular resonance frequency $\Delta\omega_c$ at the critical power is larger than the experimental shift. According to Eq. 5.4, when γ_3 is negligible, $\Delta\omega_c$ depends only on γ, a parameter extracted from the initial circle fit. The discrepancy in $\Delta\omega_c$ means that either the circle fit is wrong or that the model does not describe our system properly.

One could argue that the fitting method 1 does not predict γ_2 and γ_3 accurately as discussed earlier. But according to Eq. 5.4, when γ_3 is not negligible, the shift is even higher and not smaller. Moreover, because the resonator is in the overcoupled regime, γ is dominated by γ_1 making the error on γ_2 not so relevant in the frequency shift at the critical power. On the other hand, we can see in Fig. 5.2a that the circle fit of the phase is broader than the measured one, meaning that the fitted γ is higher than the experimental value. This could explain the predicted $\Delta\omega_c$ being larger than the measured one because $\Delta\omega_c$ scales as γ.

Besides that, we saw in the previous chapter that gate drift could happen in the system making the resonance frequency shift at higher frequency with respect to time. The power dependence measurement being not instantaneous, it could also explain the mismatch in $\Delta\omega_c$. Indeed, the Kerr shift being negative, a positive frequency drift would make $\Delta\omega_c$ smaller. But a measurement at low power was taken 10 minutes after the power dependence and showed a shift of 5 MHz compared to what was measured at the beginning of the power dependence. This sets an upper limit on the frequency shift happening during the power dependence measurement itself (which lasted 5 minutes) and is not enough to explain the observed difference in $\Delta\omega_c$.

Finally, by combining the effects caused by the inaccurate γ_1 and γ_2 extracted from the circle fit, and the time drift, it might be sufficient to explain the $\Delta\omega_c$ discrepancy observed in Fig. 5.2a. This is why we developed a second fitting model less sensitive to microwave background.

On the other hand, in Fig. 5.2b corresponding to another operating point, the circle fit at P_0 fits very well the phase meaning that γ is found accurately. We also checked for a potential time drift of the resonance frequency and we did not measure any. Despite that, the measured Kerr frequency shift does not correspond to the model. This means that at this operating point, the two-photon loss model is not working accurately. This also explains why it was hard to fit directly the data even with a few free parameters.

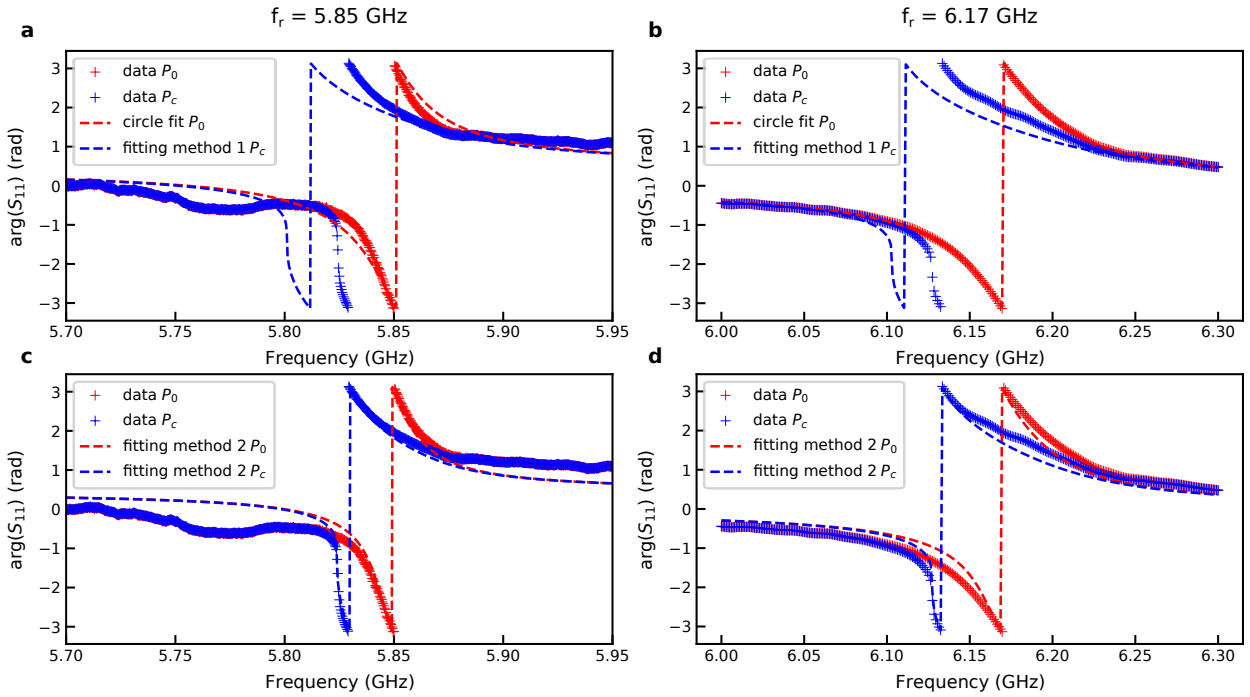

Figure 5.2: Phase of S_{11} at low power P_0 and critical power P_c at two different resonance frequencies f_r = 5.85 GHz and f_r = 6.17 GHz. (a) and (b) show the result of the fitting method 1 while (c) and (d) show the result of the fitting method 2.

5.1.2.b Fitting method 2

The trick of the fitting method 2 is to use a trace at a low power $P_0 << P_c$ as a normalization trace. The microwave background being not power dependent, it should fully remove it. The problem of this method is that we cannot use the circle fit to obtain the low power parameters making the parameter space very large. Moreover, sensitivity of the ratio $S_{11}(P_c)/S_{11}(P_0)$ with respect to changes in the parameters is complicated: each parameter can affect a shift in frequency or a change in intensity of the features observed in $S_{11}(P_c)/S_{11}(P_0)$. Therefore we used the experimental value of $\Delta\omega_c$ to fix γ_2 with respect to γ_1 using Eq. 5.4 in the limit $\gamma_3 << K$. We also used Eq. 5.3 to fix K with respect to γ_1, γ_3 and b_c^{in}. By doing so

we were able to remove two free parameters.

Here is the detailed fitting procedure:
• Circle fit on $S_{11}(P_0)$ to extract ω_r and a first guess on γ_1 (here we suppose that P_0 is low enough to have $\omega_r(P_0) = \omega_r(P = 0)$).
• Finding manually the critical power as in the fitting method 1 $\rightarrow$ get b_c^{in}
• Obtaining $\Delta\omega_c$ by comparing ω_r to the frequency at which the absolute value of the derivative of the phase of $S_{11}(P_c)$ is maximum.
• Fitting $|S_{11}(P_c)/S_{11}(P_0)|$ with only γ_1 and γ_3 as free parameters, γ_2 being obtained with Eq. 5.4 and K with Eq. 5.3.
• Comparison of the numerically obtained $S_{11}(P_0)$ to the measured $S_{11}(P_0)$. If P_0 is not small enough compared to P_c there might be a slight frequency shift because the experimentally fixed $\Delta\omega_c$ corresponds to the frequency shift at the limit $P = 0$. Moreover because of the approximation $\gamma_3 << K$, the computed γ_2 obtained from Eq. 5.4 is smaller than its real value meaning that the theoretical $\Delta\omega_c$ is smaller than the experimental one.
$\rightarrow$ Correction of the resonance angular frequency ω_r by comparing the frequency at which the phase makes a 2π shift such that the numerically obtained $S_{11}(P_0)$ matches the measured $S_{11}(P_0)$.
• Because ω_r has changed, we modify $\Delta\omega_c$ accordingly as in the third step.
• Fitting $|S_{11}(P_c)/S_{11}(P_0)|$ with only γ_1 and γ_3 as free parameters as in the fourth step.

The advantage of the fitting method 2 is that it allows the estimation of γ_3 even with a strong microwave background. Moreover it allows to fix $\Delta\omega_c$ which is good if the two-photon loss model describes accurately the data. Fig. 5.2c and d show the results of the fitting method 2 on the same data as Fig. 5.2a and b. We can see that for f_r = 5.85 GHz, the fits at low power and critical power match the data very well meaning that the problem with the fitting method 1 were probably not caused by an inaccurate model. On the other hand, for f_r = 6.17 GHz, the fitted phase at input power P_0 is worse than the circle fit. In fact we saw in Fig. 5.2b that the circle fit gave a perfect fit at P_0 but that this was giving a too large $\Delta\omega_c$. By forcing $\Delta\omega_c$ to match the experimental value, we forced γ, i.e. the width of the resonance to be smaller and thus not matching the experimental phase at P_0.

To conclude, we always used the fitting method 2 as a starting point because it allows to extract the internal loss γ_2 and nonlinear loss γ_3 with more accuracy. When the fitting method 2 was not working, either because of difficulties to converge to a proper solution, or when the model seemed not to describe the data, we adopted the fitting method 1 which is more resilient in these cases in order to get an estimation of the parameters. In the next section we will discuss of the possible origins of the model discrepancy.

5.1.3 Origin of the model discrepancy

5.1.3.a Full development of the Josephson potential

The model discrepancy manifests as an inaccurate predicted $\Delta\omega_c$. Moreover, we see here that it happened at a working frequency closer to the bare resonator frequency, meaning that the nonlinearity is smaller and the critical power higher. In the two-photon loss model, only the first nonlinear term (quartic term) is included in the development of the Josephson

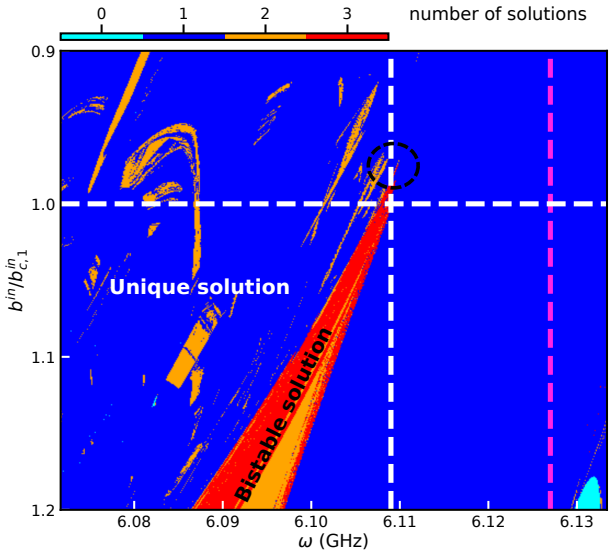

Figure 5.3: Computation of the number of solutions of the equation of motion incorporating the full development of the Josephson potential for the operation frequency $f_r = 6.17$ GHz. The model depends only on the loaded quality factor $Q_l = 87$ obtained by the circle fit. The black dashed circle indicates the area where the bifurcation point is located. The intersection of the white dashed lines corresponds to the bifurcation point if only the first nonlinear term (quartic term) of the expansion of the Josephson potential is taken into account. The pink line correspond to the frequency of the measured bifurcation point.

potential. Because of a higher critical power, neglecting the higher order nonlinear terms might be the origin of the observed discrepancy. We therefore performed calculations with a model accounting for the full development of the Josephson potential. Such a model was proposed by Kochetov et al. but includes neither linear nor nonlinear losses [93].

In Fig. 5.3, we computed the number of solutions of the equation of motion of the system with respect to the input frequency and the input field normalized by the critical input field ($b^{in}_{c,1}$) obtained by considering only the quartic nonlinear term in the Josephson energy (Eq. 5.3 with $\gamma_2 = \gamma_3 = 0$):

$$\left[\frac{1}{4Q^2} + \left(\frac{1}{2} - \Omega + \frac{J_1(4\sqrt{n})}{4\sqrt{n}}\right)^2\right] n = \frac{b^{in}_1 / b^{in}_{c,1}}{\sqrt{27}Q^3} \tag{5.5}$$

where Q is the total quality factor, $\Omega = \omega_p/\omega_r$ and J_1 the Bessel function of the first kind of order 1. We see regions with 0, 1, 2 or 3 solutions. However, as shown in Chapter 2, the JPA physics shows that there are either one stable solution or three solutions (1 unstable/ 2 bistable) when the system bifurcates. Therefore, the areas where 0 or 2 solutions are found correspond to numerical error. For example, the small orange areas in the wide blue area must correspond to a unique solution and the same hold for the light blue area. The orange areas in the red triangle must correspond to three solutions, i.e. bistable solutions.

In the graph, the point we are interested in is the bifurcation point which is the summit of the bistable solution triangle. Because at this point all the solutions are very close to each other, it is complicated to obtain them numerically. This explains why the summit is not very

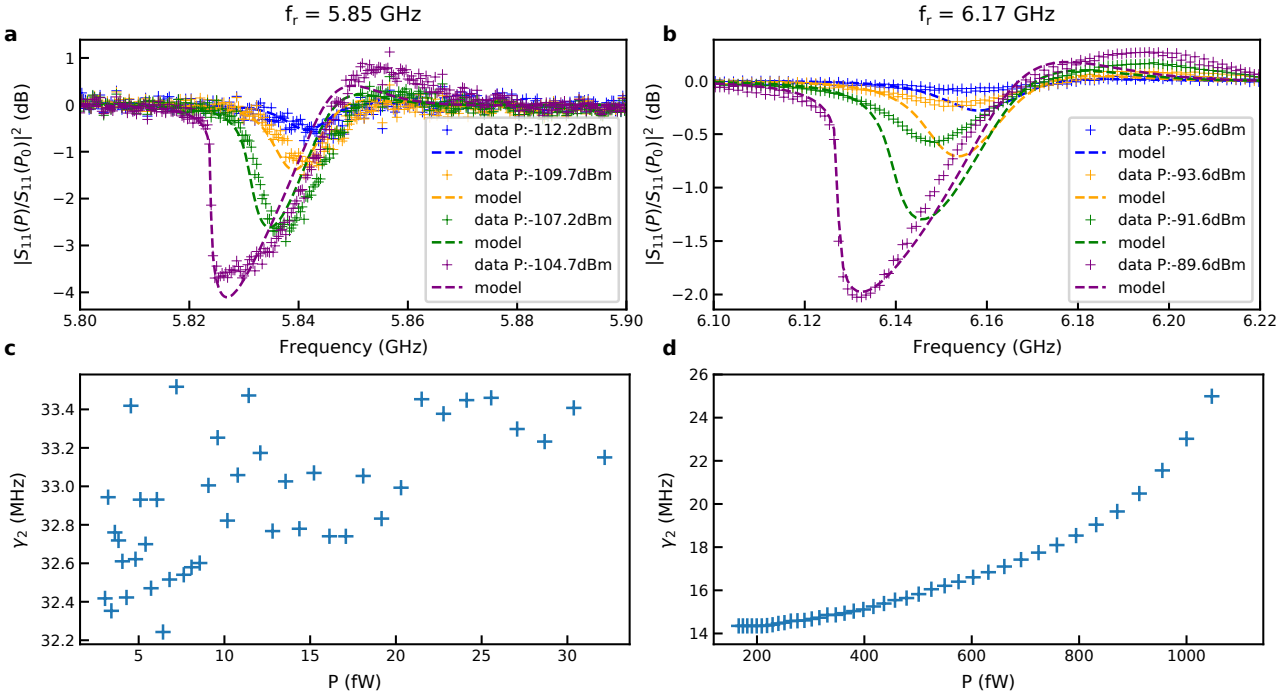

Figure 5.4: (a) and (b): Ratio of the amplitude of S_{11} at an input power P with S_{11} at an input power P_0 for different input powers at operation frequencies f_r = 5.85 GHz and 6.17 GHz respectively. The model curves where obtained with the two-photon loss model with the parameters extracted from the fitting method 2. The purple curves correspond to the critical power. (c) and (d): power dependence of the internal losses γ_2 at working frequencies f_r = 5.85 GHz and 6.17 GHz respectively. γ_3 was set to zero during this fitting process.

sharp. The black dashed circle indicates the localization of this point. When the Josephson energy is developed only to the quartic term, we can compute $b_{c,1}^{in}$ and $\Delta\omega_c$ as indicated by the white dashed line. The intersection of these lines corresponds to the bifurcation point of a JPA where the Josephson energy is only developed to the quartic term, i.e. the bifurcation point of the two-photon loss model. By comparing the position of the bifurcation point including the full development of the Josephson energy (center of the black circle) to the bifurcation point including only the quartic term (intersection of white lines), we can see if $\Delta\omega_c$ and $b_{c,1}^{in}$ predicted by the two-photon loss model should be smaller or higher than what is predicted by the full development of the Josephson energy. By doing so, we see that the measured critical power of the gJPA might be slightly lower than what is predicted with the two-photon loss model ($b_1^{in}/b_{c,1}^{in} < 1$). We also see that there might be a slight frequency shift but it is too small to explain the error on $\Delta\omega_c$. In fact, we indicated the frequency of the bifurcation point extracted from the measurement by the pink vertical line and we see a 20 MHz difference. We can conclude from this that the discrepancy is probably not caused by the neglected higher order nonlinear terms in the expansion of the Josephson energy.

5.1.3.b Nonlinear loss

The two-photon loss model takes into account a loss in the form $\gamma_2 + \gamma_3|A|^2$ meaning that the total loss is increasing linearly with the power. This works as a first approximation but

the microwave induced loss in a gJJ might have a more complex power dependence. From the fit of S_{11} at the critical power and at low power with the methods presented before, we get all the parameters of the device. This means that we can predict S_{11} whatever the input power. In order to see the evolution of the loss with power, we plotted in Fig. 5.4a and b the magnitude of the ratio of S_{11} at an input power P with S_{11} at the lowest input power P_0 for the same operating frequencies as in Fig. 5.2. Both in Fig. 5.4a and b, the purple curves correspond to the critical input power and are described properly by the two-photon loss model. In Fig. 5.4a, each input power is well fitted by the model. Nevertheless, in Fig. 5.4b, we can see that only the critical power is fitted properly. The model predicts a more intense amplitude dip for lower powers meaning that the loss is too high in the model. Indeed, because we extracted γ_3 from S_{11} at the critical power, it is normal that the model is good at this power value. But if the loss increases more than linearly with power, it means that the nonlinear loss extracted at P_c is higher than the one at $P < P_c$. This would explain the observed discrepancy in the power dependence at the working frequency f_r = 6.17 GHz.

Because the two-photon loss model is intrinsically limited by considering only linear dependent loss with power, we adopted another strategy to quantify the nonlinear loss. The strategy was very simple and possible because at the working frequencies f_r = 5.85 GHz and 6.17 GHz the microwave background is not dominant compared to the amplitude of the dip in the magnitude of the S_{11} parameter at resonance. We first fitted $S_{11}(P_0)$ with the circle fit method to get γ_1 and ω_r. Because γ_2 is the only parameter supposed to change the dip amplitude at resonance, we only fitted the minimum of $|S_{11}|$ at each power with γ_2 as the only free parameter. This simple method allows not to take into account the frequency shift caused by the Kerr effect which was an issue for the general fit.

Fig. 5.4c and d shows γ_2 obtained this way with respect to the input power at operation frequencies f_r = 5.85 GHz and 6.17 GHz. The maximal power of each graph corresponds to the critical power. We can see that at the working frequencies f_r = 5.85 GHz, γ_2 barely increases with increasing power (we note that the normalization procedure of Fig. 5.4a can be misleading because the dip amplitude mostly comes from the Kerr shift and not the internal loss). In this case we saw that the two-photon loss model was modeling the data properly with the fitting method 2. Indeed, $\gamma_2(P)$ could be fitted with a linear slope with respect to the power which corresponds to the model. However, at the working frequency f_r = 6.17 GHz, we see that the internal loss does not evolve linearly with the input power. This explains why the modeled S_{11} is off in Fig. 5.4b at $P < P_c$. Considering a linear evolution of the loss with power and determining the nonlinear loss at $P = P_c$, is equivalent of having γ_2 being a straight line between the lowest and the highest power in Fig. 5.4d. We speculate that evolution of the nonlinear loss with power is due to the high critical power at f_r = 6.17 GHz compared to f_r = 5.85 GHz (15 dB of difference). Such a power would make the generalized phase difference ϕ across the gJJ higher. This would mean that the device is not working close to $\phi = 0$ in the current phase relation (CPR) and could lead to additional dissipation because of the reduced gap in the Andreev bound states energy levels as explained in Chapter 1.

5.1.3.c Non sinusoidal current phase relation

The characterization of the evolution of the loss with the input power showed that the two-photon loss model is not accurate when the loss is not of two-photon type. We will now

discuss the effects of a more complex loss model. Eq. 5.4 shows that $\Delta\omega_c$, the Kerr frequency shift at the critical power, depends linearly on γ in the limit where there is only linear loss. When introducing nonlinear loss, another term appears which depends on γ_3 and K. Again, increasing γ_3 would make this term bigger and so $\Delta\omega_c$ would increase as well. This comes from the fact that adding losses makes the critical power higher because it has to compensate for these losses. And a higher input power means more Kerr effect and thus more frequency shift. From this, we can conclude that higher orders terms of losses should make $\Delta\omega_c$ even higher. Nevertheless, we saw that for $f_r = 6.17$ GHz, the measured $\Delta\omega_c$ is smaller than what is predicted by the two-photon loss model. Even more surprising, by taking γ extracted from the circle fit at low power, and taking $\gamma_3 = 0$, we get $|\Delta\omega_c/(2\pi)| = 62$ MHz > 37 MHz which is the measured $|\Delta\omega_c/(2\pi)|$. There is almost a factor 2 which cannot be explained by errors on the fitted γ because the circle fit at low power was fitting the data very well (Fig. 5.2b). It shows that a model including more precise nonlinear loss terms could not explain the discrepancy in $\Delta\omega_c$.

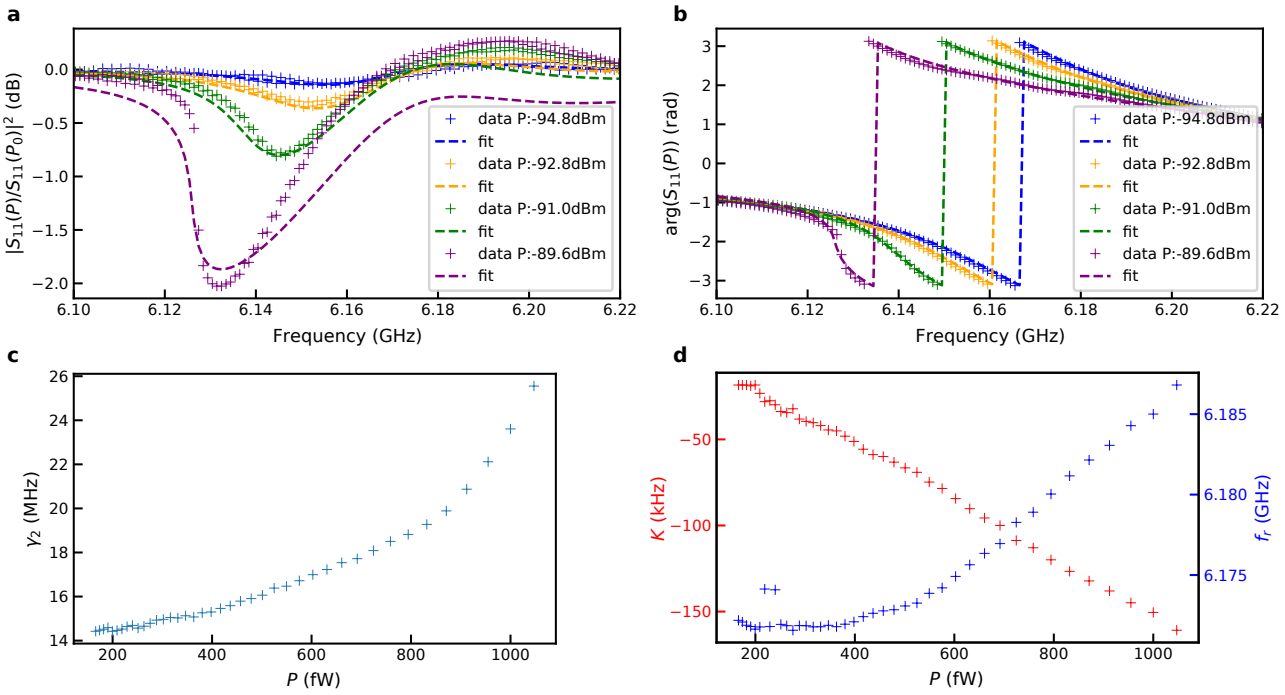

Figure 5.5: (a) Normalized magnitude of S_{11} at different input powers. (b) Phase of S_{11} at different input powers. The fits obtained in (a) and (b) are obtained by letting f_r, γ_2 and K change with respect to the power in the two-photon loss model with $\gamma_3 = 0$. The purple curves correspond to the critical power. (c) Fitted γ_2 with respect to the input power. (d) Fitted f_r and K with respect to the input power.

We developed a fitting method with $\gamma_3 = 0$ but with a power dependent γ_2 and ω_r. The goal was to see if simply allowing the resonance frequency to shift with the input power could reproduce the data, i.e. see if $\Delta\omega_c$ was the only problem. In this fitting procedure, γ_1 was extracted from the circle fit at low power and K from the fit of S_{11} at the critical power. By doing so, we saw that it was not possible to fit the data by letting γ_2 and ω_r power dependent. Despite obtaining a correct $\Delta\omega$ at each power, the shape of the S_{11} parameter (the maximum

of its derivative typically characterizing the ratio b^{in}/b_c^{in}) was not correct. This means that this model was not predicting correctly how far the JPA was from bifurcation at a given power.

In order to correct that, we made K being power dependent as well. Fig. 5.5a and b respectively show the normalized magnitude and the phase of S_{11} at the working frequency f_r = 6.17 GHz, for different input powers. The dashed curves correspond to the fit obtained with the fitting procedure we just described. We can see that the amplitude ratio is better described by this model than the two-photon loss model (compared to Fig. 5.4b). Besides that, the fit on the phase matches really well the experimental data. Fig. 5.5c shows the power dependence of γ_2. We can see that it is very similar to what was obtained with the simple way of extracting $\gamma_2(P)$ that we used in Sec. 5.1.3.b. Fig. 5.5d show the power dependence of K and f_r. As expected from the discrepancy in the measured Kerr frequency shift, f_r shifts at higher frequencies with increasing power. We note that there is a plateau at lower power. It looks like there is a correlation between γ_2 and f_r. When the slope of $\gamma_2(P)$ is constant (nonlinear loss linear in P), f_r does not depend on the power. When the slope of $\gamma_2(P)$ increases (nonlinear loss not linear in P), f_r has to be compensated meaning that the Kerr shift do not respect the two-photon loss model. Moreover, we see that $|K|$ is increasing linearly with the power. This means that the 4^{th} order nonlinear term of the form $KA^\dagger A^\dagger AA$ does not describe the system accurately.

To conclude, we demonstrated that a full development of the of the Josephson potential cannot correct the Kerr frequency shift but might be needed to take into account the power dependent non-linearity. We also showed that power dependence in the losses follows a more complicated function than a linear slope. We argue that the model discrepancy could come from the assumption that the CPR is sinusoidal in the two-photon loss model. We indeed argued in the previous chapter that the device was showing evidence of a forward skewness of the CPR. A non sinusoidal CPR could induce three wave mixing processes and would modify the intensity of the four wave mixing process that is the only one at play in the two-photon loss model. The three wave mixing could have been measured experimentally with the use of a spectrum analyzer but we did not do it because we did not have the same comprehension of the device at this time. Moreover, the CPR of a SNS JJ can be strongly influenced by microwave irradiation [168]. So, an ideal model would tackle the microscopic behavior of the gJJ by looking directly at the Andreev bound state population. This would allow to compute the CPR, its power dependence and also non-linear losses caused by excitation and relaxation of quasiparticles in the Andreev bound states.

5.1.4 Gate dependence of K and γ_3

Despite the evidences on the two-photon loss model inaccuracy to describe the behavior of our device, we used it anyway because it allowed to get estimations of the parameters and see their evolution with respect to the gate. Moreover developing a new theoretical model with all the mentioned ingredients is beyond the scope of this thesis. The goal here is to focus on K which is an important parameter determining the dynamic range of the amplifier, and γ_3 which can only degrade the performances of the gJPA because it will add noise. Because we estimated the error on the total attenuation of the microwave lines to be close to 4 dB,

it implies an error of a factor 2.5 on K and γ_3. Indeed, K and γ_3 are proportional to the intracavity number of photons in the equation of motion making them having the same error as the power. This confirms that we only have access to order of magnitudes and legitimates the use of the two-photon loss model. We performed input power dependencies at several gate voltages in order to see the evolution of K and γ_3 with respect to V_g. It was a challenge to fit all of them because there are several reasons why fitting methods 1 and 2 can struggle fitting the data:

- When $\gamma_3 > K/\sqrt{3}$ the device cannot bifurcate, but both methods relies on fitting S_{11} at the critical power.

- The fitting method 2 forces $\Delta\omega_c$ to match the experimental value. But we saw that this quantity was often smaller than what is predicted by the model. So the fit has to make γ_1 smaller which sometimes does not match experimental data. Therefore it can make γ_2 go to negative values because it is computed from γ_1 and $\Delta\omega_c$. This is of course not physical and overestimate the fitted γ_3 because it compensates for the non physical negative loss.

- The fitting method 2 uses Eq. 5.4 in the limit where $K >> \gamma_3$ which is not always the case.

- The fitting method 1 is very sensitive to microwave background such that the estimation of γ_3 is impossible when the amplitude of the background is larger than the amplitude of the resonance dip in $|S_{11}|$.

- The fitting method 1 assumes that the measured S_{11} at low power P_0 is in the limit where power has no effect on the resonator, i.e. when there is no Kerr shift. This is not always true in the data sets we analyzed and was only realized after data analysis.

For all data sets we compared fitting method 1 and 2. By default we chose the fitting method 2 when both fits where good because it cancels the microwave background and correct the Kerr shift at P_0. When the fitting method 2 was not working we chose the fitting method 1. Except for the problem of $\Delta\omega_c$, the fitting method 1 gives often great results for fitting the phase and the normalized amplitude $|S_{11}(P_c)/S_{11}(P_0)|$.

Fig. 5.6a shows the fitted resonance frequency with respect to the gate voltage for all the power dependence data sets we fitted. We compared it to the resonance frequency fitted by the circle fit obtained doing a slow gate voltage sweep. It is important to compare the power dependence to this slow map because as we saw in the previous chapter, the device has some gate instabilities. As expected, the difference between the fitted f_r from the power dependence data sets and the slow map is more important at gate voltages where the resonance frequency is more sensitive to V_g (higher $|\partial f_r/\partial V_g|$). Because of this, it is more natural to refer to the resonance frequency than the gate voltage to label the operating point of the gJPA. Indeed, a resonance frequency corresponds directly to a Josephson inductance which corresponds to a certain critical current that is the knob of control of the JPA. Tuning the gate voltage allows to control I_c but we can see that for the same V_g there are many possible f_r and so, many possible I_c because of the gate instability.

Fig. 5.6b shows the fitted Kerr coefficient with respect to the gate voltage. The error bars on K only consider the error on the input power of 4 dB meaning that K can be 4 dB higher or lower than the fitted value. The error bars on V_g are obtained from Fig. 5.6a. We simply took the maximal distance in V_g from f_r extracted from the power dependence data sets to f_r

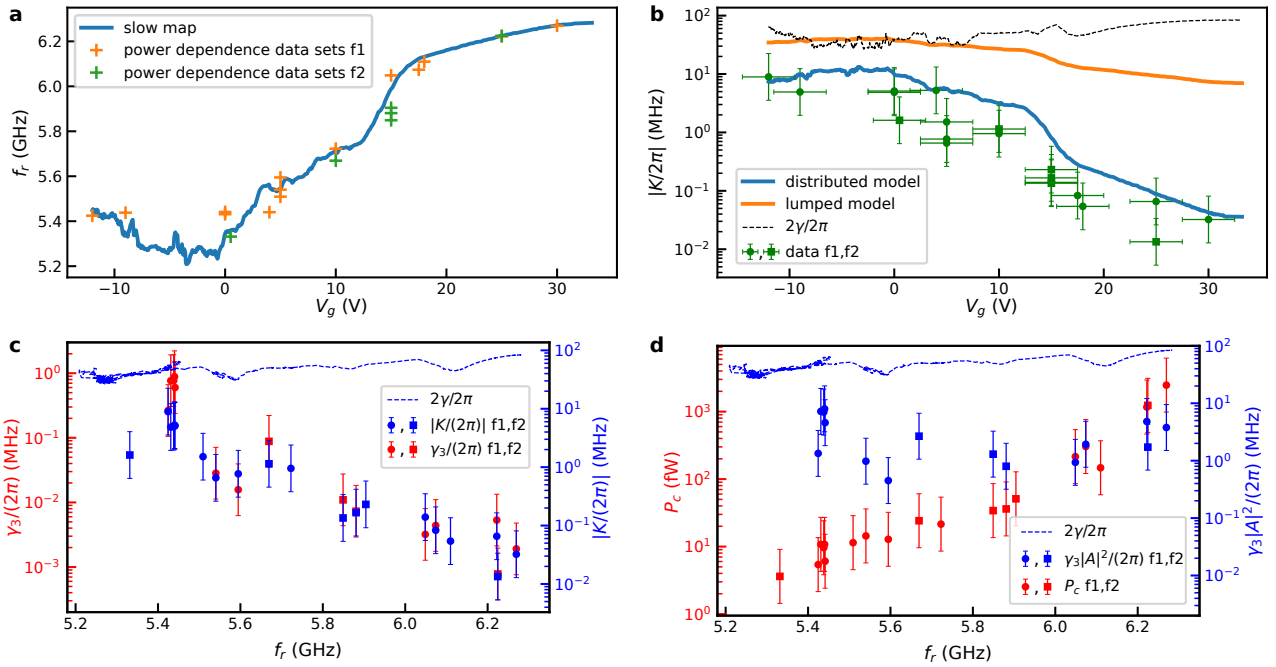

Figure 5.6: (a) Resonance frequency extracted from the circle fit of a slow gate voltage dependence at low power (blue) and from the power dependence data sets we analyzed using fitting method 1 (f1 in orange) or 2 (f2 in green). (b) Kerr coefficient with respect to the gate voltage. The orange and blue curves are the modeled value of Kerr coefficient using two different models and the device parameters extracted at low power input (see previous chapter). The green points are values extracted by fitting the power dependence data sets with fitting method 1 or 2 (f1 or f2). The dashed black line is obtained from the circle fit of a slow gate voltage dependence at low power. (c) Fitted nonlinear loss coefficient and Kerr coefficient with respect to the fitted resonance frequency with fitting method 1 or 2 (f1 or f2). (d) Critical power and product of the nonlinear loss coefficient with the squared intracavity field with respect to the gate voltage obtained by fitting method 1 or 2 (f1 or f2).

extracted from the slow map. By doing so we found an error of 2.5 V which is overestimated because most of the points do not show such a shift. In the previous chapter we modeled the device with a lumped model and a distributed model thanks to parameters obtained from simulations and the bare device measurement. We can see that the data follow closely the distributed model.

Fig. 5.6c shows the fitted γ_3 and K with respect to the resonance frequency. These two parameters have to be compared with $\gamma \approx \gamma_1$ to predict the performances of the gJPA. We can see that close to the charge neutrality point, there is less than one order of magnitude between 2γ and K meaning that the dynamic range of the JPA, which is influenced by their ratio, will be limited. Moreover, we also see that γ_3 is higher in this region which could limit the maximum gain and increase the added noise. The graph shows a decrease of γ_3 and the ratio $|K/2\gamma|$ when the resonance frequency increases. This means that the dynamic range should increase and the added noise caused by the nonlinear loss should decrease at higher resonance frequencies. The nonlinear loss being proportional to the square of the field amplitude in the device $|A|^2$, we have to take into account the power at which is working the

device. Fig. 5.6d shows the evolution of the critical power and the product $\gamma_3|A|^2$ with respect to the working resonance frequency. We can see that the critical power has an exponential dependence in f_r which is not surprising because $(b_c^{in})^2 \propto 1/K$ and K shows an exponential dependence in f_r as well. Nevertheless, this increased working power makes the effect of the nonlinear loss higher at high f_r. We have to compare the product $\gamma_3|A|^2$ to γ to estimated its impact. We can see that $\gamma_3|A|^2$ is close to γ near the charge neutrality point, then decreases and is more or less constant between 5.5 and 6.1 GHz to finally increase again above 6.2 GHz.

5.2 Amplification

Now that we have characterized the gJPA at higher input powers, we can focus on the amplification regime. In this section, the VNA sends a small signal and measures how it is amplified. An additional microwave source is used as a pump. We will focus here on the gain at the signal frequency. Frequency mixing processes are studied in Appendix A.

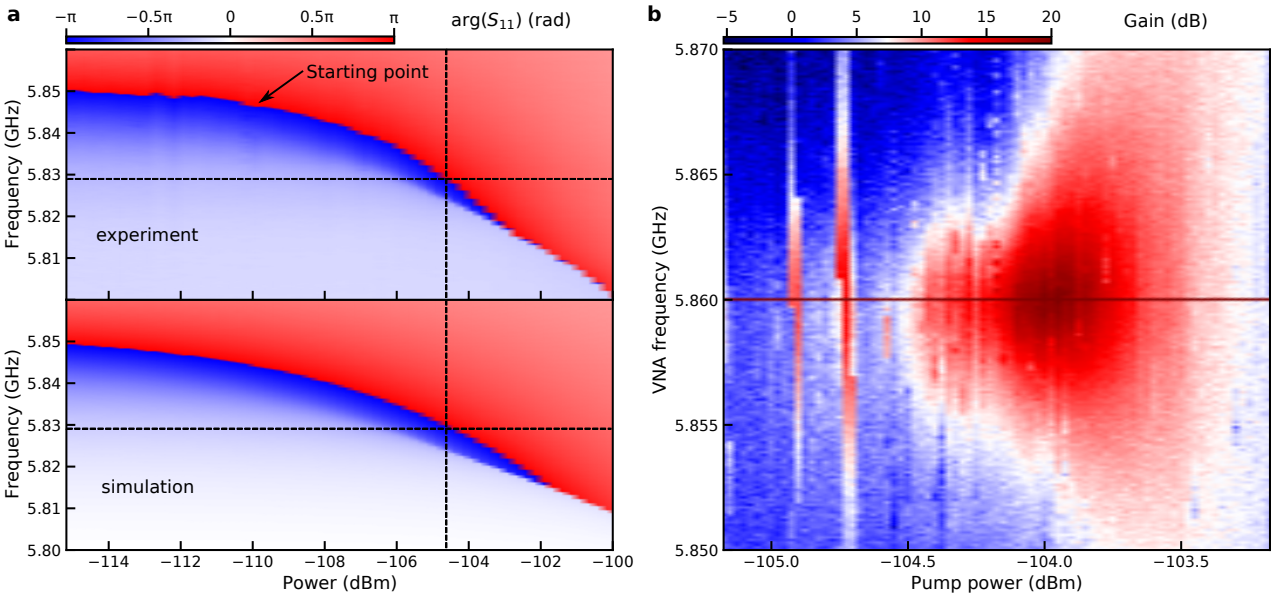

Figure 5.7: (a) Measured and simulated VNA power dependence of the phase of S_{11} at V_g = 15 V. The simulation is done using the two-photon loss model and the parameters are extracted with the fitting method 2. The arrow indicates the starting point (frequency and power) of the amplification research procedure. (b) Gain (measured $|S_{11}|^2$ divided by the averaged $|S_{11}(V_g)|^2$ at different gate voltages as in the previous section) with respect to the pump power and VNA frequency. The pump frequency is $f_p = 5.860$ GHz. This figure has been obtained after several repetitions of the amplification searching procedure.

5.2.1 Amplification procedure

The amplification process depends on several parameters: the VNA power and frequency which is the small microwave signal that we want to amplify, the pump power and frequency which gives the energy for the amplification process, and the gate voltage which sets the

operating frequency of the device. We thus have to find an optimal set of 5 parameters which is not trivial especially because of the gate instability which continuously changes the parameters of the device. Therefore we adopted a systematic amplification searching procedure:

- Fixing the gate voltage such that the gJPA resonates at a given frequency
- Measuring a VNA power dependence and note down at which frequency the Kerr shifts starts to be sizable (as shown by an arrow on Fig. 5.7a) as well as an estimation of the critical power
- Fixing the pump frequency at the frequency noted in the previous step
- Fixing the VNA power at -140 dBm in order to have a very low number of photons and avoid saturation processes
- Taking VNA traces with VNA frequency centered around the pump frequency (because amplification is maximal at the pump frequency) and sweep the pump power around the critical power.
- Noting down the maximal gain obtained and then decrease the pump frequency
- Repeating the two last steps until finding the maximum gain: this way the optimal pump power and frequency are obtained

We will now illustrate the amplification searching procedure. Fig 5.7a shows a typical power dependence of the phase of the S_{11} parameter. This measurement was taken at V_g = 15 V by measuring S_{11} with the VNA at different VNA input powers and corresponds to the data shown in Fig. 5.4a. We saw that at this resonance frequency, the two-photon loss model was able to fit the data. Indeed, we can see in Fig 5.7a that the simulation reproduces well the data until the critical power indicated by the vertical line. Around the critical power, we can see that the slope of the 2π phase shift increases faster than what is predicted by the model which means that we arrive at the limit of validity of the two-photon loss model. At a higher VNA power we can see that the phase shift is no longer 2π but π. This always happens above the critical power and sets the maximum pump power that we will use during the amplification searching procedure. From Fig 5.7a we know that we can start with a pump frequency between 5.84 and 5.85 GHz and sweep the pump power from -110 and -102 dBm.

Fig 5.7b shows a typical sweep of VNA frequency and pump power at a fixed pump frequency in order to see what is the maximal gain corresponding to this particular pump frequency. It was taken one hour after Fig 5.7a explaining why the system drifted at higher resonance frequency because of the gate voltage instability (V_g = 15 V being a particularly unstable point because of the important $\partial f_r/\partial V_g$). The pump frequency is fixed at 5.86 GHz and is visible as a single pixel dark red horizontal line on Fig 5.7b. It blinds the VNA at this single frequency because it is approximately 40 dB more intense than the input signal. At pump power below -104.5 dBm, we do not see amplification of the VNA signal except at some local pump powers. This is linked to the gate voltage instability: when there is a sudden charging effect, it changes the parameters of the gJPA and because the pumping parameters are very close to the optimal ones, it can in turn create amplification. Around -104.5 dBm, amplification appears and reaches a maximum with a near 20 dB gain around -104 dBm. Above this power the gJPA is not optimally tuned and the gain decreases. We can repeat the experiment done in Fig 5.7b at a lower pump frequency in order to see if we get a better maximal gain. Repeating this process over and over gives the best amplification pump

parameters. Nevertheless this process is delicate because of the gate instability. As we saw, a small drift in the parameters of the gJPA can quench the amplification because the pump power has to be optimal in a range smaller than 0.5 dBm and the pump frequency in a range smaller than 5 MHz.

5.2.2 Amplification modeling and gate tunability

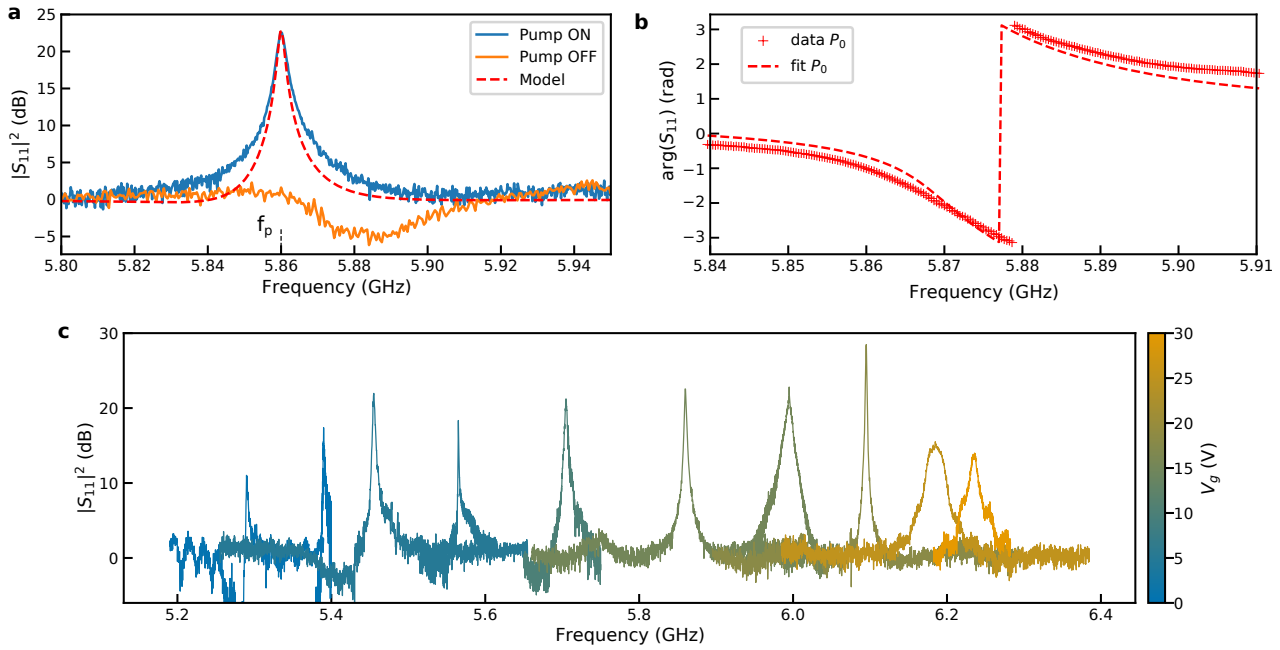

Figure 5.8: (a) Magnitude of the S_{11} parameter with respect to the signal frequency with and without the presence of the pump. The model uses the parameters extracted by the fitting method 2 of a signal power dependence with the pump off. The pump frequency f_p is indicated by a dashed line. The data were normalized with an averaging of the gate dependence of S_{11}. (b) Measured and fitted phase of the S_{11} parameter at low power P_0 after the frequency drift with the pump off. (c) Gain profiles measured at several gate voltages. The data were normalized with an averaging of the gate dependence of S_{11}.

The two-photon loss model also allows to compute the gain of the device as we saw in Chapter 2. Nevertheless it does not include saturation effects. This means that the gain should be infinite if the pump is well tuned and the nonlinear losses are not present. This is why we adopted a phenomenological approach to model the gain within this model. The experiment fixes the pump frequency f_p, pump power P_p and signal frequency f_s. Fitting a signal power dependence (one tone measurement) at the same operation point allows to extract f_r, γ_1, γ_2, γ_3, P_c and K. Because there is some error on the way we extract P_c (manual determination and possible gate drift in between the signal power dependence and the optimal gain measurement) and thus K (because K is computed with P_c using Eq. 5.3), we fix $P_p = 0.95P_c$ and compute K accordingly. Two possible mechanisms of saturation were described in Chapter 2: the pump back-action and some parasitic nonlinear terms in the equation of motion when going beyond the linearization procedure. In both the mechanisms, putting a stronger input signal makes the Kerr shift larger which causes the pump parameters to be detuned from

the optimal ones [92]. We account for this increased Kerr shift by artificially shifting the fitted resonance frequency f_r until the maximum gain predicted by the model corresponds to the maximal measured gain. Shifting f_r at lower or higher frequency both enable to obtain a reduced gain. We chose to shift f_r at higher frequency because it corresponds to what is happening physically. The extra Kerr shift means that the detuning between $f_r(P = P_c)$ and $f_r(P = 0)$ becomes larger such that we have to increase $f_r(P = 0)$ to simulate this effect.

Fig 5.8a shows the measured magnitude of S_{11} with respect to the input signal frequency when the pump is off and when it is on with optimally tuned parameters at V_g = 15 V. We can see that the reflected signal is amplified by more than 20 dB around the pump frequency indicated by the dashed line at 5.86 GHz. We used the fitting method 2 of the signal power dependence map as well as the modeling method described above in order to model the gain. We can see that the fitting method 2 predicts a narrower gain than the measured one. Indeed, the measured gain bandwidth product is $BW\sqrt{G}$ = 33 MHz which has to be compared to the total energy damping rate $2(\gamma + \gamma_3|A|^2)/2\pi$. The parameters extracted by the fitting method 2 are $2\gamma = 2\pi$ x 23.9 MHz and $2\gamma_3|A|^2 = 2\pi$x2.6 MHz which makes a total modeled energy damping rate of 2πx26.5 MHz. Nevertheless, as we saw in Fig 5.7b, the system slightly drifted in between the signal power dependence that was used to extract the parameters, and the amplification procedure. A fit of $|S_{11}|^2$ at low power after the drift enable to extract $2\gamma = 2\pi$x29 MHz which makes a total energy damping rate of 31.6 MHz much closer to the measured gain bandwidth product. Last but not least, there is some error on the fitted γ as shown in Fig 5.8b where we can see that the fitted phase is narrower than the measured one. It means that the fitted γ is smaller than the real value and it should explain why we predict a gain bandwidth product of 31.6 MHz while we measured 33 MHz. This example shows that the two-photon loss model can predict the shape of the gain profile.

As we saw in Fig 5.8a, the gain of the gJPA is limited to a narrow bandwidth around the pump frequency which corresponds to the resonance frequency at the critical power. We therefore used gate tunability of the device to change its resonance frequency and managed amplification at different frequencies. Fig 5.8c shows measured amplification profiles at different gate voltages. For each gate voltage, the pump parameters are tuned with the procedure described in Sec. 5.2.1 to find the maximal gain. We can see that amplification occurs on a 1 GHz frequency range with a gain higher than 15 dB. It corresponds to a frequency range more than 100 times larger than the amplification bandwidth of the device and shows that the gate voltage brings a very useful functionality to the device.

5.2.3 Limits of the model

While the two-photon loss model is able to describe the gain profile at V_g = 15 V corresponding to a working frequency of 5.85 GHz, there are some working frequencies for which it does not work properly. Fig 5.9a, b and c show the gain profile and modeling for different working frequencies (5.455 GHz, 6.13 GHz and 6.18 GHz respectively). The fitting method 2 was not working to extract the parameters for Fig 5.9a and c and explains why only the model using the fitting method 1 parameters is shown. In Fig 5.9a we can see that the gain has a distorted lorentzian shape on the low frequency range compared to the pump. This operating point was particularly unstable because of the gate instability and it might

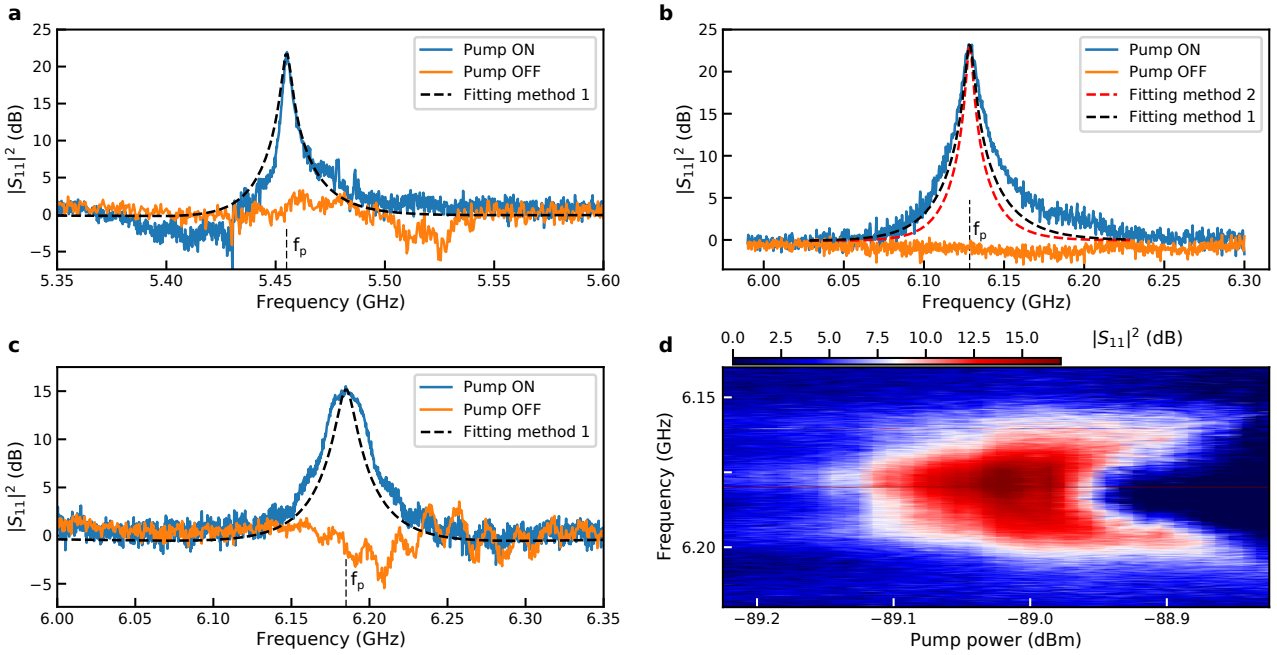

Figure 5.9: (a), (b), (c) Magnitude of the S_{11} parameter with respect to the signal frequency with and without the presence of the pump. The model uses the parameters extracted by the fitting method 1 and 2 (when possible) of a signal power dependence without the pump. The pump frequency f_p is indicated by a dashed line. The data of (a) and (c) were normalized with an average of the gate dependence of S_{11}. The data of (b) were taken in the XL dilution fridge where we did not perform a gate dependence of S_{11}. Thus the data where normalized with a S_{11} trace of a 50 Ω PCB. (d) Gain as a function of the signal frequency and the pump power. The data were normalized with an average of the gate dependence of S_{11}.

explain the modified shape compared to the model. Fig 5.9b corresponds to the operation point we analyzed in Fig. 5.2b and d. We could see that the fitting method 2 of S_{11} was too narrow and that the fitting method 1 was fitting the width of the phase at low power perfectly. Because at this operation point we did not measure any drift, it means that the width of the modeled amplification with the fitting method 1 should correspond to the measured width. Nevertheless we see that it is not the case meaning that the nonlinear loss γ_3 is probably underestimated. Moreover we saw in Fig 5.4d, that at this operation point the nonlinear loss was not evolving linearly with the input power. This might be another reason why the model fails to reproduce the experimental gain profile.

While in Fig 5.9a and b the gain profile is close to a lorentzian shape, it is not the case at the working frequency 6.18 GHz as shown in Fig 5.9c. The amplification profile is broader than what is predicted with the model, and we can see the presence of side lobes. Fig 5.9d shows a pump power dependence of the amplification at the same operation point and we see the appearance of amplification peak splitting at higher pump powers. This could be caused by variations in the environmental impedance. Such variations will reflect the outgoing amplified tones back into the JPA creating standing waves and thus affecting the device gain because of the presence of constructive and destructive interferences [121]. Moreover, changes in the environmental impedance can have the effect of creating two amplification

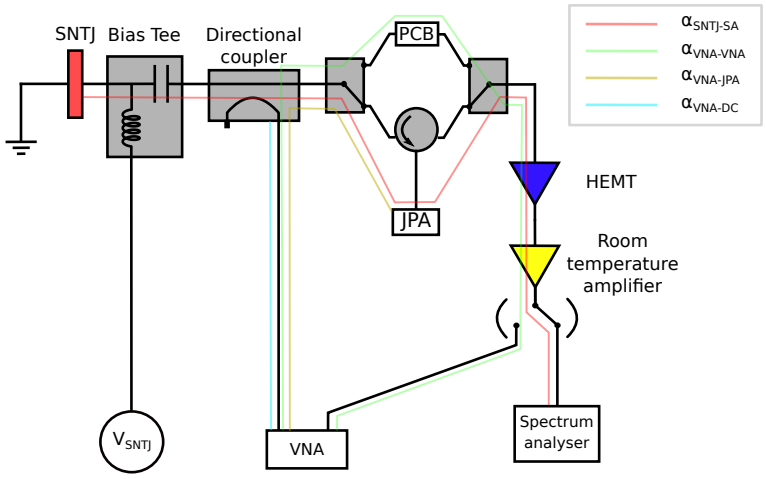

Figure 5.10: Simplified noise measurement setup. The α coefficients indicate the attenuation that we will use in Sec. 5.4.1.a.

lobes as we see in Fig 5.9d [122, 148]. Low quality factors (Q = 70 at this operation point) makes the impacts of variation in the environmental impedance stronger because of the larger range of frequency that the device interact with. One can suspect that it may play a role in the oscillating coupling quality factor that we measured in Chapter 4. Moreover, it might also perturb the power dependence behavior that we analyzed in Sec. 5.1.1 and be a cause to the observed model discrepancy.

5.3 Noise performances

We saw in the last sections that the gJPA is able to provide amplification over a large frequency range which is an important requirement that we can expect from a quantum amplifier. The second aspect of such an amplifier is its added noise which should be as close as possible to the quantum limit, i.e half a photon, the vacuum fluctuation coming from the coupled idler mode (because we are not working at $\omega_s = \omega_i$). Nevertheless, we also saw the presence of nonlinear losses which might be a problem to meet this requirement. Intrinsic loss means coupling to some other modes which have there own vacuum fluctuations. In return, coupling to additional modes can only increase the added noise of the gJPA.

5.3.1 Noise measurement

5.3.1.a Noise extraction

The noise measurement consists of sending a known signal to the amplifier and measure how many photons were added to the known input signal. This process requires a very well calibrated photon source because we would like to measure a photon difference between the input and output of less than one photon. Noise measurements were performed in the XL dilution fridge where we used a shot noise tunnel junction (SNTJ) as a broadband calibrated noise source. The amplified signal was then measured with a spectrum analyzer (SA). A simplified measurement setup is shown in Fig. 5.10 (note that the full measurement setup can

be found in Chapter 3). We can model the power spectrum (PS) measured at the SA plane at the frequency f_s by:

$$PS(f_s) = B\left[G_{ss}(N_s + N_{int}) + G_{si}N_i\right] \tag{5.6}$$

where B is the bandwidth of the SA, G_{ss} is the gain at the signal frequency f_s, G_{si} the conversion gain from the idler to the signal frequency, N_s the power spectral density emitted by the SNTJ at the signal frequency, N_i the power spectral density emitted by the SNTJ at the idler frequency $f_i = 2f_{pump} - f_s$, and N_{int} the intrinsic noise added by the whole chain. Because the SNTJ is a broadband noise source, the emitted signal at the idler frequency is also amplified and converted to the signal frequency. This justifies the term $G_{si}N_i$ in Eq. 5.6 which contributes to the measured power at a frequency f_s [169, 170].

We can express the power spectral density (PSD) emitted by the SNTJ as:

$$\begin{aligned} N(f) = \frac{1}{2}\Bigg[&\left(\frac{e(V_{SNTJ} - V_{shift}) + hf}{2}\right)\coth\left(\frac{e(V_{SNTJ} - V_{shift}) + hf}{2k_BT}\right) \\ &+ \left(\frac{e(V_{SNTJ} - V_{shift}) - hf}{2}\right)\coth\left(\frac{e(V_{SNTJ} - V_{shift}) - hf}{2k_BT}\right)\Bigg] \end{aligned} \tag{5.7}$$

where T is the electronic temperature of the SNTJ, V_{SNTJ} the voltage biasing the SNTJ and V_{shift} an offset voltage. We can separate the gain contribution of the JPA and the rest of the chain such that $G_{ss} = G_{chain}G_{JPA,ss}$. We made the approximation $G_{JPA,si} = G_{JPA,ss} - 1$ which is exact if there is no intrinsic loss in the JPA, and we simplify the notation: $G_{JPA,ss} = G_{JPA}$. Eq.5.6 gives:

$$PS = BG_{chain}\left[G_{JPA}(N_s + N_{int}) + (G_{JPA} - 1)N_i\right] \tag{5.8}$$

with N_s and N_i given by Eq. 5.7 at frequency f_s and f_i respectively. At high gain, we can make the approximation $G = G_{JPA} \approx G_{JPA} - 1$ which shows that the total noise added by the system is: $N_{added} = N_{int} + N_i$ where $N_i = hf_s/2$ when there are only quantum fluctuations in the idler channel. Thus, at best, if there is no intrinsic noise coming from the JPA, the minimal added noise is half a photon coming from the idler channel: this is the standard quantum limit (SQL).

From what was said previously, extracting the added noise at a given frequency requires to fit the SNTJ bias voltage dependence of the measured PS with Eq. 5.8. Experimentally, for each bias voltage we measure the spectrum of the amplified noise emitted by the SNTJ. Fig. 5.11a shows the PS measured by the SA for different values of the SNTJ bias voltage when the gJPA was set at an operating frequency of 6.13 GHz. Eq. 5.7 shows that the power spectral density emitted by the SNTJ is minimal for $V_{SNTJ} = V_{shift} \approx 0$ μV. This is why the PS measured by the SA is higher for increasing $|V_{SNTJ}|$. We can see an increase in the measured PS when approaching the pump frequency (f_p = 6.13 GHz) because of the gain of the gJPA centered around this frequency. Approaching to much the pump frequency makes noise fitting impossible because the pump strongly perturbs the measured PS. Fig. 5.11b shows the measured PS at a fixed frequency of 6.143 GHz corresponding to the dotted line on Fig. 5.11a. For each frequency, we fitted the data with Eq. 5.8 to extract the frequency dependent intrinsic noise N_{int} of the gJPA.

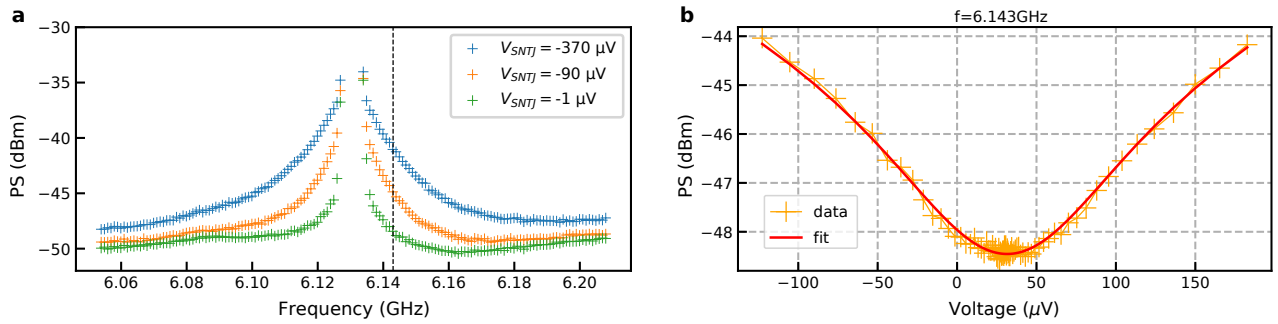

Figure 5.11: (a) Power spectrum measured by the spectrum analyzer for different SNTJ bias voltages. The pump frequency is 6.13 GHz. (b) SNTJ bias voltage dependence of the PS at a fixed frequency of 6.143 GHz corresponding to the dashed line in (a). The fit was performed using Eq. 5.8

5.3.1.b Fitting procedure

Fitting the SNTJ bias voltage dependence of the measured PS with Eq. 5.8 is not straightforward because of the numerous fitting parameters: T, V_{shift}, G_{chain}, G_{JPA} and N_{int}. We thus perform a series of fits with less parameters in order to make the fit of N_{int} easier.

The experimental setup incorporates RF switches making possible to measure the noise performances with the SNTJ signal going through a 50 Ω PCB instead of the gJPA. This is useful to extract separately G_{chain} and thus reduce the number of parameters. For the PCB measurement we thus have to modify Eq. 5.8 by putting $G_{JPA} = 1$. We first determined V_{shift} which is an easy parameter to fit because it is the only one shifting the minimum of the fitted PS with respect to V_{SNTJ}. To do so, we fix T = 150 mK and fit the PS of the PCB measurement at each frequency with three unknown parameters: $V_{shift}(f)$, $G_{chain}(f)$ and $N_{int}^{PCB}(f)$ where $N_{int}^{PCB}(f)$ is the intrinsic noise of the measurement chain (without the gJPA) at the frequency f. From this fit we only keep the frequency averaged fitted V_{shift} = 32±2 μV where the error is the standard deviation of the fitted frequency dependent $V_{shift}(f)$.

We then fit the same set of data with the same equation but with V_{shift} fixed to the previous value and $T(f)$, $G_{chain}(f)$, $N_{int}^{PCB}(f)$ as free parameters. An example of such a fit is shown in Fig. 5.12a where we show the PS as well as the fit for a single frequency $f = 6.14$ GHz. From this fit we only keep the frequency averaged fitted T = 160±60 mK where the error is the standard deviation of the fitted frequency dependent $T(f)$. Fig. 5.12b shows the fitted electronic temperature with respect to the frequency. The value of the electronic temperature depends on DC filtering and grounding of the SNTJ and it is not surprising that it largely exceeds the base temperature of the dilution fridge. The electronic temperature might be frequency dependent but the points are too scattered to actually see a variation with respect to frequency. This is why we averaged over all the fitted $T(f)$ to in order to have a more precise value. This is particularly important because T has a major impact at low bias voltage and is the main source of error on the fitted intrinsic noise.

The last step consists of fitting one last time the same set of data with V_{shift} and T fixed to the previous obtained values and with $G_{chain}(f)$, $N_{int}^{PCB}(f)$ as free parameters. This time we

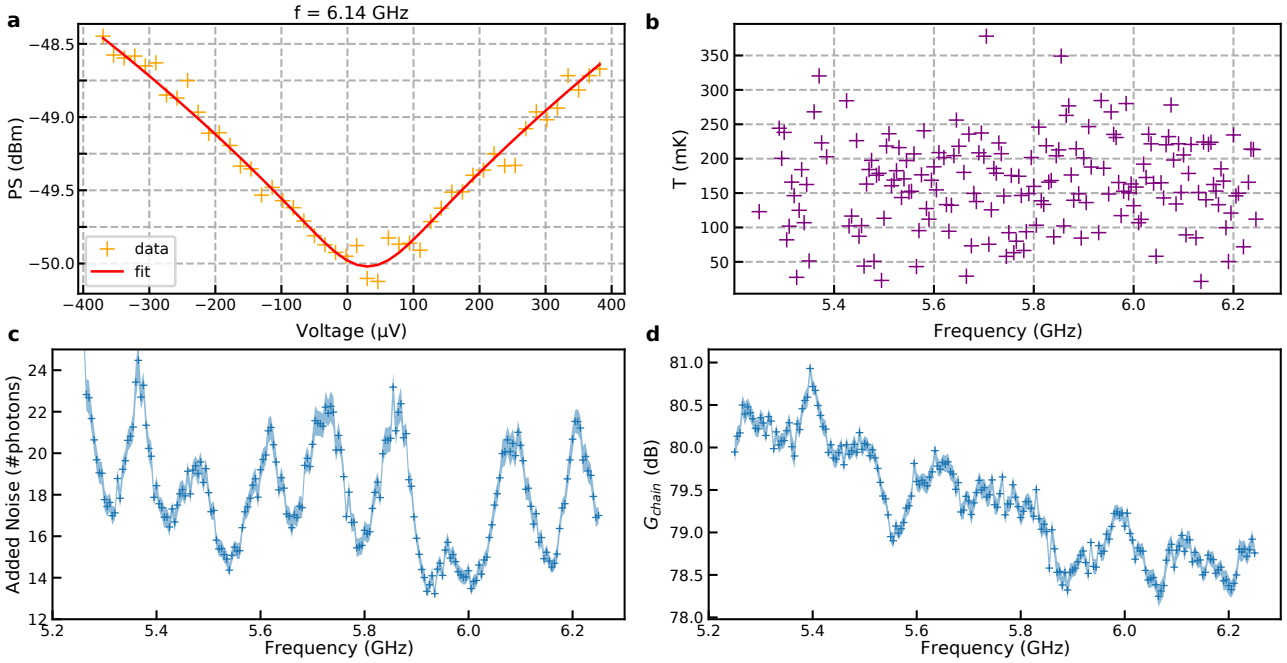

Figure 5.12: (a) SNTJ bias voltage dependence of the PS measured through the 50 Ω PCB at a fixed frequency of 6.14 GHz. (b) Fitted electronic temperature for each frequency with the power spectrum measured through the 50 Ω PCB. Each point of this graph corresponds to a fit equivalent to what is shown in (a). Fitted added noise (c) and gain (d) of the amplification chain with the measurement of the 50 Ω PCB.

do not average the parameters over frequency because the gain does vary over frequency and the error is low compared to the frequency variation. Fig. 5.12c and d show respectively the fitted added noise and the fitted gain of the amplification chain when sending photons through the PCB. The error corresponds to the standard deviation of the fitted parameters. We converted the fitted added noise power spectral density in photon number by dividing $N_{int}^{PCB}(f)$ by hf. We can see that the noise added by the full chain is ranging between 15 and 25 photons which are typical values for a high electron mobility transistors (HEMT) amplifier. The gain shows a negative trend which is confirmed by VNA measurement of the 50 Ω PCB where we see the same profile on $|S_{11}|^2$.

Now that $G_{chain}(f)$, T and V_{shift} are obtained thanks to analysis of the PCB noise measurement, we can come back to the gJPA noise measurement. The PCB noise measurement was not performed right before the gJPA noise measurement making necessary to check whether T and V_{shift} did not shift. We thus performed the same methodology to extract them from the gJPA noise measurement. We obtained this way the same V_{shift} but a different electronic temperature $T = 220 \pm 60$ mK. Because of saturation effect that we will discuss later, the extracted parameters are less accurate on the gJPA noise measurement. For this reason we chose to use T and V_{shift} extracted by the PCB noise measurement. We then fitted the PS of the gJPA noise measurement with Eq. 5.8 and only two free parameters: G_{JPA} and N_{int}.

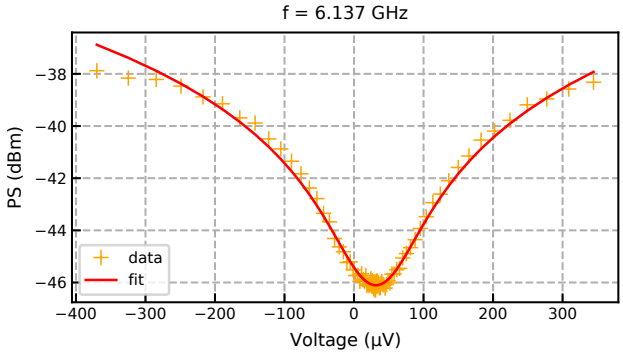

Figure 5.13: Power spectrum as a function of the SNTJ bias voltage at the frequency f = 6.137 GHz.

5.3.1.c Saturation

The fitting noise procedure is more accurate when we can fit the PS over a large SNTJ bias voltage range. Nevertheless, the gJPA is not able to amplify an arbitrary large signal because of saturation effects. Because of this, we were limited on the SNTJ bias voltage range we could use to fit N_{int}. Fig. 5.13 shows the measured PS with respect to the SNTJ bias voltage at f = 6.137 GHz. We can see that at high SNTJ bias voltage, the measured PS is lower than the value predicted by the model. This is because the gJPA saturates and is not able to amplify a stronger signal with the same gain. As a result, we had to limit the SNTJ bias voltage range from -125 to 185 μV whereas the 50 Ω PCB measurements where performed with a range from -400 to 400 μV.

5.3.2 Noise performances of the gJPA

5.3.2.a Fitted noise

By applying the fitting procedure described in the previous section, we obtained G_{JPA} and N_{int} for the gJPA set to operate at f = 6.13 GHz. Fig. 5.14 shows the added noise by the gJPA (a and b), i.e. N_{int} plus half a photon coming from the vacuum noise on the idler mode, and the fitted gJPA gain (c). The error on N_{added} mainly comes from uncertainty on the electronic temperature of the SNTJ. Increasing T has the effect of fitting a lower noise and lowering T does the opposite. We fitted the added noise at T = 100 mK to fix a higher bound on the extracted noise and at T = 220 mK to fix a lower bound. In addition, each fit allows to extract the standard deviation ΔN_{int} on the extracted intrinsic noise. So, the minimum part of the error bars are $N_{added}^{220mK} - \Delta N_{int}^{220mK}$ and the maximum part of the error bars are $N_{added}^{100mK} + \Delta N_{int}^{100mK}$.

We can see that when G_{JPA} is close to 0 dB, the added noise is dominated by the intrinsic noise of the HEMT ($\approx$ 20 photons). When the gJPA gain increases, the total added noise decreases because the HEMT contribution scales as $1/G_{JPA}$ as we will see later. Therefore, at high gain, the total added noise main contribution comes from the added noise of the gJPA. We can see that for the maximal fitted gain, the added noise goes below twice the quantum limit proving that the gJPA noise performance is comparable to standard resonant JPA [8].

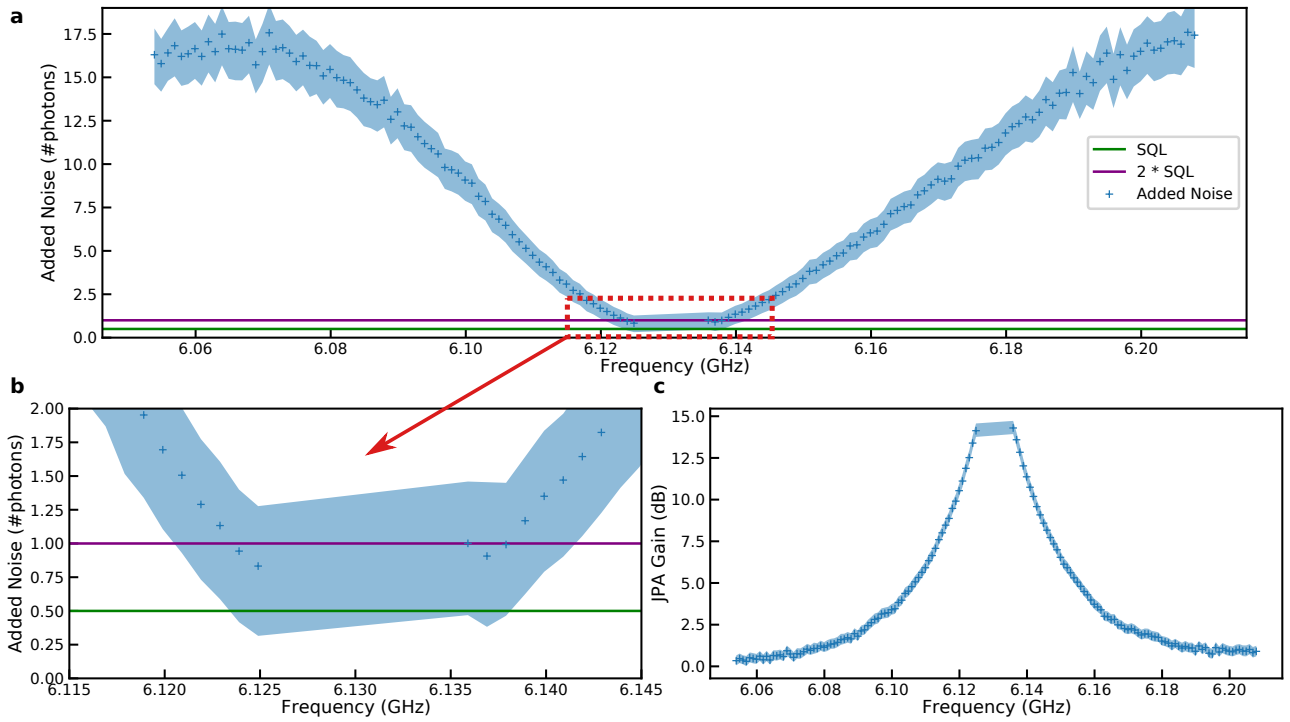

Figure 5.14: (a) Added noise of the gJPA with respect to the frequency. (b) Zoom of (a) corresponding to the delimited area by the dotted red rectangle. (c) Fitted gain of the gJPA with respect to the frequency.

Fig. 5.14 shows that the presence of intrinsic loss did not dramatically decrease the noise performance of the gJPA. Linear intrinsic loss γ_2 increases the added noise of the gJPA by a factor $1 + \frac{\gamma_2}{\gamma_1}$ [90]. The operating point presented here corresponds to the data shown in Fig. 5.4b and d where we saw the presence of nonlinear loss. As a first approximation, we can express the added noise factor including nonlinear loss as $1 + \frac{\gamma_2+\gamma_3|A|^2}{\gamma_1}$. By using the fitted γ_1, γ_2 and γ_3 we find that the noise should have a 10% increase compared to the SQL, i.e. $N_{added} = 0.55$ photon. This proves that our result is consistent, and that despite nonlinear loss, the gJPA can still have noise performances very close to the quantum limit. Nonlinear losses could be mitigated even further by lowering the coupling quality factor $Q_c \propto \frac{1}{\gamma_1}$.

5.3.2.b Effects of attenuation

The error bars on the added noise indicate that the gJPA adds between 0.5 and 1.25 photon of noise. Nevertheless we did not take into account attenuation in between the SNTJ and gJPA in the noise fitting process. As we will show in the rest of the section, it has the effect of overestimating the fitted intrinsic loss. We can rewrite Eq. 5.8 in a simpler way (without the idler part) to simplify the following discussion (it does not change the conclusion):

$$PS = BG_{chain}G_{JPA}(N_s + N_{int}) \tag{5.9}$$

Fig. 5.15 shows a simplified version of the measurement setup. The JPA provides a gain G_{JPA} and an intrinsic noise N_{JPA}, the high electron mobility transistor (HEMT) a gain G_{HEMT} and intrinsic noise N_{HEMT}, the room temperature amplifier a gain G_{300K} and intrinsic noise

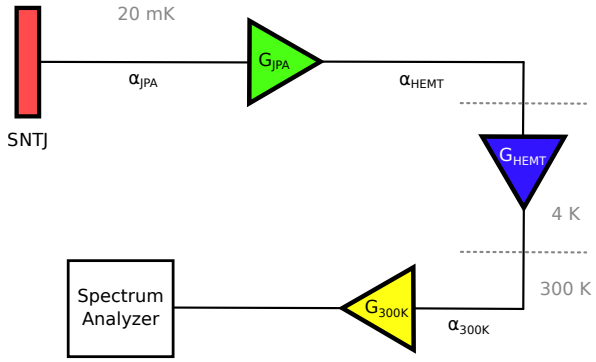

Figure 5.15: Simplified scheme of the amplification setup in the SNTJ measurement. α indicates the loss in between two components ($\alpha \geq 1$, meaning that a signal s becomes s/α after attenuation). We chose not to take into account the loss in between the 300 K amplifier and the spectrum analyzer because it does not bring anything to the discussion.

N_{300K}. Because there is attenuation between each component ($\alpha_{JPA}, \alpha_{HEMT}, \alpha_{300K} > 1$), we can rewrite Eq. 5.9 as:

$$PS = BG_{JPA}G_{HEMT}G_{300K}\left(\frac{N_s}{\alpha_{tot}} + \left[\frac{N_{JPA}}{\alpha_{HEMT}\alpha_{300K}} + \frac{N_{HEMT}}{G_{JPA}\alpha_{300K}} + \frac{N_{300K}}{G_{JPA}G_{HEMT}}\right]\right) \tag{5.10}$$

where $\alpha_{tot} = \alpha_{JPA}\alpha_{HEMT}\alpha_{300K}$ is the total attenuation of the line. To derive Eq. 5.10 we took into account that the noise added by the JPA is attenuated by the rest of the lines and is amplified by all the amplifiers. A similar reasoning was applied for the HEMT and the room temperature amplifier. In the following discussion we can neglect the noise added by the room temperature amplifier because the gain of the HEMT is about 40 dB making the term in N_{300K} negligible. We can thus rewrite the PS measured by the SA as:

$$PS = B\frac{G_{JPA}G_{HEMT}G_{300K}}{\alpha_{tot}}\left(N_s + \left[\alpha_{JPA}N_{JPA} + \frac{\alpha_{JPA}\alpha_{HEMT}N_{HEMT}}{G_{JPA}}\right]\right) \tag{5.11}$$

By fitting the PS measured by the SA without taking the loss into account, i.e. with Eq. 5.9, the extracted gain is:

$$G = \frac{G_{JPA}G_{HEMT}G_{300K}}{\alpha_{tot}} \tag{5.12}$$

and the intrinsic noise is:

$$N_{int} = \alpha_{JPA}N_{JPA} + \frac{\alpha_{JPA}\alpha_{HEMT}N_{HEMT}}{G_{JPA}} \tag{5.13}$$

We can first see that the HEMT contribution to the fitted intrinsic noise scales as $1/G_{JPA}$ as mentioned previously. This is why the first amplifier of the amplification chain sets the noise performance of the whole amplification chain. Indeed, the following amplifiers intrinsic noise contributions are strongly canceled by the first amplifier gain. In the limit of strong JPA gain, we see that the extracted added noise is $\alpha_{JPA}N_{JPA} > N_{JPA}$. This shows that not taking into account the losses makes the extracted noise higher than the real added noise by a factor

α_{JPA}. On the other hand, the extracted gain is smaller than the real gain by a factor $1/\alpha_{tot}$. Nevertheless, because we first fit noise measurement data with the SNTJ sending photons to the PCB, we extract $G_{chain} = G_{HEMT}G_{300K}/\alpha_{tot}$. The fitted G_{JPA} is thus not affected by the presence of attenuation.

We can now try to quantify how much we overestimated the noise by looking at the insertion loss of the different components in between the SNTJ and the JPA:
- SNTJ packaging + bias tee: 1 dB [171]
- Directional coupler C20-0R518: 0.7 dB
- Cryo-switch Radiall R591722600: 0.3 dB
- Circulator LNF-ISC4_12A: 0.2 dB

The total insertion loss is thus 2.2 dB but probably lower because the data sheets of the directional coupler, cryo-switch and circulator give maximal values measured at a temperature above 25 mK. This means that the fitted intrinsic noise should be reduced at maximum by 2.2 dB. We emphasize once more that we plotted the added noise: N_{int} + 0.5 photon. In Fig. 5.14b, we see that the added noise is ranges between 0.5 and 1.25 photon meaning that the intrinsic noise ranges between 0 and 0.75 photon. By taking the 2.2 dB attenuation into account, the intrinsic noise ranges between 0 and 0.45 photon. In conclusion, by taking the attenuation into account, the added noise should range in between 0.5 and 0.95 photon which is also compatible with the value we computed from $\gamma_{1,2,3}$ in the previous section.

5.3.2.c Pump tone effect

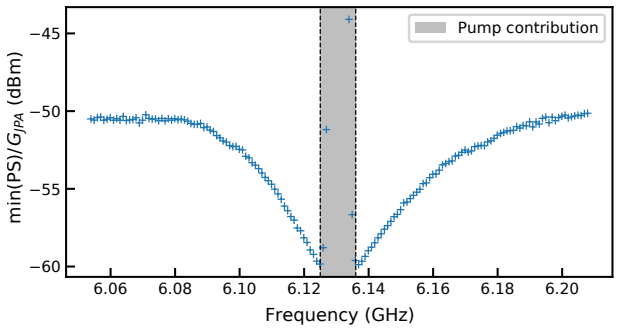

Figure 5.16: Minimum of the PS divided by the gJPA gain as a function of the frequency. The grey part indicates the region where the pump contribution to the measured PS is not negligible with respect to the SNTJ contribution.

In the previous section we saw that reaching a high gJPA gain is important to cancel out the intrinsic noise of the HEMT. This means that the points close the pump frequency are the most important to determine the gJPA noise contribution. Nevertheless, the pump tone was affecting the PS measured by the SA close to the pump frequency. All the measurements were carried with a SA bandwidth of 2 MHz (corresponding to the 3 dB bandwidth) but we can see that the pump affects the measured PS in a bandwidth of 10 MHz around the pump frequency which can be surprising at first. The specifications of the SA indicate that the ratio between the 60 dB and the 3 dB bandwidth is 5. In our measurement we fixed a bandwidth of 2 MHz meaning that we expect the pump to have a 60 dB attenuation at the extremity of a

10 MHz bandwidth. The pump power reaching the device is -90±3 dBm meaning that the SA measures -150 dBm times the gain of the chain at the extremity of a 10 MHz bandwidth. We can compute the power emitted per unit of bandwidth by the SNTJ using Eq. 5.7. In a 2 MHz bandwidth the SNTJ sends -166 dBm also amplified by the gJPA (contrary to the pump). At the extremity of the 10 MHz bandwidth, the gain of the gJPA is ≈15 dB meaning that the SNTJ contribution is -151 dBm times the gain of the chain. If we include the idler amplification, it doubles this value meaning that the SNTJ contribution is -148 dBm. We can see that at the extremity of a 10 MHz bandwidth, the contribution of the pump is not negligible compared to the contribution of the SNTJ explaining why it is not possible to determine the noise in the center region.

Fig. 5.16 shows the minimum of the PS divided by the gain of the gJPA measured with the SA when illuminating the gJPA with the SNTJ. We can see that at low gain, the PS is dominated by the noise emitted by the HEMT. When the gJPA gain increases, the contribution of the noise of the HEMT decreases. We see that getting too close to the pump frequency adds another contribution to the minimum of the PS (the pump) which is confirmed by our calculation.

5.3.2.d Comparison with a quantum limited JPA

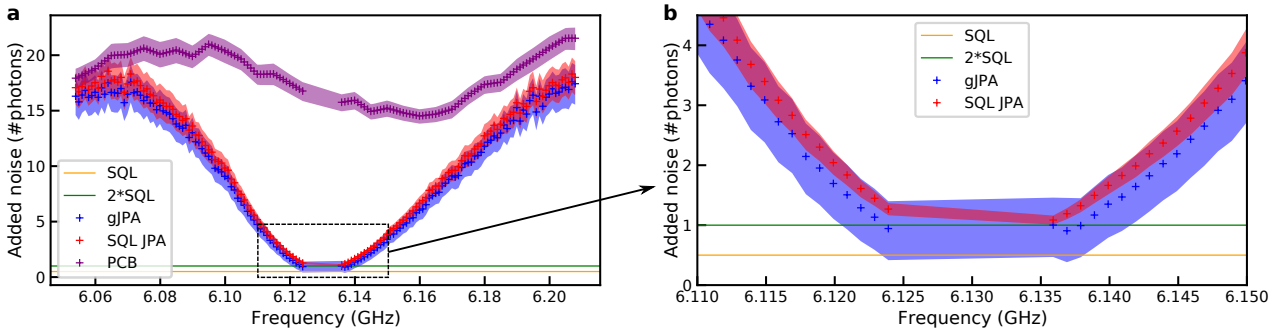

Figure 5.17: (a) and (b) extracted added noise with respect to the frequency. The blue curve represents the extracted added noise from the gJPA measurement. The purple curve represents the added noise extracted by the PCB measurement. The red curve represents the added noise computed from the added noise extracted by the PCB measurement and the measured gain of the gJPA in the limit where the gJPA does not add intrinsic noise (Eq. 5.14).

Despite the fact that we could not extract the added noise in a regime where the gJPA gain is high enough to fully neglect the HEMT noise contribution, and despite the fact that we did not take into account the effect of attenuation, we have enough information to compare the noise performance of the gJPA to a quantum limited JPA. The noise of a quantum limited amplifier means that $N_{JPA} = 0$ which makes the total noise:

$$N_{SQL} = \frac{\alpha_{JPA}\alpha_{HEMT}N_{HEMT}}{G_{JPA}} \tag{5.14}$$

To compute it from the experimental data we use the fitted N_{int}^{PCB}, and the fitted G_{JPA}:

$$N_{SQL} = \frac{N_{int}^{PCB}}{G_{JPA}^{fit}} \tag{5.15}$$

By comparing Eq. 5.14 to Eq. 5.13 we see that the extracted noise for a quantum limited amplifier obtained from the measurement of the PCB and the gJPA can only be smaller than the extracted gJPA noise obtained from the measurement of the gJPA. This might sound trivial, but as we saw earlier, because we did not take into account the effect of attenuation, it is important to verify that we can indeed compare the two noise values. The above statement is valid only if the attenuation between the SNTJ and the gJPA is the same as the attenuation between the SNTJ and the PCB. Because of the presence of the circulator on the gJPA path, there should be at maximum a 0.2 dB attenuation difference that we neglected. Fig. 5.17a and b show the comparison of the added noise of the gJPA and the added noise of a hypothetical quantum limited gJPA. We can see that the gJPA added noise is very close to what we would have obtained if it was at the SQL. This is coherent with the theoretical value of 0.55 photon of added noise that we computed earlier. To conclude, the fact that we extract an added noise which seems to be at twice the quantum limit is only due to the limited gain which is not high enough to fully overcome the added noise of the HEMT.

5.3.2.e Gate voltage dependence

We showed in the previous section that the gJPA was very close to the quantum limit when set to operate at 6.13 GHz. We now try to characterize its noise performances for different gate voltages corresponding to different operating frequencies. The task was more complicated compared to the previous operating frequency. Indeed the 6.13 GHz operation point was ideal in many aspects. First, it corresponds to a low ratio $K/2\gamma$ meaning that the gJPA saturates at higher power. As we saw earlier, saturation makes the SNTJ bias voltage range that we can use to extract the added noise smaller and thus reduces the accuracy of the fit. Moreover, the quality factor is lower at this frequency, meaning that the amplification peak width is larger. This is important because the pump tone forbids to extract the noise close to the maximal gain of the gJPA. As a result, having a broader amplification peak allows to extract the added noise for frequencies where the gain is still high enough to suppress sufficiently the HEMT noise. Last but not least, the gate voltage instability was not strong at this operation point. This allowed to make longer measurements to increase the precision.

Fig. 5.18 shows the added noise of the gJPA with respect to the frequency at different gate voltages corresponding to working frequencies of 5.742 GHz (a), 5.657 GHz (b) and 5.585 GHz (c). We can see that the added noise does not reach the SQL but for the reasons we mentioned earlier, i.e. mainly due to the fact that we could not access large gain frequencies because of the presence of the pump tone. This is why we also plotted the computed added noise that we would have found if $N_{JPA} = 0$ (i.e. if the gJPA was quantum limited) given the measured G_{JPA} and N_{int}^{PCB} as explained in Sec. 5.3.2.d. Comparing the blue and red curves indicates that the gJPA is close to the quantum limit for all the operation points shown here. We note that in Fig. 5.18b, the measured added noise seems to go under the SQL JPA added noise. At this operation point, the error on the fitted N_{int} is comparable to the temperature

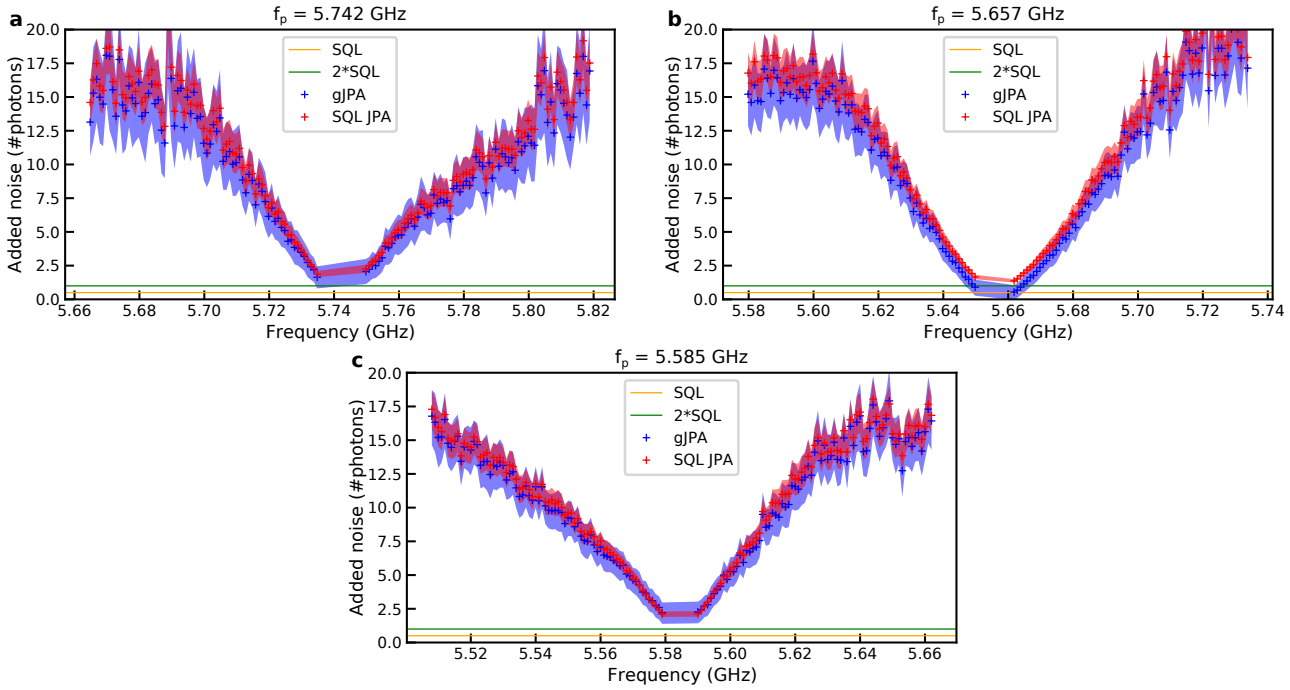

Figure 5.18: Added noise of the gJPA (blue) with respect to the frequency at different gate voltages corresponding to working frequencies of 5.742 GHz (a), 5.657 GHz (b) and 5.585 GHz (c). The theoretical added noise of a quantum limited JPA (given the measured gJPA gain) obtained by the procedure described in the last section is shown in red. The data were taken with a SA bandwidth of 2 MHz.

induced error. Because the error comprises only one standard deviation, it could explain why we get such a non physical result.

5.4 Compression point

We have demonstrated in the previous sections that the gJPA can reach gains over 20 dB with a gate tunable frequency and an added noise close to the standard quantum limit. The last important characteristic to address is its saturation behavior. The compression point tells how much photons can be amplified without reducing the gain. To characterize it, we measure the input power at which the gain drops by 1 dB. We call this power the 1 dB compression point (P_{1dB}).

5.4.1 Compression point in the sionludi XL

5.4.1.a Attenuation calibration

Measuring the 1 dB compression point requires to know exactly the power reaching the gJPA. Considering the large number of elements in between the VNA sending the input power and the gJPA, it is hard to get a precise value because of the uncertainty on the attenuation and loss of each of them. Nevertheless, the XL dilution fridge offers a way to calibrate the attenuation in a more precise way. The presence of the SNTJ allows to extract the gain of

the amplification chain as we saw in Sec. 5.3. Therefore, by combining the information of the noise measurement and VNA measurement, we can deduce the attenuation in between the VNA and the gJPA. Fig. 5.10 represents a simplified version of the experimental setup and will be useful to understand the following discussion. Note that the complete measurement setup can be found in Chapter 3.

From the noise measurement of the gJPA pump off, we can extract the gain and attenuation between the SNTJ and the SA: $\alpha_{SNTJ-SA}$ = 55±2 dB where the error comes from the standard deviation on the fitted gain. From the VNA measurement of the PCB we can extract the gain and attenuation from VNA to VNA: $\alpha_{VNA-VNA}$ = -58.5±1 dB. Because the P_{1dB} was not measured at the same output powers than the calibration measurement, we added 1 dB of error on $\alpha_{VNA-VNA}$. By taking the difference between the two, we get the attenuation between the VNA and the directional coupler α_{VNA-DC} = -113.5±3 dB.

α_{VNA-DC} has to be corrected because $\alpha_{SNTJ-SA}$ includes loss between the SNTJ and the directional coupler which is not on the path of the VNA measurement. The loss of the ensemble SNTJ + bias tee is estimated to 1 dB such that α_{VNA-DC} = -114.5 dB. The value of interest being the attenuation between the VNA and the JPA: $\alpha_{VNA-JPA}$, we need to add the attenuation of the RF switch (0.3 dB), the circulator (0.2 dB) and the microwave cables (0.65 + 0.45 dB at maximum): $\alpha_{VNA-JPA}$ = -116.1±3 dB. Then, because we used the VNA measurement of the PCB and we compared it to the SNTJ measurement of the device pump off, we also need to correct the difference coming from not taking the same path between the two switches. The presence of the circulator adds 2 x 0.2 dB and the loss of the device pump off compared to the PCB is at max 2 dB. This means that the total corrected attenuation between the VNA and the gJPA is -118.5±3 dB.

Computing the attenuation given by the specifications of all the components (including the cables) in between the VNA and the gJPA gives a total attenuation of -118 dB by taking typical attenuation found in the specifications sheets and can reach 130 dB by taking the maximum indicated attenuation. This value is not straightforward to estimate because of the temperature dependence (for the cables in particular) and uncertainty on the components attenuation and loss. Nevertheless, the estimated value is consistent with the value extracted from the measurements.

5.4.1.b Measurement of the compression point

The compression point was measured at the operating frequency 6.1285 GHz. The maximal gain was found using the method described in Sec. 5.2.1. We then performed a VNA power dependence overall several frequencies as shown in Fig. 5.19a. We can see that for a fixed frequency, the gain is constant over a certain range of signal power. Above a signal power threshold, the gain starts to drop meaning that the gJPA is saturated. As a reference, we chose to show the 1 dB compression for a gain of 20 dB in Fig. 5.19b. We can see a 1 dB drop of the gain at an input power of -123 dBm. Because there is some uncertainty on the attenuation we can conclude that at this operation point the 1 dB compression point is -123±3 dBm. Such value is comparable to the best values obtained with single Josephson junction JPA [103].

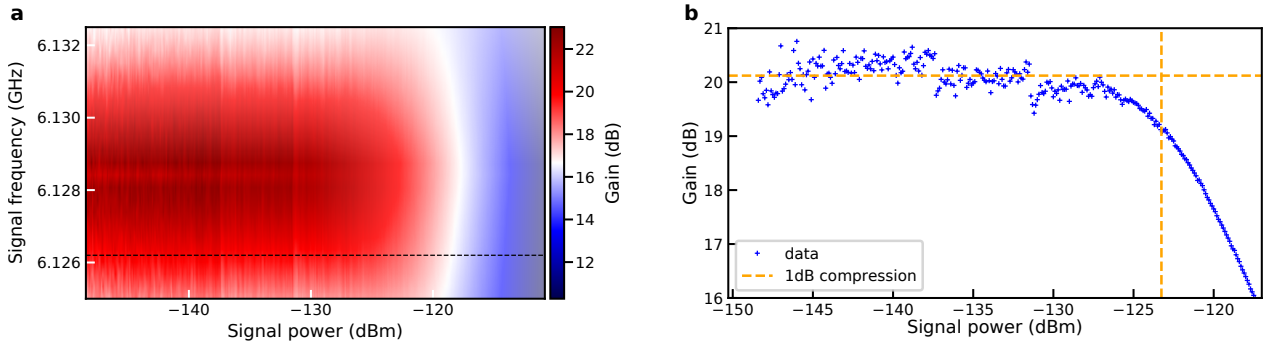

Figure 5.19: (a) Gain as a function of the signal power and frequency. The gain is computed by dividing $|S_{11}|^2$ pump on by $|S_{11}|^2$ pump off. (b) Gain as a function of the signal power at f = 6.1262 GHz corresponding to the dashed line in (a). The orange lines indicate the 1 dB compression point.

The compression point should scale as $2\gamma/K$ as shown in Chapter2. At this operation point we find a ratio $2\gamma/K$ = 2.4 x 10^3. As calculated in [90], this should correspond to a 1 dB compression point of 2-3 photons. One can estimate the number of signal photon in the resonator using the following equations:

$$P_{in} = P_{ref} + P_{loss} \tag{5.16}$$

$$P_{ref} = |S_{11}|^2 P_{in} \tag{5.17}$$

$$P_{loss} = 2\gamma_2 < n > \hbar\omega \tag{5.18}$$

where P_{in} is the input power, P_{loss} the power lost because of internal loss, P_{ref} the power reflected by the JPA and $< n >$ the mean number of photons inside the resonator. By using this simple model with an input power of -123 dBm, we find $< n >$ = 6 which is compatible with the value given by the pump back-action model given the error on P_{1dB}.

5.4.2 Compression point in the sionludi L

When measuring the gJPA in the sionludi XL, we only measured the compression point at the operation point presented in the previous section. The rest of the compression point measurements were done in the sionludi L which is not optimal because there is no SNTJ to calibrate the attenuation $\alpha_{VNA-JPA}$ in between the VNA and the gJPA. By summing the attenuation of all the components we find $\alpha_{VNA-JPA}$ = 124±4 dB. Moreover, because of the gate instability it was difficult to maintain optimal amplification parameters long enough to perform a precise compression point measurement. This was an issue because for low compression points, the power of the input signal is very small requiring long averaging time.

Moreover, it was not always possible to reach a 20 dB gain making difficult the comparison between the P_{1dB} at different operation points. Fig. 5.20a shows the product of the measured P_{1dB} with the associated gain as well as the ratio $2\gamma/K$ at different operation points. When the main source of saturation is pump back-action, the compression point has almost a linear dependence on the gain and justifies to use such a quantity (Fig. 7.7 of [92]). In all the saturation mechanisms presented in Chapter 2, the saturation point scales as $2\gamma/K$. We can see in

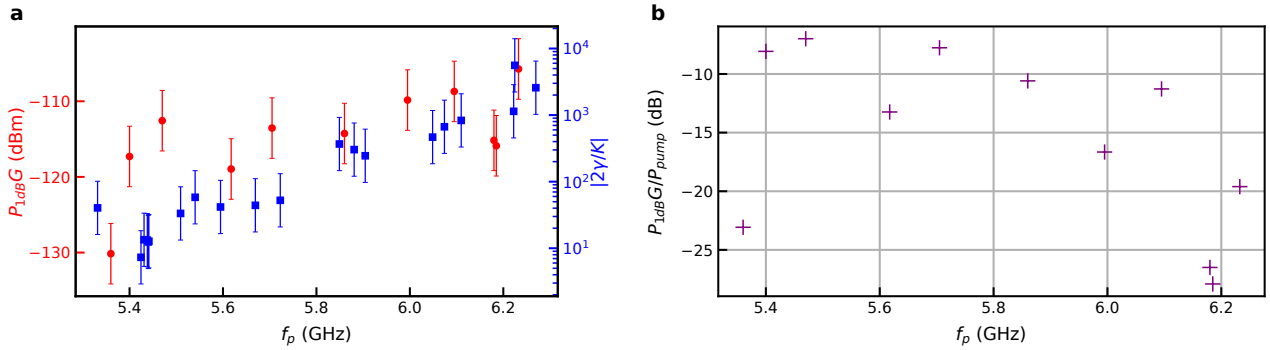

Figure 5.20: (a) Output power at the 1 dB compression point (red) and $2\gamma/K$ ratio (blue) for different operating points frequencies f_p. The error bars correspond to the 4 dB uncertainty on the attenuation between the VNA and the gJPA. (b) Ratio of the output power at the 1 dB compression point over the pump power for different operating points frequencies f_p.

our data that the product $P_{1dB}G$ seems to decrease with decreasing $2\gamma/K$ ratio as predicted in these models. By fixing G = 20 dB, we can see that P_{1dB} is between -140 and -130 dBm on most of the accessible frequency range. This is comparable to single tunnel Josephson junction JPAs [100, 101]. Note that this result is compatible with the -123±3 dBm 1 dB compression point measured in the XL dilution fridge. There is indeed 4 dB of error on the measurement performed in the L dilution fridge. Moreover, the approximation considering the compression point having a linear dependence with the gain is not exact neither.

Fig. 5.20b shows the ratio of the output power at the 1 dB compression point over the pump power for different operation frequencies. This quantity is useful to compare the pump power to the amplified signal and thus estimating if pump back-action was likely to occur. Usually, pump back-action typically occurs when this ratio reaches -20 to -15 dB [92]. We can see that many points are above this ratio. As indicated in the beginning of the section, it was difficult to make long and precise measurement such that the error on this ratio is on the order of a few dB. Nevertheless this does not explain all the points having a $P_{1dB}G/P_{pump}$ ratio above 10 dB. Another reason could come from our way of measuring the data. The amplification research procedure was done at an input power of -140±3 dBm and was designed to find the maximum of amplification. So, there is a possibility that at this input power the gJPA was already at saturation and that we found the optimal parameters including the pump back-action effect. By compensating the pump back-action with a shift in the parameters it is possible to have $P_{1dB}G/P_{pump}$ ratios higher than -15 dB. This possible explanation is particularly relevant for points with a low saturation power (low $2\gamma/K$) and points with high gains. Indeed, the higher the gain, the lower the saturation point.

5.5 Summary of the gJPA performances

We saw in this chapter that the gJPA presents nonlinear loss that can partially be described by the two-photon loss model. Despite the presence of nonlinear loss, we showed that the gJPA could reach gains above 15 dB with a gate tunability of the amplification frequency close to 1 GHz. We also demonstrated that the gJPA noise performances are close to the standard

quantum limit for the studied operation points. Finally, the compression point is comparable to JPAs built with a single tunnel junction. These results show that the gJPA can provide the same performances as a standard JPA, but with an additional control knob: the gate voltage.

Conclusion and perspectives

Conclusion

In this work we demonstrated the possibility of using a graphene Josephson junction to build a gate tunable Josephson parametric amplifier in a current pumped scheme. We managed to obtain high quality graphene devices by encapsulating a single graphene layer flake in between two h-BN flakes. The high quality is demonstrated by the extracted $I_c R_N$ product which is above any values given in the literature for diffusive devices indicating that the graphene junctions are probably ballistic. This resulted in the measurement of a critical current up to 1.5 μA for a junction width of 1.5 μm. We also demonstrated that the critical current of graphene Josephson junctions can be controlled with a simple side gate. Despite the limited graphene area impacted by the side gate, the critical current could be tuned by more than one order of magnitude.

The parametric amplifier was made with a superconducting $\lambda/2$ resonator with a graphene Josephson junction placed in the center of the cavity. We developed a design with DC lines directly connected to the resonator which offers a platform allowing to probe the DC properties of graphene as well as performing RF measurement in a single device. The low impact of these additional lines was demonstrated with electromagnetic simulations and measurements. By using electromagnetic simulations as well as measurements together with a lumped and a distributed model, we were able to extract the geometric parameters of the circuit and compute the Josephson inductance with respect to the gate voltage. The extracted inductance indicated a forward skewness of the current phase relation compatible with what is reported in the literature. As expected from the critical current measurement, the Josephson inductance can be tuned by more than one order of magnitude enabling to tune the resonance frequency of the circuit between 5.2 and 6.3 GHz.

The analysis of the device response beyond the linear regime allowed to extract its nonlinear properties. A two-photon loss model was used in order to take into account additional loss appearing at higher input microwave power originating from the dynamics in Andreev bound states population. We showed that this model could be used as a first approximation, but needs to be corrected in order to capture the complex nature of loss and a current phase relation deviating from the one of a tunnel junction. The limits of this standard two-photon loss model, as well as the strong microwave background, forced us to develop fitting procedures that allowed to harvest information about the circuit. This way, we could extract the Kerr coefficient which plays an important role in parametric amplification. By using the circuit parameters extracted in the linear regime together with a distributed model of the

device, we could also predict the value of the Kerr coefficient with respect to the gate voltage. Comparison between this model and the values obtained in the nonlinear regime using the two-photon loss model shows a good agreement.

Finally, we characterized the device in the linear amplification regime. We demonstrated amplification with 20 dB gain which is the milestone for overcoming noise of the classical amplifiers in the rest of the amplification chain. The Josephson parametric amplifier being based on a resonant structure suffers from the gain bandwidth product limiting the amplification to a few Megahertz frequency range. We used the gate tunability of the device to overcome this problem. By tuning the resonance frequency of the resonator, we performed parametric amplification on a 1 GHz frequency range which is as good as equivalent circuits controlled by a magnetic flux with the use of a SQUID. Moreover, we performed noise measurements and demonstrated that despite the presence of nonlinear loss, graphene based Josephson parametric amplifiers can reach near quantum limited amplification for all the studied gate voltages. We also studied the dynamic range and showed that the graphene based Josephson parametric amplifier can reach a 1 dB compression point of -123 dBm which is comparable to single tunnel junctions based parametric amplifiers. The four properties that we characterized: gain, tunability, noise and dynamic range, showed performances on par with similar devices made of tunnel junctions. Our results expand thus the toolset of electrically tunable superconducting quantum circuits and make them good candidates for the future of quantum computing. Note that during the writing of the present manuscript, works addressing this topic were published starting with the use of a quantum dot [172], graphene [148] and a 2D electron gas [174]. Contrary to our work [173], the graphene Josephson parametric amplifier made by Sarkar *et al.* is in a lumped geometry and is made of a graphene multilayer controlled by a graphite back-gate. They reported gate tunable gains of more 20 dB between 4.5 and 5.2 GHz with added noise close to the standard quantum limit and a compression point of -130 dBm. This independent work confirms that graphene can be used to build a gate tunable JPA and that different geometries should be explored in the future to reach optimized performances.

Perspectives

In this work, we demonstrated a current pumped parametric amplifier with a single graphene Josephson junction. Similar strategies in terms of pumping, impedance engineering and Josephson array could be used to improve the performances of the amplifier. For example, one could imagine an approach where graphene is pumped by a gate voltage at twice the signal frequency. This would be equivalent to the flux pumping of a SQUID and would allow a three wave mixing process in which the pump frequency is separated from the signal frequency. The presence of the DC lines used to probe the DC properties of the graphene junction could also be used to send a DC current allowing for another way of performing three wave mixing [120, 135]. Moreover, given the small length of the graphene Josephson junctions used in this work, it would be possible to make multiple junctions from a unique graphene stack. Exfoliated flakes can easily reach a 10 μm length, meaning that it could be possible to build around 20 junctions in series to reduce the Kerr nonlinearity and increase the dynamic range of the amplifier. Given the important control allowed by the stacking procedure, it is also possible to deposit multiple graphene stacks in the same area to increase

even more the number of junctions.

Appendix

Additional measurements

APPENDIX A

A.1 Frequency mixing

We demonstrated in the Chapter 2 that the gJPA is able to mix different frequencies due to the nonlinearity provided by the gJJ. The gain at the signal frequency f_s has a component depending on the idler frequency f_i linked by $f_s + f_i = 2f_p$ where f_p is the pump frequency. By reciprocity, if a signal is sent at a frequency f_s, it will also contribute to the gain at the frequency f_i. Therefore, one should expect to measure a signal both at frequencies f_s and f_i if a signal is sent only at a frequency f_s. We performed a measurement where the gJPA was set to operate at a frequency of 6.056 GHz (corresponding to f_p). We sent a microwave tone at a frequency f_s and measured the power spectrum (PS) with a spectrum analyzer (SA).

Fig. A.1a shows the PS with respect to the measured frequency (f_{SA}) while sweeping the signal frequency. The vertical line at $f = 6.056$ GHz corresponds to the pump tone. The diagonal line starting from the bottom left corresponds to the tone sent at the signal frequency f_s. This is why it has a slope of one. We can see that there is a symmetric diagonal line compared to the signal tone with respect to the pump frequency starting from the bottom right. This corresponds to the created photons at idler frequency. We can also see that there are diagonal lines with a smaller slope. For example, one line corresponds to a frequency f_2 such that $f_2 = 2f_s - f_p$. This is a four photon process where 2 signal photons and 1 pump photon are converted in a photon at the frequency f_2. To this process is associated an idler signal f_{2i} symmetric with respect to the pump frequency. By zooming in (white rectangle), we can see in Fig. A.1b that there is even a higher order process corresponding to a frequency $f_3 = 3f_s - 2f_p$ which is a sixth order process where 3 signal photons and 2 pump photons are converted into 1 photon at a frequency f_3. Fig. A.1c shows a signal power dependence of the PS. We can see that at low input power the processes leading to f_2 and f_{2i} are too small to be measured. We also see an asymmetry in the intensity of the peak between the f_2 process and the f_{2i} process, probably because of the idler gain being smaller. Fig. A.1d shows a line cut of Fig. A.1c at a signal power of -23 a.u. (the power is given in arbitrary unit because the total

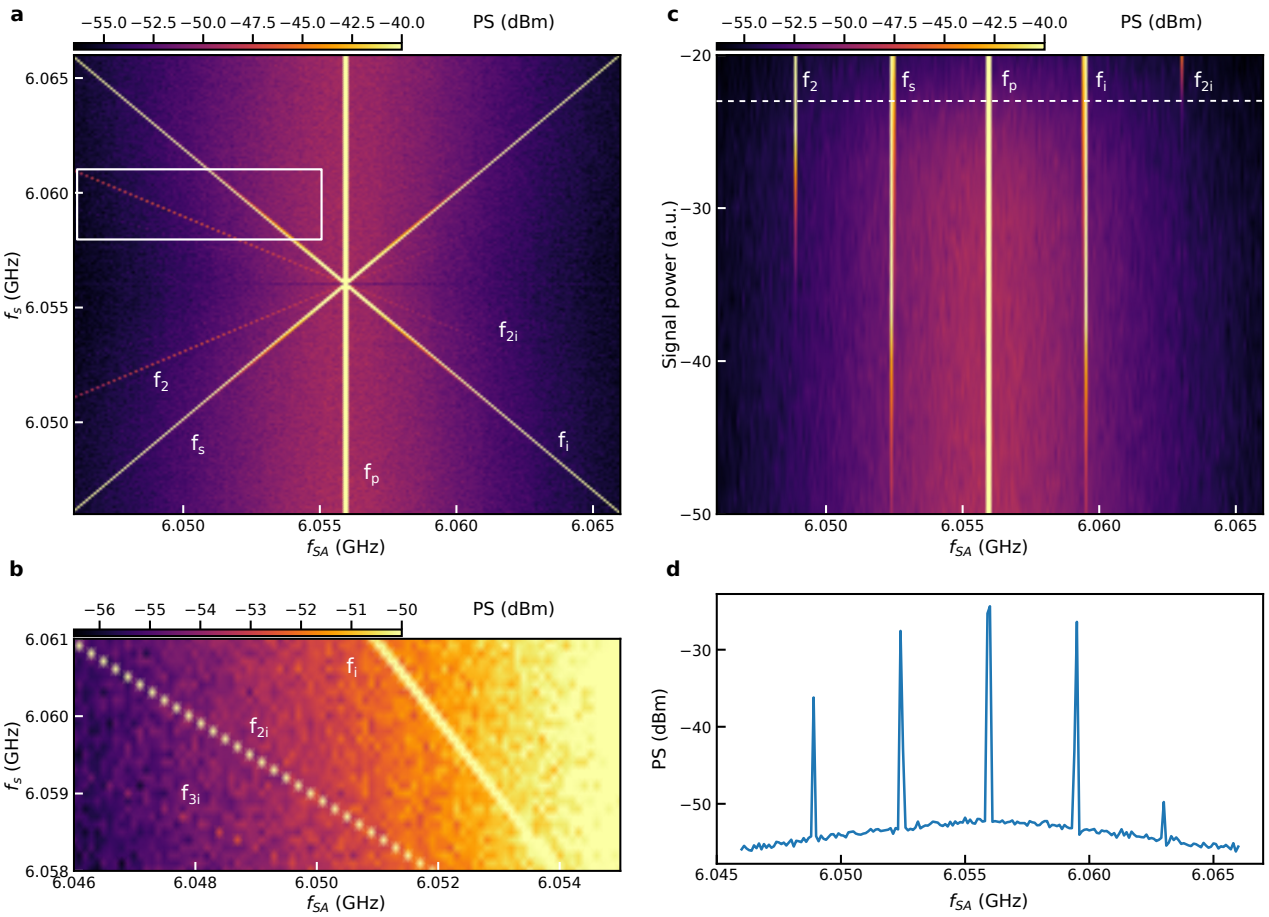

Figure A.1: (a) PS with respect to the measured frequency (f_{SA}) and the signal frequency (f_s). Frequencies corresponding to different frequency mixing mechanisms are indicated. (b) Zoom of (a) in the white rectangle. (c) PS with respect to the measured frequency and the signal power. (d) Horizontal linecut of (c) corresponding to a signal power of -23 u.a. (indicated by the white dashed line on (c)).

attenuation of the measurement chain was not properly calibrated in this experiment).

There are many reasons that could explain the appearance of these additional peaks at f_2 and f_3. To compute the output quantum operator in Chapter 2 we considered only the development of the Josephson energy to the quartic term. Higher order terms could make the measured frequency mixing possible. Moreover, during the linearization procedure we also dropped some nonlinear terms. Beside that, we saw that the nonlinear loss itself could create some frequency mixing. The mixing terms associated to the two-photon loss process do not correspond to the measured frequencies f_2 and f_3 (we saw in Chapter 2 that the frequencies associated to them is $2\omega_p$ and DC). However we saw in Chapter 5 that gJJs exhibit more complicated power dependent losses which could also lead to the measured frequency mixing. Besides that, the skewed current phase relation would modify the Josephson energy which is also a possible explanation.

A.2 Combination of RF + DC measurements

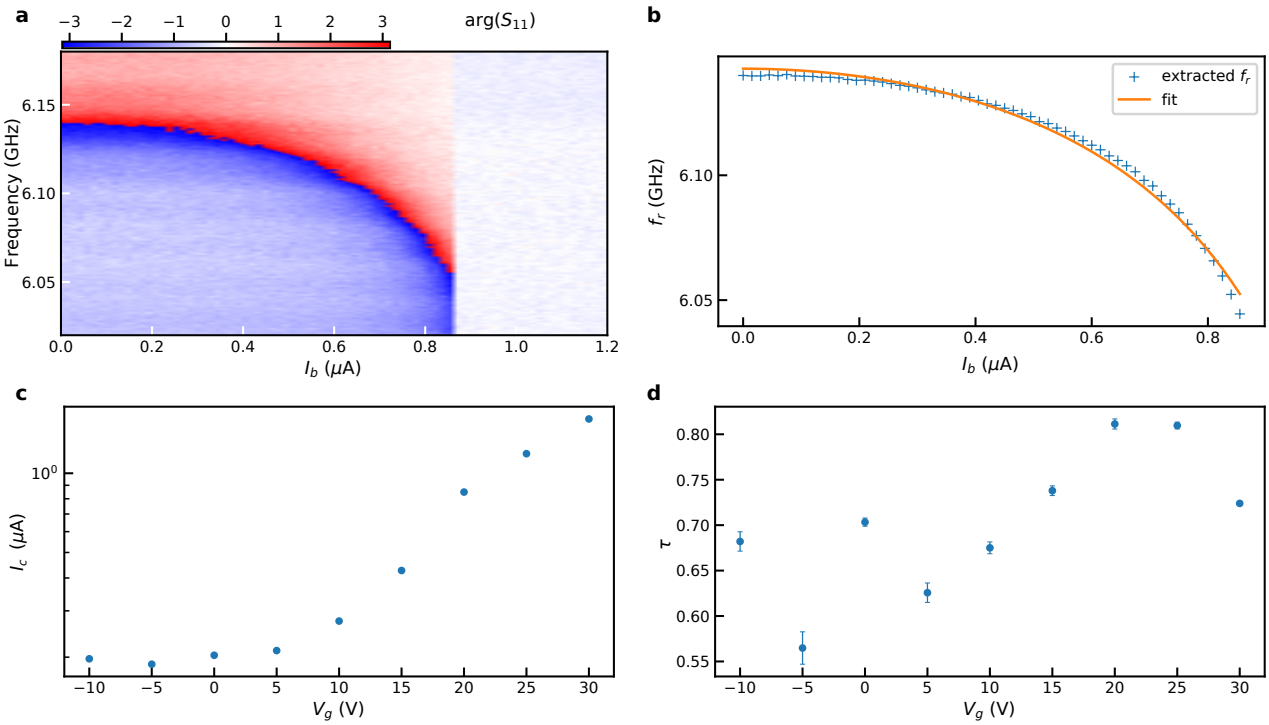

Figure A.2: (a) Phase of the reflection coefficient with respect to the input frequency and the DC bias current at a fixed gate voltage. (b) Extracted f_r from (a) by using the circle fit method. A fit of the extracted f_r is done with τ and I_c as free parameter. (c) and (d) Fitted I_c and τ respectively for different gate voltages. The error bars represent the standard deviation on the fitted parameters. Error bars on I_c are negligible.

The following measurements have been inspired from [67]. The design of the gJPA allows to probe both DC and RF properties at the same time. We saw in Chapter 1 that the CPR of a SNS JJ can be expressed as:

$$I = \sum_{i}^{N} G_N^i \frac{\pi\Delta}{e} \frac{\sin(\phi)}{\sqrt{1-\tau_i \sin^2(\phi/2)}} \tag{A.1}$$

where G_N^i is the conductance of the channel i and τ_i its transparency. By assuming N channels with identical conductance (i.e same transparency τ) we can rewrite:

$$I = I_c \frac{\sin(\phi)}{\sqrt{1-\tau \sin^2(\phi/2)}} \tag{A.2}$$

with $I_c = (\pi\Delta N\tau e)/(2h)$. Therefore, by fixing a DC bias current I_b inside the junction, it is possible to control the phase difference ϕ across the JJ. We can find ϕ as a function of I_b by inverting Eq. A.2. After a bit of algebra we obtain this expression that has to be solved to obtain ϕ:

$$\sin^4(\phi/2) - \frac{4I_c^2 + \tau I_b^2}{4I_c^2} \sin^2(\phi/2) + \frac{I_b^2}{4I_c^2} = 0 \tag{A.3}$$

The solution is thus:

$$\sin^2(\phi/2) = \frac{1}{2}\left(\frac{4I_c^2 + \tau I_b^2}{4I_c^2} - \sqrt{\left(\frac{4I_c^2 + \tau I_b^2}{4I_c^2}\right)^2 - \frac{I_b^2}{I_c^2}}\right) \tag{A.4}$$

where we kept only the solution with a minus sign before the square root term because the plus sign would have made the sinus greater than one. Finally we obtain:

$$\phi = 2\arcsin\left[\sqrt{\frac{1}{2}\left(\frac{4I_c^2 + \tau I_b^2}{4I_c^2} - \sqrt{\left(\frac{4I_c^2 + \tau I_b^2}{4I_c^2}\right)^2 - \frac{I_b^2}{I_c^2}}\right)}\right] \tag{A.5}$$

In Chapter 4 we developed a lumped model where the resonance frequency f_r of the device was given by:

$$f_r = \frac{1}{2\pi}\frac{1}{\sqrt{(L_0 + L_J)C}} \tag{A.6}$$

and we extracted $L_0 = 3.9$ nH and $C = 0.157$ pF thanks to Sonnet simulations and measurement of a similar device but where the gJJ was replaced by a superconducting link (i.e. a bare device). Because L_J is linked to the CPR as:

$$L_J = \frac{\hbar}{2e}\left(\frac{dI}{d\phi}\right)^{-1} \tag{A.7}$$

with:

$$\frac{dI}{d\phi} = \frac{I_c}{\sqrt{1 - \tau\sin^2(\phi/2)}}\left(\cos(\phi) + \frac{1}{4}\frac{\tau\sin^2(\phi)}{1 - \tau\sin^2(\phi/2)}\right) \tag{A.8}$$

there is direct dependence of L_J with ϕ and thus with a DC bias current I_b. By using a microwave measurement to probe f_r with a VNA while sending a DC bias current allows to extract the dependence of L_J with respect to the phase and thus to extract τ and I_c.

Fig. A.2a shows the phase of the reflection coefficient S_{11} measured with a VNA with respect to the VNA input frequency and the DC bias current. The resonance frequency f_r corresponds to a 2π phase shift (blue to red) of S_{11}. We can see that increasing the bias current creates a downshift of f_r because it has the effect of increasing L_J. We used the circle fit method to extract the resonance frequency as a function of the bias current as shown in Fig. A.2b. We then fitted $f_r(I_b)$ using Eq. A.6 with L_J computed from Eq. A.7 and Eq. A.8 with I_c and τ as free parameters. We can see that the fit does not follow exactly the extracted f_r. This might come from the simplistic model where the distributed resonator is considered as lumped. By repeating this process for several gate voltages, we can extract I_c and τ with respect to the gate voltage. Fig. A.2c and d show the extracted I_c and τ respectively with respect to the gate voltage. The values of I_c are equivalent to what was measured and presented in Chapter 4 indicating that the model is coherent. We can see that the averaged transparency τ depends on the gate voltage and ranges between 0.56 and 0.81. It looks like τ is smaller close to the charge neutrality point ($V_{CNP} \approx 3$ V).

Extracting τ allows to compute the skewness S of the CPR which is an indicator of how much the Josephson energy will differ compared to the the Josephson energy of a tunnel junction. The skewness is defined as $S = (2\phi_{max}/\pi) - 1$ where ϕ_{max} is the phase at which the CPR reaches a maximum ($S = 1$ for $\tau = 1$ and $S = 0$ for $\tau = 0$). Fig. A.3a and b show the computed S and fitted τ respectively with respect to the resonance frequency at $I_b = 0$. Fig. A.3c and d show the same quantities but with respect to the fitted critical current. We can see that the average transparency is smaller at low critical current and reaches a maximum close to $I_c = 1$ μA. The skewness ranges between 0.15 and 0.26 which are typical values for gJJs [67, 59, 60].

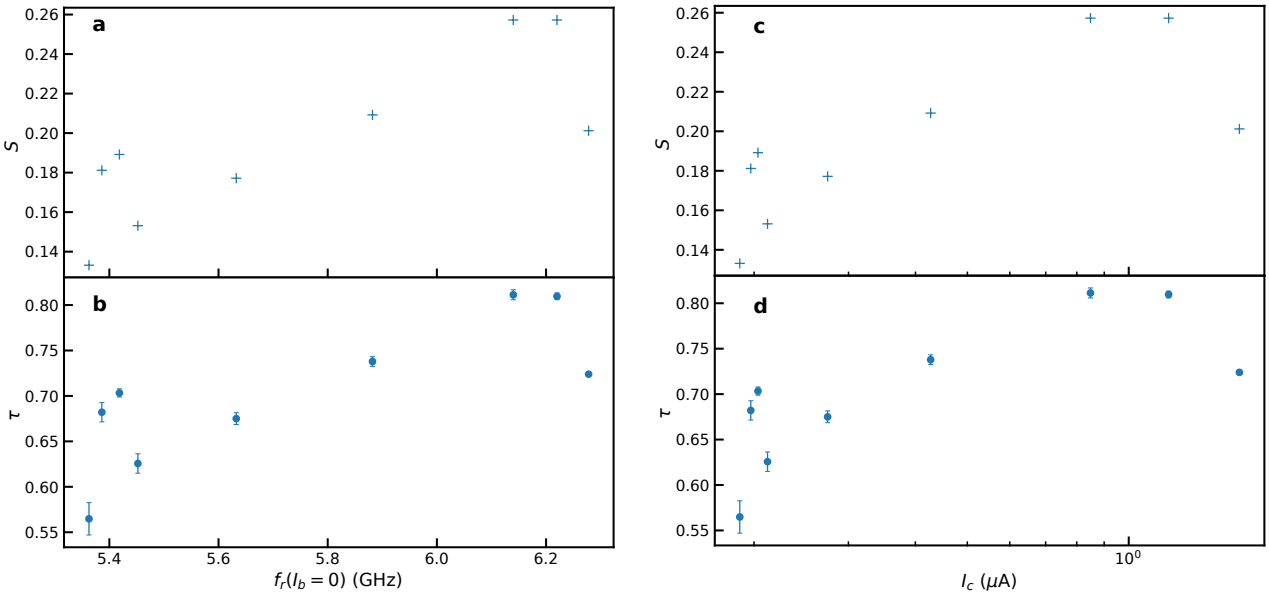

Figure A.3: (a) and (b) Computed skewness and fitted τ respectively with respect to the resonance frequency at zero bias current. (c) and (d) Computed skewness and fitted τ respectively with respect to the fitted critical current. The error bars represent the standard deviation on the fitted parameter. Error bars on S were not computed.

A.3 Additional device

We measured a similar device with a gJJ width of 2 μm, a resonator width of 5 μm and less on-chip gate filtering. In Fig. A.4a we plot the differential resistance dV/dI as a function of the bias current I_b and the gate voltage V_g. Close to V_g=-8 V and V_g=6 V the device exhibited current leakage through the gate. We were thus not able to reach the Dirac point. The critical current can be modulated from 0.5 μA to 1.2 μA. This enabled the control of the resonance frequency from 5.8 GHz to 6.05 GHz as we can see in Fig. A.4b where the phase of the S_{11} parameter is plotted with respect to the gate voltage. The S_{11} parameter was here normalized with a trace taken at 1.1 K before the device entered in the superconducting state. In Fig. A.4c the gain of the graphene based JPA is plotted for three gate voltages (-7.2 V, -6.1 V, -3.5 V). The gain is above 15 dB on the full range of frequency reachable by the device. We also measured the gain on another device which was not electrically tunable.

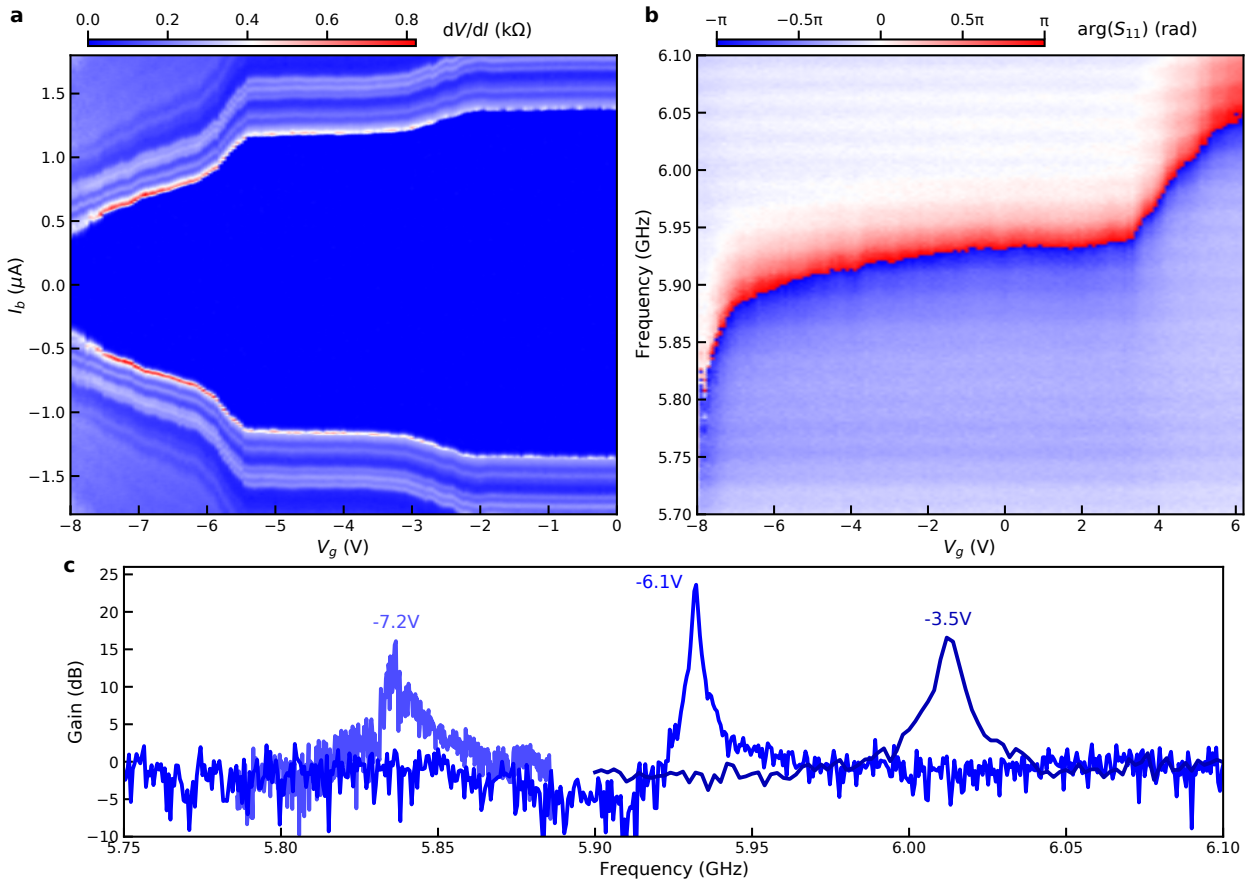

Figure A.4: Additional device measurement. (a) Differential resistance as a function of the bias current and gate voltage. (b) S_{11} as a function of gate voltage. (c) Gain measured for three different gate voltages.

List of instruments

- VNA: Anritsu MS46522B-20
- Pump and additional microwave source : R&S SMB 20GHz
- Gate: Keithley 2400
- DC bias source: Yokogawa 7651
- Lockin amplifier: SRS 830
- Multimeter: HP34401A
- Spectrum analyzer: R&S FSQ signal analyzer

List of abbreviations

- 2D: Two dimensional
- 3WM: Three wave mixing
- 4WM: Four wave mixing
- ABS: Andreev bound states
- CNP: Charge neutrality point
- CPR: Current phase relation
- CVD: Chemical vapor deposition
- DPA: Degenerate parametric amplifier
- ebeam: Electron beam
- gJJ: Graphene Josephson junction
- gJPA: Graphene Josephson parametric amplifier
- h-BN: Hexagonal boron nitrite
- HEMT: High electron mobility transistor
- IMPA: Impedance matched Josephson parametric amplifier
- IPA: Isopropyl alcohol
- JBA: Josephson bifurcation amplifier
- JJ: Josephson junction
- JPA: Josephson parametric amplifier

- MAR: Multiple Andreev reflections
- NDPA: Non-degenerate parametric amplifier
- PDMS: Polydimethylsiloxane
- PMMA: Polymethyl methacrylate
- PPC: Polypropylene carbonate
- PS: Power spectrum
- PSD: Power spectral density
- RIE: Reactive ion etching
- SA: Spectrum analyzer
- SIS: Superconducting/insulator/superconducting
- SNAIL: Superconducting nonlinear asymmetric inductive element
- SNS: Superconducting/normal/superconducting
- SNTJ: Shot noise tunnel junction
- SQL: Standard quantum limit
- SQUID: Superconducting quantum interference device
- TL: Transmission line
- TWPA: Travelling wave parametric amplifier
- VNA: Vector network analyzer

Bibliography

[1] Carlton M. Caves. Quantum limits on noise in linear amplifiers. *Physical Review D* **26**(8), 1817–1839 (1982). (Cited on page 1.)

[2] B. Yurke, L. R. Corruccini, P. G. Kaminsky, *et al.* Observation of parametric amplification and deamplification in a Josephson parametric amplifier. *Physical Review A* **39**(5), 2519–2533 (1989). (Cited on page 1.)

[3] Y Nakamura, Y.˜A. Pashkin, and J.˜S. Tsai. Coherent control of macroscopic quantum states in a single-Cooper-pair box. *Nature* **398**(April), 786–788 (1999). (Cited on page 1.)

[4] D. Vion, A. Aassime, A. Cottet, *et al.* Manipulating the quantum state of an electrical circuit. *Science* **296**(5569), 886–889 (2002). (Cited on page 1.)

[5] Alexandre Blais, Ren Shou Huang, Andreas Wallraff, *et al.* Cavity quantum electrodynamics for superconducting electrical circuits: An architecture for quantum computation. *Physical Review A - Atomic, Molecular, and Optical Physics* **69**(6), 1–14 (2004). (Cited on page 1.)

[6] A. Wallraff, D. I. Schuster, A. Blais, *et al.* Strong coupling of a single photon to a superconducting qubit using circuit quantum electrodynamics. *Nature* **431**(7005), 162–167 (2004). (Cited on page 1.)

[7] Jens Koch, Terri M. Yu, Jay Gambetta, *et al.* Charge-insensitive qubit design derived from the Cooper pair box. *Physical Review A - Atomic, Molecular, and Optical Physics* **76**(4), 1–19 (2007). (Cited on page 1.)

[8] M. A. Castellanos-Beltran and K. W. Lehnert. Widely tunable parametric amplifier based on a superconducting quantum interference device array resonator. *Applied Physics Letters* **91**(8) (2007). (Cited on pages 1, 52, 55, and 131.)

[9] Z. R. Lin, K. Inomata, W. D. Oliver, *et al.* Single-shot readout of a superconducting flux qubit with a flux-driven Josephson parametric amplifier. *Applied Physics Letters* **103**(13) (2013). (Cited on page 1.)

[10] J. Stehlik, Y. Y. Liu, C. M. Quintana, *et al.* Fast charge sensing of a cavity-coupled double quantum dot using a Josephson parametric amplifier. *Physical Review Applied* **4**(1), 1–10 (2015). (Cited on page 1.)

[11] A Bienfait, JJ Pla, Y Kubo, *et al.* Reaching the quantum limit of sensitivity in electron spin resonance. *Nature nanotechnology* **11**(3), 253–257 (2016). (Cited on page 1.)

[12] M. Tse, Haocun Yu, N. Kijbunchoo, *et al.* Quantum-Enhanced Advanced LIGO Detectors in the Era of Gravitational-Wave Astronomy. *Physical Review Letters* **123**(23), 231107 (2019). (Cited on page 1.)

[13] Kelly M Backes, Daniel A Palken, S Al Kenany, *et al.* A quantum enhanced search for dark matter axions. *Nature* **590**(7845), 238–242 (2021). (Cited on page 1.)

[14] Frank Arute, Kunal Arya, Ryan Babbush, *et al.* Quantum supremacy using a programmable superconducting processor. *Nature* **574**(7779), 505–510 (2019). (Cited on page 2.)

[15] L. Dicarlo, J. M. Chow, J. M. Gambetta, *et al.* Demonstration of two-qubit algorithms with a superconducting quantum processor. *Nature* **460**(7252), 240–244 (2009). (Cited on page 2.)

[16] K. S. Novoselov, A. K. Geim, S V Morozov, *et al.* Electric Field Effect in Atomically Thin Carbon Films Supplementary. *Science* **5**(1), 1–12 (2004). (Cited on pages 6 and 8.)

[17] K. S. Novoselov, A. K. Geim, S. V. Morozov, *et al.* Two-dimensional gas of massless Dirac fermions in graphene. *Nature* **438**(7065), 197–200 (2005). (Cited on page 6.)

[18] A. H. Castro Neto, F. Guinea, N. M.R. Peres, *et al.* The electronic properties of graphene. *Reviews of Modern Physics* **81**(1), 109–162 (2009). (Cited on page 6.)

[19] Alexis Coissard. Les états fondamentaux du graphène en régime Hall quantique et leurs canaux de bord The many-body ground states of the graphene quantum Hall effect and their edge channels. *PhD thesis* **tel-036229** (2021). (Cited on page 6.)

[20] Landry Bretheau. Localized Excitations in Superconducting Atomic Contacts : PROBING THE ANDREEV DOUBLET. *PhD thesis* (2013). (Cited on page 10.)

[21] W Chang. Superconducting Proximity Effect in InAs Nanowires. *PhD thesis* (June), 1–192 (2014). (Cited on page 10.)

[22] J. A. Sauls. Andreev bound states and their signatures. *Philosophical Transactions of the Royal Society A: Mathematical, Physical and Engineering Sciences* **376**(2125) (2018). (Cited on page 10.)

[23] Wang. Superconducting Proximity Effect in Graphene Nanodevices: A Transport and Tunneling Study. *PhD thesis* (2015). (Cited on page 10.)

[24] A F Andreev. The thermal conductivity of the intermadiate state in superconductors. *Soviet Physics JETP* **19**(5), 1228 (1964). (Cited on page 11.)

[25] Philip F. Bagwell. Suppression of the Josephson current through a narrow, mesoscopic, semiconductor channel by a single impurity. *Physical Review B* **46**(19), 12573–12586 (1992). (Cited on page 13.)

[26] Landry Bretheau, Joel I.Jan Wang, Riccardo Pisoni, *et al.* Tunnelling spectroscopy of Andreev states in graphene. *Nature Physics* **13**(8), 756–760 (2017). (Cited on pages 13, 19, 61, and 62.)

[27] Vinay Ambegaokar and Alexis Baratoff. Tunneling between superconductors. *Physical Review Letters* **11**(2), 104 (1963). (Cited on pages 14 and 95.)

[28] T.M. Klapwijk, G.E. Blonder, and M. Tinkham. Explanation of subharmonic energy gap structure in superconducting contacts. *Physica B+C* **109-110**(December 2015), 1657–1664 (1982). (Cited on pages 14, 95, and 103.)

[29] D. Averin and A. Bardas. ac Josephson effect in a single quantum channel. *Physical Review Letters* **75**(9), 1831–1834 (1995). (Cited on page 14.)

[30] E. N. Bratus', V. S. Shumeiko, and G. Wendin. Theory of subharmonic gap structure in superconducting mesoscopic tunnel contacts. *Physical Review Letters* **74**(11), 2110–2113 (1995). (Cited on page 14.)

[31] Gil Ho Lee and Hu Jong Lee. Proximity coupling in superconductor-graphene heterostructures. *Reports on Progress in Physics* **81**(5) (2018). (Cited on pages 15 and 16.)

[32] Jinho Park, Jae Hyeong Lee, Gil Ho Lee, *et al.* Short Ballistic Josephson Coupling in Planar Graphene Junctions with Inhomogeneous Carrier Doping. *Physical Review Letters* **120**(7), 77701 (2018). (Cited on pages 16, 17, 95, and 104.)

[33] M. Ben Shalom, M. J. Zhu, V. I. Fal'ko, *et al.* Quantum oscillations of the critical current and high-field superconducting proximity in ballistic graphene. *Nature Physics* **12**(4), 318–322 (2016). (Cited on page 16.)

[34] Hubert B. Heersche, Pablo Jarillo-Herrero, Jeroen B. Oostinga, *et al.* Bipolar supercurrent in graphene. *Nature* **446**(7131), 56–59 (2007). (Cited on page 16.)

[35] Jae Hyun Choi, Gil Ho Lee, Sunghun Park, *et al.* Complete gate control of supercurrent in graphene p-n junctions. *Nature Communications* **4**(May) (2013). (Cited on page 16.)

[36] Xu Du, Ivan Skachko, and Eva Y. Andrei. Josephson current and multiple Andreev reflections in graphene SNS junctions. *Physical Review B - Condensed Matter and Materials Physics* **77**(18), 1–5 (2008). (Cited on page 16.)

[37] Çağlar Girit, V. Bouchiat, O. Naaman, *et al.* Tunable graphene dc superconducting quantum interference device. *Nano Letters* **9**(1), 198–199 (2009). (Cited on page 16.)

[38] Feng Miao, Wenzhong Bao, Hang Zhang, and Chun Ning Lau. Premature switching in graphene Josephson transistors. *Solid State Communications* **149**(27-28), 1046–1049 (2009). (Cited on page 16.)

[39] C. Ojeda-Aristizabal, M. Ferrier, S. Guéron, and H. Bouchiat. Tuning the proximity effect in a superconductor-graphene-superconductor junction. *Physical Review B - Condensed Matter and Materials Physics* **79**(16), 1–5 (2009). (Cited on page 16.)

[40] I. V. Borzenets, U. C. Coskun, S. J. Jones, and G. Finkelstein. Phase diffusion in graphene-based Josephson junctions. *Physical Review Letters* **107**(13), 1–4 (2011). (Cited on page 16.)

[41] U. C. Coskun, M. Brenner, T. Hymel, *et al.* Distribution of supercurrent switching in graphene under the proximity effect. *Physical Review Letters* **108**(9), 1–5 (2012). (Cited on page 16.)

[42] Dongchan Jeong, Jae Hyun Choi, Gil Ho Lee, *et al.* Observation of supercurrent in PbIn-graphene-PbIn Josephson junction. *Physical Review B - Condensed Matter and Materials Physics* **83**(9), 1–5 (2011). (Cited on page 16.)

[43] Chung Ting Ke, Ivan V. Borzenets, Anne W. Draelos, *et al.* Critical Current Scaling in Long Diffusive Graphene-Based Josephson Junctions. *Nano Letters* **16**(8), 4788–4791 (2016). (Cited on page 16.)

[44] Katsuyoshi Komatsu, Chuan Li, S. Autier-Laurent, *et al.* Superconducting proximity effect in long superconductor/graphene/ superconductor junctions: From specular Andreev reflection at zero field to the quantum Hall regime. *Physical Review B - Condensed Matter and Materials Physics* **86**(11), 1–9 (2012). (Cited on page 16.)

[45] V. E. Calado, S. Goswami, G. Nanda, *et al.* Ballistic Josephson junctions in edge-contacted graphene. *Nature Nanotechnology* **10**(9), 761–764 (2015). (Cited on page 16.)

[46] F. Amet, C. T. Ke, I. V. Borzenets, *et al.* Supercurrent in the quantum Hall regime. *Science* **352**(6288), 966–969 (2016). (Cited on page 16.)

[47] I. V. Borzenets, F. Amet, C. T. Ke, *et al.* Ballistic Graphene Josephson Junctions from the Short to the Long Junction Regimes. *Physical Review Letters* **117**(23), 1–5 (2016). (Cited on page 16.)

[48] M. T. Allen, O. Shtanko, I. C. Fulga, *et al.* Spatially resolved edge currents and guided-wave electronic states in graphene. *Nature Physics* **12**(2), 128–133 (2016). (Cited on page 16.)

[49] Monica T. Allen, Oles Shtanko, Ion C. Fulga, *et al.* Observation of Electron Coherence and Fabry-Perot Standing Waves at a Graphene Edge. *Nano Letters* **17**(12), 7380–7386 (2017). (Cited on page 16.)

[50] M. J. Zhu, A. V. Kretinin, M. D. Thompson, *et al.* Edge currents shunt the insulating bulk in gapped graphene. *Nature Communications* **8**, 6–11 (2017). (Cited on page 16.)

[51] M. Titov and C. W.J. Beenakker. Josephson effect in ballistic graphene. *Physical Review B - Condensed Matter and Materials Physics* **74**(4), 1–4 (2006). (Cited on pages 16, 61, and 103.)

[52] P. Dubos, H. Courtois, B. Pannetier, *et al.* Josephson critical current in a long mesoscopic S-N-S junction. *Physical Review B - Condensed Matter and Materials Physics* **63**(6), 1–5 (2001). (Cited on page 16.)

[53] IO Kulik and AN Omel'yanchuk. Jept lett. 21 (1975). *Sov. J. Low Temp. Phys* **3**, 459 (1977). (Cited on pages 16 and 17.)

[54] IO Kulik. Omel, yanchuk, an. *Sov. J. Low Temp. Phys* **3**, 459–462 (1977). (Cited on pages 16 and 17.)

[55] IO Kulik. Macroscopic quantization and the proximity effect in sns junctions. *Soviet Journal of Experimental and Theoretical Physics* **30**, 944 (1969). (Cited on page 17.)

[56] Evgueni F. Talantsev. Dc self-field critical current in superconductor dirac-cone material/superconductor junctions. *Nanomaterials* **9**(11), 1–15 (2019). (Cited on page 17.)

[57] Yositake Takane and Ken Ichiro Imura. Josephson current through a planar junction of graphene. *Journal of the Physical Society of Japan* **80**(4), 1–4 (2011). (Cited on page 17.)

[58] Yositake Takane and Ken Ichiro Imura. Quasiclassical theory of the Josephson effect in ballistic graphene junctions. *Journal of the Physical Society of Japan* **81**(9), 1–13 (2012). (Cited on page 17.)

[59] G. Nanda, J. L. Aguilera-Servin, P. Rakyta, *et al.* Current-Phase Relation of Ballistic Graphene Josephson Junctions. *Nano Letters* **17**(6), 3396–3401 (2017). (Cited on pages 18, 100, and 151.)

[60] C. D. English, D. R. Hamilton, C. Chialvo, *et al.* Observation of nonsinusoidal current-phase relation in graphene Josephson junctions. *Physical Review B* **94**(11), 1–7 (2016). (Cited on pages 18 and 151.)

[61] Ziwei Dou, Taro Wakamura, Pauli Virtanen, *et al.* Phase-dependent dissipation and supercurrent of a graphene-superconductor ring under microwave irradiation. *arXiv* (2020). (Cited on pages 19, 20, and 100.)

[62] H. Le Sueur, P. Joyez, H. Pothier, *et al.* Phase controlled superconducting proximity effect probed by tunneling spectroscopy. *Physical Review Letters* **100**(19), 1–4 (2008). (Cited on page 19.)

[63] Dmitri A. Ivanov, Raphael von Roten, and Gianni Blatter. Minigap in a long disordered SNS junction: Analytical results. *Physical Review B - Condensed Matter and Materials Physics* **66**(5), 1–4 (2002). (Cited on page 17.)

[64] Luca Banszerus, Florian Libisch, Andrea Ceruti, *et al.* Minigap and Andreev bound states in ballistic graphene. *arXiv* pages 1–6 (2020). (Cited on page 18.)

[65] CWJ Beenakker. *Andreev billiards*, volume 174. Springer (2005). (Cited on page 18.)

[66] Roy Haller, Gergő Fülöp, David Indolese, *et al.* Phase-dependent microwave response of a graphene Josephson junction. *arXiv* (2021). (Cited on pages 19, 20, 60, 61, 98, and 100.)

[67] Felix E. Schmidt, Mark D. Jenkins, Kenji Watanabe, *et al.* Probing the current-phase relation of graphene Josephson junctions using microwave measurements. *arXiv* (2020). (Cited on pages 20, 61, 100, 110, 149, and 151.)

[68] Felix E. Schmidt, Mark D. Jenkins, Kenji Watanabe, *et al.* A ballistic graphene superconducting microwave circuit. *Nature Communications* **9**(1), 1–7 (2018). (Cited on pages 21, 22, and 96.)

[69] L. Casparis, N. J. Pearson, A. Kringhøj, *et al.* Voltage-controlled superconducting quantum bus. *Physical Review B* **99**(8), 3–9 (2019). (Cited on pages 21 and 22.)

[70] Ramón Aguado. A perspective on semiconductor-based superconducting qubits. *Applied Physics Letters* **117**(24), 240501 (2020). (Cited on page 21.)

[71] G. De Lange, B. Van Heck, A. Bruno, *et al.* Realization of Microwave Quantum Circuits Using Hybrid Superconducting-Semiconducting Nanowire Josephson Elements. *Physical Review Letters* **115**(12), 1–5 (2015). (Cited on page 22.)

[72] T. W. Larsen, K. D. Petersson, F. Kuemmeth, *et al.* Semiconductor-Nanowire-Based Superconducting Qubit. *Physical Review Letters* **115**(12), 1–5 (2015). (Cited on page 22.)

[73] Morten Kjaergaard, Mollie E. Schwartz, Jochen Braumüller, *et al.* Superconducting Qubits: Current State of Play. *Annual Review of Condensed Matter Physics* **11**, 369–395 (2020). (Cited on page 22.)

[74] R. Barends, J. Kelly, A. Megrant, *et al.* Coherent josephson qubit suitable for scalable quantum integrated circuits. *Physical Review Letters* **111**(8), 1–5 (2013). (Cited on page 22.)

[75] L. Casparis, T. W. Larsen, M. S. Olsen, *et al.* Gatemon benchmarking and two-qubit operations. *Physical Review Letters* **116**(15), 1–5 (2016). (Cited on page 22.)

[76] R. Barends, J. Kelly, A. Megrant, *et al.* Superconducting quantum circuits at the surface code threshold for fault tolerance. *Nature* **508**(7497), 500–503 (2014). (Cited on page 22.)

[77] Lucas Casparis, Malcolm R. Connolly, Morten Kjaergaard, *et al.* Superconducting gatemon qubit based on a proximitized two-dimensional electron gas. *Nature Nanotechnology* **13**(10), 915–919 (2018). (Cited on page 22.)

[78] Joel I.Jan Wang, Daniel Rodan-Legrain, Landry Bretheau, *et al.* Coherent control of a hybrid superconducting circuit made with graphene-based van der Waals heterostructures. *Nature Nanotechnology* **14**(2), 120–125 (2019). (Cited on page 22.)

[79] Thomas Kanne, Mikelis Marnauza, Dags Olsteins, *et al.* Epitaxial pb on inas nanowires for quantum devices. *Nature Nanotechnology* **16**(7), 776–781 (2021). (Cited on page 22.)

[80] J. G. Kroll, W. Uilhoorn, K. L. van der Enden, *et al.* Magnetic field compatible circuit quantum electrodynamics with graphene Josephson junctions. *Nature Communications* **9**(1) (2018). (Cited on page 22.)

[81] Alexandre Blais, Arne L. Grimsmo, S. M. Girvin, and Andreas Wallraff. Circuit quantum electrodynamics. *Reviews of Modern Physics* **93**(2) (2021). (Cited on page 24.)

[82] M. a. Castellanos-Beltran. Development of a Josephson Parametric Amplifier for the Preparation and Detection of Nonclassical States of Microwave Fields by. *PhD thesis of University of Colorado* page 300 (2010). (Cited on page 24.)

[83] J. Bourassa, F. Beaudoin, Jay M. Gambetta, and A. Blais. Josephson-junction-embedded transmission-line resonators: From Kerr medium to in-line transmon. *Physical Review A - Atomic, Molecular, and Optical Physics* **86**(1), 1–13 (2012). (Cited on pages 29, 31, 32, 33, and 99.)

[84] M. Wallquist, V. S. Shumeiko, and G. Wendin. Selective coupling of superconducting charge qubits mediated by a tunable stripline cavity. *Physical Review B - Condensed Matter and Materials Physics* **74**(22), 1–10 (2006). (Cited on page 30.)

[85] Jérôme Bourassa. Non-linéarité et couplages lumière-matière en électrodynamique quantique en circuit. *PhD thesis* (2012). (Cited on page 32.)

[86] C. W. Gardiner and M. J. Collett. Input and output in damped quantum systems: Quantum stochastic differential equations and the master equation. *Physical Review A* **31**(6), 3761–3774 (1985). (Cited on page 34.)

[87] Bernard Yurke and Eyal Buks. Performance of cavity-parametric amplifiers, employing Kerr nonlinearites, in the presence of two-photon loss. *Journal of Lightwave Technology* **24**(12), 5054–5066 (2006). (Cited on pages 34, 55, and 110.)

[88] I. Siddiqi, R. Vijay, F. Pierre, *et al.* RF-driven Josephson bifurcation amplifier for quantum measurement. *Physical Review Letters* **93**(20), 1–4 (2004). (Cited on pages 37, 51, and 95.)

[89] R. Vijay, M. H. Devoret, and I. Siddiqi. Invited Review Article: The Josephson bifurcation amplifier. *Review of Scientific Instruments* **80**(11) (2009). (Cited on pages 37 and 51.)

[90] Christopher Eichler and Andreas Wallraff. Controlling the dynamic range of a josephson parametric amplifier. *EPJ Quantum Technology* **1**(1), 1–19 (2014). (Cited on pages 42, 43, 44, 48, 55, 107, 132, and 139.)

[91] Archana Kamal, Adam Marblestone, and Michel Devoret. Signal-to-pump back action and self-oscillation in double-pump Josephson parametric amplifier. *Physical Review B - Condensed Matter and Materials Physics* **79**(18) (2009). (Cited on pages 43 and 52.)

[92] Luca Planat. Resonant and traveling-wave parametric amplification near the quantum limit. Quantum Physics [quant-ph]. Université Grenoble Alpes [2020-..]. *PhD thesis* **tel-031371** (2020). (Cited on pages 44, 51, 57, 125, 139, and 140.)

[93] Bogdan A. Kochetov and Arkady Fedorov. Higher-order nonlinear effects in a Josephson parametric amplifier. *Physical Review B - Condensed Matter and Materials Physics* **92**(22), 1–7 (2015). (Cited on pages 45, 46, 47, 107, and 115.)

[94] Samuel Boutin, David M. Toyli, Aditya V. Venkatramani, *et al.* Effect of Higher-Order Nonlinearities on Amplification and Squeezing in Josephson Parametric Amplifiers. *Physical Review Applied* **8**(5), 1–22 (2017). (Cited on pages 45 and 46.)

[95] Ananda Roy and Michel Devoret. Quantum-limited parametric amplification with Josephson circuits in the regime of pump depletion. *Physical Review B* **98**(4), 1–27 (2018). (Cited on pages 46 and 52.)

[96] G. Liu, T. C. Chien, X. Cao, *et al.* Josephson parametric converter saturation and higher order effects. *Applied Physics Letters* **111**(20) (2017). (Cited on pages 46 and 52.)

[97] D.M. Pozar. *Microwave engineering*. John Wiley & Sons, 4th edition (2012). (Cited on pages 46, 80, 81, and 82.)

[98] V. E. Manucharyan, E. Boaknin, M. Metcalfe, *et al.* Microwave bifurcation of a Josephson junction: Embedding-circuit requirements. *Physical Review B - Condensed Matter and Materials Physics* **76**(1), 1–12 (2007). (Cited on pages 47, 48, and 107.)

[99] Ananda Roy and Michel Devoret. Introduction to parametric amplification of quantum signals with Josephson circuits. *Comptes Rendus Physique* **17**(7), 740–755 (2016). (Cited on pages 50, 52, and 53.)

[100] L. Zhong, E. P. Menzel, R. Di Candia, *et al.* Squeezing with a flux-driven Josephson parametric amplifier. *New Journal of Physics* **15** (2013). (Cited on pages 51, 52, and 140.)

[101] T. Yamamoto, K. Inomata, M. Watanabe, *et al.* Flux-driven Josephson parametric amplifier. *Applied Physics Letters* **93**(4), 1–4 (2008). (Cited on pages 52 and 140.)

[102] C. Eichler, D. Bozyigit, C. Lang, *et al.* Observation of two-mode squeezing in the microwave frequency domain. *Physical Review Letters* **107**(11), 1–5 (2011). (Cited on page 52.)

[103] J. Y. Mutus, T. C. White, E. Jeffrey, *et al.* Design and characterization of a lumped element single-ended superconducting microwave parametric amplifier with on-chip flux bias line. *Applied Physics Letters* **103**(12) (2013). (Cited on pages 52 and 138.)

[104] N. Roch, E. Flurin, F. Nguyen, *et al.* Widely tunable, nondegenerate three-wave mixing microwave device operating near the quantum limit. *Physical Review Letters* **108**(14), 2–6 (2012). (Cited on pages 52 and 53.)

[105] N. Bergeal, F. Schackert, M. Metcalfe, *et al.* Phase-preserving amplification near the quantum limit with a Josephson ring modulator. *Nature* **465**(7294), 64–68 (2010). (Cited on page 52.)

[106] N. Bergeal, R. Vijay, V. E. Manucharyan, *et al.* Analog information processing at the quantum limit with a Josephson ring modulator. *Nature Physics* **6**(4), 296–302 (2010). (Cited on page 52.)

[107] Baleegh Abdo, Flavius Schackert, Michael Hatridge, *et al.* Josephson amplifier for qubit readout. *Applied Physics Letters* **99**(16) (2011). (Cited on page 52.)

[108] Baleegh Abdo, Archana Kamal, and Michel Devoret. Nondegenerate three-wave mixing with the Josephson ring modulator. *Physical Review B - Condensed Matter and Materials Physics* **87**(1), 1–18 (2013). (Cited on page 52.)

[109] N. E. Frattini, U. Vool, S. Shankar, *et al.* 3-wave mixing Josephson dipole element. *Applied Physics Letters* **110**(22), 1–5 (2017). (Cited on pages 54 and 55.)

[110] V. V. Sivak, S. Shankar, G. Liu, *et al.* Josephson Array-Mode Parametric Amplifier. *Physical Review Applied* **13**(2), 1 (2020). (Cited on pages 54 and 55.)

[111] Yu Krupko, V. D. Nguyen, T. Weißl, *et al.* Kerr nonlinearity in a superconducting Josephson metamaterial. *Physical Review B* **98**(9), 1–12 (2018). (Cited on page 55.)

[112] M. A. Castellanos-Beltran, K. D. Irwin, G. C. Hilton, *et al.* Amplification and squeezing of quantum noise with a tunable Josephson metamaterial. *Nature Physics* **4**(12), 928–931 (2008). (Cited on page 55.)

[113] X. Zhou, V. Schmitt, P. Bertet, *et al.* High-gain weakly nonlinear flux-modulated Josephson parametric amplifier using a SQUID array. *Physical Review B - Condensed Matter and Materials Physics* **89**(21), 1–6 (2014). (Cited on page 55.)

[114] C. Eichler, Y. Salathe, J. Mlynek, *et al.* Quantum-limited amplification and entanglement in coupled nonlinear resonators. *Physical Review Letters* **113**(11), 1–5 (2014). (Cited on page 55.)

[115] N. E. Frattini, V. V. Sivak, A. Lingenfelter, *et al.* Optimizing the Nonlinearity and Dissipation of a SNAIL Parametric Amplifier for Dynamic Range. *Physical Review Applied* **10**(5), 1–17 (2018). (Cited on page 55.)

[116] A. B. Zorin. Josephson Traveling-Wave Parametric Amplifier with Three-Wave Mixing. *Physical Review Applied* **6**(3), 1–8 (2016). (Cited on pages 55 and 58.)

[117] Patrick Winkel, Ivan Takmakov, Dennis Rieger, *et al.* Nondegenerate Parametric Amplifiers Based on Dispersion-Engineered Josephson-Junction Arrays. *Physical Review Applied* **13**(2), 1 (2020). (Cited on page 55.)

[118] Erik A. Tholén, Adem Ergül, Evelyn M. Doherty, *et al.* Nonlinearities and parametric amplification in superconducting coplanar waveguide resonators. *Applied Physics Letters* **90**(25), 9–12 (2007). (Cited on page 55.)

[119] E. A. Tholén, A. Ergül, K. Stannigel, *et al.* Parametric amplification with weak-link nonlinearity in superconducting microresonators. *Physica Scripta T* **T137** (2009). (Cited on page 55.)

[120] Daniel J. Parker, Mykhailo Savytskyi, Wyatt Vine, *et al.* A near-ideal degenerate parametric amplifier. *arXiv* (2021). (Cited on pages 55 and 144.)

[121] J. Y. Mutus, T. C. White, R. Barends, *et al.* Strong environmental coupling in a Josephson parametric amplifier. *Applied Physics Letters* **104**(26) (2014). (Cited on pages 56 and 126.)

[122] Tanay Roy, Suman Kundu, Madhavi Chand, *et al.* Broadband parametric amplification with impedance engineering: Beyond the gain-bandwidth product. *Applied Physics Letters* **107**(26) (2015). (Cited on pages 56 and 127.)

[123] K. M. Sundqvist, S. Kintaş, M. Simoen, *et al.* The pumpistor: A linearized model of a flux-pumped superconducting quantum interference device for use as a negative-resistance parametric amplifier. *Applied Physics Letters* **103**(10) (2013). (Cited on page 57.)

[124] Kyle M Sundqvist and Per Delsing. Negative-resistance models for parametrically flux-pumped superconducting quantum interference devices. *EPJ Quantum Technology* **1**, 1–21 (2014). (Cited on page 57.)

[125] O. Naaman, D. G. Ferguson, A. Marakov, *et al.* High Saturation Power Josephson Parametric Amplifier with GHz Bandwidth. *IEEE MTT-S International Microwave Symposium Digest* **2019-June**, 259–262 (2019). (Cited on page 57.)

[126] R. M. Fano. Theoretical limitations on the broadband matching of arbitrary impedances. *Journal of the Franklin Institute* **249**(1), 57–83 (1950). (Cited on page 57.)

[127] Rui Yang and Hui Deng. Fabrication of the Impedance-Matched Josephson Parametric Amplifier and the Study of the Gain Profile. *IEEE Transactions on Applied Superconductivity* **30**(6) (2020). (Cited on page 57.)

[128] J. Grebel, A. Bienfait, Dumur, *et al.* Flux-pumped impedance-engineered broadband Josephson parametric amplifier. *Applied Physics Letters* **118**(14) (2021). (Cited on page 57.)

[129] T. C. White, J. Y. Mutus, I. C. Hoi, *et al.* Traveling wave parametric amplifier with Josephson junctions using minimal resonator phase matching. *Applied Physics Letters* **106**(24), 1–10 (2015). (Cited on page 57.)

[130] Byeong Ho Eom, Peter K. Day, Henry G. Leduc, and Jonas Zmuidzinas. A wideband, low-noise superconducting amplifier with high dynamic range. *Nature Physics* **8**(8), 623–627 (2012). (Cited on pages 57 and 58.)

[131] C. Macklin, K. O'Brien, D. Hover, *et al.* A near-quantum-limited Josephson traveling-wave parametric amplifier. *Science* **350**(6258), 307–310 (2015). (Cited on page 57.)

[132] Martina Esposito, Arpit Ranadive, Luca Planat, and Nicolas Roch. Perspective on traveling wave microwave parametric amplifiers. *Applied Physics Letters* **119**(12) (2021). (Cited on pages 57 and 58.)

[133] Kevin O'Brien, Chris Macklin, Irfan Siddiqi, and Xiang Zhang. Resonant phase matching of Josephson junction traveling wave parametric amplifiers. *Conference on Lasers and Electro-Optics Europe - Technical Digest* **2015-Augus**(15), 1–5 (2015). (Cited on page 57.)

[134] C. Bockstiegel, J. Gao, M. R. Vissers, *et al.* Development of a broadband NbTiN traveling wave parametric amplifier for MKID readout. *Journal of Low Temperature Physics* **176**(3-4), 476–482 (2014). (Cited on page 58.)

[135] M. R. Vissers, R. P. Erickson, H. S. Ku, *et al.* Low-noise kinetic inductance traveling-wave amplifier using three-wave mixing. *Applied Physics Letters* **108**(1) (2016). (Cited on pages 58 and 144.)

[136] L. Ranzani, M. Bal, Kin Chung Fong, *et al.* Kinetic inductance traveling-wave amplifiers for multiplexed qubit readout. *Applied Physics Letters* **113**(24) (2018). (Cited on page 58.)

[137] M. T. Bell and A. Samolov. Traveling-Wave Parametric Amplifier Based on a Chain of Coupled Asymmetric SQUIDs. *Physical Review Applied* **4**(2), 1–9 (2015). (Cited on page 58.)

[138] Wenyuan Zhang, W. Huang, M. E. Gershenson, and M. T. Bell. Josephson Metamaterial with a Widely Tunable Positive or Negative Kerr Constant. *Physical Review Applied* **8**(5), 1–5 (2017). (Cited on page 58.)

[139] Arpit Ranadive, Martina Esposito, Luca Planat, *et al.* Kerr reversal in Josephson meta-material and traveling wave parametric amplification. *Nature Communications* **13**(1) (2022). (Cited on page 58.)

[140] A. B. Zorin, M. Khabipov, J. Dietel, and R. Dolata. Traveling-Wave Parametric Amplifier Based on Three-Wave Mixing in a Josephson Metamaterial. *2017 16th International Superconductive Electronics Conference, ISEC 2017* **2018-Janua**(0), 1–3 (2018). (Cited on page 58.)

[141] A. Metelmann and A. A. Clerk. Quantum-limited amplification via reservoir engineering. *Physical Review Letters* **112**(13), 1–5 (2014). (Cited on page 58.)

[142] A. Metelmann and A. A. Clerk. Nonreciprocal photon transmission and amplification via reservoir engineering. *Physical Review X* **5**(2), 1–16 (2015). (Cited on page 58.)

[143] Leonardo Ranzani and José Aumentado. Graph-based analysis of nonreciprocity in coupled-mode systems. *New Journal of Physics* **17** (2015). (Cited on page 58.)

[144] Michael Mück and Robert McDermott. Radio-frequency amplifiers based on dc SQUIDs. *Superconductor Science and Technology* **23**(9) (2010). (Cited on page 58.)

[145] Lafe Spietz, Kent Irwin, and Jośe Aumentado. Superconducting quantum interference device amplifiers with over 27 GHz of gain-bandwidth product operated in the 4-8 GHz frequency range. *Applied Physics Letters* **95**(9), 8–11 (2009). (Cited on page 58.)

[146] B. Abdo, O. Suchoi, E. Segev, *et al.* Intermodulation and parametric amplification in a superconducting stripline resonator integrated with a dc-SQUID. *Epl* **85**(6) (2009). (Cited on page 58.)

[147] M. P. Defeo, P. Bhupathi, K. Yu, *et al.* Microstrip superconducting quantum interference device amplifiers with submicron Josephson junctions: Enhanced gain at gigahertz frequencies. *Applied Physics Letters* **97**(9), 1–4 (2010). (Cited on page 58.)

[148] Joydip Sarkar, Kishor V. Salunkhe, Supriya Mandal, *et al.* Quantum noise limited microwave amplification using a graphene Josephson junction. *arXiv* pages 1–26 (2022). (Cited on pages 60, 85, 127, and 144.)

[149] J. Martin, N. Akerman, G. Ulbricht, *et al.* Observation of electron-hole puddles in graphene using a scanning single-electron transistor. *Nature Physics* **4**(2), 144–148 (2008). (Cited on page 61.)

[150] S. V. Morozov, K. S. Novoselov, M. I. Katsnelson, *et al.* Strong suppression of weak localization in graphene. *Physical Review Letters* **97**(1), 7–10 (2006). (Cited on page 61.)

[151] Jian Hao Chen, Chaun Jang, Shudong Xiao, *et al.* Intrinsic and extrinsic performance limits of graphene devices on SiO 2. *Nature Nanotechnology* **3**(4), 206–209 (2008). (Cited on page 61.)

[152] G. Cassabois, P. Valvin, and B. Gil. Hexagonal boron nitride is an indirect bandgap semiconductor. *Nature Photonics* **10**(4), 262–266 (2016). (Cited on page 61.)

[153] Gianluca Giovannetti, Petr A. Khomyakov, Geert Brocks, *et al.* Substrate-induced band gap in graphene on hexagonal boron nitride: Ab initio density functional calculations. *Physical Review B - Condensed Matter and Materials Physics* **76**(7), 2–5 (2007). (Cited on page 61.)

[154] L. Wang, I. Meric, P. Y. Huang, *et al.* One-dimensional electrical contact to a two-dimensional material. *Science* **342**(6158), 614–617 (2013). (Cited on pages 62 and 66.)

[155] Goutham Nayak. Enhancing physical properties of low dimensional materials by engineering its environment in composite Van der Waals heterostructures. *pHd thesis HAL Id : tel-02269239* (2019). (Cited on page 63.)

[156] S. J. Haigh, A. Gholinia, R. Jalil, *et al.* Cross-sectional imaging of individual layers and buried interfaces of graphene-based heterostructures and superlattices. *Nature Materials* **11**(9), 764–767 (2012). (Cited on page 66.)

[157] Peter Rickhaus, Markus Weiss, Laurent Marot, and Christian Schönenberger. Quantum hall effect in graphene with superconducting electrodes. *Nano Letters* **12**(4), 1942–1945 (2012). (Cited on page 68.)

[158] Remy Dassonneville. Qubit readouts using a transmon molecule in a 3D circuit quantum electrodynamics architecture. *pHd thesis HAL Id : tel-02274266* (2019). (Cited on page 77.)

[159] M. S. Khalil, M. J.A. Stoutimore, F. C. Wellstood, and K. D. Osborn. An analysis method for asymmetric resonator transmission applied to superconducting devices. *Journal of Applied Physics* **111**(5) (2012). (Cited on page 91.)

[160] S. Probst, F. B. Song, P. A. Bushev, *et al.* Efficient and robust analysis of complex scattering data under noise in microwave resonators. *Review of Scientific Instruments* **86**(2), 16–18 (2015). (Cited on pages 91, 92, and 112.)

[161] Andrew Seredinski, Anne W. Draelos, Ethan G. Arnault, *et al.* Quantum Hall–based superconducting interference device. *Science Advances* **5**(9), 1–7 (2019). (Cited on page 95.)

[162] J. C. Cuevas and A. Levy Yeyati. Subharmonic gap structure in short ballistic graphene junctions. *Physical Review B - Condensed Matter and Materials Physics* **74**(18), 2–5 (2006). (Cited on page 95.)

[163] H. Courtois, M. Meschke, J. T. Peltonen, and J. P. Pekola. Origin of hysteresis in a proximity josephson junction. *Physical Review Letters* **101**(6), 1–4 (2008). (Cited on page 96.)

[164] Matthew N.O. Sadiku, Sarhan M. Musa, and Sudarshan R. Nelatury. Comparison of approximate formulas for the capacitance of microstrip line. *Conference Proceedings - IEEE SOUTHEASTCON* pages 427–432 (2007). (Cited on page 96.)

[165] M. F. Ritter, A. Fuhrer, D. Z. Haxell, *et al.* A superconducting switch actuated by injection of high-energy electrons. *Nature Communications* **12**(1) (2021). (Cited on page 105.)

[166] I. Golokolenov, A. Guthrie, S. Kafanov, *et al.* On the origin of the controversial electrostatic field effect in superconductors. *Nature Communications* **12**(1) (2021). (Cited on page 105.)

[167] A. Di Bartolomeo, F. Giubileo, L. Iemmo, *et al.* Leakage and field emission in side-gate graphene field effect transistors. *Applied Physics Letters* **109**(2) (2016). (Cited on page 106.)

[168] M. Fuechsle, J. Bentner, D. A. Ryndyk, *et al.* Effect of microwaves on the current-phase relation of superconductor- normal-metal-superconductor Josephson junctions. *Physical Review Letters* **102**(12), 9–12 (2009). (Cited on page 119.)

[169] M. Malnou, M. R. Vissers, J. D. Wheeler, *et al.* Three-Wave Mixing Kinetic Inductance Traveling-Wave Amplifier with Near-Quantum-Limited Noise Performance. *PRX Quantum* **2**(1), 1 (2021). (Cited on page 128.)

[170] Arpit Ranadive, Martina Esposito, Luca Planat, *et al.* A reversed Kerr traveling wave parametric amplifier. *arXiv* (2021). (Cited on page 128.)

[171] Su Wei Chang, Jose Aumentado, Wei Ting Wong, and Joseph C. Bardin. Noise measurement of cryogenic low noise amplifiers using a tunnel-junction shot-noise source. *IEEE MTT-S International Microwave Symposium Digest* **2016-Augus**, 3–6 (2016). (Cited on page 134.)

[172] Laurence Cochrane, Theodor Lundberg, David J. Ibberson, *et al.* Quantum Dot-Based Parametric Amplifiers. *arXiv* pages 1–7 (2021). (Cited on page 144.)

[173] Guilliam Butseraen, Arpit Ranadive, Nicolas Aparicio, *et al.* A gate-tunable graphene Josephson parametric amplifier. *arXiv* pages 1–20 (2022). (Cited on page 144.)

[174] D. Phan, P. Falthansl-Scheinecker, U. Mishra, *et al.* Semiconductor quantum-limited amplifier. *arXiv* pages 1–7 (2022). (Cited on page 144.)

[175] Gil Ho Lee, Sol Kim, Seung Hoon Jhi, and Hu Jong Lee. Ultimately short ballistic vertical graphene Josephson junctions. *Nature Communications* **6** (2015).